WARSAW UNIVERSITY OF TECHNOLOGY

DISCIPLINE OF SCIENCE - PHYSICAL SCIENCES

FIELD OF SCIENCE - NATURAL SCIENCES

Ph.D. Thesis

Diana Pawłowska, M.Sc. Eng.

Femtoscopy of strange mesons produced in relativistic Au+Au collisions at the STAR experiment

Supervisor

Hanna Paulina Zbroszczyk, Ph.D. D.Sc. Eng.

Professor WUT

Warsaw 2023

W pierwszej kolejności swoje podziękowania kieruję do
Kochanych Rodziców i Siostry
- Wasze wsparcie i nieustająca wiara w moje możliwości pozwoliły mi być tym kim jestem.
Dziękuję Pawłowi
- za cierpliwość, wyrozumiałość i pokazanie, że każdy problem można rozwiązać podchodząc do niego na spokojnie.

To Wam - moim najbliższym - dedykuję tę pracę.

Chciałabym podziękować Hani
- za uwierzenie w nieśmiałą studentkę 2-go roku i wprowadzenie jej w świat fizyki.
Dziękuję również moim najbliższym współpracownikom:
Danielowi, Hani, Pawłowi i Sebastianowi
- za dzielenie się wiedzą i pomysłami, za czas, który wspólnie spędziliśmy na konferencjach i wyjazdach naukowych.
My final words of thanks go to the members of the HIRG group and the STAR collaboration
- for discussions and exciting ideas.

Abstract

Relativistic collisions of gold ions at the energies achieved in the RHIC experimental complex allow one to study a system that, in the evolution process, has passed through the stage of parton matter (quark-gluon plasma state). Particularly sensitive to this state are particles containing a strange quark and characterized by a small cross-section for interaction with hadronic matter. The lightest particles of this type are charged and neutral kaons. One of the methods enabling the study of the space-time characteristics of the particle emitting source is femtoscopy. This method allows one to determine parameters that cannot be measured directly. Among them, one can distinguish the size, shape, and lifetime of the kinetic freeze-out region of the particles formed in the collision. A two-particle correlation function combines the final state momentum distributions (measured by a dedicated detector) with the space-time particle emission distributions on the order of a few femtometers. The correlations are sensitive to the quantum statistical effects, as well as the final state interaction: strong and Coulomb.

This thesis presents one-dimensional correlation functions of the $K^0_S K^0_S$ system in Au+Au collisions at $\sqrt{s_{NN}}$ = 39 and 200 GeV. This is the first study in the STAR experiment showing differences in centrality and energy of the collisions. The thesis also includes studies of $K^0_S K^+$ pairs in collisions of gold ions at the top RHIC energy. Comparing the results obtained from both analyses will allow one to study the $a_0(980)$ resonance structure responsible for the strong interaction in the case of $K^0_S K^\pm$ correlation. Agreement between sizes will indicate that $a_0(980)$ is a four-quark. However, the divergence will indicate that the resonance is a diquark.

Keywords: quantum chromodynamics, heavy ion collisions, correlation femtoscopy, charged and neutral kaons.

Streszczenie

Relatywistyczne zderzenia jonów złota przy energiach osiąganych w kompleksie eksperymentalnym RHIC pozwalają na badanie systemu, który w procesie ewolucji przeszedł przez etap materii partonowej (stan plazmy kwarkowo-gluonowej). Szczególnie wrażliwe na ten stan są cząstki zawierające kwark dziwny i charakteryzyjące się małym przekrojem czynnym na oddziaływanie z materią hadronową. Najlżejszymi cząstkami tego typu są naładowane i neutralne kaony. Jedną z metod umożliwiającą badanie czasowo-przestrzennych charakterystyk źródła emitującego cząstki jest femtoskopia. Metoda ta pozwala wyznaczyć parametry, których nie można badać w sposób bezpośredni. Wśród nich wyróżniamy rozmiar, kształt oraz czas życia kinematycznego obszaru wymrażania cząstek powstałych w zderzeniu. Aby tego dokonać używa się dwucząstkowej funkcji korelacyjnej łączącej rozkłady pędu cząstek w stanie końcowym (zmierzone przez dedykowany detektor) z czasowo-przestrzennymi rozkładami emisji cząstek, które są rzędu kilku femtometrów. Uzyskane w ten sposób korelacje są wrażliwe na efekty statystyki kwantowej, jak również oddziaływanie w stanie końcowym: silne i kulombowskie.

Niniejsza praca przedstawia jednowymiarowe funkcje korelacyjne układu $K^0_S K^0_S$ w zderzeniach Au+Au przy $\sqrt{s_{NN}}$ = 39 i 200 GeV. Są to pierwsze badania w eksperymencie STAR pokazujące zróżnicowanie pod kątem centralności i energii zderzenia. W pracy zamieszczone zostały również funkcje korelacyjna dla par $K^0_S K^+$ w zderzeniach jonów złota przy najwyższej energii RHIC. Porównanie wyników uzyskanych z obu analiz pozwoli zbadać strukturę rezonansu $a_0(980)$ odpowiedzialnego za oddziaływanie silne w przypadku korelacji $K^0_S K^\pm$. Zgodność pomiędzy rozmiarami będzie równoznaczna z tym, że $a_0(980)$ jest czterokwarkiem. Natomiast rozbieżność będzie wskazywała, że rezonans jest dikwarkiem.

Słowa kluczowe: chromodynamika kwantowa, zderzenia ciężkich jonów, femtoskopia korelacyjna, naładowane i neutralne kaony.

Academic achievements and publications

Since 2017, I have been an active member of the STAR collaboration, which brings together scientists worldwide. As part of the work for the experiment, I was part of the team collecting data from elementary and nuclear collisions several times (April 2018, March - April 2019, February 2020, April 2021 and 1-8 March 2022 - online). At that time, I was the Shift Crew, i.e., the person responsible for the correctness of the collected data. My task was to compare online plots on the quality of colliding beams and data with reference ones and report changes to the team leader.

In addition, in April - June 2018, I performed Service Work to check the correct operation of the new iTPC detector. It was related to an upgrade of the TPC detector, which replaced all inner TPC sectors. This increased readout pad raws from 13 to 40, increasing coverage from 20% to $\sim$100%. The main goal of modernizing the detector was better particle identification and momentum resolutions. The first iTPC sector was installed and tested in 2018. As part of my Service Work, I analyzed data from test runs (collisions of gold ions to check the correctness of the detectors before starting the real run) and cosmic data (data from cosmic rays passing through the detector). It was measured, e.g., the number of hits inside the detector, p_T, and η distributions. The obtained results are presented in Figures 1 and 2 and showed that iTPC performs better than TPC:

- increasing the maximum hits per track from 45 to 72;
- reducing the transverse momentum threshold to 60 MeV/c;
- η coverage extended by 0.4 units;

These results were first shown at the 27th International Conference on Ultrarelativistic Nucleus-Nucleus Collisions (Quark Matter) in 2018 in Venice, Italy.

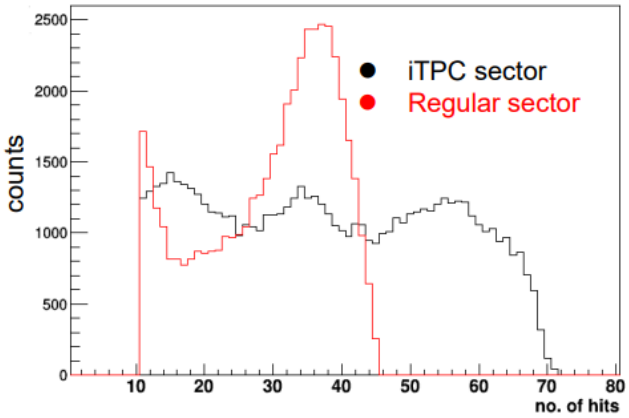

Figure 1: Distribution of number of hits per track in TPC and iTPC sectors.

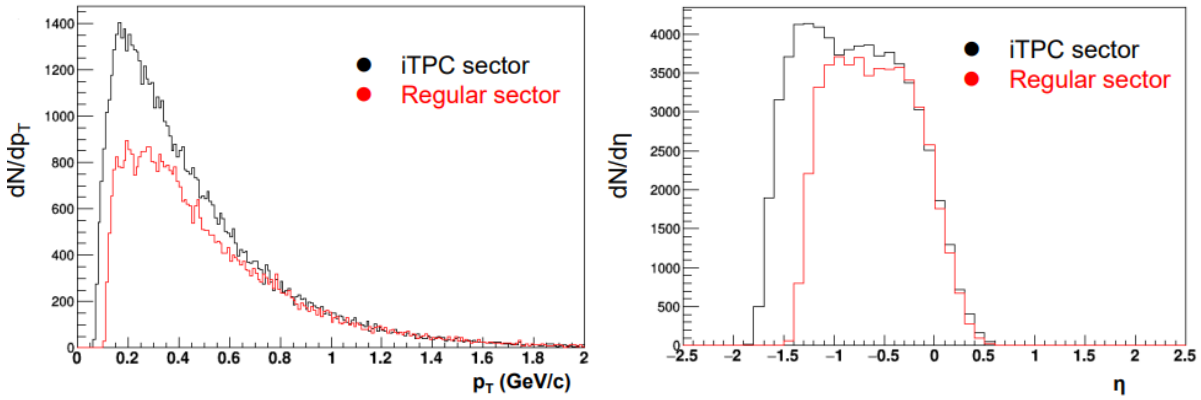

Figure 2: The transverse momentum (the left plot) and pseudorapidity (the right plot) distribution in TPC and iTPC sectors.

I regularly provided updates on my analysis at STAR collaboration meetings. In addition, I presented the results of my work at multiple conferences:

1. 15th Workshop on Particle Correlation and Femtoscopy (WPCF 2022), East Lansing, USA 2022 (**invited talk**):
   Charged and neutral kaons femtoscopy measured by the STAR experiment.

2. 14th International Conference on Hypernuclear and Strange Particle Physics (HYP2022), Prague, Czech Republic 2022:
   Femtoscopic measurements of two-kaon combinations in Au+Au collisions at the RHIC energies.

3. 20th International Conference on Strangeness in Quark Matter (SQM 2022), Busan, Republic of Korea 2022:
   Femtoscopic measurements of two-kaon combinations in Au+Au collisions at the STAR experiment.

4. 29th International Conference on Ultra-relativistic Nucleus-Nucleus Collisions (Quark Matter 2022), Cracow, Poland 2022 (poster):
   Femtoscopic measurements of strange hadrons in Au+Au collisions at the STAR experiment.

5. 21st ZIMÁNYI SCHOOL WINTER WORKSHOP ON HEAVY ION PHYSICS, Budapest, Hungary 2021:
   Femtoscopy of particles with strange quarks.

6. 20th ZIMÁNYI SCHOOL WINTER WORKSHOP ON HEAVY ION PHYSICS, Budapest, Hungary 2020:
   Femtoscopy of neutral kaons.

7. XLVI-th IEEE-SPIE Joint Symposium on Photonics, Web Engineering, Electronics for Astronomy and High Energy Physics Experiments, Wilga, Poland 2020:
   Femtoscopy of particles with starnge quark.

8. 19th ZIMÁNYI SCHOOL WINTER WORKSHOP ON HEAVY ION PHYSICS, Budapest, Hungary 2019:
   Neutral kaon femtoscopy in Au+Au collision at $\sqrt{s_{NN}}$ *= 200 GeV at STAR*.

9. 28th International Conference on Ultra-relativistic Nucleus-Nucleus Collisions (Quark Matter 2019), Wuhan, China 2019 (poster):
   Neutral kaon femtoscopy in Au+Au collisions measured at STAR experiment.

10. GDRI – International Research Network Meeting, Nantes, France 2019
    Neutral kaon femtoscopy in STAR.

11. 18th International Conference on Strangeness in Quark Matter (SQM 2019), Bari, Italy 2019 (poster):
    Kaon femtoscopy in STAR.

12. 14th Workshop on Particle Correlation and Femtoscopy (WPCF 2019), Dubna, Russia 2019:
    Neutral kaon femtoscopy in STAR.

13. XLIV-th IEEE-SPIE Joint Symposium on Photonics, Web Engineering, Electronics for Astronomy and High Energy Physics Experiments, Wilga, Poland 2019:
    Kaon femtoscopy in STAR.

14. 18th ZIMÁNYI SCHOOL WINTER WORKSHOP ON HEAVY ION PHYSICS, Budapest, Hungary 2018:
    Charged kaon femtoscopy in Au+Au collisions.

15. XX GDRE Workshop on relativistic heavy-ion physics, Nantes, France 2018:
    Identical kaon femtoscopy.

16. XIII Polish Workshop on Relativistic Heavy-Ion Collisions, Wroclaw, Poland 2018:
    Kaon femtoscopy using THERMINATOR model.

17. NICA days, Warsaw, Poland 2017:
    Femtoscopic measurements in the frame of theoretical models.

18. XIX GDRE Workshop on relativistic heavy-ion physics, Nantes, France 2017:
    Femtoscopic measurements in the frame of theoretical models.

19. XXXIX-th IEEE-SPIE Joint Symposium on Photonics, Web Engineering, Electronics for Astronomy and High Energy Physics Experiments, Wilga, Poland 2017:
    Study of the heavy-ion collisions using the femtoscopic correlations of the two protons system.

Publications and conference proceedings related to this analysis:

1. D. Pawłowska, "Femtoscopic measurements of two-kaon combanations in Au+Au collisions at the STAR experiment", EPJ Web Conf. 276 (2023) 01016.

2. D. Pawłowska, "Femtoscopic measurements of two-kaon combanations in Au+Au collisions at the RHIC energies", EPJ Web Conf. 271 (2022) 08009.

3. D. Pawłowska, "Femtoscopy of particles with strange quark", Proc.SPIE Int.Soc.Opt.Eng. 11581 (2020) 1158107.

4. D. Pawłowska, "Neutral kaon femtoscopy in STAR", Phys.Part.Nucl. 51 (2020) 3.

5. D. Pawłowska, "Kaon femtoscopy in STAR", Proc.SPIE Int.Soc.Opt.Eng. 11176 (2019) 111764C.

6. D. Pawłowska, "Femtoscopic measurements in the frame of theoretical models", Acta Phys.Polon.Supp 11 (2018) 699.

7. D. Pawłowska, "Study of the heavy-ion collisions using the femtoscopy correlations of the two protons system", Proc.SPIE Int.Soc.Opt.Eng. 10445 (2017) 1044545.

I am also on the STAR Collaboration Publication List and a co-author of publications prepared by the Physics Working Group - Correlations and Fluctuations. As a member of this group, I participated not only in data collection but also actively participated in discussions related to published analyses at the initial stages of work and later in preparing the paper proposals and publication drafts. These were the following publications:

8. STAR Collaboration, "Higher-order cumulants and correlation functions of proton multiplicity distributions in $\sqrt{s_{NN}}$ = 3 GeV Au+Au collisions at the RHIC STAR experiment", Phys.Rev.C 107 (2023) 2, 924908.

9. STAR Collaboration, "Beam energy dependence of fifth and sixth-order net-proton number fluctuations in Au+Au collisions at RHIC", Phys.Rev.Lett. 130 (2023) 8, 082301.

10. STAR Collaboration, "Measurements of Proton High Order Cumulants in $\sqrt{s_{NN}}$ = 3 GeV Au+Au Collisions and Implications for the QCD Critical Point", Phys.Rev.Lett. 128 (2022) 20, 202303.

11. STAR Collaboration, "Measurement of the Sixth-Order Cumulant of Net-Proton Multiplicity Distributions in Au+Au Collisions at $\sqrt{s_{NN}}$ = 27, 54.4, and 200 GeV at RHIC", Phys.Rev.Lett. 127 (2021) 26, 262301.

12. STAR Collaboration, "Cumulants and correlation functions of net-proton, proton, and antiproton multiplicity distributions in Au+Au collisions at energies available at the BNL Relativistic Heavy Ion Collider", Phys.Rev.C 104 (2021) 2, 024902.

13. STAR Collaboration, "Flow and interferometry results from Au+Au collisions at $\sqrt{s_{NN}}$ = 4.5 GeV", Phys.Rev.C 103 (2021) 3, 034908.

Other publications of the STAR experiment in which I am a co-author, as I participated in data collection and in discussions during collaboration meetings:

14. STAR Collaboration, "Pattern of global spin alignment of ϕ and K^{*0} mesons in heavy-ion collisions", Nature 614 (2023) 7947.

15. STAR Collaboration, "Tomography of ultrarelativistic nuclei with polarized photon-gluon collisions", Sci.Adv. 9 (2023) 1, eabq3903.

16. STAR Collaboration, "Measurement of ${}^{4}_{\Lambda}$H and ${}^{4}_{\Lambda}$He binding energy in Au+Au collisions at $\sqrt{s_{NN}} = 3$ GeV", Phys.Lett.B 834 (2022) 137449.

17. STAR Collaboration, "Azimuthal transverse single-spin asymmetries of inclusive jets and identified hadrons within jets from polarized pp collisions at $\sqrt{s_{NN}} = 200$ GeV", Phys.Rev.D 106 (2022) 7, 072010.

18. STAR Collaboration, "Projections of two-particle correlations onto transverse rapidity in Au+Au collisions at $\sqrt{s_{NN}} = 200$ GeV at STAR", Phys.Rev.C 106 (2022) 4, 044906.

19. STAR Collaboration, "Centrality and transverse momentum dependence of higher-order flow harmonics of identified hadrons in Au+Au collisions at $\sqrt{s_{NN}} = 200$ GeV", Phys. Rev. C 105 (2022) 6, 064911.

20. STAR Collaboration, "Collision-System and Beam-Energy Dependence of Anisotropic Flow Fluctuations", Phys.Rev.Lett. 129 (2022) 25, 252301.

21. STAR Collaboration, "Light nuclei collectivity from $\sqrt{s_{NN}} = 3$ GeV Au+Au collisions at RHIC", Phys.Lett.B 827 (2022) 136941.

22. STAR Collaboration, "Evidence of Mass Ordering of Charm and Bottom Quark Energy Loss in Au+Au Collisions at RHIC", Eur.Phys.J.C 82 (2022) 12, 1150 .

23. STAR Collaboration, "Evidence for Nonlinear Gluon Effects in QCD and Their Mass Number Dependence at STAR", Phys.Rev.Lett. 129 (2022) 9, 092501.

24. STAR Collaboration, "Longitudinal double-spin asymmetry for inclusive jet and dijet production in polarized proton collisions at $\sqrt{s}$ = 510 GeV", Phys.Rev.D 105 (2022) 9, 092011.

25. STAR Collaboration, "Measurements of H^3_Λ and H^4_Λ Lifetimes and Yields in Au+Au Collisions in the High Baryon Density Region", Phys.Rev.Lett. 128 (2022) 20, 202301.

26. STAR Collaboration, "Measurement of cold nuclear matter effects for inclusive J/Ψ in p+Au collisions at sNN=200 GeV", Phys.Lett.B 825 (2022) 136865.

27. STAR Collaboration, "Measurement of inclusive electrons from open heavy-flavor hadron decays in p+p collisions at $\sqrt{s} = 200$ GeV with the STAR detector", Phys.Rev.D 105 (2022) 3, 032007.

28. STAR Collaboration, "Differential measurements of jet substructure and partonic energy loss in Au+Au collisions at $\sqrt{s_{NN}} = 200$ GeV", Phys.Rev.C 105 (2022) 4, 044906.

29. STAR Collaboration, "Probing the Gluonic Structure of the Deuteron with J/Ψ Photoproduction in d+Au Ultraperipheral Collisions", Phys.Rev.Lett. 128 (2022) 12, 122303.

30. STAR Collaboration, "Search for the chiral magnetic effect with isobar collisions at $\sqrt{s_{NN}} = 200$ GeV by the STAR Collaboration at the BNL Relativistic Heavy Ion Collider", Phys.Rev.C 105 (2022) 1, 014901.

31. STAR Collaboration, "Disappearance of partonic collectivity in sNN=3GeV Au+Au collisions at RHIC", Phys.Lett.B 827 (2022) 137003.

32. STAR Collaboration, "Probing strangeness canonical ensemble with K^-, $\Phi(1020)$ and Ξ^- production in Au+Au collisions at $\sqrt{s_{NN}}$ = 3 GeV" , Phys.Lett.B 831 (2022) 137152.

33. STAR Collaboration, "Global Λ-hyperon polarization in Au+Au collisions at $\sqrt{s} = 3$ GeV", Phys.Rev.C 104 (2021) 6, L061901.

34. STAR Collaboration, "Search for the Chiral Magnetic Effect via Charge-Dependent Azimuthal Correlations Relative to Spectator and Participant Planes in Au+Au Collisions at $\sqrt{s_{NN}} = 200$ GeV", Phys.Rev.Lett. 128 (2022) 9, 092301.

35. STAR Collaboration, "Invariant Jet Mass Measurements in pp Collisions at $\sqrt{s} = 200$ GeV at RHIC", Phys.Rev.D 104 (2021) 5, 052007.

36. STAR Collaboration, "Azimuthal anisotropy measurements of strange and multistrange hadrons in U+U collisions at $\sqrt{s_{NN}} = 193$ GeV at the BNL Relativistic Heavy Ion Collider", Phys.Rev.C 103 (2021) 6, 064907.

37. STAR Collaboration, "Longitudinal double-spin asymmetry for inclusive jet and dijet production in polarized proton collisions at $\sqrt{s} = 200$ GeV", Phys.Rev.D 103 (2021) 9, L091103.

38. STAR Collaboration, "Observation of $D_S^{\pm}/D^0$ enhancement in Au+Au collisions at $\sqrt{s_{NN}}$ = 200 GeV",Phys.Rev.Lett. 127 (2021) 092301.

39. STAR Collaboration, "Global Polarization of Ξ and Λ Hyperons in Au+Au Collisions at $\sqrt{s} = 200$ GeV", Phys.Rev.Lett. 126 (2021) 16, 162301.

40. STAR Collaboration, "Measurement of transverse single-spin asymmetries of π^0 and electromagnetic jets at forward rapidity in 200 and 500 GeV transversely polarized proton-proton collisions", Phys.Rev.D 103 (2021) 9, 092009.

41. STAR Collaboration, "Comparison of transverse single-spin asymmetries for forward π^0 production in polarized *pp*, *pAl* and *pAu* collisions at nucleon pair central mass energy $\sqrt{s}$ = 200 GeV", Phys.Rev.D 103 (2021) 7, 072005.

42. STAR Collaboration, "Measurements of W and Z/γ^* cross sections and their ratios in p+p collisions at RHIC", Phys.Rev.D 103 (2021) 1, 012001. .

43. STAR Collaboration, "Measurement of inclusive J/Ψ polarization in p+p collisions at by the STAR experiment $\sqrt{s} = 200$ GeV by the STAR experiment", Phys.Rev.D 102 (2020) 9, 092009.

44. STAR Collaboration, "Beam-energy dependence of the directed flow of deuterons in Au+Au collisions", Phys.Rev.C 102 (2020) 4, 044906.

45. STAR Collaboration, "Investigation of the linear and mode-coupled flow harmonics in Au+Au collisions at $\sqrt{s_{NN}} = 200$ GeV", Phys.Lett.B 809 (2020) 135728.

46. STAR Collaboration, "Pair invariant mass to isolate background in the search for the chiral magnetic effect in *Au+Au* collisions at $\sqrt{s_{NN}} = 200$ GeV", Phys.Rev.C 106 (2022) 3, 034908.

47. STAR Collaboration, "Measurement of inclusive charged-particle jet production in Au+Au collisions at $\sqrt{s_{NN}} = 200$ GeV", Phys.Rev.C 102 (2020) 5, 054913.

48. STAR Collaboration, "Measurement of the central exclusive production of charged particle pairs in proton-proton collisions at $\sqrt{s} = 200$ GeV with the STAR detector at RHIC", JHEP 07 (2020) 07, 178.

49. STAR Collaboration, "Results on total and elastic cross sections in proton–proton collisions at $\sqrt{s} = 200$ GeV", Phys.Lett.B 808 (2020) 135663.

50. STAR Collaboration, "Measurement of groomed jet substructure observables in *p+p* collisions at $\sqrt{s} = 200$ GeV with STAR", Phys.Lett.B 811 (2020) 135846.

51. STAR Collaboration, "Beam energy dependence of net-Λ fluctuations measured by the STAR experiment at the BNL Relativistic Heavy Ion Collider", Phys.Rev.C 102 (2020) 2, 024903.

52. STAR Collaboration, "Nonmonotonic Energy Dependence of Net-Proton Number Fluctuations", Phys.Rev.Lett. 126 (2021) 9, 092301.

53. STAR Collaboration, "Underlying event measurements in *p+p* collisions at $\sqrt{s} = 200$ GeV at RHIC", Phys.Rev.D 101 (2020) 5, 052004.

54. STAR Collaboration, "Measurement of D^0-meson + hadron two-dimensional angular correlations in Au+Au collisions at $\sqrt{s} = 200$ GeV, Phys.Rev.C 102 (2020) 1, 014905.

55. STAR Collaboration, "Methods for a blind analysis of isobar data collected by the STAR collaboration", Nucl.Sci.Tech. 32 (2021) 5, 48.

56. STAR Collaboration, "First measurement of Λ_C baryon production in Au+Au collisions at $\sqrt{s_{NN}} = 200$ GeV", Phys.Rev.Lett. 124 (2020) 17, 172301.

57. STAR Collaboration, "Measurement of e^+e^- Momentum and Angular Distributions from Linearly Polarized Photon Collisions", Phys.Rev.Lett. 127 (2021) 5, 052302.

58. STAR Collaboration, "Bulk properties of the system formed in *Au+Au* collisions at $\sqrt{s_{NN}}$ = 14.5 GeV at the BNL STAR detector", Phys.Rev.C 101 (2020) 2, 024905.

59. STAR Collaboration, "Beam-energy dependence of identified two-particle angular correlations in $\sqrt{s_{NN}}$ = 7.7-200 GeV Au+Au collisions", Phys.Rev.C 101 (2020) 1, 014916.

60. STAR Collaboratin, "Measurement of away-side broadening with self-subtraction of flow in Au+Au collisions at $\sqrt{s_{NN}}$ = 200 GeV", Chin.Phys.C 44 (2020) 104001.

61. STAR Collaboration, "Strange hadron production in Au+Au collisions at $\sqrt{s_{NN}}$ = 7.7, 11.5, 19.6, 27 and 39 GeV", Phys.Rev.C 102 (2020) 3, 034909.

62. STAR Collaboration, "Charge-dependent pair correlations relative to a third particle in *p+Au* and *d+Au* collisions at RHIC", Phys.Lett.B 798 (2019) 134975.

63. STAR Collaboration, "Longitudinal double-spin asymmetry for inclusive jet and dijet production in pp collisions at $\sqrt{s} = 510$ GeV", Phys.Rev.D 100 (2019) 5, 052005.

64. STAR Collaboration, "Measurement of inclusive J/Ψ suppression in Au+Au collisions at $\sqrt{s_{NN}} = 200$ GeV through the dimuon channel at STAR", Phys.Lett.B 797 (2019) 134917.

65. STAR Collaboration, "Polarization of Λ ($\bar{\Lambda}$) hyperons along the beam direction in Au+Au collisions at $\sqrt{s_{NN}} = 200$ GeV", Phys.Rev.Lett. 123 (2019) 13, 132301.

66. STAR Collaboration, "Measurements of the transverse-momentum-dependent cross sections of J/Ψ production at mid-rapidity in proton+proton collisions at $\sqrt{s} = 510$ and 500 GeV with the STAR detector", Phys.Rev.D 100 (2019) 5, 052009.

67. STAR Collaboration, "First Observation of the Directed Flow of D^0 and $\bar{D^0}$ in Au+Au Collisions at $\sqrt{s_{NN}} = 200$ GeV", Phys.Rev.Lett. 123 (2019) 16, 162301.

68. STAR Collaboration, "Measurement of the mass difference and the binding energy of the hypertriton and antihypertriton", Nature Phys. 16 (2020) 4, 409-412.

69. STAR Collaboration, "Beam energy dependence of (anti-)deuteron production in Au + Au collisions at the BNL Relativistic Heavy Ion Collider", Phys.Rev.C 99 (2019) 6, 064905.

70. STAR Collaboration, "Collision-energy dependence of second-order off-diagonal and diagonal cumulants of net-charge, net-proton, and net-kaon multiplicity distributions in Au + Au collisions", Phys.Rev.C 100 (2019) 1, 014902 (with erratum: Phys.Rev.C 105 (2022) 2, 029901).

71. STAR Collaboration, "Collision-energy dependence of p_T correlations in Au + Au collisions at energies available at the BNL Relativistic Heavy Ion Collider", Phys.Rev.C 99 (2019) 4, 044918.

Contents

Chapter 1

Introduction

For centuries, people have been asking themselves how the world around them was created and what principal laws of Nature govern it. The answer lies in the fundamental science - physics - which allows us to understand and describe everything from the largest galaxies to the smallest subatomic particles. During the development of this field, it turned out that there are four fundamental interactions: strong, weak, electromagnetic, and gravitational. The first two act only at very small distances (10^{-15} m and 10^{-18} m, respectively). On the other hand, the other two dominate the scale of the entire Universe, where the distances are infinite.

From the point of view of this thesis, the most important is the strong interaction, which is responsible for binding free quarks and gluons into hadrons. The theory describing the strong force is QCD. It explains many properties of strongly interacting matter. In order to understand them, the conditions related to the beginning of the Universe - the Big Bang - are recreated in laboratory conditions. The most extensive experiments of this type are the RHIC at BNL and the LHC at CERN.

There are many experimental methods to study QGP, the state where quarks and gluons are free. One of the methods of studying the first moments of the Universe's existence is correlation femtoscopy, which enables one to measure the space-time size of the source emitting particles and the properties of fundamental interactions. The effects of quantum statistics and final state interactions: Coulomb and strong are responsible for particle correlations. It is possible to analyze all types of particles using the femtoscopy method, but initially, pairs of identical π mesons (called later as pions) were used due to their multiplicities. The obtained results allow one to draw several conclusions. First, the size of the emission area increases linearly with the

multiplicity of registered particles, which means that the emission process takes place at a constant density. Secondly, according to the predictions of hydrodynamic models, the size of the particle emitting source in the direction transverse to the beam axis decreases with the increase of transverse momentum of the pair. This is due to the existence of a relationship between the spatial and momentum characteristics of the particles. Femtoscopy measurements are related to the range of correlation, called *homogeneity length*.

This Ph.D. dissertation presents the results of two K mesons (called later as kaons) femtoscopy analyses performed in Au+Au collisions registered by the STAR experiment. The thesis is organized as follows: the introduction of high energy physics and a description of selected Quark-Gluon Plasma signatures are presented in Chapter 2; the characteristics of heavy ion collisions models used to compare experimental results with theoretical predictions are included in Chapter 3; Chapter 4 presents the RHIC experimental complex and the STAR detector located there; a detailed description of the theoretical aspects of femtoscopy is described in Chapter 5; Chapter 6 focuses on the properties of neutral kaons; experimental technique and data selection and corrections are presented in Chapter 7; experimental correlation functions of the systems $K^0_S K^0_S$ and $K^0_S K^{\pm}$ can be found in Chapter 8; the last Chapter 9 is a discussion of the results and conclusions of the femtoscopic analysis. In the thesis are also glossary and two appendixes related to signal to background study for $K^0_S K^0_S$, and studies of Therminator2.

Chapter 2

The base concept of high-energy physics

2.1 Standard Model

An important event in the history of physics is the discovery of an electron over 100 years ago. It initiated the development of a new field of science: particle physics. For the next 50 years, more particles were discovered as a result of, among others studying cosmic rays. This desire to explore new elements of matter became the impulse to build the first high-energy accelerators. Many experimental results find their explanation in *the Standard Model*. This theory was developed in the 1970s and assumes that all matter that surrounds us consists of half-spin particles - *fermions* and total-spin - *bosons*. The SM also takes into account the Higgs mechanism, which assumes that there is a scalar field in all space, called the Higgs field [1]. This field couples with all the fundamental particles and gives them masses. This mechanism is related to the Higgs boson, which excites the Higgs field. Experimentally, the existence of the "God particle" was confirmed at the end of 2013 in ATLAS and CMS experiments at the LHC [2].

Fundamental fermions

Fermions are the essential components of matter - there are 6 *quarks* and 6 *leptons* and the corresponding antiparticles - Figure 2.1.

Quarks are particles with a fractional charge with values $+\frac{2}{3}|e|$ or $-\frac{1}{3}|e|$ ($|e|$ is the absolute value of the elementary charge - the electron). There are three generations of quarks: up (u) and down (d), charm (c) and strange (s), top (t) and bottom (b). According to the present knowledge, quarks do not exist in the free state in ordinary conditions. The strong interactions between

quarks have a unique property: quarks are observed only in combinations (two or three quarks called hadrons), never singly.

Leptons, similarly to quarks, are electrically charged with that of an integer. The most common particle of this type is an electron having a negative charge. The unstable particles are similar to it but much heavier: muon and tau, which decay spontaneously. Each flavor is associated with a specific neutrino. The theory of neutrinos first appeared in 1930 and was formulated by Pauli

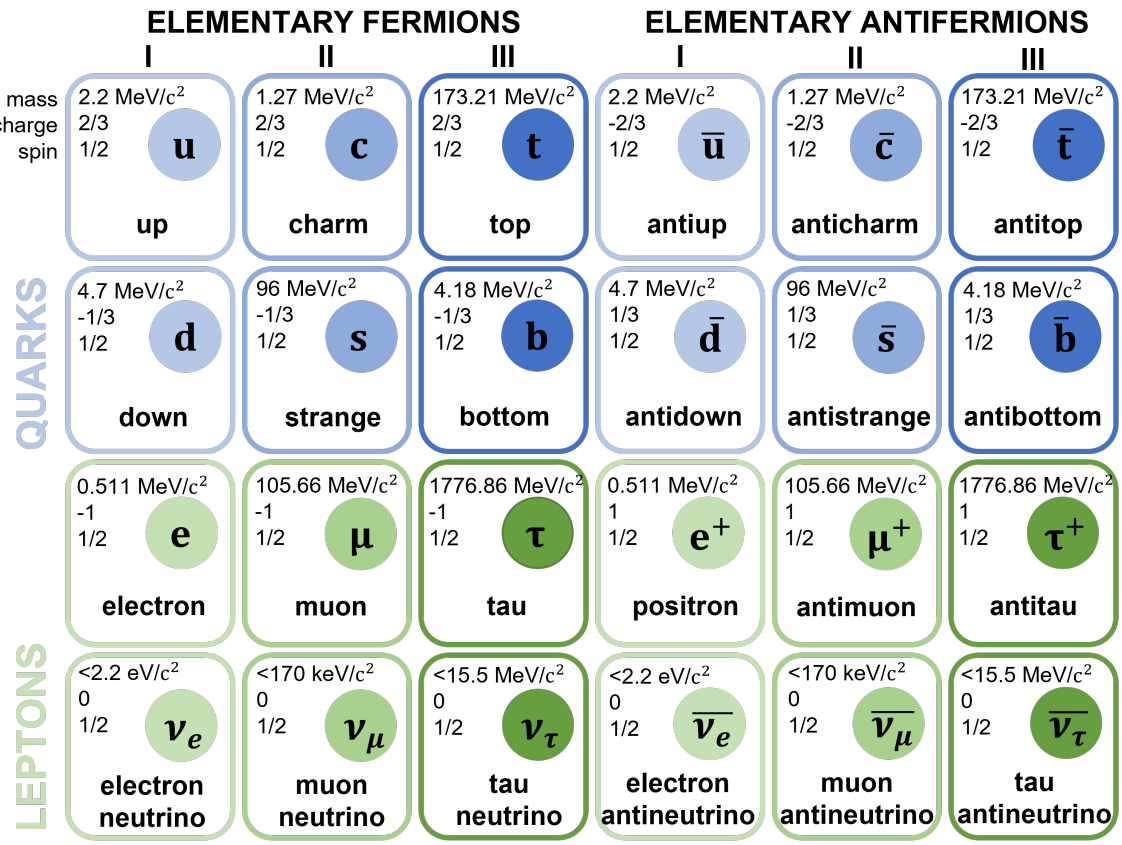

Figure 2.1: Illustration of the fundamental particles proposed by the Standard Model with information on mass, charge, and spin [this thesis]. Properties supplemented from information collected by the Particle Data Group [3].

as an explanation for the energy and momentum deficiencies in the β-decay [4]. However, it was not until 1956 that direct evidence of their existence and interaction with other particles appeared [1].

Intermediary bosons

Bosons are particles with a total spin, carriers of interactions between fundamental fermions - Figure 2.2. Table 2.1 lists all currently known mediators and their associated interactions:

strong, electromagnetic, weak, and gravitational (not described in the SM).

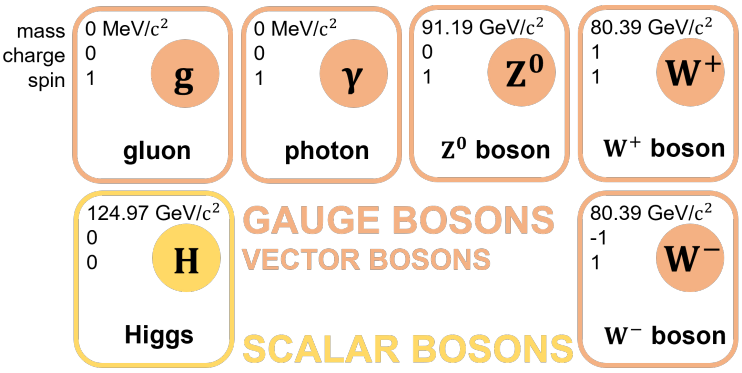

Figure 2.2: Illustration of gauge bosons responsible for the interactions proposed by the Standard Model with information on mass, charge, and spin [this thesis]. Properties supplemented from information collected by the Particle Data Group [3].

The strong interaction involves the exchange of a massless gluon. It is responsible for binding quarks into hadrons (the existing world is built of atoms consisting of protons and neutrons) and neutrons and protons in atomic nuclei. The strong interaction theory is the QCD, described in detail in Chapter 2.2. The electromagnetic interaction involves the exchange of a photon. It is responsible for most physics phenomena on scales above the nuclear one, primarily for the bound states of electrons in the field of atomic nuclei and intermolecular forces in solids and liquids. As a result, it is the best-known interaction described in the SM. Maxwell's equations

Table 2.1: Fundamental interactions.

Gauge boson	**Interaction**	**Relative strength**	**Range**
gluon - g	strong	1	$\leq 10^{-15}$ m
photon - γ	electromagnetic	10^{-2}	∞
bosons - $W^{\pm}$, Z^0	weak	10^{-5}	10^{-18} m
graviton - G	gravitational	10^{-39}	∞

are usually used to describe electromagnetic interaction at large scales. At the microscale, where quantum effects become important, QED is used. In turn, the weak interaction describes the exchange of $W^{\pm}$ bosons and Z^0, whose masses are nearly 100 times greater than the proton. An example is the slow decay of β radioactive nuclei at low energies. Then the radioactive nucleus emits an electron and a neutrino.

The only interaction not covered by the Standard Model is gravity. Presumably, it involves the replacement of a spin two boson, a graviton that has yet to be discovered. It is the weakest known interaction, although dominant in the Universe scale.
The above-described interactions are independent and unrelated to each other. In the seventies of the twentieth century, research was carried out (the Nobel Prize in 1979 for S. Glashow, A. Salam, and S. Weinberg), which showed that weak and electromagnetic interactions could be unified. They will also be equal to strong at sufficiently high energies. However, at lower energies, the relative strength is very different.

Limitations of the Standard Model

The Standard Model is a compact theory of the properties of the essential components of matter and the strong, electromagnetic, and weak interactions. However, this is a theory with some limitations:

- does not take into account gravitational interactions dominating the Universe;
- assumes the masslessness of neutrinos (Takaaki Kajita, a member of the research team of the Super-Kamiokande neutrino detector in Japan, and Arthur B. McDonald, an employee of the Sudbury Neutrino Observatory in Canada, discovered that neutrinos have mass - Nobel Prize 2015 [5]);
- contains at least 17 arbitrary parameters (e.g., masses, angles, coupling constants), the values of which can not be determined theoretically [1];
- does not explain why there are precisely six flavors of quarks and leptons;
- does not explain the existence of "dark energy", "dark matter," and a significant asymmetry between matter and antimatter;
- does not justify why particle charge is quantized.

2.2 The Quantum Chromodynamics

The origins of the quantum theory of the color strong interactions between quarks date back to 1963 when Gell-Mann and Zweig proposed an explanation for the structure of the hadron (each of them separately) [6]. According to them, there were smaller particles inside the hadron

- according to the state of knowledge at the time, they were u, d, and s quarks. This is how the theory known as *quantum chromodynamics* was born. Its name and basic assumptions were analogous to those in QED. An important role in both theories is played by charge. In the case of QCD is a color charge characterizing particles associated with strong interaction (quarks and gluons). With six quarks and three colors (red, blue, and green), it is possible to build hadrons whose final charge is total and the color is white. For this, one needs to follow simple rules [1]:

- baryon - a state consisting of three differently colored quarks qqq;
- antibaryon - a state composed of three antiquarks in different anticolors $\bar{q}\bar{q}\bar{q}$;
- meson - quark-antiquark pair $q\bar{q}$.

In addition, QCD is based on the SU(3) symmetry group, which obtains the correct decomposition of products of the basic triplet representations [7].
In order to correctly classify hadrons, one cannot use only the calculations created for QED because they are adapted to a small coupling constant of $\alpha = e^2/hc = 1/137$. The coupling constant α_s in QCD is not a de facto constant and may be equal to one. This parameter depends on the momentum transfer Q^2. It decreases logarithmically with the increase of this momentum [7]:

$$\alpha_s(Q^2) \propto \frac{1}{ln(Q^2/\Lambda^2)} \tag{2.1}$$

where Λ is a scale constant. From the above relationship, it follows that:

- "hard" collisions (large Q^2), the system is in the perturbation region; therefore, the calculations prepared for QED are feasible;
- "soft" collisions (small Q^2) require very complicated numerical calculations.

The QCD potential of the quark-antiquark interaction expressed by the formula 2.2 contains an obvious Coulomb term and a linear one with the separation distance r.

$$V(r) = -\frac{4}{3}\frac{\alpha_s}{r} + kr \tag{2.2}$$

where k is a constant that determines the "elastic" properties of the string. Figure 2.3 shows how the potential changes with increasing distance. One can observe two characteristic behaviors. Firstly, at small distances, the potential has a Coulomb character, which means that the first term of the above formula prevails. Then it is possible to observe typical for QCD - *asymptotic*

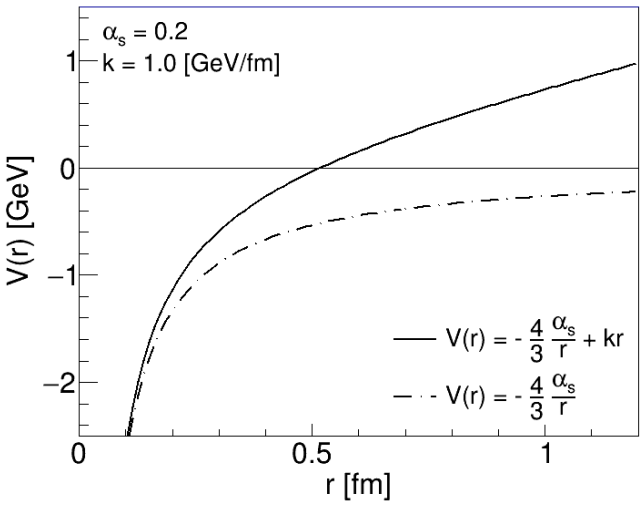

Figure 2.3: The QCD potential between a quark and antiquark as a function of the separation distance, where $\alpha_s = 0.2$ and $k = 1$ GeV/fm [this thesis].

freedom. This phenomenon consists of the fact that at a sufficiently small distance between quarks, they begin to behave as quasi-free or unbound particles. With a sufficiently high matter density, quarks can occur as free particles. This state is called QGP. Asymptotic freedom was discovered in 1974 by Politzer [8], Gross, and Wilczek [9], and 30 years later, it contributed to their Nobel Prize.

Secondly, the positive part of the equation prevails at considerable distances, somewhat similar to a rubber band's potential. It describes intuitively the interactions between a quark and an

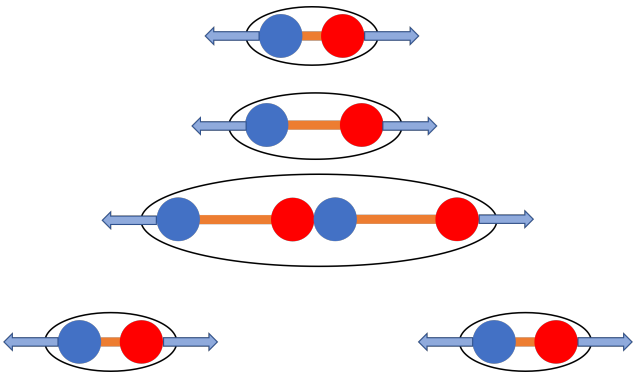

Figure 2.4: String breaking - an attempt to separate two quarks leads to forming of new quark-antiquark pairs [this thesis].

antiquark connected by an elastic string or a color flux tube. When trying to separate the quarks, the attractive force increases, which results in the inability to tear them apart. This is called the phenomenon of *confinement of quarks*. In other words, each attempt to break the bound quarks

leads to another quark-antiquark pair, as shown in Figure 2.4. QCD calculations allow one to create a phase diagram of the temperature T as a function of the baryon chemical potential μ_B (determining the change in energy of the system after adding or subtracting one baryon) - Figure 2.5. As can be seen from the diagram, QGP is formed at very high energies. Between the

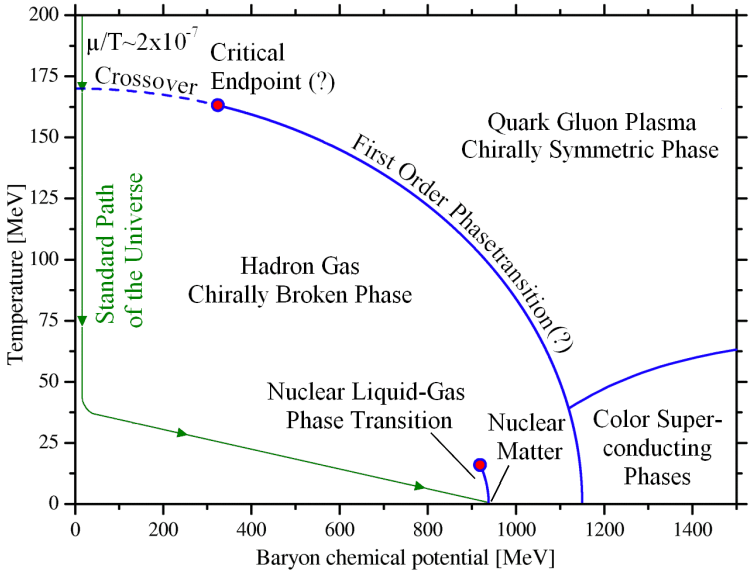

Figure 2.5: Quantum Chromodynamic Phase diagram [10].

plasma state and hadronic matter, a first-order transition with a non-vanishing baryon chemical potential is expected. When the potential reaches values close to zero, a smooth transition called "cross-over" exists (there are rapid and sudden changes in the system's physical parameters). The point where the transitions change is named *the critical point*. The desire to study and learn about the phenomena described above became the reason for creating high-energy experiments where ions of heavy elements collide.

2.3 Relativistic heavy-ion collisions

The primary motivation for examining heavy ion collisions at relativistic energies is to understand the equation of the state of nuclear, hadronic, and parton matter at very high energies and low densities. This will allow one to recreate the conditions that took place at the time of the creation of the Universe - the Big Bang. Therefore, numerous research centers have been established worldwide to collect information about the structure of matter. The effect of collisions at sufficiently high energies is the state of *quark-gluon plasma*. Then the collision

process will consist of several stages. The first stage is the *pre-equilibrium state*, which can be best described as a state with a rapid emission of quarks and gluons, called partons. The most energetic collisions of partons create strings which, breaking apart, form jets - bundles of strongly collimated particles. Overlap time of two nuclei changes with energy, for example, for

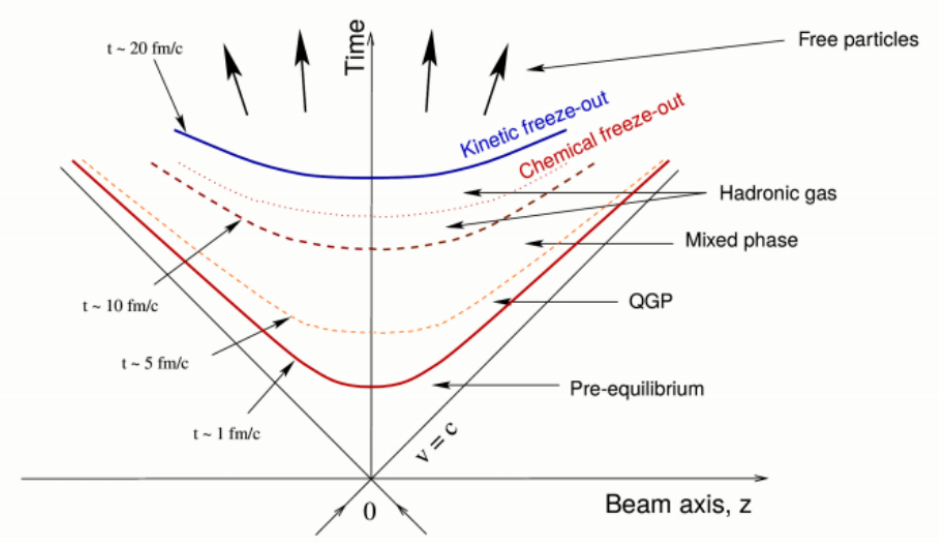

Figure 2.6: Time-space evolution of heavy ion collisions [11].

$\sqrt{s_{NN}}$ = 10 GeV is 2.5 fm/c while for $\sqrt{s_{NN}}$ = 100 GeV it is only about 0.25 fm/c [12]. The second phase, in which QGP is produced, can occur when the collision energy is sufficiently high, and thermalization of the matter produced in the collision takes place. QGP, as a dense and very hot matter, is constantly expanding. Because its behavior resembles an almost perfect liquid, many theoretical models use hydrodynamic equations to describe QGP. The final moment of this stage is when the hitherto free quarks begin to merge into hadrons - hot hadron gas is formed. This is the result of the decreasing density and temperature of matter. For collision energies of $\sqrt{s_{NN}}$ = 200 GeV, the QGP lifetime is estimated to be less than 10 fm/c [13]. Last but not the minor stage is when the hadron gas expands further. If the initial energy of hadrons is high, it is possible to form new particles until chemical freezeout. After this time, all inelastic processes cease, so the chemical composition of the products is fixed. The only mechanism for producing new particles is the decay of existing ones. However, hadronic gas still is described by sufficient density for elastic collisions between particles to take place and their momentum to change. It is only when thermal freezeout occurs that the hadron's mean free path becomes much larger than the size of the system. Thermal freezeout can be considered the point at which the particle's momentum is established, estimated to be around 20 fm/c after the collision [14].

Figure 2.6 shows the space-time evolution of heavy ion collisions. In order to describe the initial geometric properties of heavy ion collisions, the Glauber model is used, which assumes two forms:

- the "traditional" (optical) Glauber model, which includes quantum wave functions [15, 16]; Figure 2.7 shows an example of a collision of two nuclei, A and B, assuming this model. The two nuclei approach each other with the impact parameter b (the minimum distance between the lines along which the ion centers move before interacting with each other), thanks to the extraction of the b parameter and the cross sections for the given reaction σ, the number of collisions N_{coll} and the number of nucleons participating in the collision N_{part} can be estimated;

- the Glauber Monte Carlo model, the operation of which is based on computer simulations [17, 18]; this is the approach used when a more detailed picture of the collision is planned; then the nucleons of both nuclei are placed in a three-dimensional coordinate system - Figure 2.8; the collision parameter is randomized from the cross-section distribution $d\sigma/db = 2\pi b$, while single nucleon processes are calculated using probability distributions.

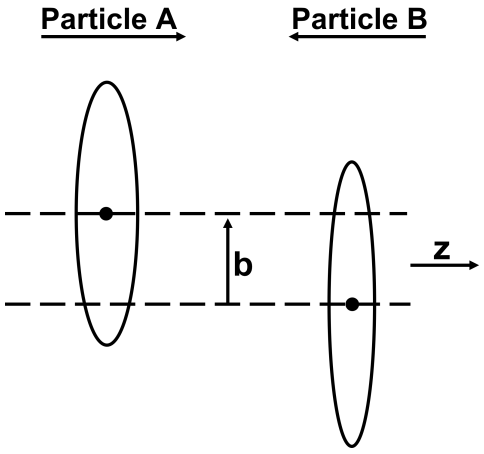

Figure 2.7: Heavy ion collision, assuming optical Glauber model, seen from the plane parallel to the beam direction [this thesis].

In both cases, previously obtained experimental results are used as input, such as nuclear charge densities $\rho(r)$ (Fermi distribution is used for description) and inelastic nucleon-nucleon cross-section (an experimental cross-section is needed for calculations) [19].

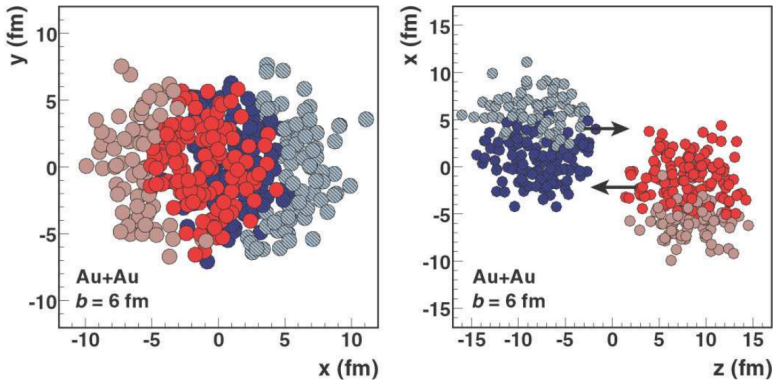

Figure 2.8: Au+Au collision at $\sqrt{s_{NN}}$ = 200 GeV, assuming Glauber Monte Carlo model, seen from the transverse plane (left plot) and along to the beam direction [19]. Darker points correspond to the participants in the collision.

Unfortunately, there are no experimental methods to directly measure N_{coll} and N_{part}. The mapping procedure should be used to extract information about the average values of these quantities. It consists in isolating the classes of measured collisions (N_{evt}). This distribution is obtained by Glauber calculations. The calculation focuses on defining "centrality classes" in experimental distribution and computed one. The next step is to compare the average values in a specific centrality range for both distributions. The general description of the mapping procedure varies slightly between experiments. An example of a procedure for Au+Au collision at $\sqrt{s_{NN}}$ = 200 GeV is shown in Figure 2.9.

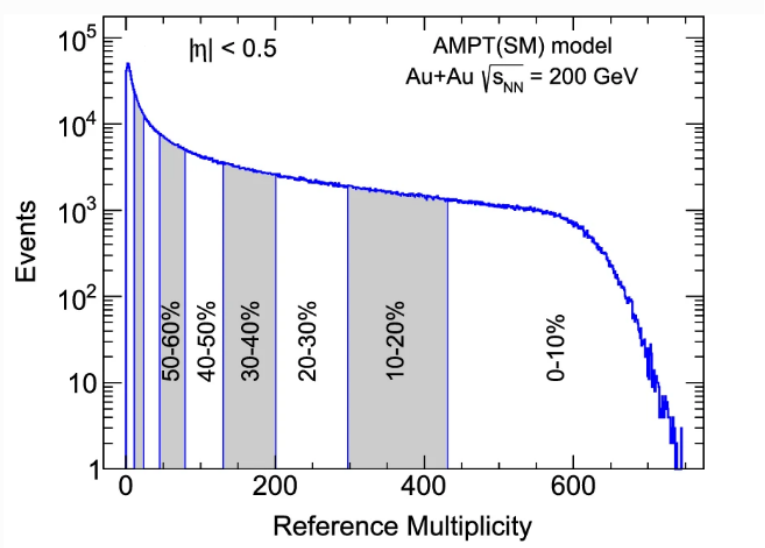

Figure 2.9: The multiplicity distribution for Au+Au collisions at $\sqrt{s_{NN}}$ = 200 GeV for the corresponding centralities from Glauber Monte Carlo calculation [20].

2.4 Selected signatures of a Quark Gluon Plasma

The small part of the QGP produced in a relativistic heavy ion collision is a system with sizes of a few femtometers (10^{-15} m) and lives for only a brief time (10^{-23} s). Thus, there are no methods to study this state of the matter directly. However, thanks to particles produced in the final state of the collision and recorded by detectors, it is possible to confirm the existence of QGP. The proposed signatures focus on particles that have mostly stayed the same from their creation (in QGP) to the time of their registration. The most important and selected probes are described below: collective enhancement of strangeness, jet quenching, anisotropic flow, direct photons, and charmonium suppression. Another way to study the properties of strongly interacting matter and to learn about the size and lifetime of the QCD medium is the technique of correlation femtoscopy described in detail in Chapter 5.

Collective enhancement of strangeness

The most famous signature for spontaneously broken chiral symmetry in the dense hadronic matter is the enhancement of strangeness and the production of antibaryons proposed in the 1980s. Many experimental groups like collaborations WA97 [21], NA49 [22], NA57 [23], and STAR [24] have worked on this topic. Increased production of strange particles in high-energy nuclear collisions is observed. It also turned out that the enhancement is not a reliable QGP signature. Hadronic reactions can produce particles such as K mesons and Λ hyperons before the fireball reaches the equilibrium state. This phenomenon has been studied in detail by hadron cascade models, which showed that the enhancement comes primarily from meson-baryon reactions initiated by mesons with a strongly nonthermal spectrum (produced in the first collisions) [25]. However, for collisions with energies of $\sqrt{s_{NN}}$ = 200 GeV, adding more advanced mechanisms to the cascade models is necessary: decaying multi-quark droplets, multiple string breaking, and color rope formation [26]. Experimentally, the particle yield (number of particles of a given type in a rapidity range dN/dy) is calculated to verify if there is an enhancement in the production of strange particles. Figure 2.10 presents the results obtained by the STAR, CERES, NA49, and NA57 experiments. In the case of K^0_S, $\bar{\Lambda}$ and $\bar{\Xi}^+$, there is a clear dependence on the collision energy - the number of particles produced increases with the energy. All experiments, even with a different detector acceptance, produce very consistent results. In turn, Λ and Ξ^- baryons show energy dependence that is inconsistent with expectations. The apparent

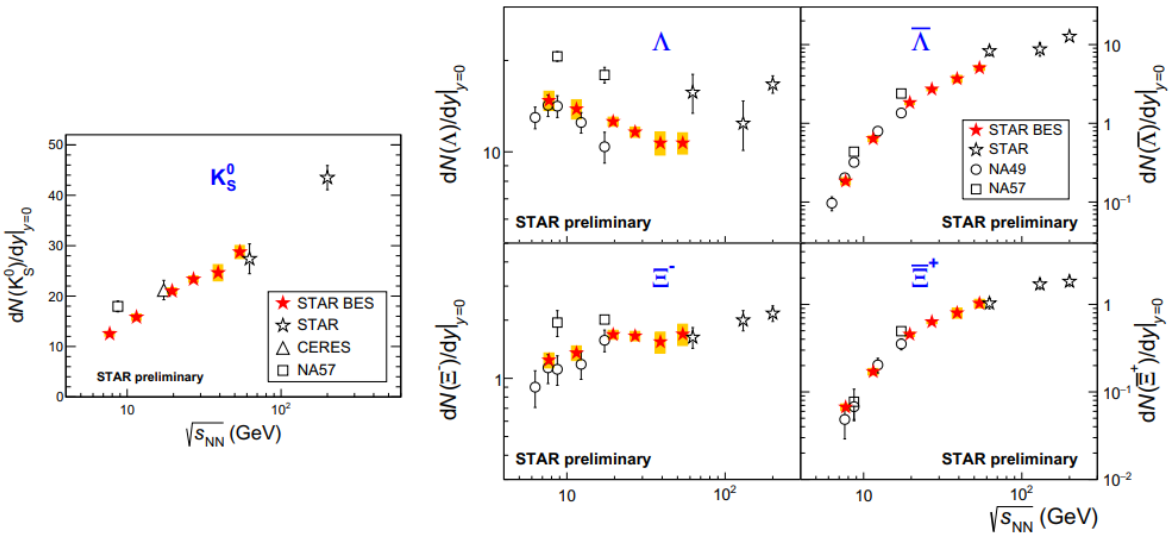

Figure 2.10: The strange hadrons (K^0_s, Λ and Ξ) yields as a function of collision energy in the most central Au+Au collisions [27].

increase in the production of Λ for low energies is due to the significant value of baron stopping in midrapidity. As shown by the data from the BES-I program, this effect diminishes with energy. Therefore, it can be concluded that the observed energy dependence may be caused by the crossover of the production of Λ - $\bar{\Lambda}$, which depends on the beam energy. It is also influenced by the production of Λ with kaons in the nucleon-nucleon scattering, which increases with the net-baryon density and decreases with the collision energy [28, 29].

Jet quenching

The system's lifetime created due to a high-energy collision is very short, so its properties cannot be studied using external probes. To learn the system's structure, performing some "tomography" is necessary based on energetic and highly penetrating particles created in parton-parton scattering. Such partons are characterized by high transverse momentum and lose energy passing through the QGP state. Energy loss is due to collision processes (elastic scattering of the primary parton and the parton from the medium) and radiation processes [30]. A remarkable feature of partons is that they fragment into the spray of hadrons (the jet). Figure 2.11 shows the jets in the proton-proton (p+p) and nucleus-nucleus (A+A) collisions. In the case of p+p collisions, there are two collinear jets called "back-to-back", and momentum conservation causes this. A+A collisions are characterized by one damped jet - this is the so-called "jet quenching" phenomenon. In order to investigate such a phenomenon, the nuclear modification factor R_{AA}

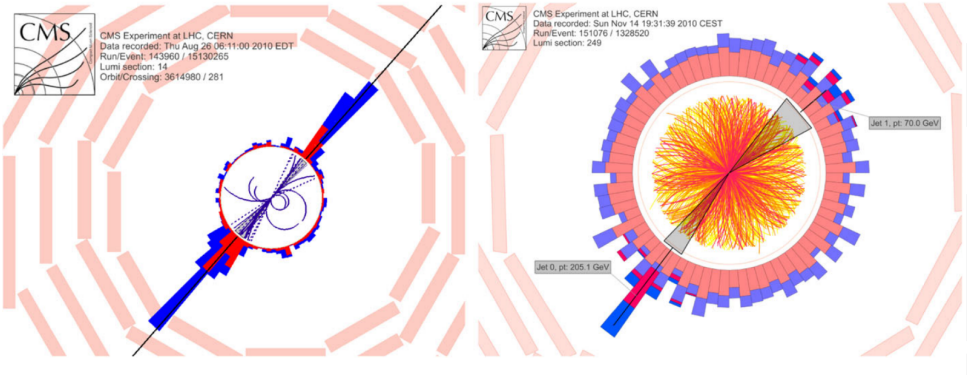

Figure 2.11: Jets observed by the CMS experiment in p+p (left) and Pb+Pb (right) collisions at $\sqrt{s_{NN}}$ = 2.76 TeV [30].

should be measured. It is the ratio of the normalized yields of single particles in p+p (N_{pp}) and A+A (N_{AA}) collisions and is expressed by the formula:

$$R_{AA} = \frac{d^2N_{AA}/dp_T/dy}{< N_{coll} > d^2N_{pp}/dp_T/dy} \tag{2.3}$$

where $< N_{coll} >$ is the average number of binary nucleon-nucleon collisions given by calculation from the Glauber model [7]. The first studies were carried out at the RHIC experimental complex. It was then observed that with high p_T, there is a strong suppression of light hadrons like π^0, η and $K^{\pm}$ - R_{AA} <1, while for direct photons, R_{AA} = 1, as is expected (Figure 2.12). The obtained results show that the energy loss of parton in the hot medium is possible, which is unacceptable in the case of ordinary nuclear matter. This proves that a quark-gluon plasma is formed in the collisions of heavy ions.

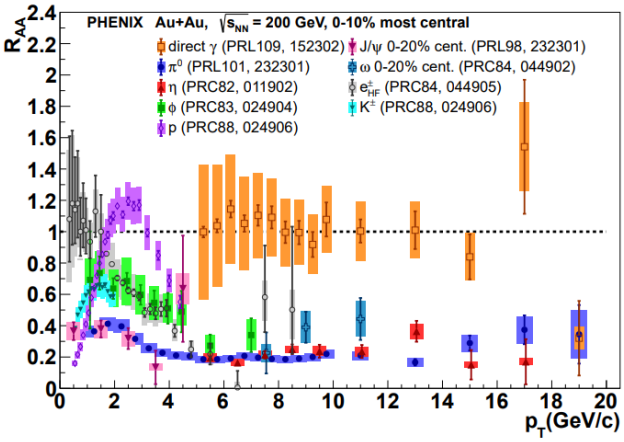

Figure 2.12: Nuclear modification factor R_{AA} for various particles in most central Au-Au collisions at $\sqrt{s_{NN}}$ = 200 GeV [31].

The elliptic flow

The region where the two Lorentz contracted nuclei overlap in central collisions is circular. However, this shape resembles an almond as it progresses to peripheral collisions. The relationship between the mean free path of the particles λ and the size of the created system R influences the particle emission:

- $\lambda > R$ - particle emission is isotropic in the transverse direction to the reaction plane;
- $\lambda << R$ - particle emission is anisotropic and described by hydrodynamics.

The hydrodynamic flow results from the pressure gradient steeper in the reaction plane for A+A collisions. The result is the production of more particles in this plane. Thus, the azimuthal distribution exhibits the characteristics of an elliptic flow (characteristic $\cos(2\phi)$ modulation) that is sensitive to the initial phase of the collision. Experimentally, to analyze the particle distribution in the transverse plane, Fourier expansion is used:

$$E\frac{d^3N}{d^3p} = \frac{1}{2}\frac{d^2N}{p_T dp_T dy}\left(1+2\sum_{n=1}^{\infty} v_n(p_T,y)\cos[n(\phi-\Psi_R)]\right) \tag{2.4}$$

where E is the energy, y is the rapidity, ϕ is the azimuthal angle and Ψ_R is the position of the reaction plane [7]. The coefficients v_n can be calculated using the following equation:

$$v_n(p_T,y) = \langle\cos[n(\phi-\Psi_R)]\rangle \tag{2.5}$$

The most common measurement is the second harmonic v_2, i.e., the aforementioned elliptic flow - Figure 2.13, the positive value of which gives information about the interaction in the final state.

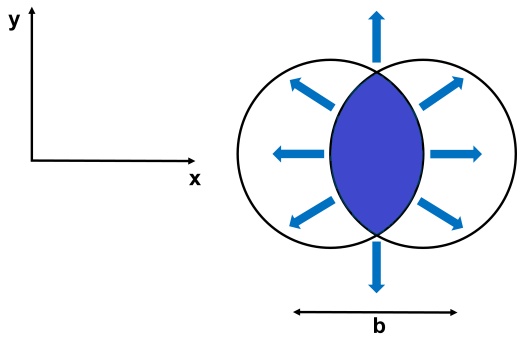

Figure 2.13: Elliptic flow phenomena [this thesis].

Examinations of various harmonics show that when v_n in the function p_T is divided by the number of constitutive quarks, n_q, the dependence for different particle species will be identical.

However, it turns out that introducing a modified scaling function $v_n/n_q^{n/2}$ vs. scaled kinetic energy ($KE_T = m_T - m_0$) works better. As shown in Figure 2.14, this is true. Rescaling v_2 in the KE_T function for π, K, p, λ, ϕ and K_S^0 shows that collective flow develops during the parton phase.

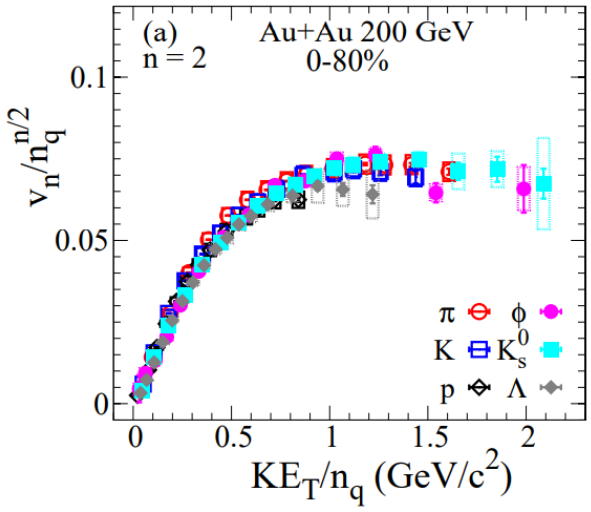

Figure 2.14: The scaled identified particle elliptic flow as a function of the scaled transverse kinetic energy for different particle types in minimum bias Au+Au collisions at $\sqrt{s_{NN}}$ = 200 GeV measured by the STAR experiment [32].

Direct photons

Direct photons are photons created due to the interaction of various charged particles resulting from the collision of heavy ions. Thus, they do not result from final-state decay and describe the collision's early evolution very well. This is because the mean free path length is much

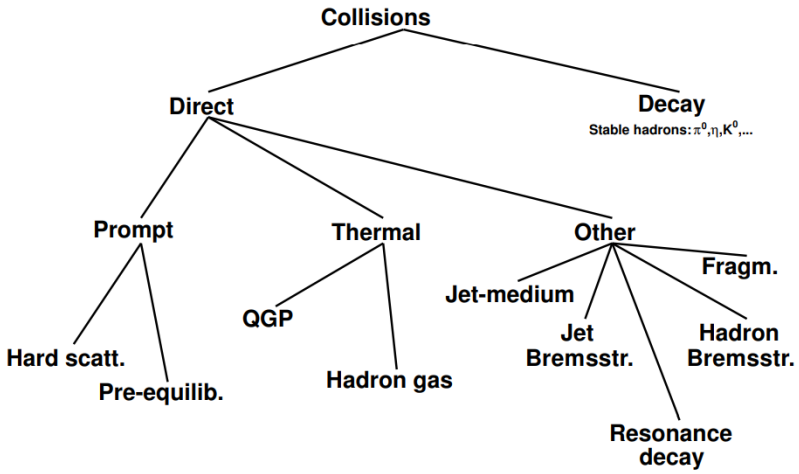

Figure 2.15: Types of direct photons [33].

larger than the resulting system size. As a result, direct photons leave the system without being affected by its other elements and transfer information about its temperature. In addition, photons with high transverse momentum indicate whether suppressing high p_T particles affects the initial or final state [7]. Direct photons can be divided into two types according to their origin (Figure 2.15):

- thermal - emitted from QGP or hot hadronic matter; photons from QGP come from various electromagnetic processes involving quarks and strong processes (Compton scattering, annihilation or reactions $gq \to gq\gamma$ and $qq \to qq\gamma$); in turn, photons from hadronic gas may come from the processes $\pi\pi \to \rho\gamma$ or $\pi\rho \to \pi\gamma$, and single photons are formed as a result of decays: $\omega \to \pi\gamma$ and $\rho \to \pi\pi\gamma$; all thermal photons are observed at low values of p_T;
- prompt - come from "hard" collisions of initial state partons from colliding nuclei; observed in the high p_T range.

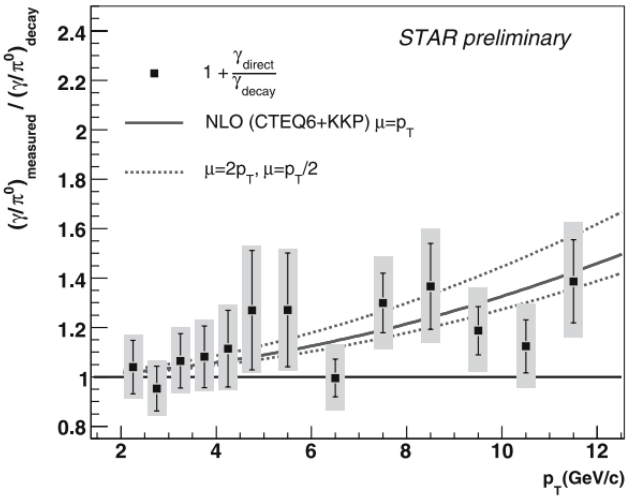

Figure 2.16: The parameter R as a function of the transverse momentum measured by the STAR experiment at d+Au collisions at $\sqrt{s_{NN}}$ = 200 GeV [34].

The experimental study of direct photons is challenging because their amount in the total yield is only a few percent. Additionally, rapidity decreases for low values of transverse momentum. In order to quantify the investigated effect, the parameter R (called double ratio) is calculated, described by the formula:

$$R = \frac{\gamma_{inclusive}}{\gamma_{decay}} = 1 + \frac{\gamma_{direct}}{\gamma_{decay}} \tag{2.6}$$

Figure 2.16 shows the results obtained by the STAR experiment. As p_T increases, it is noticeable that the R parameter reaches values above unity, indicating the direct photon signal. The double ratio is consistent with the perturbative QCD (the full line) computation based on the parton density (CTEQ6M), and fragmentation (KKP) functions [34]. In this analysis, cut to insulation was not used. Therefore prompt and fragmentation photons are included in direct photon yield.

Charmonium Suppression

In 1986, Matsui and Satz [35] proposed a new QGP signature - charmonium suppression. They believed that in plasma, the color charge of quarks is obscured by other quarks and gluons (a phenomenon similar to the Debye screening effect in solids). The result is a weakening interaction between the heavy quark c and $\bar{c}$ (particles J/ψ and ψ'). This leads to the melting of the produced pair, from which the J/ψ meson cannot be formed. In general, this effect applies not only to charmonium but also to bottomonium, the Υ particles.

In order to experimentally identify the J/ψ particle, its decay products, i.e., a pair of leptons (muons or electrons), are examined. This makes it possible to study the spectrum of dileptons with large invariant masses of 3097 MeV (J/ψ mass). The first experiment to make this type of measurement was NA50. The results obtained for Pb+Pb collisions at the energy of 158 AGeV (the highest SPS energy) showed that the most potent suppression takes place for the most central collisions [36]. In later years, RHIC and the LHC experiments also addressed this topic. However, a quantitative understanding of yields is complicated for high collision energies. There are two competing effects: suppression due to the screening effects and enhancement due to the recombination process [30]. Weaker-bound quarkonium, i.e., those whose radius is larger than the Debye length, are dissolved in the QGP. On the other hand, those with a smaller radius will be characterized by a stronger bound, weakening the dissolution effect. Therefore, when the suppression of different types of quarkonia is compared, the expected result will be sequential suppression of yields as a function of binding energy. This is evidenced by the results of the CMS experiment presented in Figure 2.17. They confirm the assumptions about the existence of QGP.

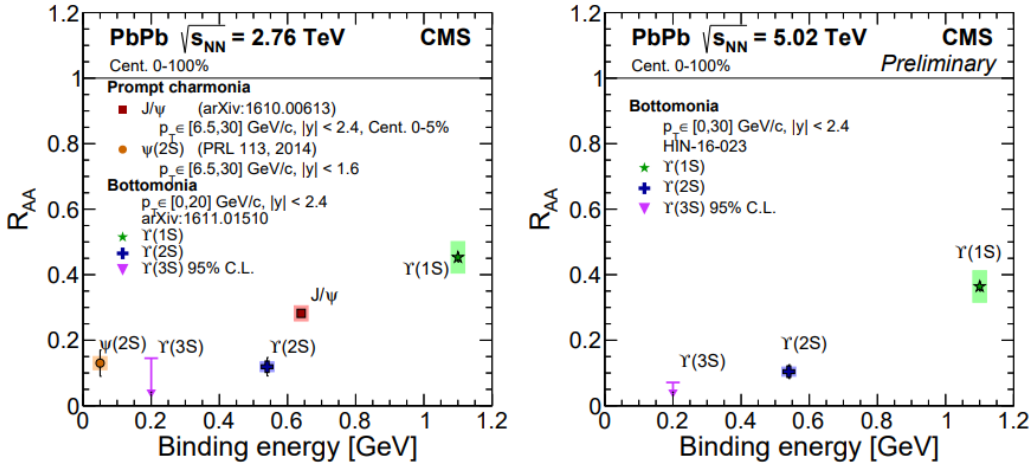

Figure 2.17: Nuclear suppression factor R_{AA} of quarkonium state as a function of the binding energy in Pb+Pb collisions at $\sqrt{s_{NN}}$ = 2.76 TeV (left plot) and 5.02 TeV (right plot) measured by the CMS experiment [37].

Chapter 3

Heavy-ion collision models

QCD does not describe the production of particles in soft processes in which the transverse momentum p_T transmission has a value of less than 2 GeV/c. That is where modeling heavy ion reactions based on known facts and certain theoretical assumptions is useful. Different quantities describe each step of the collision. An example is a triangular flow v_3 which allows the study of fluctuations in the initial state. The analysis of the emission of dileptons and photons allows the probing of the QGP state, and its viscosity is measured through an elliptical flow. In contrast, the thermalization and hadron gas stage can be studied using the hadron yields and resonances [38]. There are three classes of relativistic heavy ion collisions models [39]:

- statistical models, which assume that a grand-canonical ensemble describes the system of non-interacting fermions and bosons in thermal and chemical equilibrium with a temperature T, a chemical potential μ, and the volume V for an average system; does not describe the dynamics; an example is Therminator2 [40, 41];

- (ideal-)hydrodynamical models, which assume thermal and chemical equilibrium, preservation of the laws of physics, and the equation of state; one-fluid and three-fluid models are used to describe the space-time dynamics of the reaction; an example is iHKM [42];

- microscopic transport approaches, which are based on the transport theory of the interacting many-body system on a microscopic level (properties and interaction in elementary degrees of freedom); describe the whole dynamics of the system; an example is UrQMD [43, 44] and SMASH [45].

Two models, UrQMD and Therminator2 generator, used in this work for comparison with experimental data are described below.

3.1 UrQMD

The Ultra-relativistic Quantum Molecular Dynamics is a model based on microscopic transport theory [43, 44]. The hadrons produced as a result of the collision are propagated along classical trajectories, taking into account stochastic scattering, color string formation, as well as resonance decays. The hadron-hadron and nucleus-nucleus collisions at low energies (below $\sqrt{s_{NN}}$ = 3 GeV) are modeled using cross sections between hadrons and resonances. At higher energies, the excitation of color strings and their subsequent fragmentation into hadrons is used. Collisions in UrQMD can be accomplished by 40 mesons including strange particles - Table 3.1 and 55 baryons including nucleons, deltas, and hyperons with masses up to 2.25 GeV/c^2 - Table 3.2, along with the corresponding antiparticles and isospin-related states. Moreover, this

Table 3.1: Mesons used in UrQMD [46]. Mesons with strangeness -1 have a negative sign.

ityp	0^{-+}	**ityp**	1^{--}	**ityp**	0^{++}	**ityp**	1^{++}	**ityp**	charmed
101	π	104	ρ	111	a_0	114	a_1	133	D
106	K	108	K^*	110	K_0^*	113	K_1^*	134	D^*
102	η	103	ω	105	f_0	115	f_1	135	J/Ψ
107	η'	109	ϕ	112	f_0^*	116	f_1'	136	χ_c
ityp	1^{+-}	**ityp**	2^{++}	**ityp**	$(1^{--})^*$	**ityp**	$(1^{--})^{**}$	137	Ψ'
122	b_1	118	a_2	126	ρ_{1450}	130	ρ_{1700}	138	D_s
121	K_1	117	K_2^*	125	K_{1410}^*	129	K_{1680}^*	139	D_s^*
123	h_1	119	f_2	127	ω_{1420}	131	$\omega_1 662$		
124	h_1'	120	f_2'	128	ϕ_{1680}	132	ϕ_{1900}		

model assumes the same number of baryons and antibaryons and identical cross-sections for the interaction of the baryon-baryon and antibaryon-antibaryon pairs. Two hadrons collide when the distance between them is less than $\sqrt{\sigma/\pi}$, where σ is the total cross-section depending on the energy and type of pair. The most precise method of determining such a cross-section is to compare it to the data from dedicated experiments. However, this is only possible for some

Table 3.2: Baryons used in UrQMD [46]. Antibaryons have a negative sign.

ityp	**nucleon**	**ityp**	**delta**	**ityp**	**lambda**	**ityp**	**sigma**	**ityp**	**xi**	**ityp**	**omega**
1	N_{938}	17	Δ_{1232}	27	Λ_{1116}	40	Σ_{1192}	49	Ξ_{1317}	55	Ω_{1672}
2	N_{1440}	18	Δ_{1600}	28	Λ_{1405}	41	Σ_{1385}	50	Ξ_{1530}		
3	N_{1520}	19	Δ_{1620}	29	Λ_{1520}	42	Σ_{1660}	51	Ξ_{1690}		
4	N_{1535}	20	Δ_{1700}	30	Λ_{1600}	43	Σ_{1670}	52	Ξ_{1820}		
5	N_{1650}	21	Δ_{1900}	31	Λ_{1670}	44	Σ_{1775}	53	Ξ_{1950}		
6	N_{1675}	22	Δ_{1905}	32	Λ_{1690}	45	Σ_{1790}	54	Ξ_{2025}		
7	N_{1680}	23	Δ_{1910}	33	Λ_{1800}	46	Σ_{1915}				
8	N_{1700}	24	Δ_{1920}	34	Λ_{1810}	47	Σ_{1940}				
9	N_{1710}	25	Δ_{1930}	35	Λ_{1820}	48	Σ_{2030}				
10	N_{1720}	26	Δ_{1950}	36	Λ_{1830}						
11	N_{1900}			37	Λ_{1890}						
12	N_{1990}			38	Λ_{2100}						
13	N_{2080}			39	Λ_{2110}						
14	N_{2190}										
15	N_{2200}										
16	N_{2250}										

pairs, including protons, pions, and kaons [47]. In the case of the baryon-antibarion interaction at low energies, the annihilation process contributes significantly to the total cross-section. In UrQMD, the experimental data describe the cross-section for $p\bar{p}$ (without annihilation), and the same value is assumed for baryon-antibaryon pairs heavier than the $p\bar{p}$ pairs. Simulating the system's evolution in collisions with an energy $\sqrt{s_{NN}}$ of a few GeV to a few TeV is based on solving the nonrelativistic equations type 3.1 using the Monte-Carlo method:

$$\frac{df_i(x,p)}{dt} = \frac{\partial p}{\partial t}\frac{\partial f_i(x,p)}{\partial p} + \frac{\partial x}{\partial t}\frac{\partial f_i(x,p)}{\partial x} + \frac{\partial f_i(x,p)}{\partial t} = Stf_i(x,p) \tag{3.1}$$

where $df_i(x,p)$ is the phase density as a function of momentum p and position x of i-type particles, $Stf_i(x,p)$ describes the term responsible for the collision of a given type of particles with other types of particles.

The GLISSANDO 3 – GLauber Initial-State Simulation AND mOre package [48, 49, 50] was used to divide the collisions generated from the UrQMD model into different centrality com-

partments, from central to peripheral. It is based on a model of wounded partons, which recreates particle production at RHIC and LHC energies with phenomenological success. In GLISSANDO, each collision is simulated in three stages:

- generation of nucleons positions, which is based on the nuclear density distribution $\rho(r)$; the density distribution is affected by effects such as the shift of the generated coordinates to the center-of-mass frame of the nucleus and nucleon-nucleon expulsion distance d (top-rated in the Glauber model to simulate short-range repulsion); for heavy ions (mass number of nucleus A > 16) the density is given by the Woods-Saxon equation:

$$\rho(r) = \frac{\rho_0}{1 + \exp^{(r - R(1+\beta_2 Y_{20} + \beta_4 Y_{40}))} / \alpha} \tag{3.2}$$

  where ρ_0 is a density in the center of the nucleus, R is the radius, β_2 and β_4 are the deformation parameters, Y_{20} and Y_{40} are the spherical harmonics, and α is the Woods-Saxon width.

- generation of sources' transverse positions and their relative deposited strength (RDS - the measure proportional to the deposited transverse energy);

- calculation of the event-by-event averaged physical quantities and fireball profiles; it performed at the same time as the 2nd stage.

The most crucial stage is the generation of nucleon positions, as it depends on what type of particles will be collided. Given this information, the Woods-Saxon equation can be solved using Table 3.3 constants. In the case of the analyzes described in this dissertation, the most important nucleon were gold ions and collisions at two energies of the BES program. Table 3.4 shows the impact parameter ranges corresponding to the specific centrality.

3.2 THERMINATOR 2 model

Another way to study the statistical production of particles from high-energy collisions in experimental complexes like SPS, RHIC, and LHC is to generate events using Monte Carlo methods (which is useful for simulating systems with many coupled degrees of freedom). This approach has been implemented in the THERMal heavy IoN generator (THERMINATOR) model [40, 41]. Initially, this model allowed for analyzing the highest energies achieved in the LHC

Table 3.3: Parameters of the Woods-Saxon nuclear density distribution for different nuclei [49].

nucleus	**R [fm]**		α **[fm]**		β_2	β_4
	d = 0 fm	d = 0.9 fm	d = 0 fm	d = 0.9 fm		
^{63}Cu	4.24	4.21	0.54	0.459	0.162	-0.006
^{129}Xe	5.49	5.43	0.54	0.459	0.143	-0.001
^{197}Au	6.37	6.29	0.54	0.459	-0.130	-0.030
^{238}U	6.80	6.71	0.54	0.459	0.280	-0.093

Table 3.4: The impact parameter ranges corresponding to the specific centrality classes.

$\sqrt{s_{NN}}$ **[GeV]**	**39**	**200**
0-10%	0.00 - 4.59 fm	0.00 - 4.67 fm
10-70%	4.59 - 12.13 fm	4.67 - 12.27 fm

and RHIC. However, thanks to work [51], it became possible to adapt the Therminator to the lower energy spectrum and to study the collisions from the Beam Energy Scan I (BES-I) program at RHIC.

THERMINATOR uses a thermal model of particle production in which chemical and kinetic freeze-out are simultaneous (single freeze). Various physical models have also been implemented in it:

- Blast - Wave Model [52] - used at this work,
- Krakow Single Freeze-Out [53, 54],
- hydrodynamic models
  - 2 + 1 boost-invariant hydrodynamics [55],
  - 3 + 1 hydrodynamic [56].

This model includes a complete list of resonances and stable and unstable particles. The simulation begins with generating the position and velocity of all the particles. They then follow classical trajectories with velocities calculated as the sum of thermal motion and collective velocity. Resonance decays continue until the remaining particles are stable. Unlike other models,

where the collision energy is given as an input parameter, a set of parameters that define this energy is given here. They are grouped into parameters:

- thermodynamic - temperature T [MeV] and chemical potentials: baryon μ_B [MeV], isospin (3rd component) μ_{I3} [MeV] and strange μ_S [MeV] (determined according to thermal model prediction),
- geometrical - source size at freeze-out ρ_{max}, mean lifetime of fireball τ,
- dynamical - velocity at freeze-out V_t.

Table 3.5 shows the input parameters for all energies from the BES program. The simulation result will be a complete history of generated collisions, including the number of particles produced, the type of particle (presented in the PDG code), and the four-vector of the momentum and position of the particle.

Table 3.5: The THERMINATOR's parameters for the BES program [51].

$\sqrt{s_{NN}}$[GeV]	T [MeV]	μ_B [MeV]	μ_{I3} [MeV]	μ_S [MeV]	ρ_{max}	τ	V_t
7.7	138.95	406.36	-10.378	94.026	8.00	8.30	0.65
11.5	150.12	303.22	-7.825	70.369	8.00	8.35	0.80
19.6	156.17	196.77	-5.189	45.951	8.20	8.75	0.85
27.0	157.60	148.99	-4.006	34.991	8.85	8.75	0.80
39.0	158.38	106.89	-2.064	25.335	8.70	8.60	0.75
62.4	158.78	68.92	-2.024	16.626	9.00	9.40	0.75

Chapter 4

The Relativistic Heavy Ion Collider

One of the largest research centers in the world is BNL, located in Long Island, NY, USA. For over 70 years of activity, BNL has been conducting research in nuclear physics and its application in medicine or high energy physics, important not only to the world of science but also to the lives of ordinary people, like the production of radioisotopes. Some of these studies (such as the discovery of the muon neutrino or the detection of cosmic neutrinos) were appreciated by the Nobel Committee and received the Nobel Prize coveted by scientists [57]. This was only possible with the AGS built in 1960. It is the first device that used and still uses highly focused beams of particles, enabling experiments with a single beam and a fixed target. The collision energies obtained this way were low, mainly from the energy stored in the beam. A more practical solution would be to accelerate two beams of particles moving in the opposite direction in the storage rings and collide them at a specific point. Thus, the idea of building the RHIC was born, and AGS was used as an injector. Construction began in the early 1990s, and the first collisions of gold ions at $\sqrt{s_{NN}}$ = 62 GeV occurred in the summer of 2000. A year later, the designed nominal energy of $\sqrt{s_{NN}}$ = 200 GeV was achieved. Since then, RHIC has continued the legacy of AGS and is one of the best nuclear physics experimental facilities.

4.1 Overview of the RHIC experiment

The Relativistic Heavy Ion Collider is the second-largest heavy ion collider in the world. RHIC can accelerate and collide heavy element ions (mainly Au, but also Cu, U), deuterons, and polarized proton beams over various energies. Protons can be accelerated to 250 GeV, and ion beams to 100 GeV per nucleon. The ions' acceleration occurs in stages, and they pass through

the RHIC complex, as shown in Figure 4.1. In the case of proton-proton collisions, a Linear Accelerator is used as the proton source, which injects a beam into the AGS Booster.

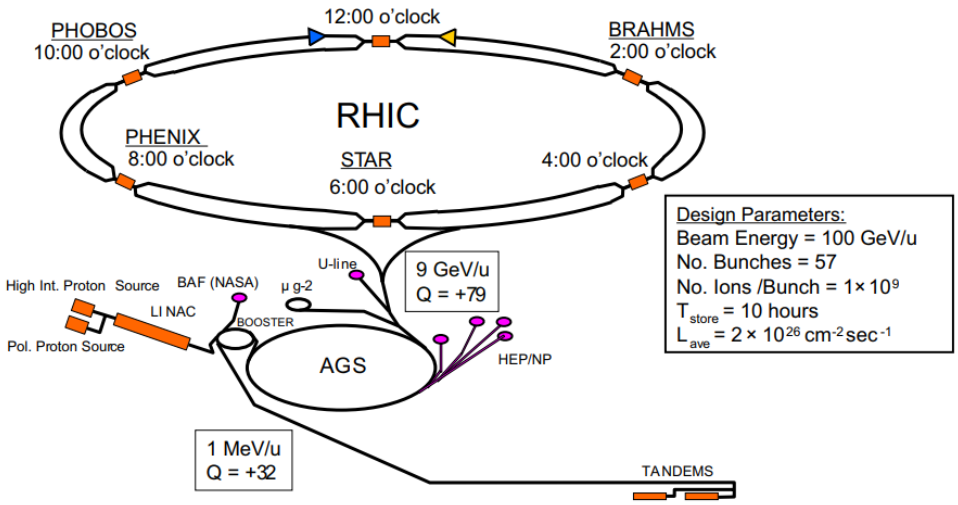

Figure 4.1: RHIC experimental complex [58].

1st stage: Tandem Van de Graaff

This electrostatic accelerator delivers beams of elements ranging from hydrogen to uranium [58]. The Tandem consists of two accelerators arranged one behind the other, one of which is the source of ions for the RHIC, and the other is a backup. In the case of collisions of unequal species, e.g., d+Au, the second accelerator is crucial, as it allows one to quickly switch between different system configurations. Before the beam enters the Heavy Ion Transfer Line (HITL), it must be stripped of some electrons.

2nd stage: Alternating Gradient Synchrotron Booster

This synchrotron allows the AGS to accelerate ions of elements heavier than silicon [59]. It was created because the ions reaching the AGS must be entirely or almost completely stripped of electrons, and the heavier the ions are to collide, the more energy is needed. In Booster, the nuclei are accelerated to 101 MeV/nucleon and pass to the Booster to AGS (BTA) transport line.

3rd stage: Alternating Gradient Synchrotron

Four booster cycles with six bunches per fill are required to fill the AGS. Thus, there are 24 beams that, to meet RHIC beam intensity requirements, combine into

four beams. These, in turn, are accelerated to the energy of 8.86 GeV/nucleon, and thanks to the AGS-to-RHIC Transfer Line (ATR), they go to two independent RHIC rings.

4th stage: Relativistic Heavy Ion Collider

RHIC consists of two rings with a length of 3.834 km. The main element of the collider is superconducting dipole magnets with a total number of 1740, capable of creating a magnetic field with an intensity of up to 3.5 Tesla. To ensure their correct operation, the magnets are placed in vacuum containers and cooled with liquid helium to a temperature of 4.6K (about -269^{o}C). In Figure 4.1, RHIC rings are marked with two colors: blue (clockwise movement) and yellow (contrary to clockwise direction). Beams accelerated to a speed of 0.99995c are directed to clip at 6 points of interaction. There are experiments at four of these points: STAR, PHENIX, PHOBOS, and BRAHMS. STAR is still taking data, but other experiments completed data collection - PHOBOS in 2005, BRAHMS in 2006, and PHENIX in 2016. The modern sPHENIX detector is being constructed and will start collecting data in 2023.

4.2 The Solenoidal Tracker At RHIC detector

The Solenoidal Tracker at RHIC [60] was designed to study the properties of QGP, the structure of the proton, and the interactions of photons and pomerons in ultra-peripheral collisions. Thanks to the improvement of the systems, it became possible to research the QCD phase diagram.

The entire detector is built so that the z-axis (coinciding with the nominal trajectory of the beam) is set parallel to the east-west direction. This arrangement divides the detector into the western part when $z > 0$ and the eastern part when $z < 0$. The $x - y$ plane is located transversely to the axis of the beam, assuming that the x-axis is directed outside the ring and the y-axis is directed upwards. This is how a right-hand Cartesian system is defined. The STAR detector is in a 0.5 T solenoid magnetic field with full azimuthal coverage for tracking charged particles.

STAR comprises many sub-systems, as shown in Figure 4.2. The main sub-detector is the Time Projection Chamber, which provides charged particle tracks. It is used to identify particles with

specific mass and momentum based on measuring the ionization energy loss (dE/dx). This identification method is effective (high single-particle purity is achieved) for particles with low transverse momentum. A Time of Flight detector extends the range to higher momentum. It works by calculating the mass of a particle based on the track length and momentum, i.e., estimating the time of flight. Since these two detectors are the most important for femtoscopic analysis, they will be described in more detail in the following chapters. The particle identification process will be presented in Chapter 7.1.2.

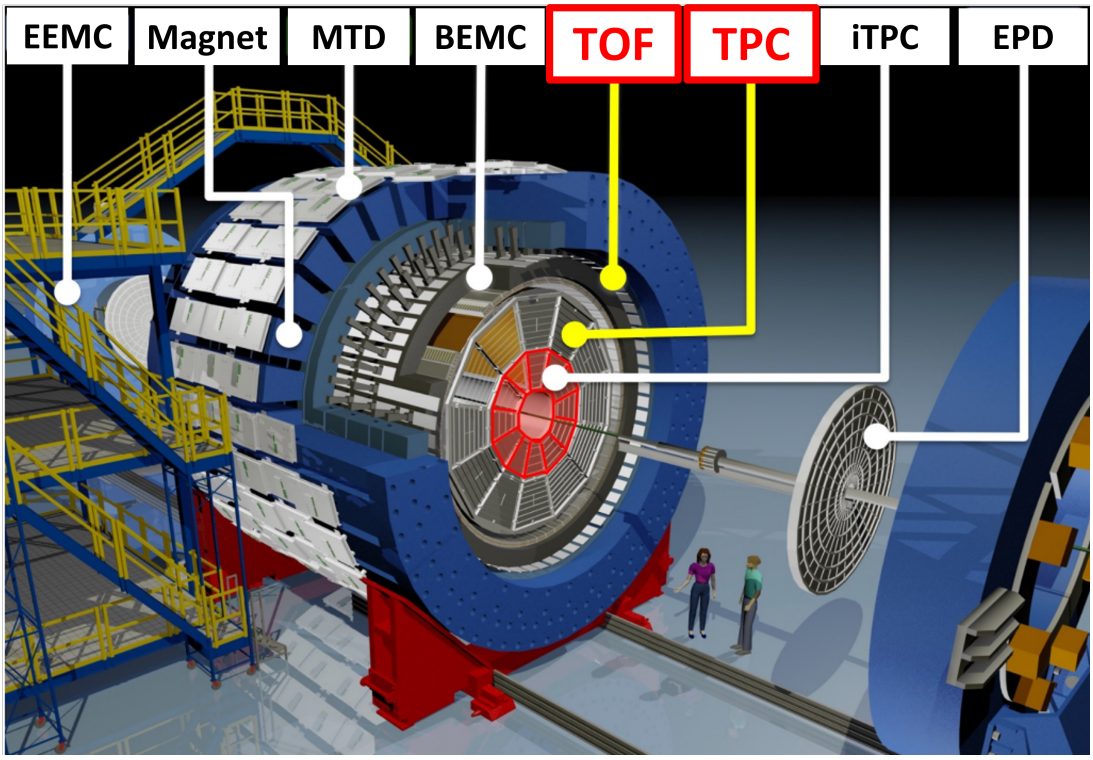

Figure 4.2: Cross-section of the STAR detector [61].

As mentioned earlier, STAR is researching to explore the phase diagram. All this takes part as part of the Beam Energy Scan program - Figure 4.3, which allows for measurements in a wide energy range (BES I - $\sqrt{s_{NN}}$ = 7.7 - 200 GeV, BES II - $\sqrt{s_{NN}}$ = 3 - 7.7 GeV in fix target mode and $\sqrt{s_{NN}}$ = 7.7 - 19.6 GeV in collider mode) using one detector complex. This makes it possible to become independent of any measurement uncertainties resulting from using different machines. The main goals of the BES program include the following [62]:

- to study the phase diagram at different energies to find areas where QGP signatures are off;

- to examine the space between hadronic and quark matter, i.e., the first-order phase transition;
- to find the critical point, the correlation length discrepancy is observed.

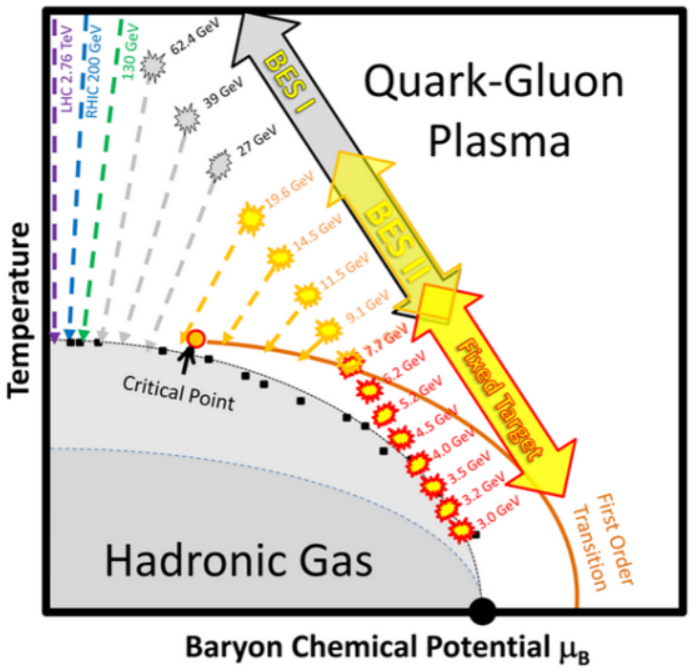

Figure 4.3: QCD phase diagram and energies of the BES program [63].

4.2.1 The Time Projection Chamber

The TPC [64] is a detector of a 4.2 m long barrel with 0.5 m inner and 4 m outer diameter - Figure 4.4. The whole detector is located inside a magnet with a magnetic field strength B = 0.5 T. Thanks to the strong field, it is possible significantly reconstruct the tracks of two particles flying close to each other. It also reduces the resolution uncertainty of the detector. The radius of the STAR detector magnet is 7.32 m, and its length is in the order of 6.85 m. TPC provides acceptance in the pseudorapidity interval $|\eta| < 1.8$ in full azimuthal angle. The interior of the detector is filled with P10 gas, consisting of 10% methane and 90% argon, in which moving particles leave their energy on ionization dE/dx [GeV/cm]. In such a medium, the particle drift velocity is 5.45 cm/μs, so the maximum drift time is $\sim$40 μs.

Positive ions formed due to gas ionization drift to the center of the TPC, where the cathode is located. At the same time, electrons are directed toward the anodes at both ends of the TPC. The

entire apparatus responsible for particle registration consists of over 130,000 pads, giving 12 Multi Wire Proportional Chambers (MWPC) on both sides. The particle's track is reconstructed based on three-dimensional spatial information of a string of ionized clusters located along the particle's trajectory. Each such cluster is built of 45 pads corresponding to trajectory points. The position of the particles obtained in this way is one of many measurements that can be made with the TPC. This detector also identifies charged particles in the momentum range from 100 MeV/c to 1 GeV/c.

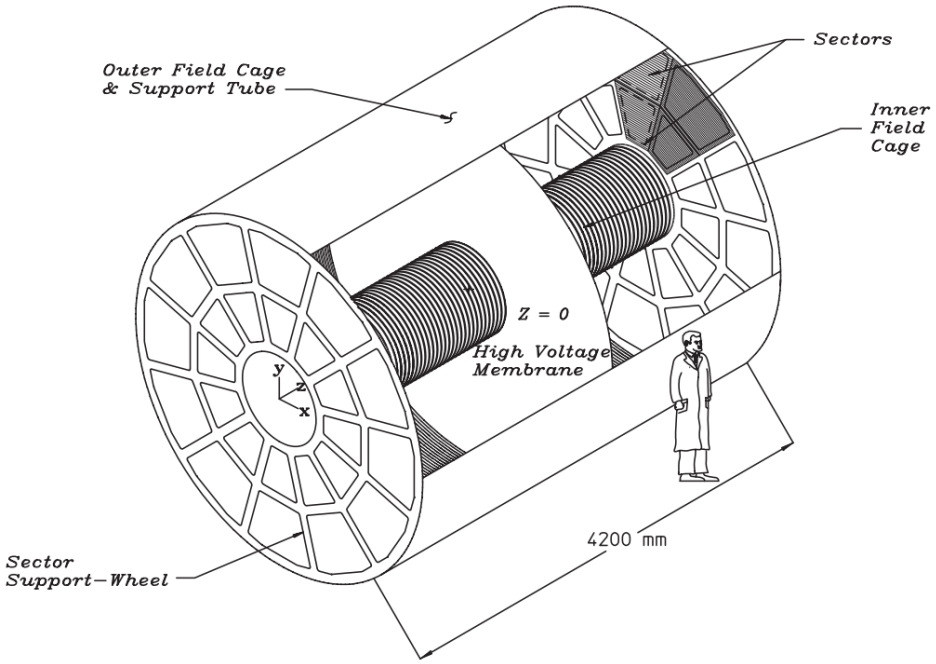

Figure 4.4: Schamatic diagram of the TPC field cage [64].

4.2.2 The Time Of Flight detector

The TOF detector [65] was developed to improve the ability to identify charged particles such as π, K, and p with larger momentum in the range of 0.6 - 3 GeV/c - Figure 4.5. A cylindrical detector around the TPC covers the full azimuthal angle and the pseudorapidity range $|\eta| > 1.0$. TOF is built, among others, of gas gaps filled with a mixture of 90% freon (R134a), 5% butane, and 5% isobutane. It also includes two sub-systems: Pseudo Vertex Position Detector (pVPD) - start detector, and Time of Flight Patch (TOFp) - stop detector.

The main task of TOF is to measure the time of flight of a particle. To do this, high-energy photons from the collision excite the pVPD scintillation plates, turning on the clock. Then the

charged particles reach the TOFp scintillation plates, and the resulting pulse stops the clock. The other tasks of the detector are to measure the momentum and determine the length of the particle's path. TOF also makes it possible to determine the location of the collision in the detector (the farther from this place, the more significant differences in the time of flight will be observed).

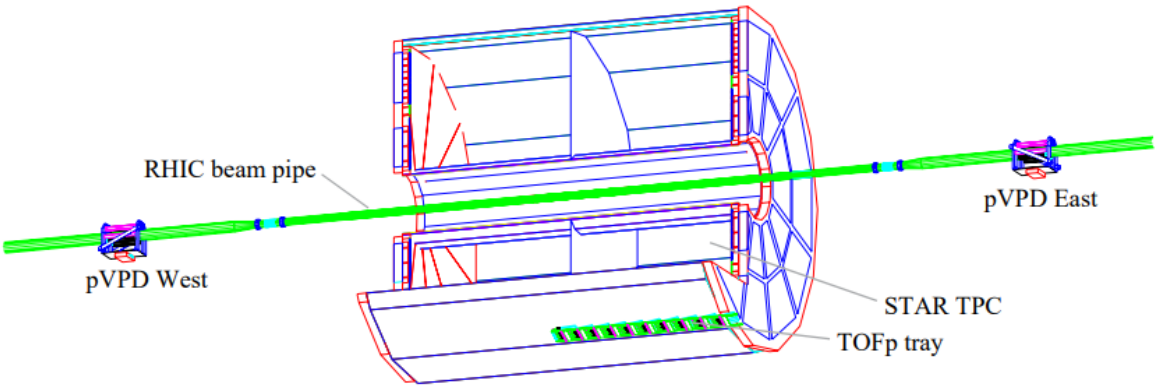

Figure 4.5: Schematic diagram of the TOF highlighted [66].

Chapter 5

Theoretical aspects of two-particle femtoscopy

As mentioned earlier, the QGP state in nuclear collisions arises when the energy is high enough. It is expected that the expansion of the newly formed system will be slower than it would be in collisions at low energies. This effect will be a long lifetime of the system, and its size in the direction of the pair's momentum will be larger. Hanbury-Brown-Twiss interferometry, also known as femtoscopy [67, 68, 69], is a method that allows one the discovery of properties of strongly interacting matter and the study of the space-time characteristic of the particle-emitting source. The size of such an object is in the order of 10^{-15} m, and the lifetime is about 10^{-23} s.

5.1 Historical perspective

The beginnings of femtoscopy date back to the 1950s, when the astronomer Hanbury-Brown and the mathematician Twiss proposed an innovative method for determining the angular sizes of stars (size $\sim 10^{15}$ m) [70]. It was based on photon intensity interferometry, in other words, on studying the intensity of electromagnetic waves emitted from a stellar source. The basic principle consisted of registration by two detectors located at x_3 and x_4, the amplitude of light waves. These waves were superpositions of electromagnetic waves emitted from points x_1 and x_2 lying on the star - Figure 5.1. The detectors measured the amplitude of the signals as a function of the distance between them d. Thanks to the correlation analysis between both signals, it was possible to determine the momentum and angular size of the observed star. The

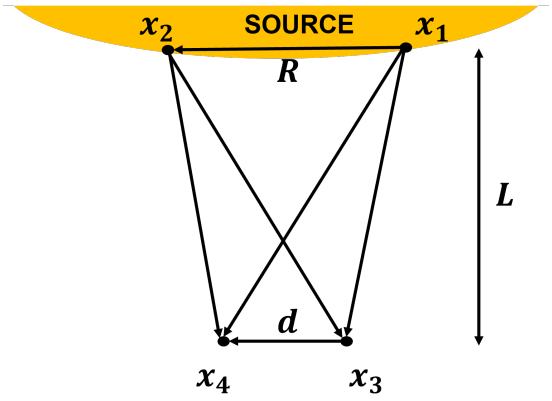

Figure 5.1: Idea of the Hanbury-Brown-Twiss interferometry in astronomy [this thesis].

applied method of measuring spatial correlations inspired the creation of a similar method of measuring momentum correlations, which allows for determining the sizes of sources in (high) energy experiments. The main difference between these two methods is that:

- instead of the distance between the stars (HBT method), the differences in momenta of the analyzed particles are measured (correlation femtoscopy method);
- instead of the angular sizes of stars ($\sim 10^{15}$ m), information about the sizes of emission sources ($\sim 10^{-15}$ m) of a given type of particles is obtained (length of homogeneity).

Then, in 1960, Goldhaber, Lee and Pais noticed that in annihilating protons and antiprotons, pions of the same sign are emitted closer together in phase space than those of the opposite sign. As a result, the distribution of π mesons does not correspond to the predictions of the Fermi model [71]. This finding was explained by the Bose-Einstein statistic, which assumes a higher probability of the existence of identical particles in the same quantum state.

5.2 The theoretical approach

The fundamental quantity in the femtoscopy is the two-particle correlation function $C(\mathbf{p_1}, \mathbf{p_2})$. Which, by definition, is expressed as a ratio of the inclusive two-particle distribution $P_{12}(\mathbf{p_1}, \mathbf{p_2})$ to the product of the inclusive one-particle distributions $P_1(\mathbf{p_1})$ and $P_2(\mathbf{p_2})$:

$$C(\mathbf{p_1}, \mathbf{p_2}) = \frac{P_{12}(\mathbf{p_1}, \mathbf{p_2})}{P_1(\mathbf{p_1}) P_2(\mathbf{p_2})} \tag{5.1}$$

where $\mathbf{p_1}$ and $\mathbf{p_2}$ are the four-momenta of two particles. Therefore, the P_{12} distribution can be interpreted as the probability that both a particle with momentum $\mathbf{p_1}$ and one with momentum $\mathbf{p_2}$ can be observed simultaneously. The product of single-particle distributions is related the probability of observing these particles separately.

Another definition of the correlation function often encountered and used in theoretical models is the description of the source functions $S_1(\mathbf{x_1}, \mathbf{p_1})$, $S_2(\mathbf{x_2}, \mathbf{p_2})$ and $S_{12}(\mathbf{x_1}, \mathbf{p_1}, \mathbf{x_2}, \mathbf{p_2})$ [72]. In this case, the one-particle emission functions S_1 and S_2 can be interpreted as the probability of emission of the first and second particles from specific points ($\mathbf{x_1}$ and $\mathbf{x_2}$, which are four-vector of the position of the first and second particle, respectively) and with specific momentums ($\mathbf{p_1}$ and $\mathbf{p_2}$ respectively). Meanwhile, S_{12} is for a pair of particles. Substituting these quantities into the equation 5.1 will result in a multi-dimensional object, and thus the calculations will be highly complex. To solve the issue, further assumptions are made to reduce the number of analyzed dimensions. The basic assumption is that the emission process is treated as independent when two particles interact in the final state. So this gives the following expression to describe the correlation function:

$$C(\mathbf{p_1}, \mathbf{p_2}) = \frac{\int d^4x_1 d^4x_2 S_{12}(\mathbf{x_1}, \mathbf{p_1}, \mathbf{x_2}, \mathbf{p_2}) |\Psi_{12}|^2}{\int d^4x_1 S_1(\mathbf{x_1}, \mathbf{p_1}) \int d^4x_2 S_2(\mathbf{x_2}, \mathbf{p_2})} \tag{5.2}$$

where S_{12} includes all two-particle correlation without this from FSI and Ψ_{12} is a pair wave function describing interactions between particles. The wave function of a pair is a linear combination of two-particle emission assumptions. The first one says that a particle with momentum $\mathbf{p_1}$ is emitted from space point $\mathbf{x_1}$, while a particle with momentum $\mathbf{p_2}$ is emitted from point $\mathbf{x_2}$. The second assumption corresponds to a symmetric situation, i.e., a particle with momentum $\mathbf{p_1}$ is formed at $\mathbf{x_2}$ and a particle with momentum $\mathbf{p_2}$ at $\mathbf{x_1}$. Thus, the wave function of the particle pair is described by an equation that is well-known from quantum mechanics:

$$\Psi_{12} = \frac{1}{\sqrt{2}} \left(e^{i\mathbf{p_1}\mathbf{x_1} + i\mathbf{p_2}\mathbf{x_2}} \pm e^{i\mathbf{p_1}\mathbf{x_2} + i\mathbf{p_2}\mathbf{x_1}} \right) \tag{5.3}$$

This function must be symmetric for baryons subject to Bose-Einstein statistics ("+" in the above equation) and antisymmetric for fermions subject to Fermi-Dirac statistics ("-" in the equation).

When two identical particles are analyzed, there is some simplification $S_1 \equiv S_2 \equiv S$, and the wave function is not time-dependent, then the correlation function will be given by:

$$C(\mathbf{p_1}, \mathbf{p_2}) = \frac{\int d^3x_1 d^3x_2 S_{12}(\mathbf{x_1}, \mathbf{p_1}, \mathbf{x_2}, \mathbf{p_2}) |\Psi_{12}|^2}{\int d^3x_1 S(\mathbf{x_1}, \mathbf{p_1}) \int d^3x_2 S(\mathbf{x_2}, \mathbf{p_2})} \tag{5.4}$$

5.2.1 Correlations of identical bosons

As mentioned earlier, the first correlation observations between two identical bosons (π mesons) were made by Goldhaber and others [71]. A few years later, similar relationships (the difference in the open angle distribution between identical and non-identical pions) were observed in pion-proton collisions. It has been noticed that this effect comes mainly from pion pairs with close momenta [7]. Later research also confirmed this by focusing on pairs of strange baryons: $K^{\pm}K^{\pm}$ [73] and $K_s^0K_s^0$ [74].

In order to accurately describe the effect of the Bose-Einstein statistics on the correlation function, a simple model should be used that will take into account the symmetrization of the wave function for pions. Again, one considers two particles emitted from space points $\mathbf{x_1}$ and $\mathbf{x_2}$ and having $\mathbf{p_1}$ and $\mathbf{p_2}$. Having information about the momentum, two observables should be introduced: the relative momentum $\mathbf{q}$ which is the difference of the momenta of both particles (equation 5.5) and the momentum of the pair in the center of mass $\mathbf{k}$ described by the equation 5.6 [75].

$$\mathbf{q} = \mathbf{p_1} - \mathbf{p_2} \tag{5.5}$$

$$\mathbf{k} = \frac{1}{2}(\mathbf{p_1} + \mathbf{p_2}) \tag{5.6}$$

Using these quantities, the wave function expressed by the equation 5.3 will look like this:

$$\Psi_{12} = \frac{1}{\sqrt{2}} e^{i\mathbf{k}(\mathbf{x_1}+\mathbf{x_2})} \left(e^{i\mathbf{q}(\mathbf{x_1}-\mathbf{x_2})/2} + e^{-i\mathbf{q}(\mathbf{x_1}-\mathbf{x_2})/2} \right) \tag{5.7}$$

The two-particle distribution for identical pions is as follows:

$$P_{12}(\mathbf{p_1}, \mathbf{p_2}) = \int d^3x_1 d^3x_2 \rho(\mathbf{x_1}) \rho(\mathbf{x_2}) |\Psi_{12}|^2 \tag{5.8}$$

where $\rho(x)$ is a density distribution of the points. So, substituting the formula for the wave function, one gets:

$$P_{12}(\mathbf{p_1}, \mathbf{p_2}) = \int d^3x_1 d^3x_2 \rho(\mathbf{x_1}) \rho(\mathbf{x_2}) \left[1 + \frac{1}{2} \left(e^{i\mathbf{q}(\mathbf{x_1}-\mathbf{x_2})} + e^{-i\mathbf{q}(\mathbf{x_1}-\mathbf{x_2})} \right) \right] \tag{5.9}$$

The single-particle distribution is determined in a similar way and is described by the equation:

$$P(\mathbf{p}) = \int d^3x \rho(\mathbf{x}) \left| e^{i\mathbf{p}\mathbf{x}} \right|^2 = \int d^3x \rho(\mathbf{x}) \tag{5.10}$$

Substituting one- and two-particle distribution into the equation 5.1 will define the correlation function for this case:

$$C(\mathbf{k}, \mathbf{q}) = 1 + \frac{\left| \int d^3x e^{-i\mathbf{q}\mathbf{x}} \rho(\mathbf{x}) \right|^2}{\left| \int d^3x \rho(\mathbf{x}) \right|^2} \tag{5.11}$$

The fundamental problem with this equation is that it does not consider the time dependence of the pion-emitting source. To solve this issue, it should associate the density matrix $\rho(\mathbf{p_1},\mathbf{p_2})$ with the emission function $S(x,\mathbf{k})$ while remembering that $\mathbf{p_1}=\mathbf{k}+1/2\mathbf{q}$, $\mathbf{p_2}=\mathbf{k}-1/2\mathbf{q}$. Then the dependence is obtained:

$$\rho(\mathbf{p_1},\mathbf{p_2})=\rho\left(\mathbf{k}+\frac{1}{2}\mathbf{q},\mathbf{k}-\frac{1}{2}\mathbf{q}\right)=\int d^4x e^{i\mathbf{qx}}S(\mathbf{x},\mathbf{k}) \tag{5.12}$$

Knowing that the momentum distribution of pions is the space-time integral of the emission function and using the smoothness approximation (the denominator of the correlation function is weakly dependent on the $\mathbf{q}$ variable), the correlation function is obtained in the reduced form:

$$C(\mathbf{k},\mathbf{q})=1+\frac{\left|\int d^4x e^{i\mathbf{qx}}S(\mathbf{x},\mathbf{k})\right|^2}{\left|\int d^4x S(\mathbf{x},\mathbf{k})\right|^2} \tag{5.13}$$

The interpretation of this equation is straightforward and suggests that the correlation function is the Fourier transform of the emission function. It follows that the range $C(\mathbf{k},\mathbf{q})$ is related to the size of the particle emitting source [75].

5.3 Bertsch-Pratt parametrization

The equations presented in the previous chapters show that the correlation functions depend on the difference in the momentum of the particle pair. There are several ways to describe this difference - it is possible to reduce the function to a one- or multi-dimensional form. In the latter case, the Bertsch-Pratt parameterization is used [76], which describes three directions:

- *long* - parallel to the beam axis; the same for each pair of particles;
- *out* - perpendicular to the *long* direction and parallel to the vector of the total momentum of the particle pair; determined individually for each pair;
- *side* - perpendicular to the *out* and *long* directions.

When using this parameterization, two reference systems are usually used: the Longitudinal Co-Moving System and the Pair Rest Frame .

Longitudinal Co-Moving System

In the LCMS system (used in the analysis of identical particles), a three-dimensional correlation

function is measured, i.e., the source characteristics are obtained in three dimensions. Considering the Gaussian source (only QS effects), three radii are defined R_{out}, R_{side} and R_{long}, and the correlation function itself will be described as:

$$C(\mathbf{q}) = 1 + \lambda e^{-q_{out}^2 R_{out}^2 - q_{side}^2 R_{side}^2 - q_{long}^2 R_{long}^2 - 2q_{out}q_{side}R_{out,side}^2 - 2q_{out}q_{long}R_{out,long}^2} \tag{5.14}$$

where λ is the coefficient of incoherence and q_{out}, q_{side} and q_{long} are the relative momenta in the *out*, *side*, and *long* directions (Figure 5.2), respectively. The coefficient of incoherence takes

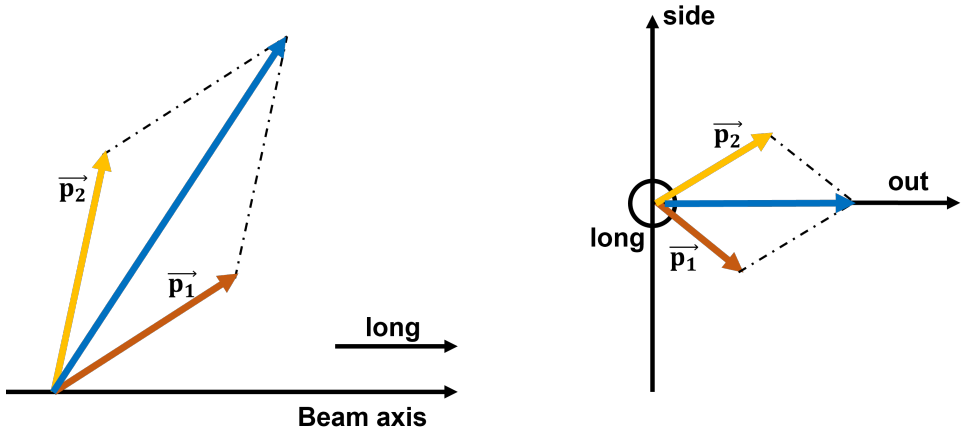

Figure 5.2: Definition of the LCMS system [this thesis].

the value of 1 for bosons for a completely chaotic source, i.e., when the particles are emitted independently. There is also a possibility that λ will be less than 1, then a significant contribution to the production of particles will be halo.

With appropriate assumptions, the femtoscopic radii for pairs of identical particles can be expressed as:

$$R_{out} = \frac{R_{geo}}{\sqrt{1 + \frac{m_T \eta_f^2}{T}}} \tag{5.15}$$

$$R_{out}^2 - R_{side}^2 = \Delta\tau^2 \beta_T^2 \tag{5.16}$$

$$R_{long} = \tau_0 \left(\frac{T}{m_T}\right)^2 \tag{5.17}$$

where R_{geo} is the geometric size of the source, m_T is the transverse mass, η_f is the source expansion parameter, T is the kinetic freeze temperature, $\Delta\tau$ is the particle emission time, β_T is the pair velocity in the *out* direction, and τ_0 is the source lifetime [77]. The transverse mass depends on the average transverse momentum of the pair $\mathbf{k_T}$ and the mass of the particle m according to the equation:

$$m_T = \sqrt{\mathbf{k_T}^2 + m^2} \tag{5.18}$$

Whereas $\mathbf{k_T}$ is described by the transverse momentum of individual particles and expressed by a formula similar to the equation 5.6. Scaling of femtoscopic radii from $\mathbf{k_T}$ is expected in the LCMS system for pairs of identical particles. Moreover, as current scientific research shows, such scaling is present and is interpreted as a consequence of the collective expansion of the source. As a result, there is a visible relationship between the momentum and the place of particle creation.

Pair Rest Frame

The PRF system expresses the correlation function depending on the first particle's momentum $\mathbf{k}^* = |\mathbf{p_1}| = |\mathbf{p_2}|$ (Figure 5.3), and not as it was in LCMS as a function of $\mathbf{q}$. However, it

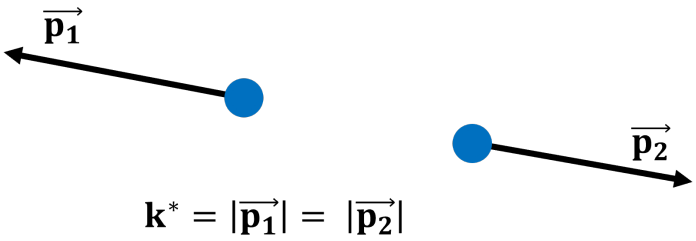

Figure 5.3: Definition of the PRF system [this thesis].

is possible easily relate the two quantities to each other. PRF moves together with a pair of identical particles (the momentum of the pair is zero), and then one can get:

$$|2\mathbf{k}^*| = \mathbf{q_{inv}} \tag{5.19}$$

The difference appears in the out direction, wherein in the PRF system, the pair momentum is zero, while in LCMS, it is not - as a result, the equation 5.19 does not apply. Despite this, the similarities between the two systems are so significant that the relative coordinates can be calculated using the equations [78]:

$$r^*_{out} = \gamma_T (r_{out} - \beta_T \Delta t) \tag{5.20}$$

$$r^*_{side} = r_{side} \tag{5.21}$$

$$r^*_{long} = r_{long} \tag{5.22}$$

$$\Delta t^* = \gamma_T (\Delta t - \beta_T r_{out}) \tag{5.23}$$

where asterisks * mean value in PRF, r_{out}, r_{side} and r_{long} are a relative separation of particles in the pair, γ_T is the Lorentz factor related to the movement of the pair in the transverse direction

and expressed by the formula:

$$\gamma_T = \frac{1}{\sqrt{1 - \left(\frac{V_t}{c}\right)^2}} \tag{5.24}$$

5.4 Length of homogeneity

The concept of *length of homogeneity* appeared in the late 1980s thanks to Sinyukov [79, 80], who referred to the source dynamics resulting from flows. The quantities determined by correlation femtoscopy methods do not describe the fireball created in the collision. They only characterize averaged homogeneity length. Basic assumptions derived from hydrodynamics describe that the velocity of each particle consists of two components: random (thermal) velocity and collective once. The thermal component is dominant when the particle pairs come from regions with low relative momentum (femtoscopic signal limitation) and have low transverse momentum. This means the particles come from two distant points on the fireball (a large radius). On the other hand, particles produced close together (a small radius) with a similar flow direction and thermal velocity vectors have a large transverse momentum.

5.5 The experimental approach

When studying the experimental correlation function, it should be remembered that it will be determined differently than in theory. It will be defined as the ratio of the signal $A(\mathbf{q})$, which is the relative distribution of the momentum of pairs of particles from the same collision (correlated pairs), to the background $B(\mathbf{q})$, which is the distribution of pairs belonging to different collisions (uncorrelated pairs):

$$C(\mathbf{q}) = \frac{A(\mathbf{q})}{B(\mathbf{q})} \tag{5.25}$$

Where $\mathbf{q}$ is described by the equation 5.5. In the case of an experimental function, it is difficult to build a $B(\mathbf{q})$ background because there is no universal method for it. Ideally, the distributions of $A(\mathbf{q})$ and $B(\mathbf{q})$ should be equal except for the correlation effect. The most popular method of creating a background is the event-mixing technique. It consists of particles from two different but similar collisions that form a pair. The similarity should be in terms of the multiplicity and the primary vertex location. Other methods of background construction are the relative momentum distribution of pairs with different charges and distributions generated using Monte Carlo methods.

5.6 Final State Interaction

In addition to the effects of QS (Bose-Einstein and Fermi-Dirac statistics), correlations of particles produced in collisions can also be induced by Coulomb and strong FSI. Each of these interactions has a different effect on the appearance/shape of the final correlation function.

Coulomb FSI

The Coulomb interaction plays a dominant role in the area of the smallest relative momenta. Depending on whether identical or nonidentical particles are subject to analysis, it will lead to a decrease or increase in correlation effects. These effects can make data analysis difficult, but at the same time, they are an essential source of information. The charge of the particle emitting system is also crucial, especially when at least one particle from the pair is charged. The value that determines the shape of Coulomb FSI is the Gamow factor expressed by the formula:

$$A_c^{\pm}(k^*) = \pm\frac{2\pi}{k^* a_c}\left(e^{\pm\frac{2\pi}{k^* a_c}} - 1\right)^{-1} \tag{5.26}$$

where $a_c \sim (\pm\mu z_1 z_2 e^2)^{-1}$ is the Bohr radius for a given two-particle system (e.g., for a K^+K^- pair, it is -110 fm [81]). As the research shows, the size of the Coulomb interaction area is inversely proportional to the Bohr radius and increases with the mass of the particles. The $\pm$ sign in the equation relates to the repulsion and attraction of the particles in the pair, respectively. Initially, the Gamow factor was used to correct the correlation function. However, as it turned out later, it is not applicable in the case of large sizes of the source emitting particles and significant masses of pairs. Then the effects of the Coulomb interaction carry information about the length of homogeneity.

Strong FSI

The strong interaction plays an essential role in baryon correlations, but as the results obtained in this work will show, also in the analysis of the $K_S^0K_S^0$ and $K_S^0K^{\pm}$ systems. The interaction between a pair of particles is described by an effective range approximation where the pair is treated as a scattering of low-energy particles. Thanks to this, the wavelength of the particles is so large that the strong FSI is not sensitive to the shape of the potential. Such a simplification means that detailed knowledge of the shape of the potential is not needed. Moreover, the interaction itself will be characterized by two parameters - the scattering length f_0^s and the effective radius d_0^s. Unfortunately, for pairs of exotic particles, these two quantities are unknown.

However, in the case of baryon-antibaryon analysis, f_0^s and d_0^s are often known, and the Lednicky-Lyuboshitz analytical model can then be used [82]. Then the correlation function dependent on the wave function Ψ takes the form:

$$CF(\mathbf{k}^*) = 1 + \sum_s \rho_s \left[\frac{1}{2} \left| \frac{f^s(k^*)}{R} \right|^2 \left(1 - \frac{d_0^s}{2\sqrt{\pi}R} \right) + \frac{2\,\mathrm{Re}\, f^s(k^*)}{\sqrt{\pi}R} F_1(2k^*R) - \frac{\mathrm{Im}\, f^s(k^*)}{R} F_2(2k^*R) \right] \tag{5.27}$$

where s describes different spin states (singlet or triplet), ρ_s is related to the spin-charge of the pair, while $f^s(k^*)$, $F_1(z)$ and $F_2(z)$ are analytical functions expressed:

$$f^s(k^*) = \left(\frac{1}{f_0^s} + \frac{1}{2} d_0^s k^{*2} - ik^* \right)^{-1} \tag{5.28}$$

$$F_1(z) = \int_0^z dx \frac{e^{x^2 - z^2}}{z} \tag{5.29}$$

$$F_2(z) = \frac{1 - e^{-z^2}}{z} \tag{5.30}$$

The equation 5.27 omits summation over spin orientations and sets the value of the effective radius to zero for calculations. Then a simplified form of this equation is obtained. The imaginary part of this formula is responsible for the baryon-antibaryon annihilation process. Thus, two cases can be considered when the imaginary component of the correlation function is computed with non-zero and zero values of the scattering length.

The left part of Figure 5.4 shows the first scenario when the annihilation process is considered. A broad anticorrelation extending to hundreds of MeV can be seen. On the other hand, the right part of Figure 5.4 shows the situation when $\mathrm{Im}(f_0)$ is set to zero, i.e., no annihilation is observed. The range of anticorrelation is limited.

5.7 Correlation function parametrizations

The basic assignment of femtoscopic analysis is to extract the size of the particles emitting source from the experimental data. For this purpose, the equation 5.13 should be integrated to obtain the correlation function formula that can be used in the fitting procedure. Knowledge of the wave function for two pions Ψ_{12} and the functional form of the emission function $S(\mathbf{x}, \mathbf{k})$ is required. To know the form $S(\mathbf{x}, \mathbf{k})$ one should make the following assumptions [84]:

- the emission function is described by a Gaussian distribution in LCMS;

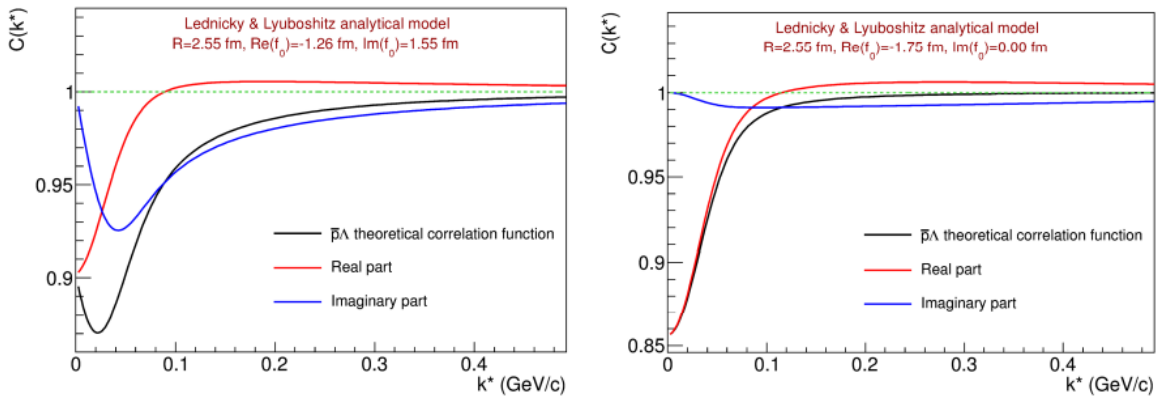

Figure 5.4: The $\bar{p}-\lambda$ theoretical correlation functions calculated from Lednicky-Lyuboshitz model with the non-zero (the left panel) and zero (the right panel) imaginary component of the scattering lenght [83].

- its dependence on the longitudinal component **k** is neglected;
- $\mathbf{k_T}$ binning (the emission function is independent of **k** within each interval of $\mathbf{k_T}$) is used to analyze its dependence on the transverse component **k**.

The result of this is the emission function of the form:

$$S(\mathbf{x}) \approx \exp\left(-\frac{x_{out}^2}{4R_{out}^2} - \frac{x_{side}^2}{4R_{side}^2} - \frac{x_{long}^2}{4R_{long}^2}\right) \tag{5.31}$$

In the case of p+p collisions, the Gaussian emission function is primarily used. However, as the ALICE experiment showed, it can be a combination of the Lorentzian form (in the *out* and *long* direction) and the Gaussian form (in the *side* direction) [85].
In the case of A+A collisions (analyzed in this thesis), the Gaussian function very well describes the homogeneity region. Because it gives the approximate source size for any combination of colliding particles and each experiment, it is possible to compare results between laboratories. Therefore, the simplest parameterization is expressed by the formula 5.14, which can be reduced to a one-dimensional form:

$$C(q_{inv}) = 1 + \lambda e^{-q_{inv}^2 R_{inv}^2} \tag{5.32}$$

where $q_{inv} = \sqrt{(p_1-p_2)^2-(E_1-E_2)^2}$ and $R_{inv} = \sqrt{(R_{out}^2+R_{side}^2+R_{long}^2)/3}$ characterizes the size of the emission area. This parameterization takes into account only the effects of quantum statistics. In order to take into account the Coulomb interaction, which is also important in the

analysis of pairs of identical particles, one needs to add a term associated with this interaction K_{coul} and express the wave function as follows:

$$C(\mathbf{q}) = (1-\lambda) + \lambda K_{Coul}(q_{inv}) \left(1 + e^{-q_{out}^2 R_{out}^2 - q_{side}^2 R_{side}^2 - q_{long}^2 R_{long}^2 - 2q_{out}q_{side}R_{out,side}^2 - 2q_{out}q_{long}R_{out,long}^2}\right) \tag{5.33}$$

The most commonly used description of the correlation function is the Bowler-Sinyukov parameterization, in which the Coulomb FSI is determined separately for each pair of particles in three-dimensional momentum space [86, 87]. However, the K_{Coul} function is determined in one-dimensional momentum space because the differences in the parameterization of the Coulomb interaction in three dimensions are minimal and can be neglected. Therefore, the function K_{Coul} is expressed in terms of the one-dimensional quantity q_{inv}.

The parameterization described above can be used to analyze identical pions and kaons. In the case of studies of the system of two neutral kaons, the Lednicky-Lyuboshitz parameterization considering the strong FSI should be used. The correlation function will be described by the modified equation 5.27 and will take the form:

$$CF(k^*) = 1 + \lambda \left(e^{\left[-4k^{*2}R^2\right]} + \alpha \left[\left| \frac{f(k^*)}{R} \right|^2 + \frac{4\,\mathrm{Re}\, f(k^*)}{\sqrt{\pi}R} F_1(2k^*R) - \frac{2\,\mathrm{Im}\, f(k^*)}{R} F_2(2k^*R) \right] \right) \tag{5.34}$$

where α is a parameter describing the fraction of pairs $K_S^0 K_S^0$ coming from the $K^0\bar{K^0}$ system, which assumes symmetry of production K^0 and $\bar{K^0}$ takes the value 0.5 [88], the functions F_1 and F_2 are described by the equations 5.29 and 5.30, respectively. In turn, $f(k^*)$ is the s-wave scattering amplitude of $K^0\bar{K^0}$ pair, which depends on s-wave isoscalar and isovector $f_0(980)$ and $a_0(980)$ resonances, it is described by the dependency:

$$f(k^*) = \frac{f_0(k^*) + f_1(k^*)}{2} \tag{5.35}$$

$$f_I(k^*) = \frac{\gamma_r}{m_r^2 - s - i\gamma_r k^* - i\gamma_r' k_r'} \tag{5.36}$$

where f_I is the amplitude at isospins I=0 and I=1 corresponding to resonances f_0 and a_0 respectively; γ_r and γ_r' are couplings with decay channels $K\bar{K}$, $\pi\pi$ and $K\bar{K}$, $\pi\eta$; m_r is the resonance mass; $s = 4(m_K^2 + k^{*2})$ and k_r' is the momentum in the second decay channel.

The equation 5.34 has two terms. The first term is a Gaussian function (equation 5.32) describing only the QS effects, while the latter defines the interactions in the final states. Since the described system is a pair of neutral kaons, there is no Coulomb interaction, only a strong

one. In this equation, the imaginary part of the scattering amplitude is dominant, which is determined by the ratio of couplings $f_0 \to K\bar{K}$ to $f_0 \to \pi\pi$ and $a_0 \to K\bar{K}$ to $a_0 \to \pi\eta$. Their variability is small. Therefore insufficient information about the properties of both resonances is not a problem. This thesis will describe the results for four different resonance masses and couplings (Table 5.1).

Table 5.1: The most common parameters describing $f_0(980)$ and $a_0(980)$ resonances used in the Lednicky-Lyuboshitz model.

	$\mathbf{m_{f_0}[GeV/c^2]}$	$\gamma_{\mathbf{f_0K\bar{K}}}$	$\gamma_{\mathbf{f_0\pi\pi}}$	$\mathbf{m_{a_0}[GeV/c^2]}$	$\gamma_{\mathbf{a_0K\bar{K}}}$	$\gamma_{\mathbf{a_0\pi\pi}}$
Antonelli [89]	0.973	2.763	0.5283	0.985	0.4038	0.3711
Achasov2001 [90]	0.996	1.305	0.2684	0.992	0.5555	0.4401
Achasov2003 [91]	0.996	1.305	0.2684	1.003	0.8365	0.4580
Martin [92]	0.978	0.792	0.1990	0.974	0.3330	0.2220

In the case of correlations of nonidentical particles, i.e., $K^0_S K^{\pm}$, only the strong interaction coming from the near-threshold resonance a_0 (980) should be considered. This is because two different particles are considered, and therefore there are no QS effects. Second, K^0_S is a neutral particle, so it does not interact Coulombically. Thirdly, the resonance f_0 (980) is also neutral, so it cannot affect the combination of a neutral particle with a charged one. As a result, the correlation function is described as follows:

$$CF(k^*) = 1 + \lambda\alpha\left[\frac{1}{2}\left|\frac{f(k^*)}{R}\right|^2 + \frac{2\,\mathrm{Re}\,f(k^*)}{\sqrt{\pi}R}F_1(2k^*R) - \frac{\mathrm{Im}\,f(k^*)}{R}F_2(2k^*R)\right] \tag{5.37}$$

The form of this equation differs from the equation 5.34 by the term 1/2 due to the different particles in the pair $K^0_S K^{\pm}$. Thus the wave function of the equation does not need to be symmetric [93].

5.8 The experimental review of selected results of particle correlations

Currently, many research centers (like BNL and CERN) are conducting numerous studies aimed at understanding the time-space characteristics of the source formed as a result of high-energy

collisions. As mentioned many times before, one such method is the technique of correlation femtoscopy. The most important results obtained by this method are described below.

Two-pion interferometry in Au+Au collisions at STAR experiment

One of the most important results of two-particle correlations for a system of identical pions were obtained by the STAR experiment [94]. They used data collected by the BES program, which provided a comprehensive energy scan from $\sqrt{s_{NN}}$ = 7.7 - 200 GeV for Au+Au collisions using the same detector. The result of the analyzes is the three-dimensional sizes of the source R_{out}, R_{side} and R_{long} as a function of the average transverse mass $< m_T >$ for seven different energies presented in Figure 5.5. For each of the three radii, their value decreases with the increase in the average transverse mass. The reason for this is transverse collective flow in the *out* and *side* directions, while longitudinal flow appears in the *long* direction. It is essential to remember that pairs with a larger m_T are emitted from smaller emission regions, which cannot be equated with the size of the fireball created in the collision. It is also observed that the sizes in the direction *out* and *side* for different beam energies are similar in magnitude and slope. On the other hand, the radius in the *long* direction has a similar slope for all energies, but its values increase with the collision energy. This is true for all centrality. As expected, there is a natural effect of increasing size in all three directions as one moves from peripheral collisions (60-70%) to central ones (0-5%).

As mentioned in Chapter 2.4, the femtoscopy technique is crucial in the QGP study. Its results - large source size and long lifetime - were postulated as signatures of the state of the plasma. When analyzing pairs of identical pions, there is a noticeable increase in transverse size by about 10%. It is, therefore, possible to search for a relationship between hadronic and quark matter and the shape of the particle emitting source at the moment of kinetic freezeout. The shape of the source depends on the centrality of the collision, e.g., for non-central ones, it initially resembles an almond. The dependence of R_{long} on the average transverse mass allowed us to extract the lifetime of the collision evolution. Under certain assumptions, lifetime increases by 1.7 times from collisions at AGS to 200 GeV and by 1.4 times between RHIC and LHC.

Neutral kaon interferometry in heavy ion collisions at STAR and ALICE experiment

The first femtoscopic measurement of two neutral kaon combinations was published in 2006 by the STAR experiment [88]. Data for the most central (0-10%) Au+Au collisions at top RHIC energy - 200 GeV were used for the analysis. The obtained correlation function is shown in

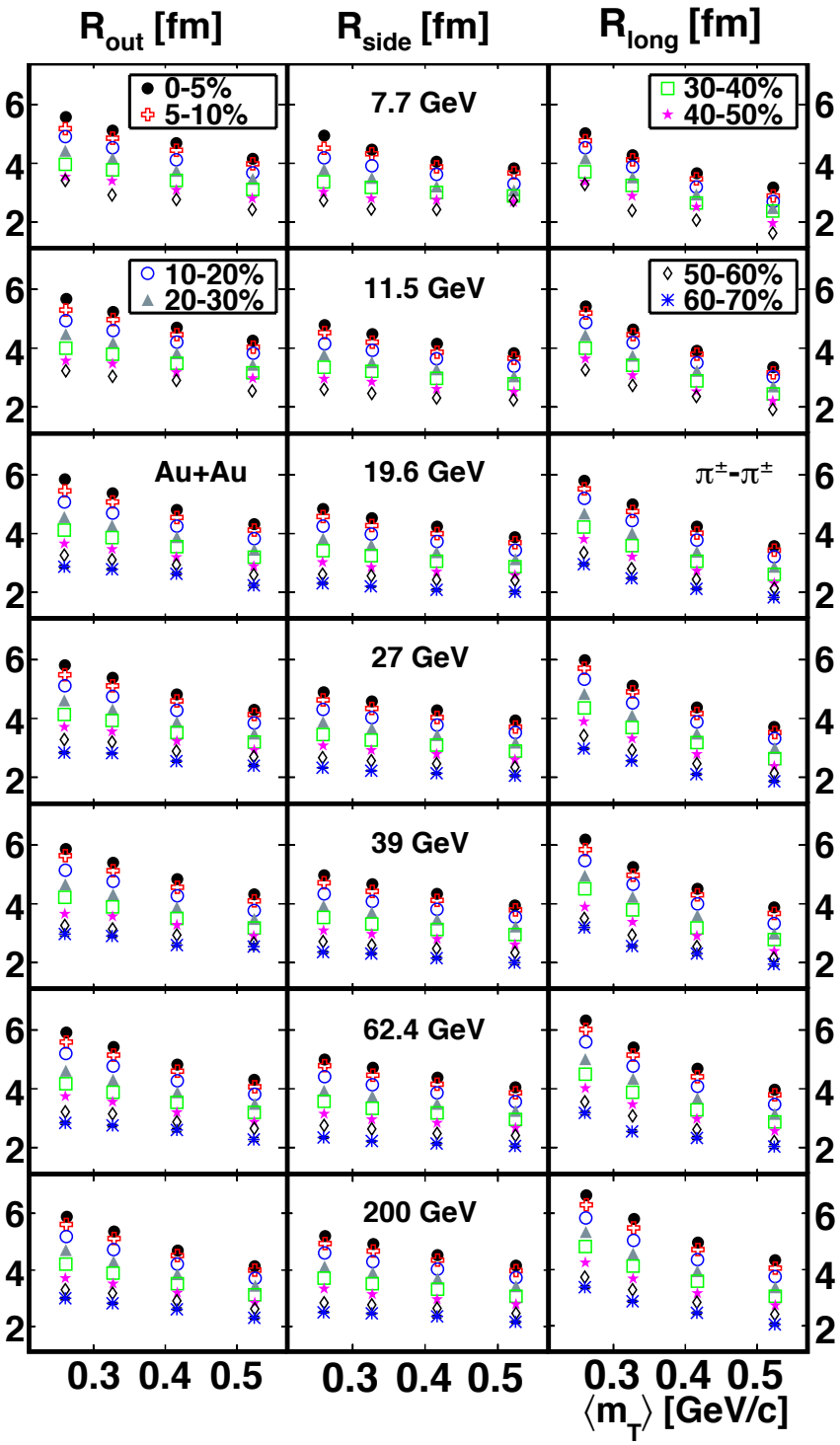

Figure 5.5: Femtoscopic source sizes in *out*, *side*, and *long* as a function of average transverse mass for seven energies from the BES program and six centrality ranges [94].

Figure 5.6. Initially, a Gaussian fit (equation 5.32) was fitted, which only considers the effects of quantum statistics. Then the source size is 5.02 ± 0.61 fm, and the parameter λ is 1.08 ± 0.29. It can be seen that the Gaussian fit does not describe the region of the correlation function

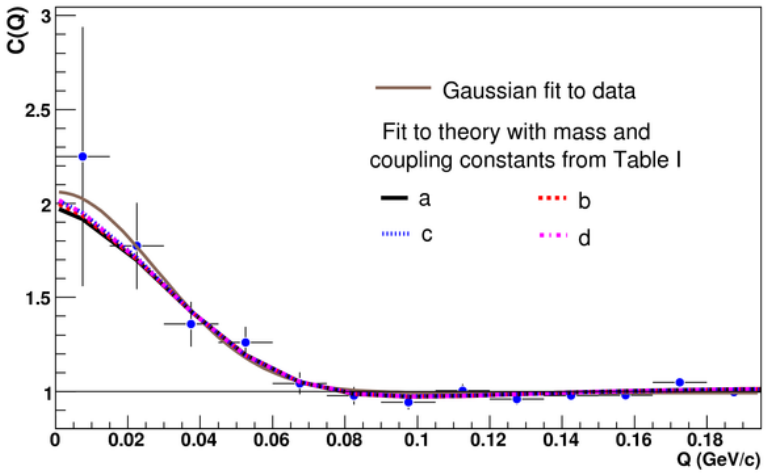

Figure 5.6: The experimental $K^0_S K^0_S$ correlation function in Au+Au collisions at $\sqrt{s_{NN}}$ = 200 GeV with fits from Lednicky-Lyuboshitz model: (a) Martin, (b) Antonelli, (c) Achasov2001 and (d) Achasov2003 [88].

below one. Therefore, the Lednicky-Lyuboshitz parameterization (equation 5.34), considering strong FSI and mapping the dip structure, should be introduced. Agreement between theory and experiment is observed. In addition, it is visible that for different resonance parameters, the fitting functions are very similar. This is confirmed by the obtained source sizes presented in Table 5.2. The results were presented depending on one decay channel of resonances $f_0(980)$ and $a_0(980)$ and after considering both channels. The difference between these radii is slight and is contained in the measurement uncertainties. Comparing the source size, taking into account various effects and interactions, it turns out that the Gaussian fit gives values larger by

Table 5.2: The sizes of the particle emitting source obtained by fitting the experimantal data from STAR experiment with Lednicky-Lyuboshitz model. The 2nd and 3rd column coresponds to the one- and two-chanel fits, respectively [88].

	$\mathbf{R_{inv}}$ **[fm]**	
	one channel fit	two channels fit
Antonelli	$3.89 \pm 0.44 \pm 0.35$	$4.09 \pm 0.46 \pm 0.31$
Achasov2001	$3.96 \pm 0.45 \pm 0.34$	$4.14 \pm 0.47 \pm 0.31$
Achasov2003	$3.91 \pm 0.44 \pm 0.34$	$4.07 \pm 0.45 \pm 0.29$
Martin	$3.90 \pm 0.45 \pm 0.37$	$4.07 \pm 0.46 \pm 0.31$

approx. 1 fm. This indicates that the omission of the strong interaction is unacceptable, and the obtained results will not be consistent with the facts.

The analysis described above was the first step to studing freezeout geometry, collective flow velocity, and evolution time. Unfortunately, it was impossible to study the correlation function's dependence on the collision's centrality due to insufficient statistics.

Centrality dependence was published a few years later by the ALICE experiment [95]. Correlation functions of the system of two neutral kaons were obtained for several intervals of centrality (0-10%, 10-30%, and 30-70%) and transverse mass. This was made possible by the significant data statistics obtained with Pb+Pb collisions at $\sqrt{s_{NN}}$ = 2.76 TeV. An example of a correlation function is shown in the left part of Figure 5.7. It was fitted using parameterization containing Bose-Einstein statistics and strong FSI. It is clear that the experimental points have minor uncertainties and are on the fit line.

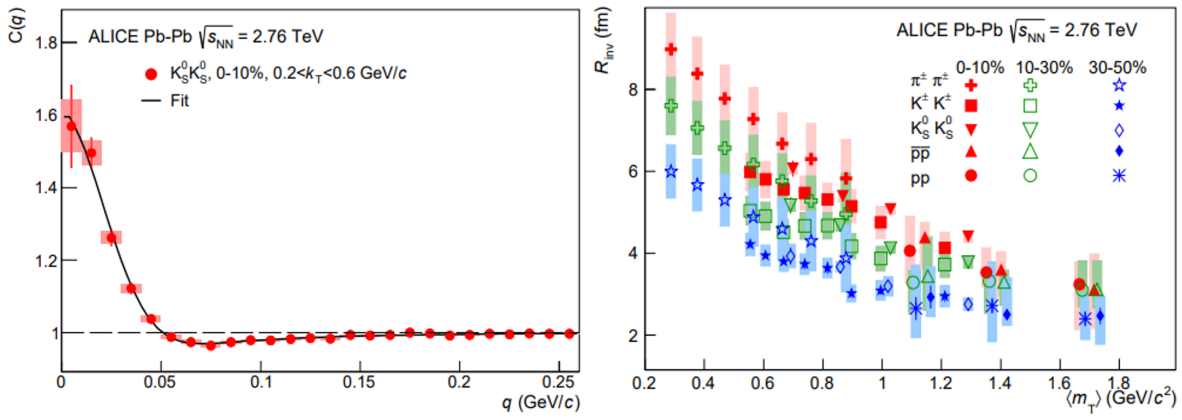

Figure 5.7: The experimental $K^0_S K^0_S$ correlation function in Pb+Pb collisions at $\sqrt{s_{NN}}$ = 2.76 TeV (the left plot) and source sizes as a function of transverse mass for different pairs: $\pi^{\pm}\pi^{\pm}$, $K^{\pm}K^{\pm}$, $K^0_S K^0_S$, $\bar{p}\bar{p}$ and pp (the right plot) [95].

In the publication, the ALICE experiment showed the dependence of the obtained radii on the transverse masses for five different systems - the right panel of Figure 5.7. The most important observation was that the radii for $K^{\pm}K^{\pm}$ and $K^0_S K^0_S$ are very consistent. Neutral kaons indeed have larger sizes of the source, but the difference between these two systems is smaller than the systematic uncertainty. As expected, the size increases with increasing centrality and decreases with increasing m_T.

$K^0_S K^\pm$ *interaction in Pb+Pb collisions measured by ALICE experiment*

In recent years, the analysis of interactions in the final state and the study of the structure of resonances have been of great interest. The study of resonances motivated the first femtoscopic measurements between K^0_S and $K^\pm$ particles. The ALICE experiment performed the analysis for Pb+Pb collisions at $\sqrt{s_{NN}}$ = 2.76 TeV [93]. The obtained correlation functions presented in Figure 5.8 are characterized by a dip structure for low k^* values dur to the strong interactions proceeding via the $a_0(980)$ resonance. Since only strong interaction is observed, the modified

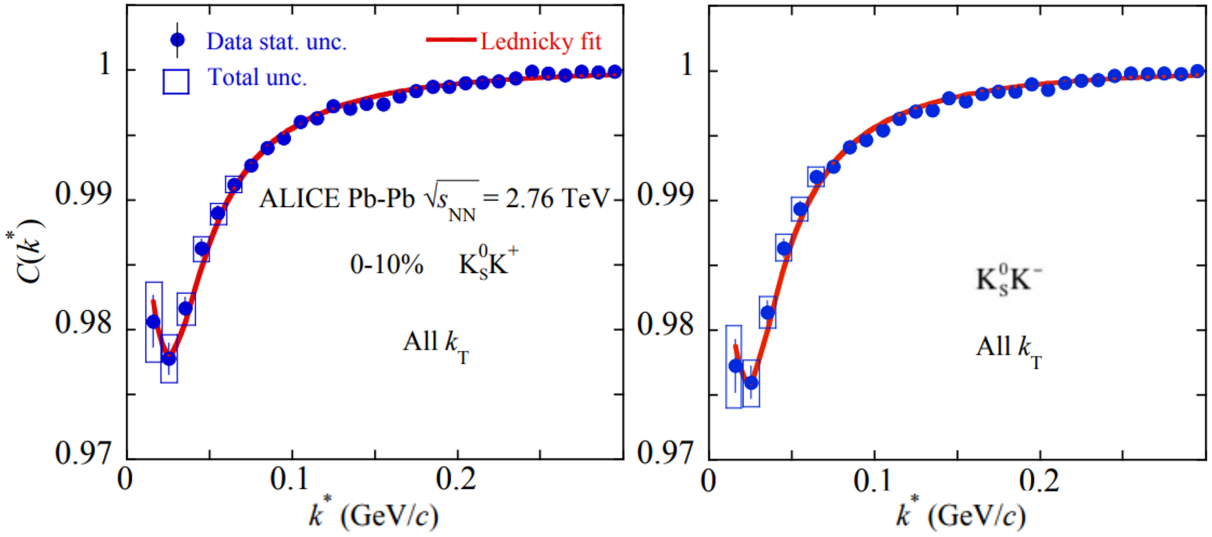

Figure 5.8: The experimental correlation function for $K^0_S K^+$ (the left plot) and $K^0_S K^-$ (the right plot) measured by the ALICE experiment in Pb+Pb collisions at $\sqrt{s_{NN}}$ = 2.76 TeV [93].

Lednicky-Lyuboshitz formula (equation 5.37) was used for parameterization. Thanks to the large statistics, the measurements agree with the theory, and the parameterization taking into account the FSI from the resonance a_0 describes the shape of the signal region very well. The calculated source sizes were compared with the radii obtained from identical kaon femtoscopy - Figure 5.9. Several conclusions can be drawn from this comparison. First, both Achasov parameterizations, described by larger masses a_0 and decay couplings, give radii most consistent with those of K^+K^+ and $K^0_S K^0_S$. Second, the Antonelli parameter set gives slightly lower values but agrees with uncertainty. At the same time, the Martin parametrization gives the smallest sizes, which are very different from the results from other systems. The measured radii should be consistent. Otherwise, K^0_S and $K^\pm$ sources would be shifted relative to each other. Moreover, due to isospin symmetry, this is not to be expected.

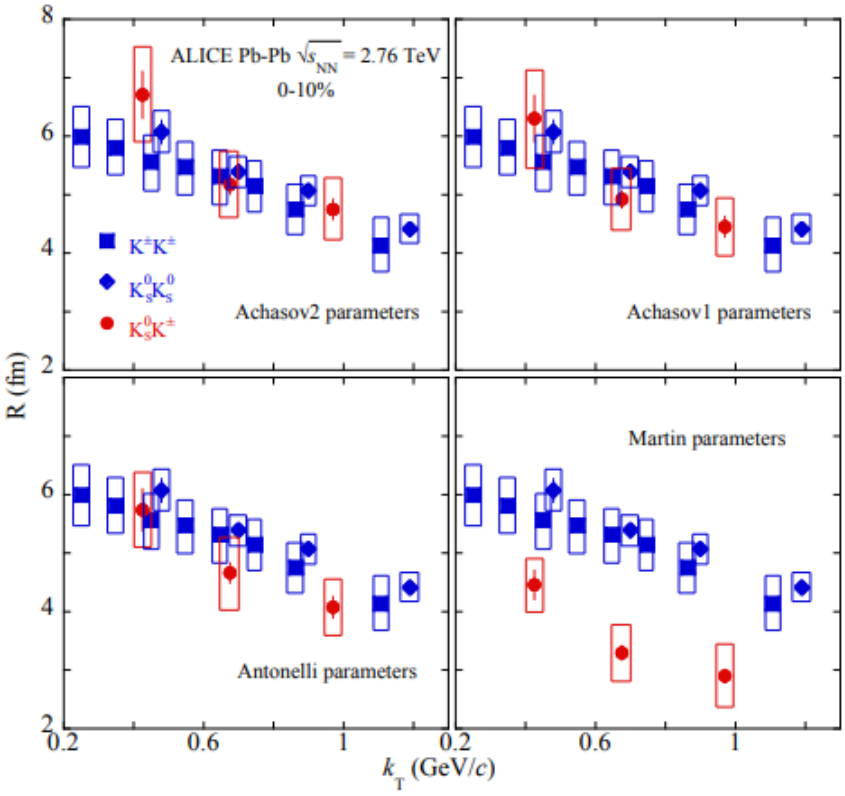

Figure 5.9: Extracted radii of the source from $K^0_S K^{\pm}$ compared with results from identical kaon femtoscopy [93].

This analysis and the obtained results show agreement with the interpretation of the a_0 (980) resonance as a tetraquark state. The ALICE experiment indicated that studying the $K^0_S K^{\pm}$ correlation functions at other collision energies would be interesting, as it would allow one to understand the interactions between these particles in different sensitivity ranges.

Chapter 6

Neutral kaons correlations

The most popular is the analysis of femtoscopic correlation functions of systems of two pions and charged kaons. This is due to their high multiplicities in collision of heavy ions. However, in the case of pions, resonances decays play a significant role (kaons are less sensitive, so a clearer signal of the correlation is obtained). The pions from the decay of long-lived resonances contribution is very limited. In contrast, pions from semi-long-lived decays can increase the size of the particle-emitting source and introduce non-Gaussian distortion. In addition, the Coulomb interaction is dominant at low values of q_{inv}. All these issues can be overcomed by going to neutral kaon analysis, which significantly complements other femtoscopic results. The reconstruction of the neutral kaon candidates using the decay geometry's topological features allows for the research's extension to higher momentum ranges. Moreover, analysis of charged and neutral kaons can be regarded as a method of mutual consistency check. As expected, there is no evidence for the obtained homogeneity length to differ for both systems. Slight differences may only be due to interactions in the final state. It follows that different methods of analysis (charged particle tracking vs. vertex reconstruction and Coulomb interaction vs. strong FSI) give the same results.

Many groundbreaking events, such as the discovery of strangeness, parity violation, and CP violation, influenced the development of kaon physics [96].

Strangeness

Kaons were discovered over 70 years ago, and their characteristic feature is combined production [97]. This means that they are formed in pairs as a result of strong interactions:

$$\pi^+ + p \to K^+ + \bar{K^0} + p$$

Adding the long lifetime of the new particles, it was concluded that there must be a new quantum number - a strangeness that is conserved in the strong interaction. This discovery enabled Gell-Mann to create the SU(3) hadron classification and introduce the fundamental quarks u, d, and s, contributing to the later development of QCD. Currently, there are four variants of the K meson: In turn, pairs (K^+, K^0) and (K^-, $\bar{K^0}$) are isospin doublets.

$$\begin{array}{lll} \text{charged} & |K^+\rangle = |\bar{s}u\rangle & |K^-\rangle = |s\bar{u}\rangle \\ \text{neutral} & \left|K^0\right\rangle = |\bar{s}d\rangle & \left|\bar{K^0}\right\rangle = \left|s\bar{d}\right\rangle \end{array}$$

CP violation

Despite observing parity violation, it was believed that the combination of parity with charge conjugation (CP) was still a good symmetry. It turned out that the neutral kaons K^0 and $\bar{K^0}$ mixing through the second-order weak interaction:

$$CP\left|K^0\right\rangle = \left|\bar{K^0}\right\rangle, CP\left|\bar{K^0}\right\rangle = \left|K^0\right\rangle$$

and while maintaining CP have eigenstates [98]:

$$\begin{array}{ll} \left|K_1^0\right\rangle = \frac{1}{\sqrt{2}}\left[\left|K^0\right\rangle + \left|\bar{K^0}\right\rangle\right] & CP = +1 \\ \left|K_2^0\right\rangle = \frac{1}{\sqrt{2}}\left[\left|K^0\right\rangle - \left|\bar{K^0}\right\rangle\right] & CP = -1 \end{array}$$

The CP symmetry forbade both eigenstates to have the same decay channel. However, as Christenson, Cronin, Fitch, and Turlay proved in 1964, such decays occur, and CP is violated. So it is possible to determine the amplitude presenting how significant this effect is:

$$\left|\frac{A(K_1^0 \to \pi^+\pi^-)}{A(K_2^0 \to \pi^+\pi^-)}\right| = 2.3 \cdot 10^{-3} \tag{6.1}$$

The above equation shows that the effect of CP violation is minimal, but the qualitative consequences are far-reaching.

It was observed that despite the same mass m_{K^0} = 497.611 $\pm$ 0.013 MeV/c [3], the eigenstates differ in a lifetime. K_1^0 has a shorter lifetime, hence it is called K_S^0 (short), while K_2^0 lives longer

Table 6.1: Lifetime and decay length of neutral kaons [3].

Eigenstates	**Lifetime [s]**	**Decay lengths [cm]**
K_S^0	$(0.8954 \pm 0.0004) \cdot 10^{-10}$	2.68
K_L^0	$(5.116 \pm 0.021) \cdot 10^{-8}$	1534

and is referred to as K_L^0 (long). Experimental quantities describing neutral kaons are listed in the Table 6.1. There are clear differences between the decay lengths. Therefore K_S^0 is preferred for experimental analyses because K_L^0 often escapes from the detector before it decays. The main decays of neutral kaons are presented in Table 6.2.

Table 6.2: Neutral kaons decay modes [3].

K_S^0	$\rightarrow \pi^+\pi^-$	$69.20 \pm 0.05\%$	hadronic mode
	$\rightarrow \pi^0\pi^0$	$30.69 \pm 0.05\%$	hadronic mode
	$\rightarrow \pi^+\pi^-\gamma$	$(1.79 \pm 0.05) \cdot 10^{-3}$	mode with photons
	$\rightarrow \pi^\pm e^\mp \nu_e$	$(7.04 \pm 0.08) \cdot 10^{-4}$	semileptonic mode
	$\rightarrow 3\pi^0$	$< 2.6 \cdot 10^{-8}$	CP violating
K_L^0	$\rightarrow \pi^\pm e^\mp \nu_e$	$40.55 \pm 0.11\%$	semileptonic mode
	$\rightarrow \pi^\pm \mu^\mp \nu_\mu$	$27.04 \pm 0.07\%$	semileptonic mode
	$\rightarrow 3\pi^0$	$19.52 \pm 0.12\%$	hadronic mode
	$\rightarrow \pi^+\pi^-\pi^0$	$12.54 \pm 0.05\%$	hadronic mode
	$\rightarrow \pi^+\pi^-$	$(1.97 \pm 0.01) \cdot 10^{-3}$	CP violating

From the point of view of correlation femtoscopy, the most important will be the two-particle $K_S^0 K_S^0$ wavefunction, which can be written as:

$$\left|K_S^0 K_S^0\right\rangle = \frac{1}{2}\left(\left|K^0 K^0\right\rangle + \left|K^0 \bar{K^0}\right\rangle + \left|\bar{K^0} K^0\right\rangle + \left|\bar{K^0} \bar{K^0}\right\rangle\right) \tag{6.2}$$

Note that the $K_S^0 K_S^0$ system is a linear combination of symmetric states $K^0 K^0$ ($\bar{K^0}\bar{K^0}$) and asymmetric state $K^0 \bar{K^0}$. Since the first two states are pairs of identical bosons, it is possible to observe Bose-Einstein enhancement. In turn, despite its non-identity, the mixed state will produce a Bose-Einstein-like enhancement for small values of the pair momentum. The boson-antiboson pair ($B\bar{B}$) is an eigenstate of the charge conjugation operator. Thus, the probability amplitude

for a given charge coupling eigenvalue C_n can be expressed as follows [99]:

$$|B\bar{B}\rangle_{C_n=\pm 1} = \frac{1}{\sqrt{2}}\left(|B(\mathbf{p})\bar{B}(-\mathbf{p})\rangle \pm |\bar{B}(\mathbf{p})B(-\mathbf{p})\rangle\right). \tag{6.3}$$

Assuming $\mathbf{p} \to 0$, the maximally enhance will be observed for C_n = +1 and the suppressed for C_n = -1. In the case of pairs $K^0_S K^0_S$, the state C_n = +1 is selected, resulting in a Bose-Einstein-like enhancement at low pair momentum. It is worth noting that every spinless pair $B\bar{B}$ has this characteristic property. Failure to specify the eigenvalue of the charge will result in a flat correlation (FSI absent). This will result from the mutual cancellation of the enhanced and suppressed effects. Therefore, the system of two neutral kaons is unique, as it allows for an easy choice of a state with a specific eigenvalue of the charge.

As mentioned in Chapter 5.7 the $K^0_S K^0_S$ correlation functions are very sensitive to strong FSI. Therefore, in order to parameterize them, the Lednicky-Lyuboshitz model is used. The figures below are examples of the different combinations in functions for two neutral kaons for different homogeneity lengths. Figure 6.1 shows the shape of the function when only the QS effects are

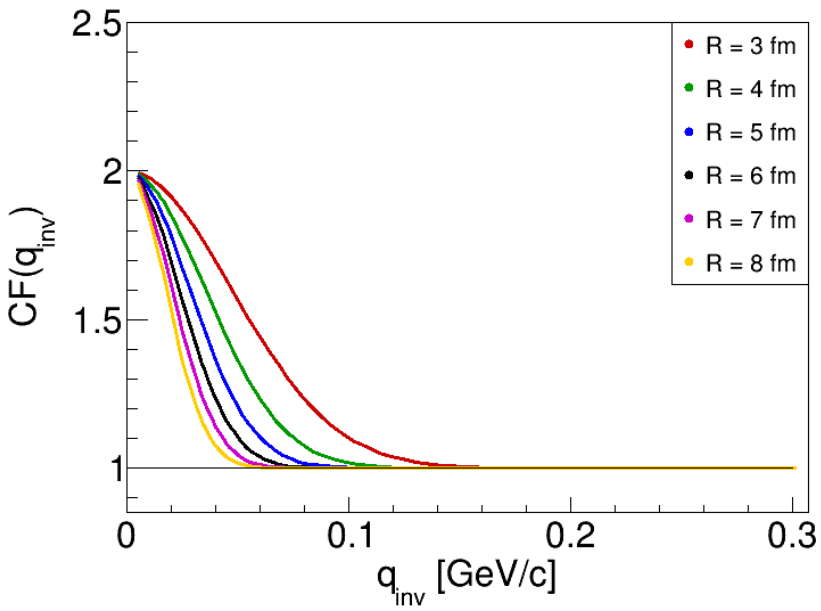

Figure 6.1: Bose-Einstein contribution to the $K^0_S K^0_S$ correlation function for various homogeneity lengths [this thesis].

taken into account, i.e., when the Gaussian equation describes it. It can be seen that the Bose-Einstein enhancement is wider for smaller particle emitting source sizes and is in line with the Fourier transform expectation. Figure 6.2 shows the shape of a strong FSI. It is noticeable that the $K^0\bar{K}^0$ interaction is repulsive and is similar to the annihilation process. As before, also

here, a broadening of the structure is observed for smaller sizes. In addition, the smaller the source's radius, the larger the dimple is visible. Figure 6.3 shows the correlation function $K^0_S K^0_S$ taking into account all effects and interactions. As one can see, the Bose-Einstein enhancement contributes the most significant to the shape of the function. Not to forget about strong FSI,

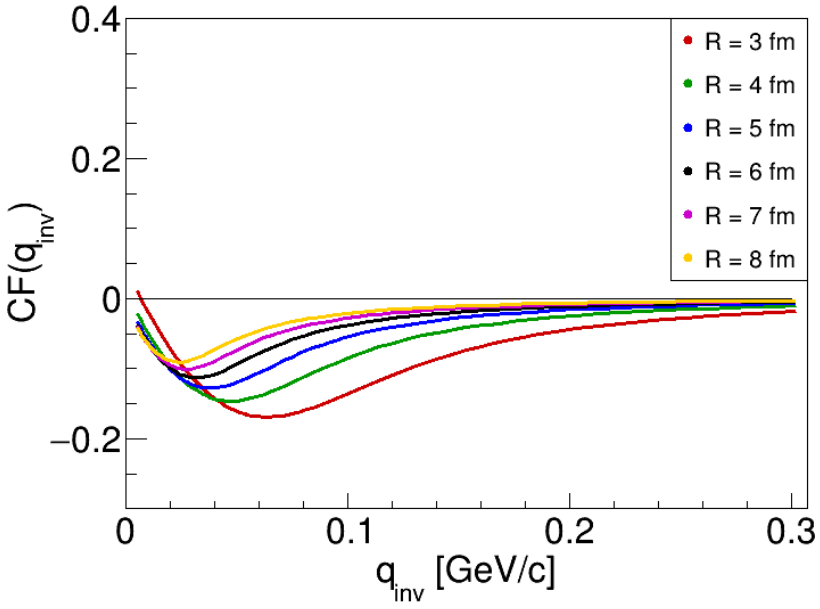

Figure 6.2: Strong FSI contribution to the $K^0_S K^0_S$ correlation function for various homogeneity lengths [this thesis].

which causes a few percent depression in the middle q_{inv} range. It is also essential to show how different parameterizations (sets of resonance parameters from Table 5.1) affect the appearance of the correlation function - Figure 6.4. There are slight differences between the sets (taking this contribution into account is important when calculating the systematic uncertainties). However, they are generally quite coherent since the coupling ratio of the decay channels expresses the dominant part of the scattering amplitude.

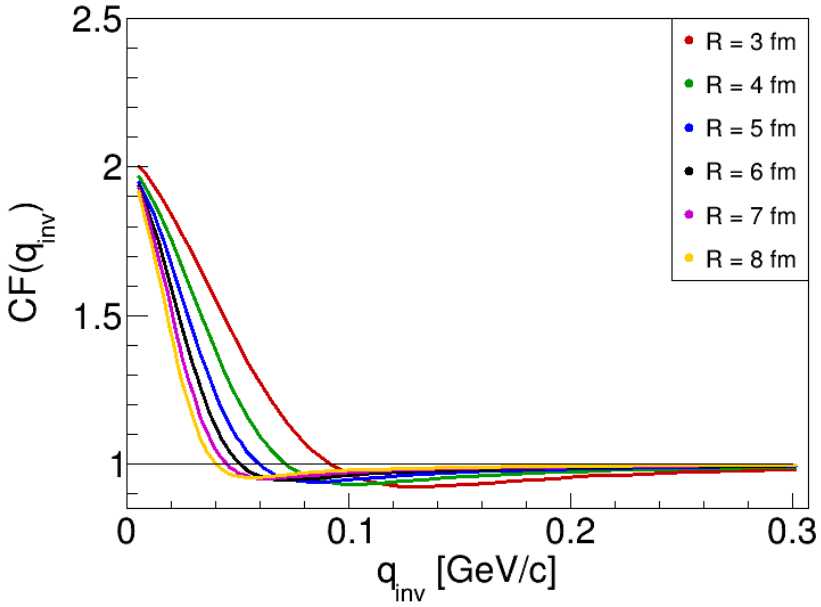

Figure 6.3: The $K^0_S K^0_S$ correlation function including all effects and interactions for various homogeneity lengths [this thesis].

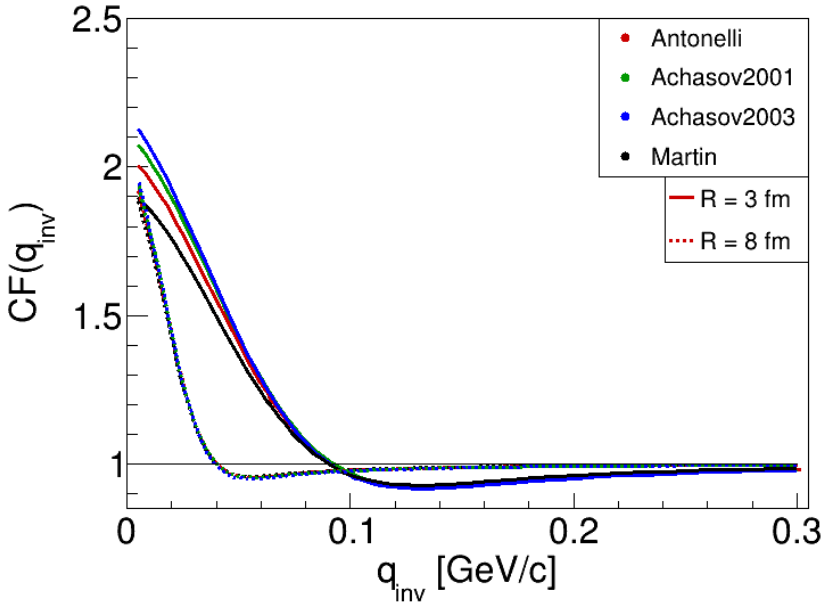

Figure 6.4: The $K^0_S K^0_S$ correlation function for different Lednicky-Lyuboshitz parametrizations [this thesis].

Chapter 7

Analysis of two-meson correlations

The results from this thesis are from Au+Au collisions collected by the STAR experiment at RHIC collider. Data for two collision energies $\sqrt{s_{NN}}$ = 39 GeV (BES-I) and 200 GeV (the top RHIC energy) collected in 2010 were used. In order to obtain experimental correlation functions, selections have been made, and the raw data have been subjected to many corrections that will allow one to obtain a clean signal without unnecessary effects. This chapter will describe all selection criteria and corrections in detail.

7.1 Data Selection

The analysis of experimental data should begin with a careful selection. The first stage is selecting the collision (removing "bad" events and determining centrality). The second stage is related to the particles and their tracks in the detector (determining the type of particle based on information about energy losses for ionization and the time of flight). The last, no less important step concerns selecting a pair of particles (checking whether there are no detector effects).

7.1.1 Event Selection

The selection of events should start with selecting only good-quality reconstructed collisions. For this purpose, the distance of the collision site from the beam axis is checked, expressed as

$$V_R = \sqrt{V_x^2 + V_y^2} \tag{7.1}$$

where V_x and V_y are distances in x and y plane, respectively. In the STAR experiment, the recommendation is less than 2 cm. It is also important that each event is symmetrical in the

rapidity y and that the events are registered not too far from the center of the detector V_z. The permissible values of the V_z parameters depend on the collision energy. Typical values used in the BES-I program and at top RHIC energy are shown in Table 7.1. The distributions for the two analyzed energies are shown in Figure 7.1.

Table 7.1: Acceptable values of the V_Z parameter in the STAR experiment for energies used in this analysis.

$\sqrt{s_{NN}}$ [GeV]	V_z limits [cm]	no. of events [M]
39	30	83
200	30	94

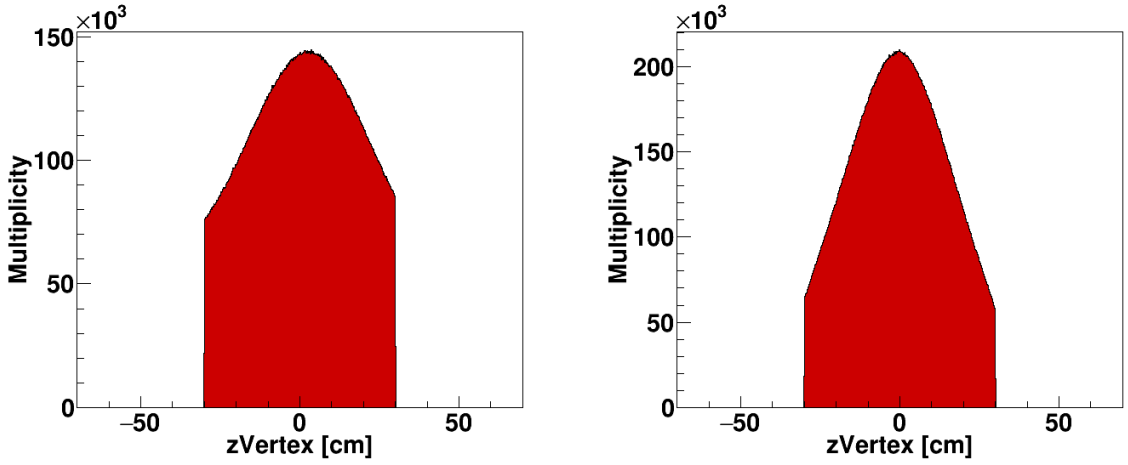

Figure 7.1: Distributions of registered collisions with a given value V_z for Au+Au collisions at $\sqrt{s_{NN}}$ = 39 and 200 GeV, respectively [this thesis].

Another important aspect to consider is the choice of the centrality classes. In the case of heavy-ion experiments, it is estimated based on the number of charged hadrons recorded in the TPC detector. The percentage of most central collisions is then calculated. When determining the centrality intervals, the pseudorapidity range should be considered because, with its change, the centrality also changes. The standard rapidity in the STAR experiment is in the range $|\eta| < 0.5$, which allows the analysis of eight different centrality classes: 0-5%, 5-10%, 10-20%, 20-30%, 30-40%, 40-50%, 50-60%, and 60-70% - Figure 7.2. Such centralities can be combined with each other to increase the statistic, like in the case of K^0_S. The correlation functions obtained in this analysis will be in the following ranges: 0-10% (central collisions), 10-70% (noncentral collisions), and 0-70% (minimum bias collisions).

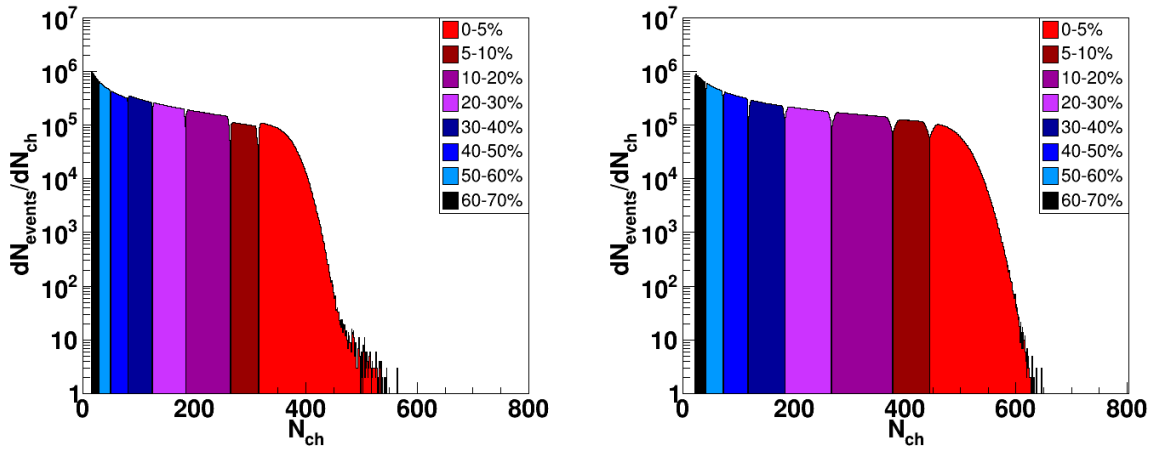

Figure 7.2: The distribution of the analyzed collisions as a function of the number of registered charged, identified particles, based on the selection of a given collision centrality. Data are from Au+Au collisions at $\sqrt{s_{NN}}$ = 39 GeV and 200 GeV, respectively. The colors correspond to successive centrality intervals [this thesis].

7.1.2 Particle Identification

As mentioned earlier, information from two detectors, TPC and TOF, is used to identify charged particles correctly. In the case of TPC, a particle passing through the active volume of the detector loses energy due to the ionization process (dE/dx). Such losses are characteristic of particles of a certain mass, charge, and velocity. The average energy loss when passing through matter is described by the Bethe-Bloch equation:

$$-\frac{dE}{dx} = \frac{4\pi}{m_e c^2}\frac{nz^2}{\beta^2}\left(\frac{e^2}{4\pi\varepsilon_0}\right)^2\left[\ln\left(\frac{2m_e c^2\beta^2}{I(1-\beta^2)} - \beta^2\right)\right] \tag{7.2}$$

where e, m_e are the charge and mass of the electron, respectively, $n = N_A Z\rho/A$ is the electron density of the material (N_A is the Avogadro number, A and Z are the atomic and mass number of the medium, ρ is the density of the medium), z is the charge of the particle, $\beta = v/c$ is the ratio of the velocity of the particle v to the speed of light in the vacuum c, ε_0 is the permittivity of the vacuum, and I is the average ionization energy of 10 eV [77].

The STAR experiment measures energy losses to ionization for many types of particles. An example may be the electron, muon, pion, kaon, proton, and deuteron distributions presented in Figure 7.3. Theoretical calculations were also adjusted. In the momentum regions, where it is possible to separate particle distributions, individual Gaussian distributions are fitted to the plot with the expected value determined by the equation 7.2. On the other hand, for those values of

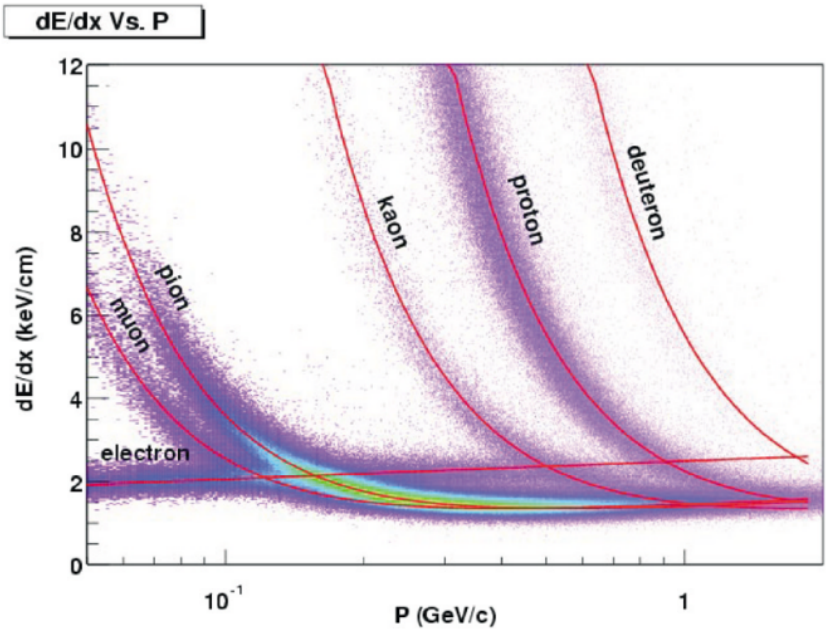

Figure 7.3: Ionization energy loss as a function of particle momentum measured by TPC [**?**].

momentum, where overlapping of different types of particles is observed, a formula is adjusted that is the sum of even several Gauss (four if one includes electrons, pions, kaons, and protons). Then, the average value of dE/dx is calculated, which is also the expected value of the distribution. Knowing this quantity, one can determine the value of the Gaussian distribution for each type of particle (G_e, G_π, G_K, G_p). This, in turn, makes it possible to calculate the probability of correct identification of the particle, and in the case of kaons, with the assumption $\sum_{i=e,\pi,K,p} G_i = G_i = 1$, it is as follows [77]:

$$P_K = \frac{G_K}{\sum_{i=e,\pi,K,p} G_i} \tag{7.3}$$

For one central Au+Au collision at $\sqrt{s_{NN}}$ = 200 GeV, more than 1000 charged particles leave ionization hits (more than 15 hits are required) in the TPC [58]. Each such hit is recorded, it allows one to reconstruct the track of individual particles and separate them from each other. The momentum of the particles passing through the detector volume is calculated based on the curvature of the tracks in the magnetic field of the magnet. The precision of such a measurement depends on the transverse momentum of the tracks. If the p_T of the particle is higher, the TPC track is straighter, making it harder to measure the curvature. On the other hand, particles with a low p_T lose more energy when passing through the TPC gas, resulting in a distorted helical track. They also leave fewer hits because they only pass a small part of the detector. The typical resolution for most detected particles is $\Delta p_T/p_T \approx 2-4\%$ [58].

Having information about energy losses for ionization from TPC, one should specify variable $N\sigma$, which is equivalent to the Gaussian standard deviation between the measured and expected dE/dx values:

$$N\sigma_i = \frac{1}{\sigma} log \frac{< dE/dx >_{measured}}{< dE/dx >^{i}_{expected}} \tag{7.4}$$

where i specifies the particle type or iterator and σ is the dE/dx resolution. It is customary to choose $N\sigma$ in the range 2 - 3. The distribution of energy losses per ionization for pions and kaons used in this thesis is shown in Figure 7.4.

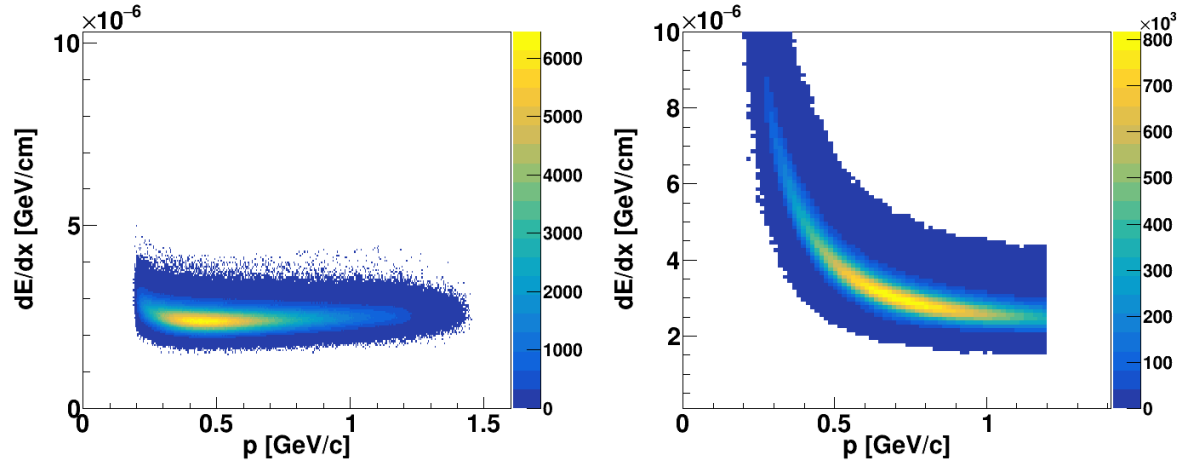

Figure 7.4: Distribution of particle energy loss as a function of momentum for pions and kaons, respectively [this thesis].

Identification of charged particles is also based on information from the TOF detector, i.e., time of flight t and the distance traveled by a given particle L. On this basis, the momentum and velocity of the particle are determined. Knowing the above values, it is possible to estimate the mass and thus make an accurate identification. To determine the mass of a particle, one can use the equation:

$$m = \frac{p}{\beta\gamma c} = \frac{p}{c}\sqrt{\frac{c^2t^2}{L^2} - 1} \tag{7.5}$$

where $\gamma = (1-\beta^2)^{-1/2}$ is the Lorentz factor. Figure 7.5 shows the mass squared distribution vs. momentum for several types of particles. In turn, Figure 7.6 shows the distributions for charged pions and kaons used in this analysis.

Another equally important quantity that can be calculated with TOF information is inverse velocity

$$\frac{1}{\beta} = \frac{ct}{L} \tag{7.6}$$

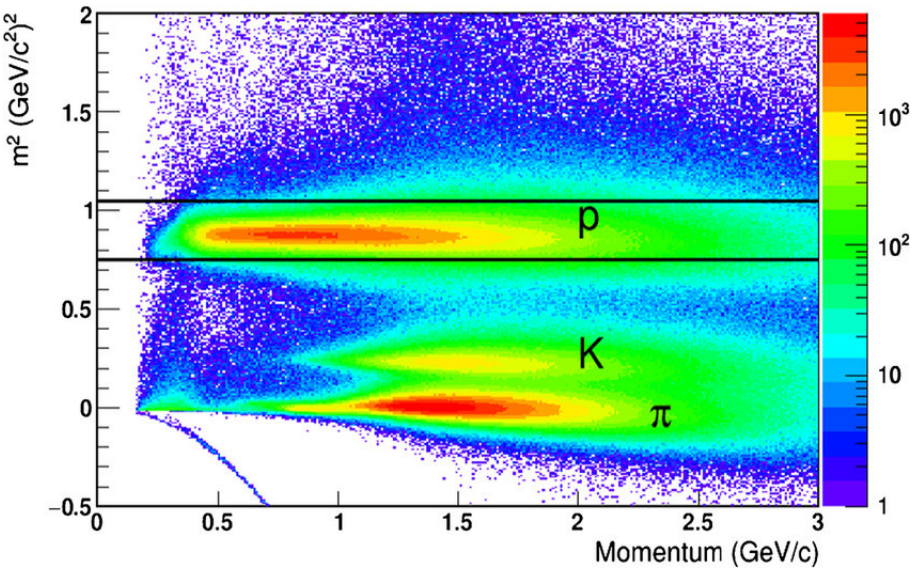

Figure 7.5: Distribution of mass squared as a function of particle momentum measured by TOF.

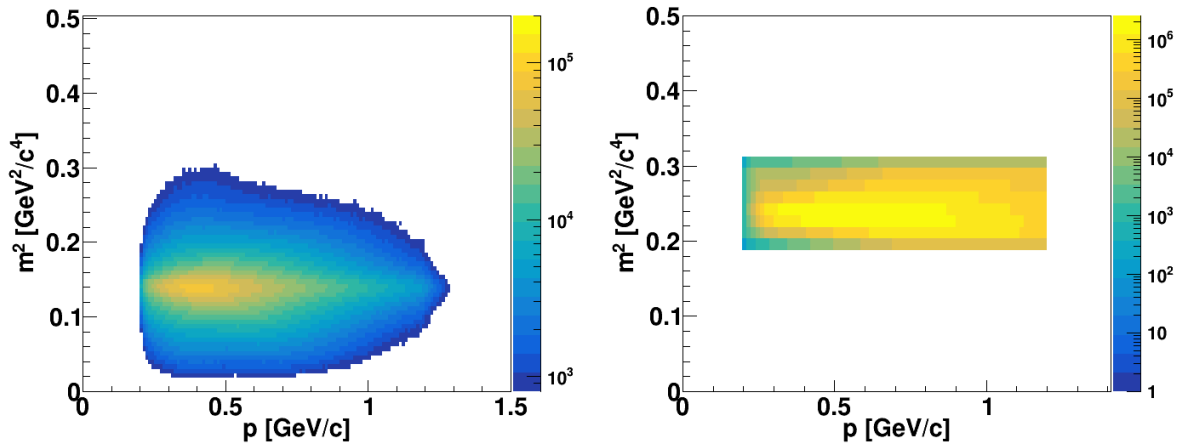

Figure 7.6: Mass squared as a function of particle momentum measured by TOF in Au+Au collisions at $\sqrt{s_{NN}}$ = 200 GeV for pions and kaons, respectively [this thesis].

Rearranging the equation and assuming $c = 1$, it is possible to get the relativistic particle momentum

$$p = m\beta\gamma \rightarrow p^2 = \beta^2(m^2 + p^2) \tag{7.7}$$

Therefore

$$\frac{1}{\beta} = \sqrt{\frac{m^2}{p^2} + 1} \tag{7.8}$$

This correlation is shown in Figure 7.7, where solid lines are theoretical predictions. This dependence was also checked for pions (daughters of neutral kaon) and charged kaons - Figure 7.8.

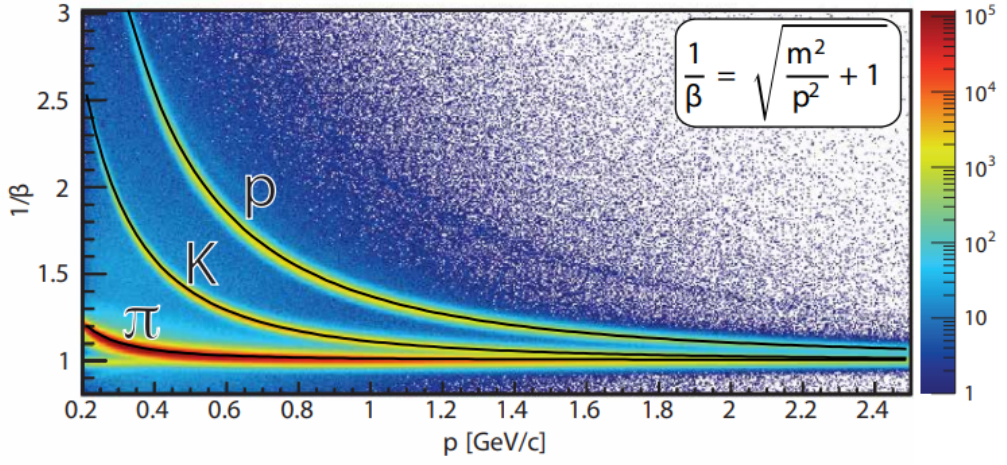

Figure 7.7: Inverse velocity as a function of particle momentum measured by TOF [100].

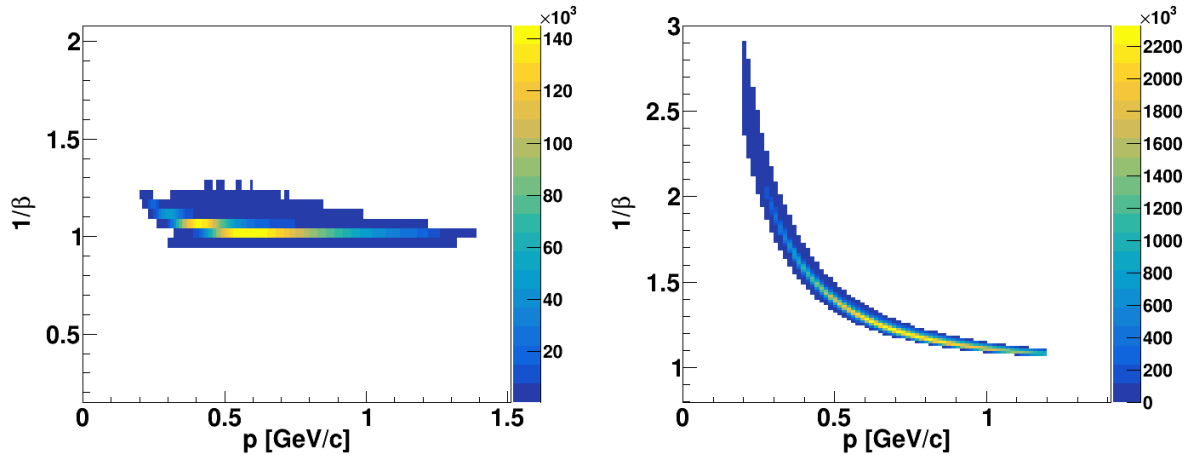

Figure 7.8: Distribution of $1/\beta$ as a function of particle momentum measured by TOF in Au+Au collisions at $\sqrt{s_{NN}}$ = 200 GeV for pions and kaons, respectively [this thesis].

As the description above shows, complete identification is based on data from two detectors. However, in practice, there are two cases. The first one occurs when dE/dx distributions as a function of momentum are well separable, then the information from TPC is sufficient, and there is no need to use TOF. If the TOF information exists, it is used. The second possibility is when the average ionization losses overlap or have similar values. Then the TOF information is necessary.

At this point, it is necessary to mention one more important quantity that enables the correct identification of particles - the Distance of Closest Approach. DCA specifies the distance between the track and the primary vertex and is used to minimize impact from non-primary particles (less than 3 cm is required).

Charged kaon selection

Charged kaons were identified using the above method. In each case, information from the TPC and TOF detectors was required, regardless of the particle's momentum range. All kaon selection criteria have been collected in Table 7.2, and they are the same for both charges.

Table 7.2: Selection criteria for charged kaons.

Transverse momentum p_T [GeV/c]	[0.2 - 1.2]
Momentum p [GeV/c]	[0.2 - 1.2]
Mass squared m^2 [GeV^2/c^4]	[0.2 - 0.3]
$\|N\sigma\|$	≤ 3.0
Pseudorapidity η	≤ 0.5
Distance of closest approach DCA [cm]	≤ 3.0

Neutral kaon reconstruction and selection

Identifying some neutral particles (including K_S^0) is impossible simply because they leave no hits in the detector and decay before TPC. The tracks of charged particles ("daughters" coming from the decay) are beneficial and allow the correct reconstruction of the V^0 particles based on specific topological parameters. Candidates for V^0 must meet several conditions:

- the DCA between the daughter tracks and the primary vertex (PV) must be large enough so that the daughter tracks are not primary;
- the DCA between daughter tracks must be small enough to ensure that they are daughters from the same decay;
- the DCA between V^0 candidate and PV must be small enough to make sure the parent is primary;
- decay length (DL) must be matched to the type of decaying particle.

All these conditions are in addition to the particle selection criteria performed on the daughters. Those V^0 candidates that pass first-order cuts can be used in further analysis. Other selection criteria should be added to ensure lower background or higher purity samples, e.g., parent invariant mass cuts.

Figure 7.9 shows the decay of the particle V^0 due to weak interactions on two oppositely charged products C^+ and C^-. "Reconstructed V^0 track" is understood as the track of a disintegrating

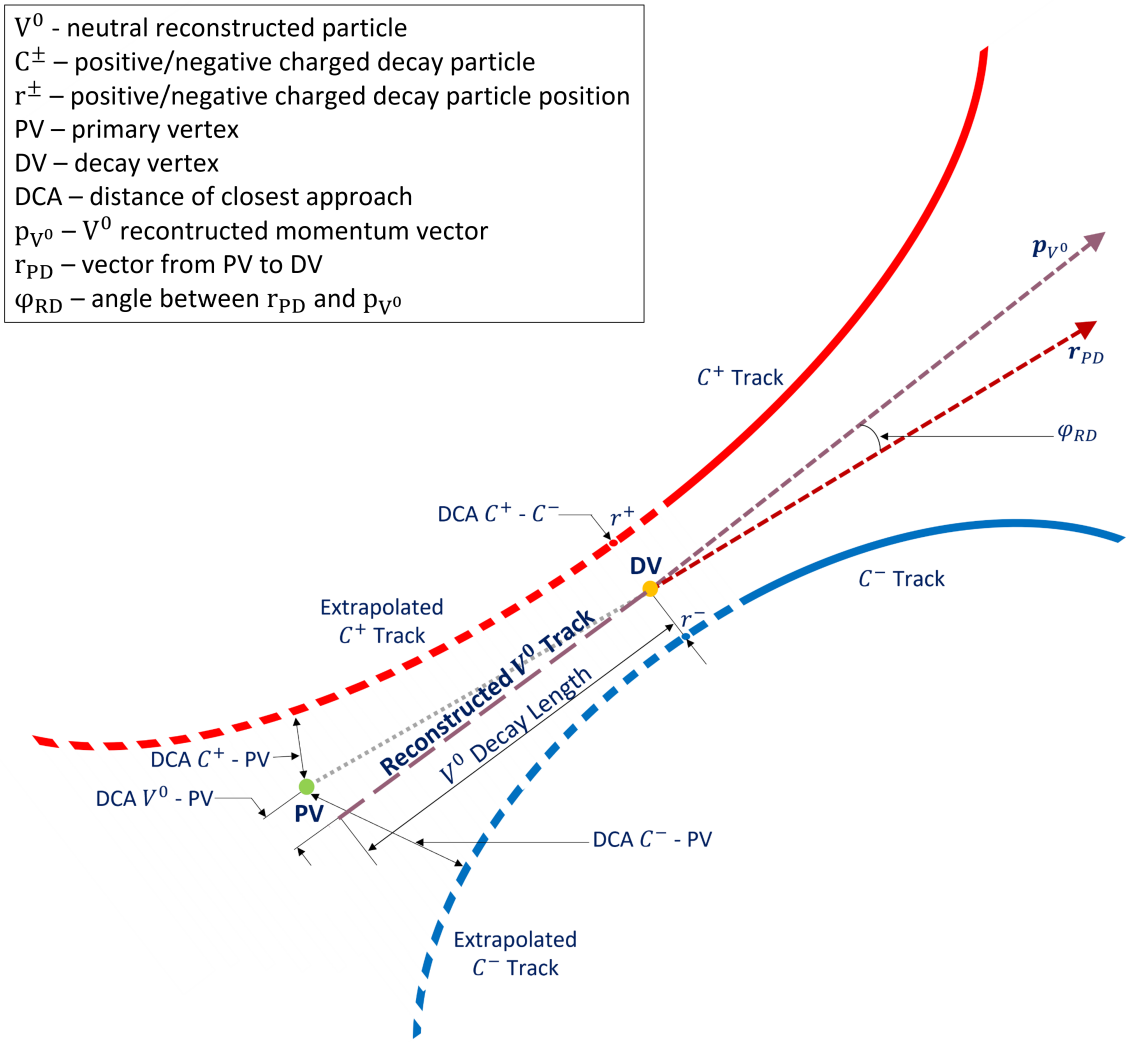

Figure 7.9: Schematic drawing of the selection criteria used in the topological reconstruction of V^0 particles [this thesis].

particle and is the area not registered in the detector. In addition, this track is shifted relative to the PV by the previously mentioned DCA. DCA C^+ - PV and DCA C^- - PV defines the distance between the extrapolated daughter trajectories and the PV. The figure also shows the DV point - the decay vertex, i.e., where the actual decay of V^0 takes place. Decay length is the distance between this point and the start of V^0. By definition, this distance is the product of the speed of light in a vacuum c and the lifetime of a neutral particle τ. The scheme also includes two vectors $\mathbf{r}_{PD}$ and $\mathbf{p}_{V^0}$. The first is the displacement vector between PV and DV. The second is the reconstructed momentum vector of the neutral particle.

The parameters of the neutral particle are calculated based on the parameters of the daughter tracks using the conservation of momentum and relativistic kinematics. So the four-momentum vector of V^0 is described by:

$$\mathbf{p}_{V^0} = \mathbf{p}_1 + \mathbf{p}_2 \tag{7.9}$$

On the other hand, the invariant mass results from the mass and momentum of the daughters and the conservation of the total four-momentum [81]:

$$M^2_{V^0} = (p_1 + p_2)^2 = (E_1 + E_2)^2 - |\mathbf{p}_1 + \mathbf{p}_2|^2 = m_1^2 + m_1^2 + 2(E_1E_2 - \mathbf{p}_1 \cdot \mathbf{p}_2) \tag{7.10}$$

where E_1, E_2, and m_1, m_2 determine the energy and mass of the particles coming from the decay, respectively.

In this thesis, the femtoscopic analysis subject is K^0_S, and the most popular decay channel is $K^0_S \rightarrow \pi^+\pi^-$ (69.20 $\pm$ 0.05%). Therefore, choosing the pion selection criteria was very important to reconstruct neutral kaons based on them. Table 7.3 shows all used selection criteria. It can be seen that the daughter particles have a transverse momentum larger than 0.2 GeV/c, which is related to higher track efficiency at the low p_T region. n addition, according to the previously mentioned conditions, the primary vertex DCA is larger than 1.3 cm.

Table 7.3: Selection criteria for daughter particles (positively and negatively charged pions).

Transverse momentum $\mathbf{p_T}$ [GeV/c]	[0.2 - 1.2]
Momentum p [GeV/c]	[0.2 - 1.2]
$\mathbf{\lvert N\sigma \rvert}$	≤ 3.0
Pseudorapidity η	≤ 0.5
DCA to PV [cm]	≥ 1.3

Table 7.4 presents selection criteria for K^0_S. For $\sqrt{s_{NN}}$ = 39 and 200 GeV, differences in the values of various parameters are observed, which results from the desire to increase the statistics for lower energy. As in the case of pion identification, the previously described conditions were used when determining the value of selection criteria. Accordingly, the DCA of the V^0's extrapolated track to PV must be less than 0.3 cm. The decay length was chosen based on the knowledge of the average lifetime of K^0_S (τ = 8.954 $\pm$ 0.004 $\times$ 10^{-11} s) and the speed of light in a vacuum (c = 299 792 458 m/s). As a result of multiplying these quantities, the average DL = 2.7 cm is obtained. Thus, for $\sqrt{s_{NN}}$ = 39 GeV, DL larger than 2 cm was chosen, while for

$\sqrt{s_{NN}}$ = 200 GeV, DL is greater than 3 cm. The distance between the decay products is larger than 0.8 cm (39 GeV) and 0.6 cm (200 GeV), respectively. Equally important is the invariant mass cut, which is in the range [0.475 - 0.525] GeV/c^2 (39 GeV) and [0.488 - 0.510] GeV/c^2 (200 GeV). The other two quantities are related to the Armenteros-Podolanski plot, which was

Table 7.4: Selection criteria for neutral kaons.

	39 GeV	**200 GeV**
Transverse momentum p_T [GeV/c]	[0.4 - 2.0]	
DCA V^0 to PV [cm]	≤ 0.3	
Decay length DL [cm]	≥ 2.0	≥ 3.0
DCA between daughters [cm]	≤ 0.8	≤ 0.6
Invariant mass m [GeV/c^2]	[0.475 - 0.525]	[0.488 - 0.510]
Armenteros $\|\alpha\|$	≤ 0.7	
Armenteros q_T [GeV/c]	[0.12 - 0.22]	

proposed in 1954 [101] to analyze the dynamics of neutral particles decaying into two products (kinematic properties). This made it possible to separate the K^0_S, and λ^0 decays without making assumptions about the masses of the decay products in the final state. As shown in Figure 7.10, this plot represents the transverse momentum of the oppositely charged daughters for V^0 - q_T, as a function of longitudinal momentum asymmetry - α. The asymmetry is related to the momentum in the *long* direction of both the positive (p_l^+) and negative (p_l^-) daughters and is expressed by:

$$\alpha = \frac{p_l^+ - p_l^-}{p_l^+ + p_l^-} \tag{7.11}$$

In the plot, the characteristics appear as semi-ellipses whose parameters allow obtaining the masses of the parent and daughter particles. Any deviation from known values provides information on detector effects and reconstruction problems due to, e.g., ignorance of the detector's magnetic field [102]. In the analysis, the values were selected to have the purest signal from neutral kaons (from where the narrow range $q_T \in$ [0.12 - 0.22] GeV/c) and to be symmetric on the x-axis ($|\alpha| \leq 0.7$) - Figure 7.11.

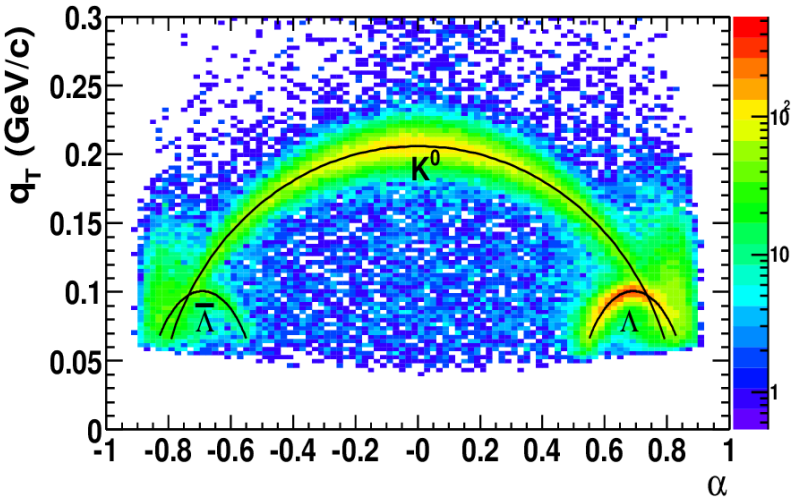

Figure 7.10: The Armenteros-Podolanski plot taken from Pb+Au collisions at $\sqrt{s_{NN}} = 17.3$ GeV by the CERN-CERES/NA45 experiment [103].

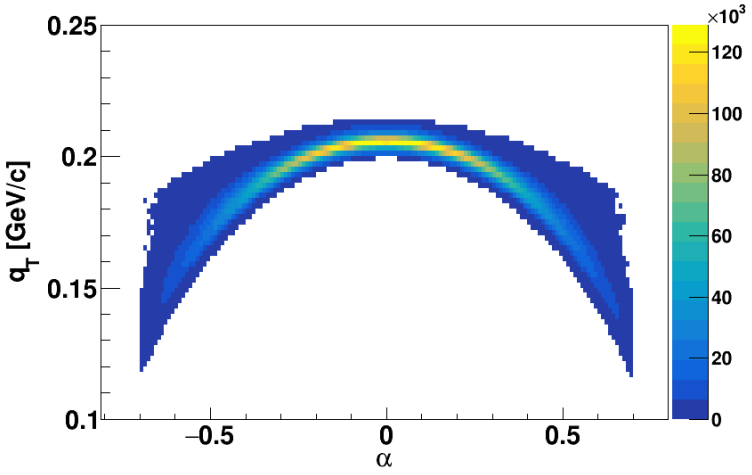

Figure 7.11: The Armenteros-Podolanski plot taken from Au+Au collisions at $\sqrt{s_{NN}} = 200$ GeV [this thesis].

Splitting effect between daughter particles

In the analysis of K^0_S, there is a problem with the so-called "split K^0_S". This is the phenomenon where a pair or three candidates for K^0_S are related to each other through their decay products. In the case of a pair, the situation is relatively simple, and it is enough to add the condition that the pair of neutral kaons must have unique daughters (most of the events in this analysis have only two K^0_S particles). The three candidates are a much bigger problem. As shown in Figure 7.12, candidates $V01$ and $V02$ share a daughter A. Additionally, $V01$ and $V03$ have the same daughter B. So these pairs will not be connected. However, $V02$ and $V03$ have no daughters in

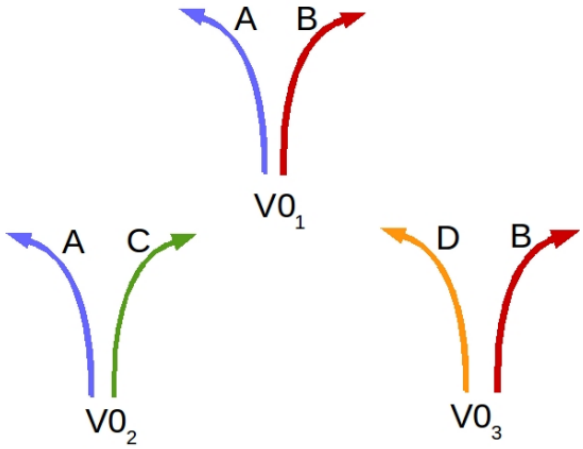

Figure 7.12: Diagram showing the "split K^0_S problem [81].

common, so that they could mate. However, this may be a false correlation. The daughters of B and C and A and D are close together in phase space because the former is paired with A and the latter with B. It follows that the candidates $V02$ and $V03$ will be similar to each other, i.e., they will have low relative momentum and will cause a false correlation. To solve this problem, it is assumed that if any two K^0_S have a daughter in common, one of them is discarded.

7.1.3 Pair Selection

The next step after correctly identifying the particles is pairing them up. To obtain results undisturbed by external factors, successive selected cuts should be applied. Two main detector effects can significantly affect the final results.

Splitting effect

The first is *splitting*, the phenomenon of reconstructing one particle as a pair or a group of several particles. The momenta of the particles formed in this way are close to each other. This effect will artificially increase the number of pairs, resulting in a peak at very low values of q_{inv} ($\approx$ 0 GeV/c) in the plotted correlation function. Therefore, for each pair of particles, the *splitting level* (*SL*) is determined and is defined as:

$$SL = \frac{\sum_i S_i}{N_{hits,1} + N_{hits,2}} \tag{7.12}$$

where S_i is an integer in the range [-1, 1] and specifies how many particles left a hit in the i-sector (S_i = -1 - both particles, S_i = 0 - none of the particles, S_i = 1 - only one particle), $N_{hits,1}$ and $N_{hits,2}$

are the total number of hits of the first and second particles, respectively. Figure 7.13 shows four different cases of particle track reconstruction with sample SL values. When SL = 1 (first

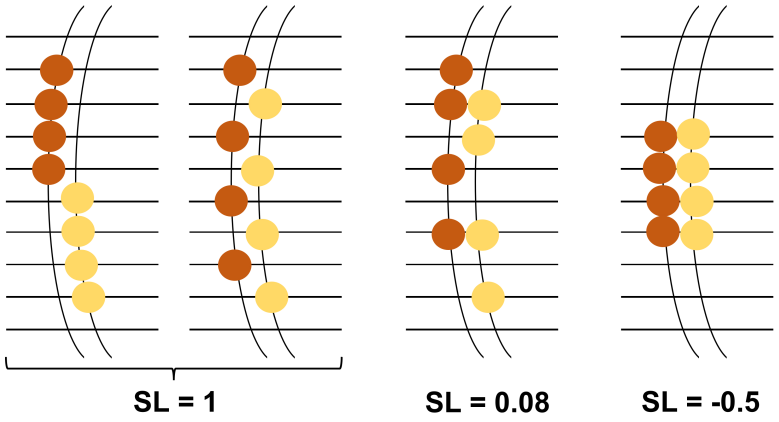

Figure 7.13: Examples of reconstruction of tracks of two particles [this thesis].

and second cases), the pair is said to have resulted from splitting, as the hits in the detector are arranged alternately. The following example, SL = 0.08, looks different because only a small part of the hits is arranged alternately, so with some probability, this pair can be considered a good one. When SL = -0.5, the tracks of two particles are visible. Many STAR experiment analyses have shown that the optimal SL value is in the range [-0.5, 0.6]. It is also important to remember to simultaneously remove incorrectly reconstructed pairs from the numerator and denominator of the correlation function.

Merging effect

The second effect is the opposite of splitting and reconstructing the pair as one particle. It is called *merging* and only affects the pairs in the correlation function's numerator. A decrease in the value of the function for small momenta of the pair manifests this phenomenon. A characteristic of particles that have been merged is a similar flight trajectory. Although it happens that despite the similar trajectories, the particles are well distinguishable. Exemplary trajectories of pairs of particles with different charges in the TPC detection sector are shown in Figure 7.14. On the left, the intersection of the helices for π^+ and π^- is visible. If the distance between them is small, the tracks of both particles will be indistinguishable in the reconstruction process. The tracks have opposite directions on the right side, and the merging effect does not occur.

For the K^0_S femtoscopy, the effects described above are secondary because pairs of V^0 are connected, not the tracks of single pions. However, it is worth considering, especially since it is

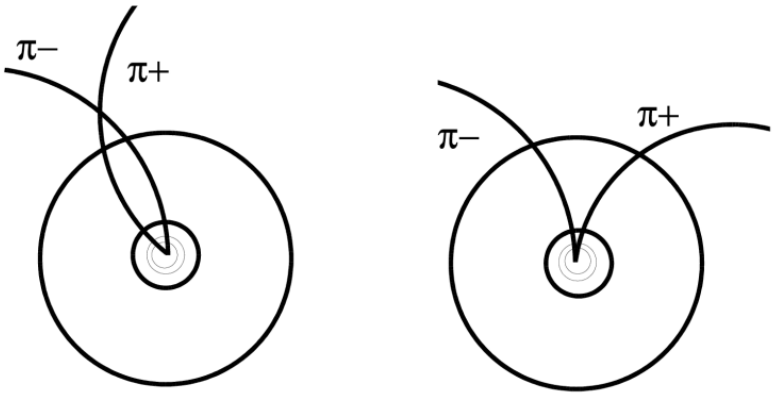

Figure 7.14: Examples of trajectories of π^+ and π^- pairs [77].

straightforward. It is necessary to measure the distance between the vertexes of both K^0_S:

$$R = V_{K^0_S,1} - V_{K^0_S,2} \tag{7.13}$$

Properly selected values will exclude the occurrence of undesirable effects. R larger than 3 cm was used in the analysis. Other values of this parameter were also tested. However, they did not significantly affect the obtained correlation functions.

In the case of the combination $K^0_S K^{\pm}$, the unwanted effect is merging between the positive (negative) daughter and the positively (negative) charged kaon. To avoid this phenomenon, a special average separation cut is used to measure the distance between the daughter track and the kaon track when passing through the TPC. It was assumed that this value must be larger than 3 cm.

7.2 Corrections

Despite detailed analysis of various particle selection criteria, the detection devices have inaccuracies affecting the obtained results. This influence on the measured values should be corrected accordingly. In the case of analyses carried out as part of this thesis, these are purity and momentum resolution corrections.

7.2.1 Purity Correction

This correction is related to the incorrect identification of particles and considers information from all detectors used to analyze experimental data. As mentioned earlier, two detectors are

used to identify charged particles - TPC and TOF. The probability of correct identification of particles depends not only on their type but also on their transverse momentum. In the case of a simple form of femtoscopic analysis, where the residual correlation effect is not significant, the correction is as follows [77]:

$$CF_{corr}(k^*) = \frac{CF_{meas}(k^*) - 1}{PairPurity(k^*)} + 1 \tag{7.14}$$

$$PairPurity(k^*) = Purity_1(p_T) Purity_2(p_T) \tag{7.15}$$

where $CF_{corr}(k^*)$ is a corrected function, $CF_{meas}(k^*)$ is a measured function, $PairPurity(k^*)$ is a pair purity factor described as the result of multiplying the purity of individual particles $Purity_1(p_T)$ and $Purity_2(p_T)$. The purity of a single particle can be calculated in two ways, depending on whether charged or neutral particles are being analyzed. In the case of neutral particles, the purity is calculated using the invariant mass distribution shown in Figure 7.15. A function (usually Gaussian) is fitted to this distribution, and the background B is subtracted

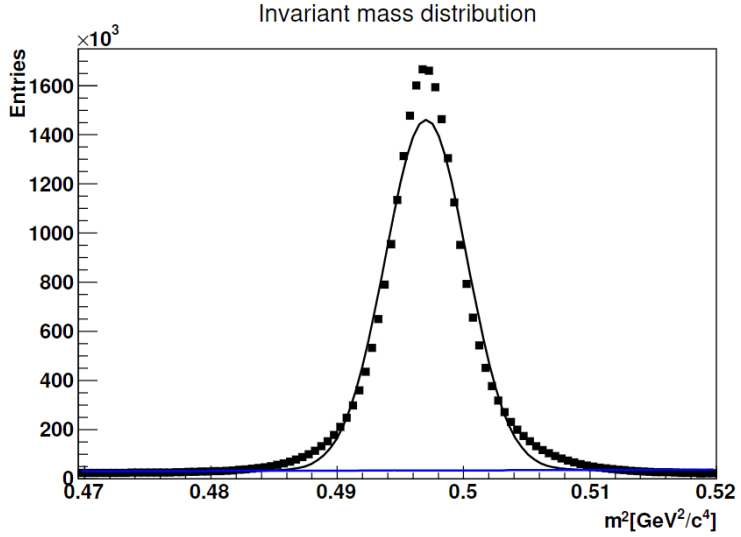

Figure 7.15: The invariant mass distribution $\pi^+\pi^-$ at $\sqrt{s_{NN}}$ = 200 GeV [this thesis].

to get the actual signal S efficiency. In femtoscopic analysis, all particles in the signal region are used because it is impossible to subtract the bad ones. What is more, they affect the signal - weakening or distorting it. Thus, taking as an example the purity of the K^0_S signal determined from the distribution of the invariant mass $\pi^+\pi^-$, the following equation is obtained:

$$Purity(p_T) = \frac{S}{S+B} \tag{7.16}$$

where $S+B$ is a value taken directly from the distribution, and B is determined by fitting a straight line to areas outside the acceptable signal region. All particle selection criteria have

been selected so that the particle purity is as high as possible. Thanks to this and information from the TPC and TOF detector, the purity of the charged kaons is 99%.

7.2.2 Momentum Resolution Correction

Similarly to the incorrect identification of particles, the momentum resolution of the detectors also affects the shape of the measured correlation function. Data from Monte Carlo simulations should be used to estimate the percentage impact of these effects. One should remember several quantities describing the particle - the transverse momentum p_T, described by a helix fit to the hits in the TPC, the polar angle θ, and the azimuthal angle ϕ. These observables allow us to determine the particle's total momentum - p. The relationship between the described quantities is presented in the following equations:

$$p_T = R|q||\vec{B}| = p\sin\theta \tag{7.17}$$

$$p_z = p\cos\theta \tag{7.18}$$

$$p_x = p_T\cos\phi \tag{7.19}$$

$$p_y = p_T\sin\phi \tag{7.20}$$

where R is the radius of the trajectory, q is an electric charge, and $\vec{B}$ is a measure of the strength of the magnetic field. Knowing these dependencies, the embedding procedure consists of the

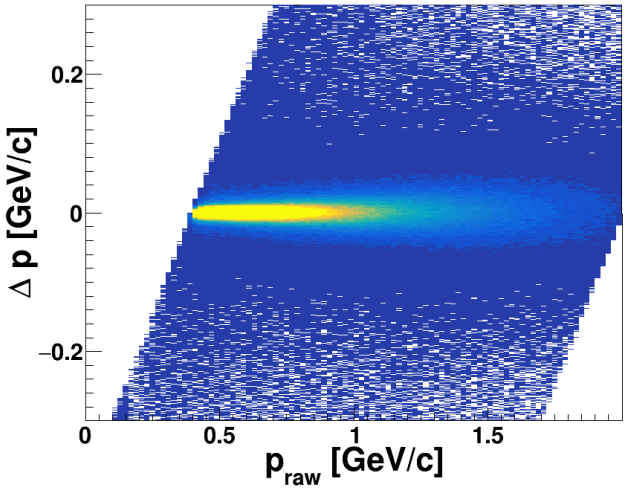

Figure 7.16: The difference of real and reconstructed momentum in real momenta dependence for K^0_S at $\sqrt{s_{NN}}$ = 200 GeV [this thesis].

simulation of the detector's response to particles with a given momentum is carried out. The real momentum p_{raw} and the reconstructed momentum p_{rec} are compared, and the differences between these quantities are histogrammed depending on the real momentum. The same applies to the angles θ and ϕ. The resulting distributions, presented in Figures 7.16, 7.17 and 7.18, are projected into parts for a given value of real momentum. A normal distribution is then fitted

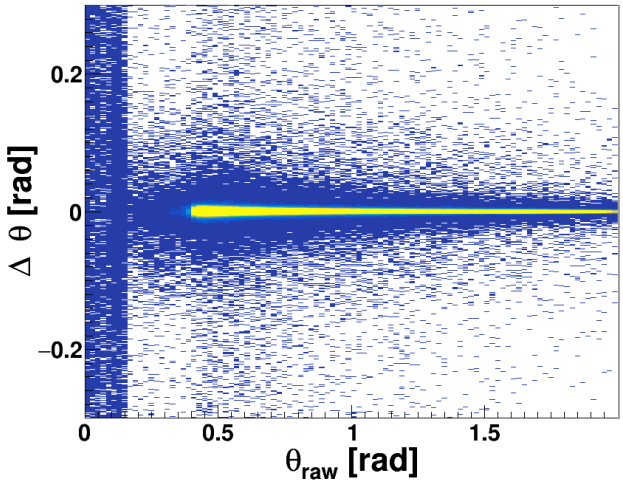

Figure 7.17: The difference of real and reconstructed θ angle in real momenta dependence for K^0_S at $\sqrt{s_{NN}}$ = 200 GeV [this thesis].

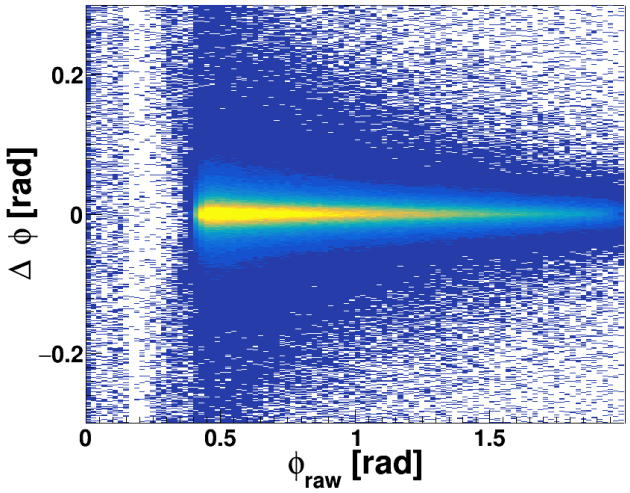

Figure 7.18: The difference of real and reconstructed ϕ angle in real momenta dependence for K^0_S at $\sqrt{s_{NN}}$ = 200 GeV [this thesis].

to each slice. As a result, the standard deviation σ can be plotted against the real momentum of the particle - Figure 7.19. By fitting the polynomials to this, the resolution is obtained. The

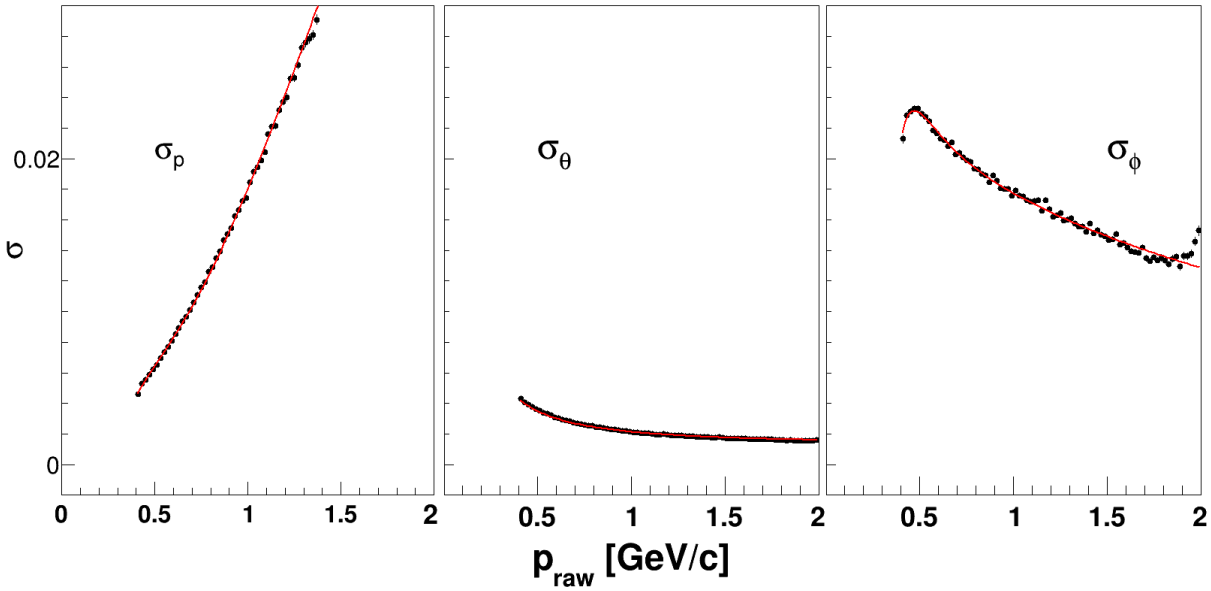

Figure 7.19: σ_p (the left panel), σ_θ (the middle panel) and σ_ϕ (the right panel) distributions with the best polynomial fits for K^0_S at $\sqrt{s_{NN}}$ = 200 GeV [this thesis].

best functions (the smallest test value χ^2) describing the standard deviation for K^0_S are presented below:

$$\sigma_p = A + B\sqrt{p_{raw}} + Cp_{raw} + Dp^2_{raw} + Ep^3_{raw} \tag{7.21}$$

$$\sigma_\theta = A + \frac{B}{p_{raw}} + \frac{C}{p^2_{raw}} + \frac{D}{p^3_{raw}} + \frac{E}{p^4_{raw}} \tag{7.22}$$

$$\sigma_\phi = A + \frac{B}{p_{raw}} + \frac{C}{p^2_{raw}} + \frac{D}{p^3_{raw}} + \frac{E}{p^4_{raw}} \tag{7.23}$$

The values of individual parameters along with the χ^2 test have been collected in Table 7.5. As mentioned earlier, Monte Carlo data are needed to study the effect of momentum resolution on correlation functions and obtained source sizes. In this case, these are data from the

Table 7.5: Momentum resolution parameteres for Equations 7.21, 7.22 and 7.23 and values of χ^2 test.

	A	B	C	D	E	χ^2
σ_p	0.0602	0.0280	-0.1047	0.0814	-0.0189	9.66
σ_θ	0.0014	-0.0001	0.0012	-0.0005	0.0001	3.60
σ_ϕ	0.0011	0.0357	-0.0314	0.0150	-0.0027	20.08

Therminator2 model, where the angles θ and ϕ are calculated according to the equations:

$$\theta = \arctan \frac{\sqrt{p_x^2 + p_y^2}}{p_z} \tag{7.24}$$

$$\phi = \arctan \frac{p_y}{p_x} \tag{7.25}$$

The next step in the procedure is to blur these quantities with numbers generated from normal distributions with a mean of zero and a standard deviation determined with embedding. This allows one to calculate the following components of the smeared momentum:

$$p_x^{smeared} = p_{raw} \cos\left(\phi^{smeared}\right) \sin\left(\theta^{smeared}\right) \tag{7.26}$$

$$p_y^{smeared} = p_{raw} \sin\left(\phi^{smeared}\right) \sin\left(\theta^{smeared}\right) \tag{7.27}$$

$$p_z^{smeared} = p_{raw} \cos\left(\theta^{smeared}\right) \tag{7.28}$$

$$E^{smeared} = \sqrt{p_x^{smeared\,2} + p_y^{smeared\,2} + p_z^{smeared\,2} + m_0^2} \tag{7.29}$$

With two sets of momentum, one can calculate two correlation functions - "real" and "smeared". Comparison of these functions will determine the effect size, which for π was on the order of 2%. In the case of $K_S^0 K_S^0$, the model correlation function CF_{real} presented in the left plot at Figure 7.20 was determined. Then the momenta from Therminator2 were smeared, and the $CF_{smeared}$ function was calculated for the new values - the right part of Figure 7.20. It is visible

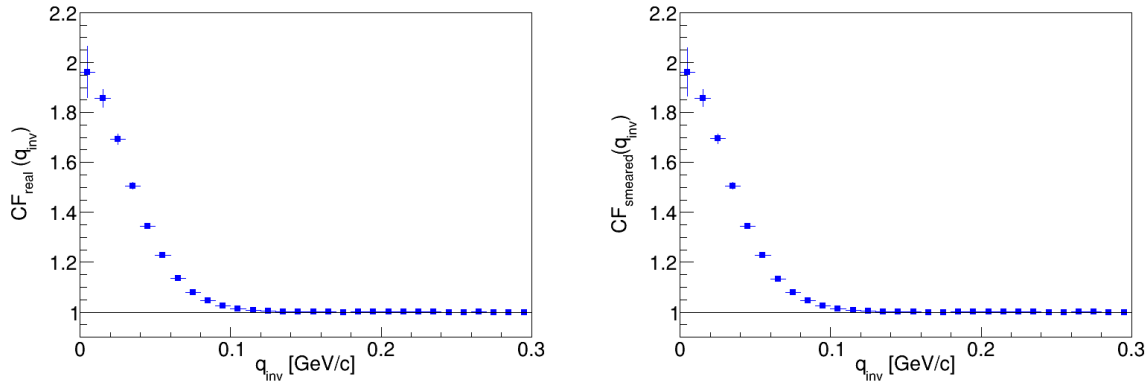

Figure 7.20: The "real" (the left plot) and "smeared" (the right plot) $K_S^0 K_S^0$ correlation functions for central Au+Au collisions at $\sqrt{s_{NN}}$ = 200 GeV. Results are from Therminator2 model.

that both functions are very similar, which is also confirmed by their ratio shown in Figure 7.21. Differences between CF_{real} and $CF_{smeared}$ are less than 0.1%, so the momentum resolution effect is negligible.

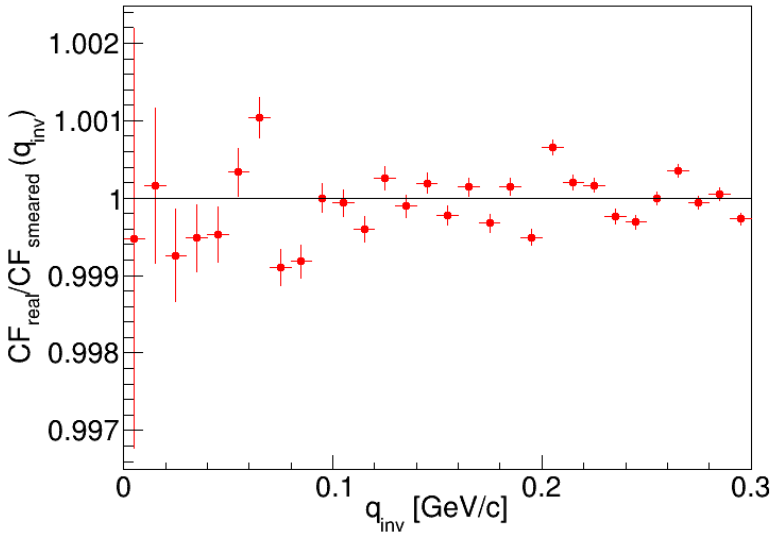

Figure 7.21: Ratio of "real" and "smered" $K^0_S K^0_S$ correlation functions for central Au+Au collisions at $\sqrt{s_{NN}}$ = 200 GeV. Results are from Terminator2 model.

Chapter 8

Experimental results on two Strange hadrons correlations

This chapter presents the results of the $K_S^0 K_S^0$ and $K_S^0 K^{\pm}$ femtoscopic correlations measured by the STAR experiment. A study of the signal-to-background dependence, correlation functions, and final functions accounted for all systematic uncertainties, including the necessary corrections, are shown. The size of the particle emitting source are also presented, taking into account statistical and systematic uncertainties.

8.1 $K_s^0 K_s^0$ correlation functions

The two-neutral kaon correlation functions are obtained for Au+Au collisions at one energy from the BES program $\sqrt{s_{NN}}$ = 39 GeV and the top RHIC energy $\sqrt{s_{NN}}$ = 200 GeV. All events were collected in 2010. Experimental data are divided into three centralities: central (0-10%), non-central (10-70%), and minimum bias (0-70%) events. In the case of the most central collisions at $\sqrt{s_{NN}}$ = 200 GeV, a study of different values of the decay length (DL > 2, 3, 4, 5, 6 cm) and DCA between daughters (DCA < 0.3, 0.4, 0.5, 0.6, 0.7, 0.8 cm) are made. Table 8.1 contains information related to the number of events, particles and pairs used to calculate the final correlation functions.

Table 8.1: Information about statistics of data used in this analysis.

	no. of events [M]	no. of K^0_S [M]	no. of pairs [M]
200 GeV	∼94	∼35	∼20
39 GeV	∼83	∼26	∼12

8.1.1 Signal to background study

As mentioned in Section 7.2.1, the purity of a single K^0_S is determined based on the invariant mass distribution in a specific range of the transverse momentum. Thus, the momentum dependence of the signal to the background can be determined. An exemplary distribution for a decay length greater than 3 cm and all tested DCA intervals is shown in Figure 8.1. Analogous characteristics for other DL values have been placed in Appendix A. It can be seen that the smaller the DCA interval, the less contaminated the signal. Below 1 GeV/c in p_T, the function $S/(S+B)$ is increasing with p_T, while above this value, it is practically flat. The figure also shows that the selected interval p_T for K^0_S allows for a high-purity sample. The purity of a single particle was determined as a weighted average over all transverse momentum bins. With this information, it is possible to calculate pair purity, which, by changing the signal to the background with p_T, is a function of the invariant four-momentum difference, q_{inv}. For all combinations of DL and

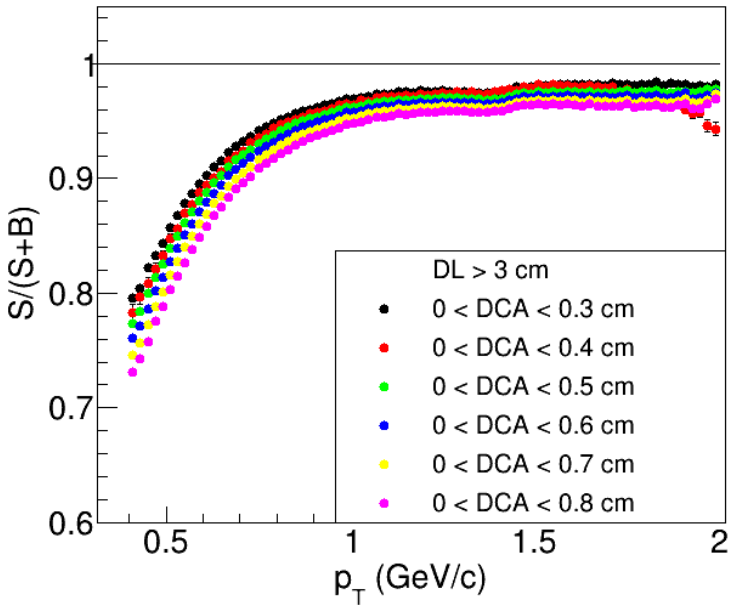

Figure 8.1: The example of the purity of K^0_S as a function of transverse momentum for the most central Au+Au collisions at $\sqrt{s_{NN}}$ = 200 GeV [this thesis].

DCA with other parameters fixed, the pair purity correlation functions are independent of q_{inv} [104]. Figure 8.2 shows the dependence of the average purity of a pair of particles on the decay lengths for different DCA values. Pair purity increases as the DL increases for all DCA values and decreases as the DCA range increases.

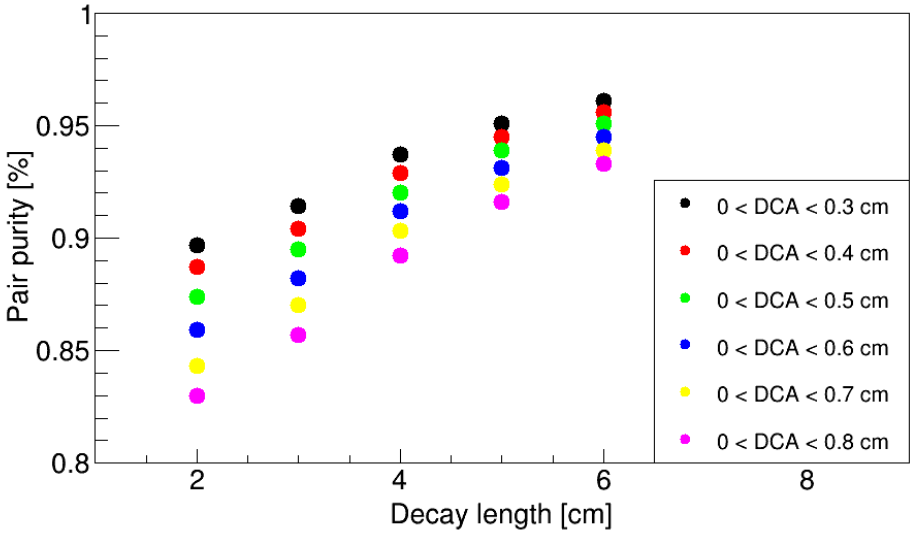

Figure 8.2: The example of the pair purity of $K^0_S K^0_S$ pairs as a function of decay lengths for the most central Au+Au collisions at $\sqrt{s_{NN}}$ = 200 GeV [this thesis].

These studies and information on the number of K^0_S particles allowed one to find the best DL (larger than 3 cm) and DCA (smaller than 0.6 cm) values. This is a trade-off between statistics and purity sample.

8.1.2 Raw data

Raw correlation functions (real function from the experiment without any corrections, also know as uncorrected data) were obtained following the experimental approach described in Section 5.5 and considering the selection criteria from Chapter 7. Figures 8.3 - 8.5 show the $K^0_S K^0_S$ correlation functions for all analyzed centralities and energies. It is visible that these functions are dominated by QS effects (first few bins) and strong FSI due to near-threshold resonances $f_0(980)$ and $a_0(980)$. The consequence of the strong interaction is a negative (below 1) correlation function in the region of q_{inv} = 0.1 GeV/c. As shown in Chapter 6, the dip structure's position and depth depend on the emitting source's size. A larger source radius shifts this structure toward smaller q_{inv} values.

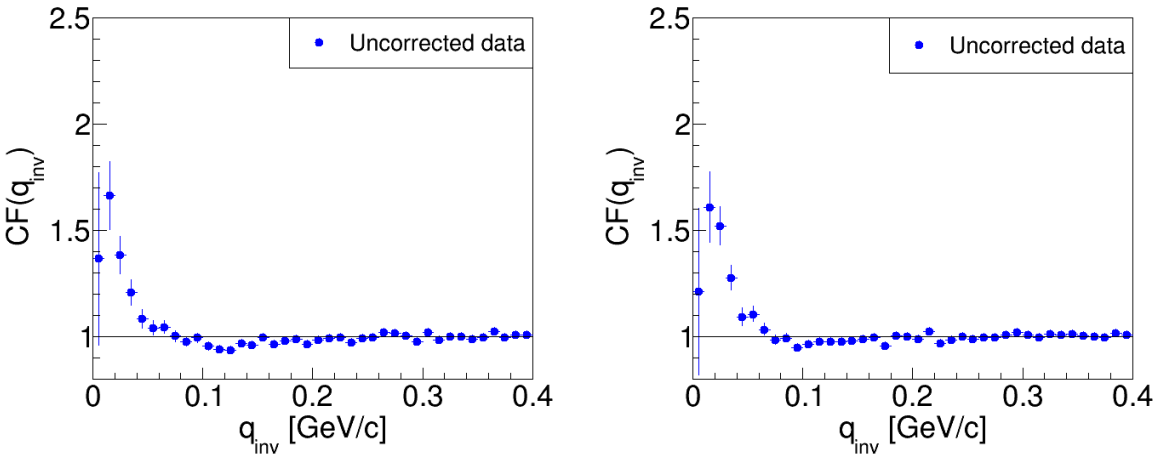

Figure 8.3: The raw correlation functions for $K^0_S K^0_S$ pairs for the most central Au+Au collisions at $\sqrt{s_{NN}}$ = 39 GeV (the left plot) and 200 GeV (the right plot) [this thesis].

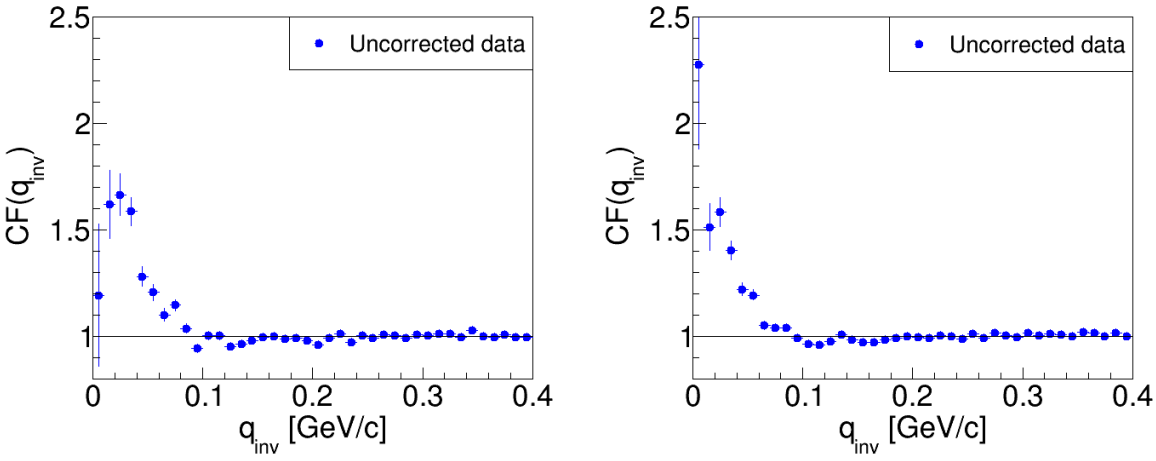

Figure 8.4: The raw correlation functions for $K^0_S K^0_S$ pairs for non-central Au+Au collisions at $\sqrt{s_{NN}}$ = 39 GeV (the left plot) and 200 GeV (the right plot) [this thesis].

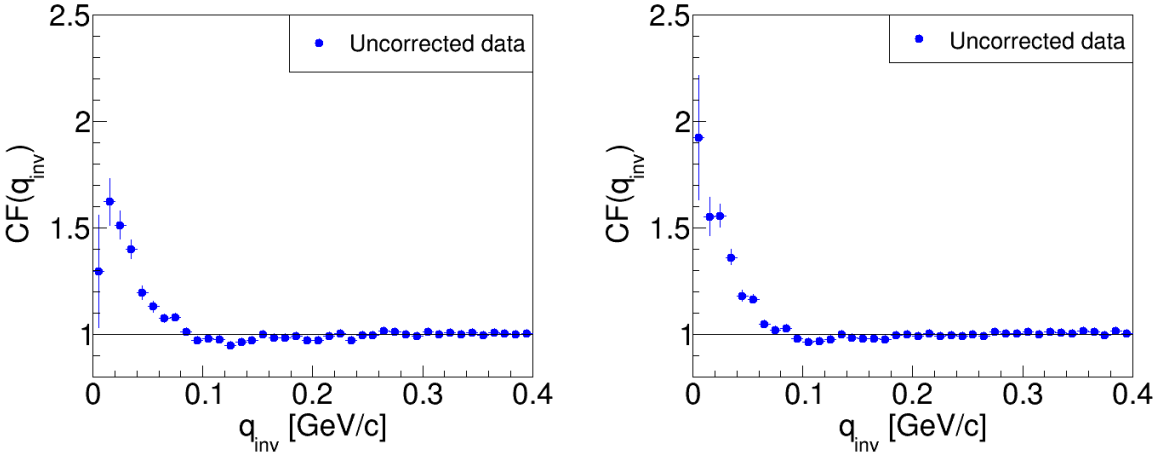

Figure 8.5: The raw correlation functions for $K^0_S K^0_S$ pairs for minimum bias Au+Au collisions at $\sqrt{s_{NN}}$ = 39 GeV (the left plot) and 200 GeV (the right plot) [this thesis].

8.1.3 Pair purity corrections

The obtained correlation functions were first corrected to pair purity, calculated according to the procedure described in Section 7.2.1 and by the equation 7.14. Table 8.2 shows the percentage values of purity of the pair for both analyzed energies and all centrality ranges. Since the purity of the pair is high, the correlation functions before and after the correction should not change significantly.

Table 8.2: The percentage values of the pair purity.

	0-10%	**10-70%**	**0-70%**
200 GeV	88%	97%	94%
39 GeV	88%	96%	94%

Figures 8.6 - 8.8 show how taking this correction into account affects the shape of the correlation function. The differences between raw and corrected functions are insignificant but crucial for the first few bins, where the correlation effect is dominant.

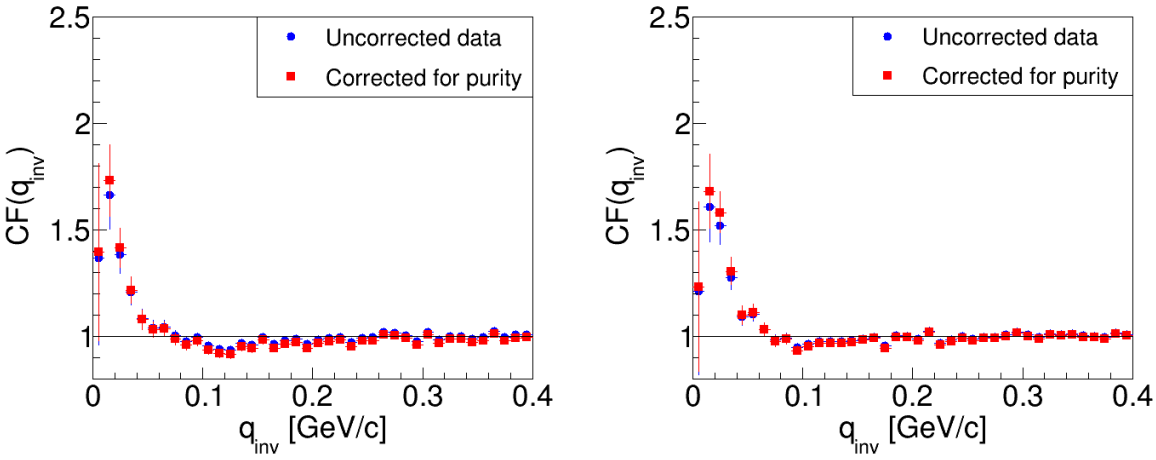

Figure 8.6: The $K^0_S K^0_S$ correlation functions before and after applying the purity correction for the most central Au+Au collisions at $\sqrt{s_{NN}}$ = 39 GeV (the left plot) and 200 GeV (the right plot) [this thesis].

8.1.4 Extraction of femtoscopic parameters

With corrected on purity correlation functions, obtaining the parameters of the source emitting a given type of particle is possible, i.e., the size of the two-neutral kaons homogeneity region - R

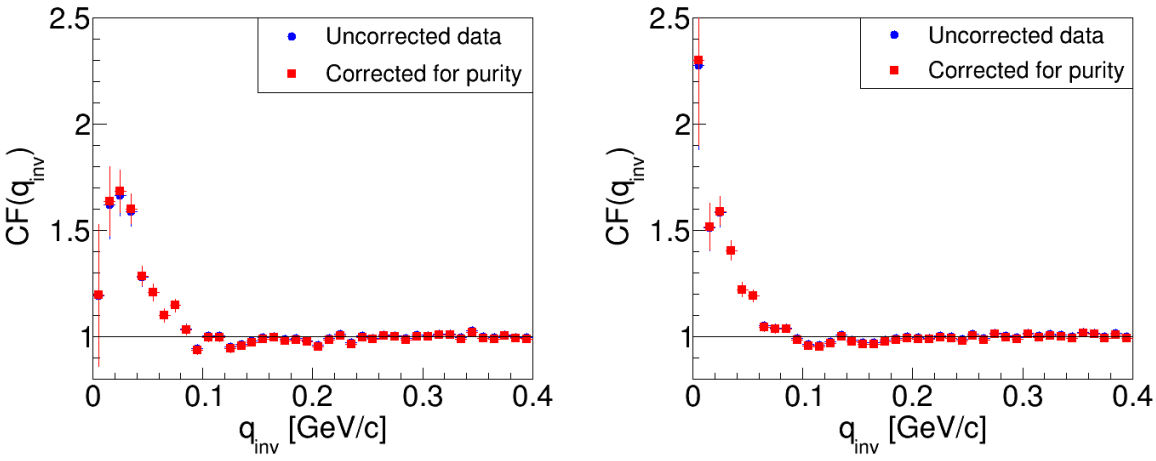

Figure 8.7: The $K^0_S K^0_S$ correlation functions before and after applying the purity correction for non-central Au+Au collisions at $\sqrt{s_{NN}}$ = 39 GeV (the left plot) and 200 GeV (the right plot) [this thesis].

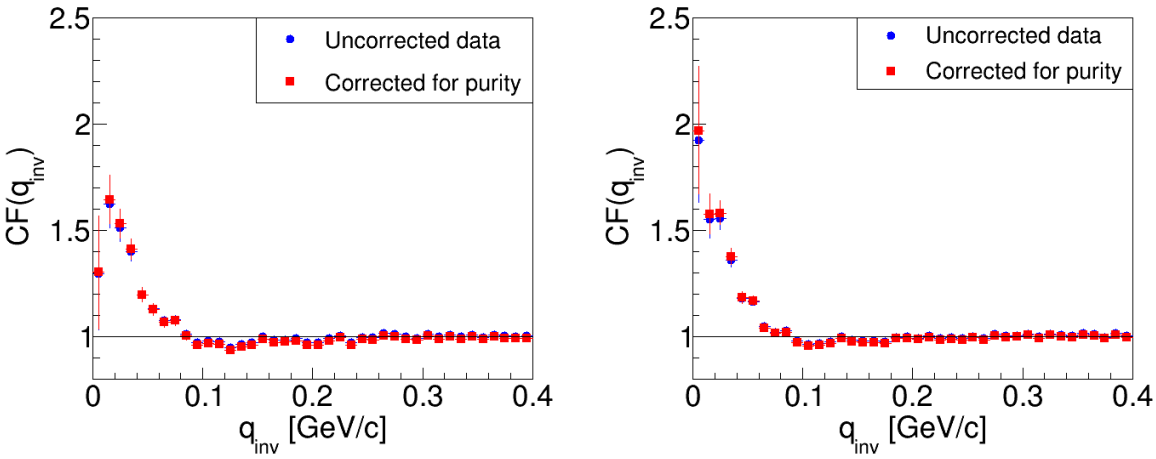

Figure 8.8: The $K^0_S K^0_S$ correlation functions before and after applying the purity correction for minimum bias Au+Au collisions at $\sqrt{s_{NN}}$ = 39 GeV (the left plot) and 200 GeV (the right plot) [this thesis].

and the coefficient of incoherence - λ. To obtain such values, it is necessary to fit the theoretical functions to the experimental data (a detailed description can be found in Section 5.7). In the case of $K^0_S K^0_S$ pairs, fitting was done in two ways. The first one considered only the QS effects, i.e., the Gaussian function (equation 5.32) was used. The statistical uncertainties obtained by this method were also considered uncertainties of the second method. This, in turn, it was considered the strong interaction, which is very important for the analyzed system. For this purpose, the Lednicky-Lyuboshitz parameterization (equation 5.34) was used, which can take four sets of parameters (Table 5.1). Figures 8.9 - 8.11 present correlation functions with the best fits. It is seen that the Gaussian fit does not correctly describe the experimental results because

it does not include the region of function below unity. This region is very well represented by other parameterizations considering strong FSI.

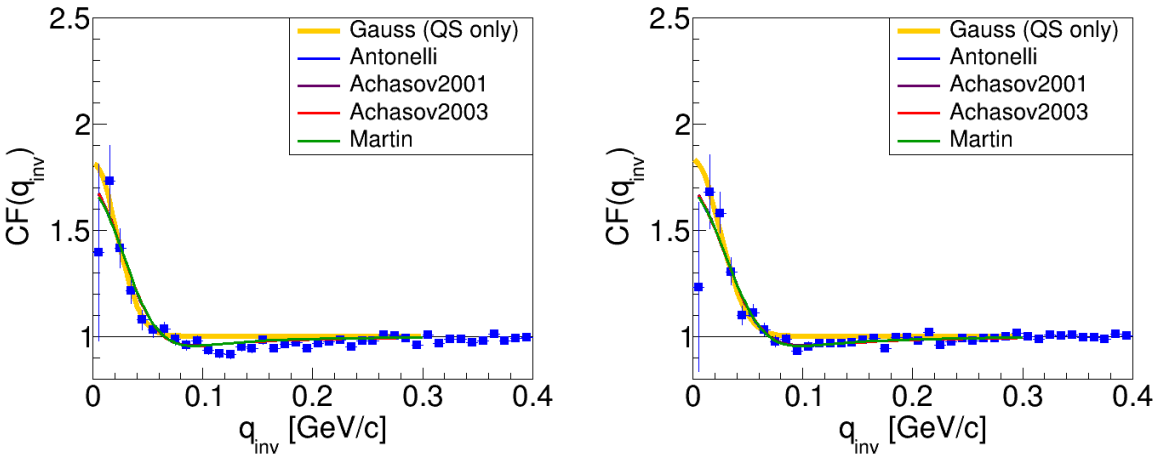

Figure 8.9: The final $K^0_S K^0_S$ correlation functions with Gaussian and Lednicky-Lyuboshitz fits for the most central Au+Au collisions at $\sqrt{s_{NN}}$ = 39 GeV (the left plot) and 200 GeV (the right plot) [this thesis].

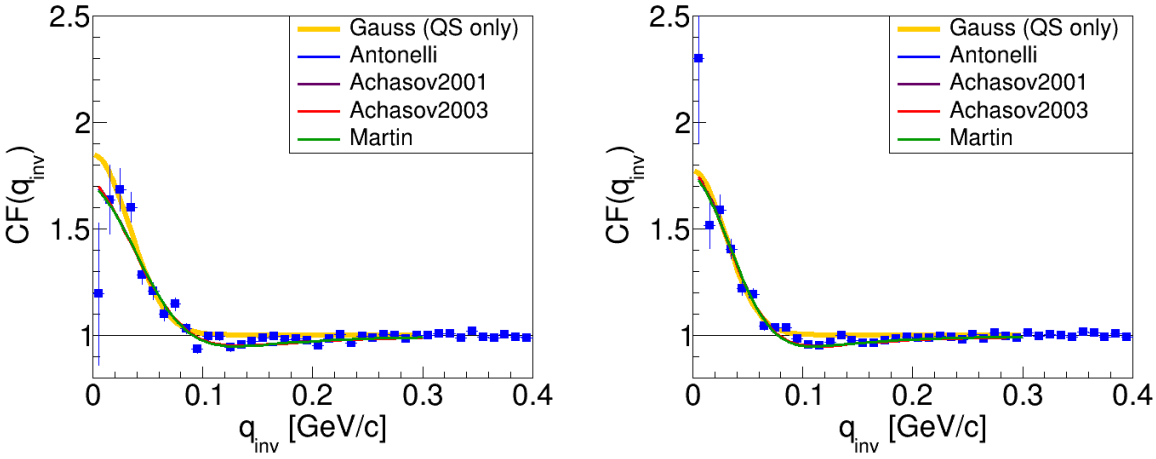

Figure 8.10: The final $K^0_S K^0_S$ correlation functions with Gaussian and Lednicky-Lyuboshitz fits for non-central Au+Au collisions at $\sqrt{s_{NN}}$ = 39 GeV (the left plot) and 200 GeV (the right plot) [this thesis].

Source parameter values with statistical and systematic uncertainties determined were presented in Tables 8.3 and 8.4. The χ^2 map curvature was used when determining statistical uncertainties. On the other hand, systematic uncertainties have been calculated considering various contributions, described in detail in the Section 8.1.5. Numerical calculations show a clear difference between the radii of Gaussian and Lednicky-Lieuboshitz fits (in the order of 1-2 fm). Different

sets of parameters for parameterization with strong force give very coherent, similar values of the homogeneity region. Due to the smaller statistics, the results for $\sqrt{s_{NN}}$ = 39 GeV have more significant uncertainty, particularly visible to central collisions.

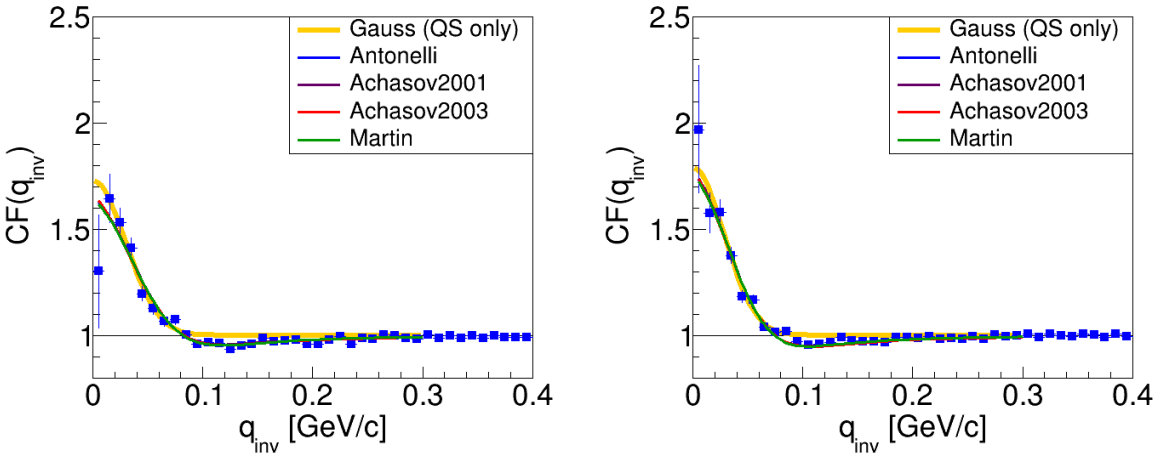

Figure 8.11: The final $K^0_S K^0_S$ correlation functions with Gaussian and Lednicky-Lyuboshitz fits for minimum bias Au+Au collisions at $\sqrt{s_{NN}}$ = 39 GeV (the left plot) and 200 GeV (the right plot) [this thesis].

Table 8.3: Extracted source parametres for $K^0_S K^0_S$ pairs at $\sqrt{s_{NN}}$ = 39 GeV.

		0-10%	**10-70%**	**0-70%**
Gauss	R	$6.50 \pm 0.66 \pm 1.26$ fm	$4.25 \pm 0.20 \pm 0.18$ fm	$4.71 \pm 0.23 \pm 0.28$ fm
	λ	$0.815 \pm 0.174 \pm 0.223$	$0.849 \pm 0.087 \pm 0.133$	$0.729 \pm 0.074 \pm 0.091$
Antonelli	R	$4.48 \pm 0.66 \pm 0.88$ fm	$3.00 \pm 0.20 \pm 0.14$ fm	$3.37 \pm 0.23 \pm 0.21$ fm
	λ	$0.693 \pm 0.174 \pm 0.208$	$0.685 \pm 0.087 \pm 0.177$	$0.632 \pm 0.074 \pm 0.136$
Achasov	R	$4.55 \pm 0.66 \pm 0.88$ fm	$3.03 \pm 0.20 \pm 0.14$ fm	$3.41 \pm 0.23 \pm 0.21$ fm
2001	λ	$0.672 \pm 0.174 \pm 0.203$	$0.651 \pm 0.087 \pm 0.173$	$0.604 \pm 0.074 \pm 0.134$
Achasov	R	$4.44 \pm 0.66 \pm 0.87$ fm	$2.96 \pm 0.20 \pm 0.14$ fm	$3.34 \pm 0.23 \pm 0.21$ fm
2003	λ	$0.649 \pm 0.174 \pm 0.197$	$0.616 \pm 0.087 \pm 0.170$	$0.578 \pm 0.074 \pm 0.132$
Martin	R	$4.47 \pm 0.66 \pm 0.87$ fm	$2.99 \pm 0.20 \pm 0.14$ fm	$3.36 \pm 0.23 \pm 0.21$ fm
	λ	$0.735 \pm 0.174 \pm 0.219$	$0.756 \pm 0.087 \pm 0.184$	$0.689 \pm 0.074 \pm 0.140$

Table 8.4: Extracted source parametres for $K^0_S K^0_S$ pairs at $\sqrt{s_{NN}}$ = 200 GeV.

		0-10%	**10-70%**	**0-70%**
Gauss	R	$5.73 \pm 0.46 \pm 0.44$ fm	$4.68 \pm 0.22 \pm 0.16$ fm	$4.96 \pm 0.22 \pm 0.13$ fm
	λ	$0.833 \pm 0.143 \pm 0.130$	$0.772 \pm 0.076 \pm 0.028$	$0.791 \pm 0.070 \pm 0.025$
Antonelli	R	$4.14 \pm 0.46 \pm 0.33$ fm	$3.61 \pm 0.22 \pm 0.16$ fm	$3.80 \pm 0.22 \pm 0.14$ fm
	λ	$0.684 \pm 0.143 \pm 0.147$	$0.750 \pm 0.076 \pm 0.130$	$0.749 \pm 0.070 \pm 0.124$
Achasov	R	$4.17 \pm 0.46 \pm 0.33$ fm	$3.65 \pm 0.22 \pm 0.16$ fm	$3.84 \pm 0.22 \pm 0.14$ fm
2001	λ	$0.657 \pm 0.143 \pm 0.144$	$0.720 \pm 0.076 \pm 0.130$	$0.720 \pm 0.070 \pm 0.124$
Achasov	R	$4.09 \pm 0.46 \pm 0.33$ fm	$3.56 \pm 0.22 \pm 0.15$ fm	$3.74 \pm 0.22 \pm 0.14$ fm
2003	λ	$0.633 \pm 0.143 \pm 0.141$	$0.687 \pm 0.076 \pm 0.129$	$0.687 \pm 0.070 \pm 0.124$
Martin	R	$4.13 \pm 0.46 \pm 0.33$ fm	$3.61 \pm 0.22 \pm 0.16$ fm	$3.80 \pm 0.22 \pm 0.14$ fm
	λ	$0.734 \pm 0.143 \pm 0.152$	$0.814 \pm 0.076 \pm 0.130$	$0.809 \pm 0.070 \pm 0.125$

8.1.5 Systematic uncertainties calculation

As mentioned in the previous section, the impact of certain contributions on the correlation function was checked when calculating systematic uncertainty. Among them can be distinguished: different DCA values between daughters, different Nσ for daughters, different value of R parameter, finite momentum resolution effect, different fit range, the difference in Lednicky-Lyuboshitz parametrization. The base and changed values used to determine the systematic uncertainties are listed in Table 8.5.

Table 8.5: Limits for different sources for $K^0_S K^0_S$ pairs.

Source	Base value	Changed value
DCA between daughters [cm]	0.8 (39 GeV) 0.6 (200 GeV)	0.6 (39GeV) 0.8 (200 GeV)
$\lvert N\sigma \rvert$ for daughters	< 3	< 2
Different R parameter [cm]	> 3	> 3.3
Fit range [GeV/c]	[0.00 - 0.30]	[0.15 - 0.30]

The influence of the first five contributions was counted based on Gaussian fits. The obtained values were presented in Tables 8.6 and 8.8. It can be seen that the most significant impact on systematic uncertainty is to change Nσ for daughters and parameter R. In the case of Lednicky-Lyuboshitz parameterization, an additional factor resulting from the differences between individual parameter sets is included. The influence of these differences in percentage was collected in Tables 8.7 and 8.9. It should be noted that the impact on the radii value is small, around $\sim$2%, while in the case of the λ parameter, these differences are much higher.

Table 8.6: Contributions of systematic uncertainties from different sources for $K^0_S K^0_S$ pairs at $\sqrt{s_{NN}}$ = 39 GeV.

Source	**0-10%**		**10-70%**		**0-70%**	
	ΔR [%]	$\Delta\lambda$ [%]	ΔR [%]	$\Delta\lambda$ [%]	ΔR [%]	$\Delta\lambda$ [%]
1. DCA between daughters	6.88	2.40	2.28	4.25	0.07	1.02
2. $N\sigma$ for daughters	14.30	25.00	2.82	0.60	4.90	3.20
3. Different R parameter	10.50	1.60	0.20	14.00	2.80	11.00
4. Momentum resolution	0.01	0.02	0.01	0.02	0.01	0.02
5. Fit range	3.86	10.67	1.96	5.71	1.77	4.84

Table 8.7: Contributions of systematic uncertainties from difference in Lednicky-Lyuboshitz parametrizations (6) for $K^0_S K^0_S$ pairs at $\sqrt{s_{NN}}$ = 39 GeV.

Parametrization	**0-10%**		**10-70%**		**0-70%**	
	ΔR [%]	$\Delta\lambda$ [%]	ΔR [%]	$\Delta\lambda$ [%]	ΔR [%]	$\Delta\lambda$ [%]
Antonelli	2.46	12.41	2.33	20.44	2.08	17.56
Achasov 2001	2.42	12.80	2.31	21.51	2.05	18.38
Achasov 2003	2.48	13.25	2.36	22.73	2.1	19.20
Martin	2.46	11.70	2.34	18.52	2.08	16.11

To determine complete systematic uncertainty that takes into account all contributions, the equation should be used:

$$\Delta\sigma^2_{sys} = \sum_{i=1}^{n} \left(\frac{\bar{x} - x_i}{\bar{x}} \right)^2 \tag{8.1}$$

where $\Delta\sigma^2_{sys}$ is a systematic uncertainty of a specific source parameter, n is the number of contributions (in this analysis, $n = 5$ for Gaussian fit and $n = 6$ for Lednicky-Lyuboshitz parametrization), $\bar{x}$ is the value of the parameter for standard cuts, and x_i is a value after modifications.

Table 8.8: Contributions of systematic uncertainties from different sources for $K^0_S K^0_S$ pairs at $\sqrt{s_{NN}} = 200$ GeV.

Source	**0-10%**		**10-70%**		**0-70%**	
	ΔR [%]	$\Delta\lambda$ [%]	ΔR [%]	$\Delta\lambda$ [%]	ΔR [%]	$\Delta\lambda$ [%]
1. DCA between daughters	1.79	8.65	1.51	0.09	0.69	1.20
2. $N\sigma$ for daughters	6.31	10.86	1.05	1.11	1.86	1.47
3. Different R parameter	1.52	6.57	2.66	1.26	1.32	0.58
4. Momentum resolution	0.00	0.24	0.00	0.24	0.00	0.24
5. Fit range	3.69	1.57	0.89	2.45	0.48	1.30

Table 8.9: Contributions of systematic uncertainties from difference in Lednicky-Lyuboshitz parametrizations (6) for $K^0_S K^0_S$ pairs at $\sqrt{s_{NN}} = 200$ GeV.

Parametrization	**0-10%**		**10-70%**		**0-70%**	
	ΔR [%]	$\Delta\lambda$ [%]	ΔR [%]	$\Delta\lambda$ [%]	ΔR [%]	$\Delta\lambda$ [%]
Antonelli	1.93	14.77	2.49	16.93	2.63	16.29
Achasov 2001	1.92	15.37	2.47	17.64	2.60	16.94
Achasov 2003	1.96	15.96	2.53	18.49	2.67	17.76
Martin	1.94	13.76	2.49	15.60	2.63	15.08

1. DCA between daughters

The first contribution to systematic uncertainty that was checked was the DCA between the daughter's tracks. As mentioned in Section 7.1.2, this distance must be small enough to make sure that both daughters originate from the same parents. Figure 8.12 shows two correlation functions, the first with a standard cut on DCA between daughters less than 0.6 cm (the left plot) and the second with a changed value, i.e., DCA < 0.8 cm (the right plot). This example is obtained for central Au+Au collisions at $\sqrt{s_{NN}} = 200$ GeV. The procedure was the same for

the other centrality intervals, and energy $\sqrt{s_{NN}}$ = 39 GeV. As Tables 8.6 and 8.8 show, this contribution has a more significant impact on the final uncertainty in the case of lower energy. However, it does not exceed 10%.

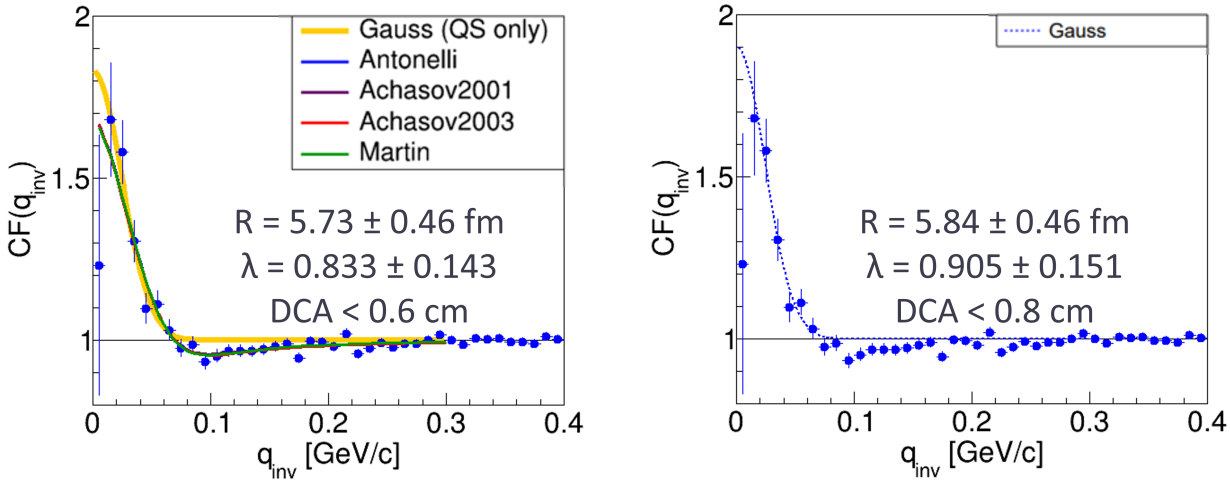

Figure 8.12: Comparison of the correlation function for standard cuts (the left plot) and the changed DCA value (the right plot) for central Au+Au collisions at $\sqrt{s_{NN}}$ = 200 GeV [this thesis].

2. Nσ *for daughters*

To check how the correct identification of particles in TPC affects the correlation function, the results for two different $N\sigma$ values were compared. The obtained correlation functions are shown in Figure 8.13, where on the left is the correlation function for the standard $N\sigma < 3$,

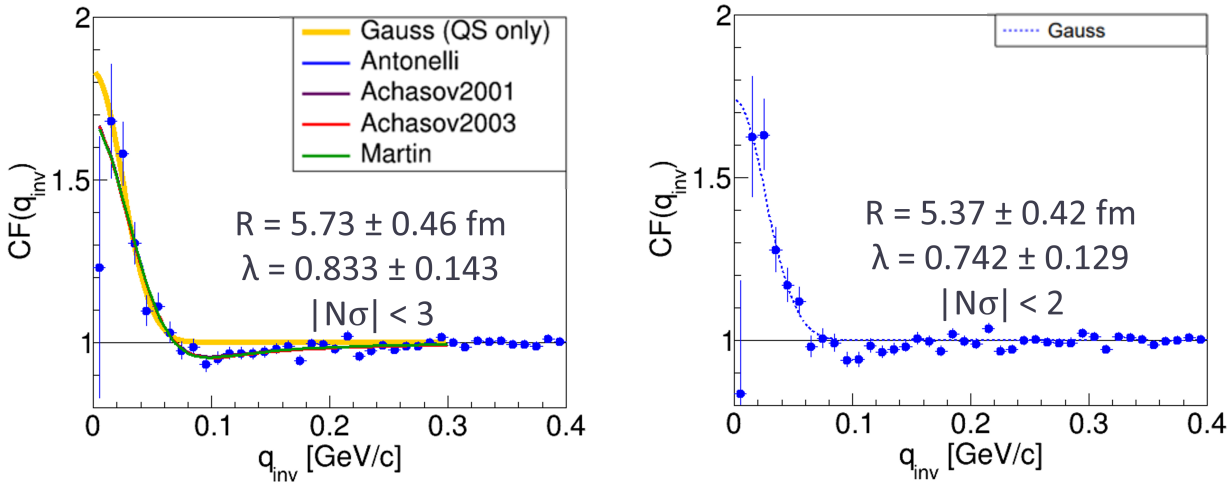

Figure 8.13: Comparison of the correlation function for standard cuts (the left plot) and the changed $|N\sigma|$ value (the right plot) for central Au+Au collisions at $\sqrt{s_{NN}}$ = 200 GeV [this thesis].

and on the right is the changed function with $N\sigma < 2$. This is also confirmed by the obtained fit parameters presented in Table 8.10. It can be seen that in the case of central collisions, the contribution to the systematic uncertainty of this contribution is significant both for energies $\sqrt{s_{NN}}$ = 39 GeV and $\sqrt{s_{NN}}$ = 200 GeV. However, as Tables 8.6 and 8.8 show, this influence decreases in the case of non-central and minimum-bias events.

Table 8.10: Parameters obtained from theoretical fits correlation functions for different $N\sigma$ values for central Au+Au collisions at $\sqrt{s_{NN}}$ = 200 GeV.

	Nσ < 3	**Nσ < 2**	**uncertainty [%]**
R [fm]	5.73	5.37	6.31
λ	0.833	0.742	10.86

3. Different R parameter

When determining the systematic uncertainties, checking how changing the pair cuts will affect the final result is essential. For this purpose, two values of the R parameter, the distance between the vertices of two neutral kaons, were compared. Sample results are shown in Figure 8.14. Again, on the left is the correlation function for standard cuts ($R > 3$ cm), and on the right, the

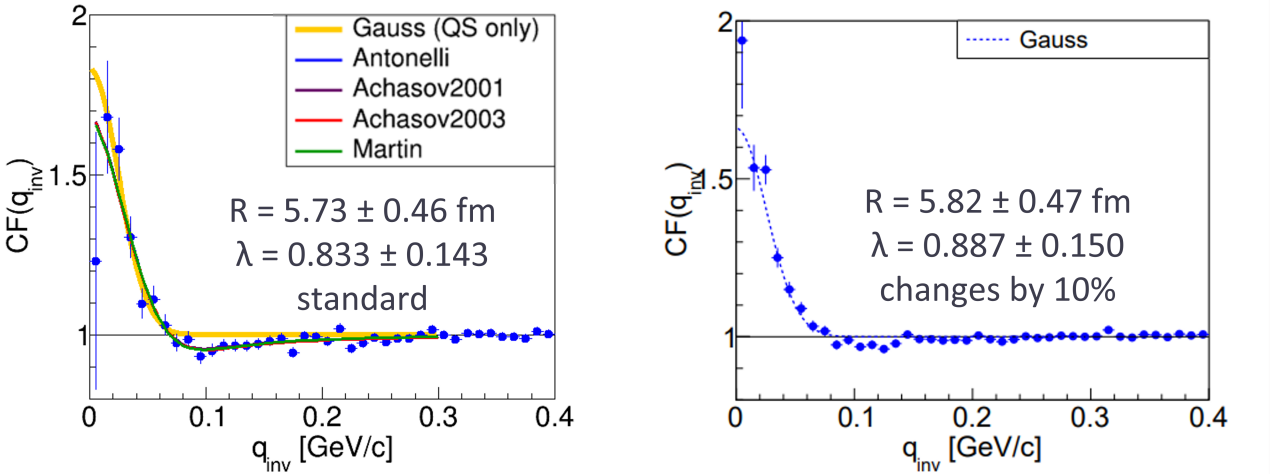

Figure 8.14: Comparison of the correlation function for standard cuts (the left plot) and the changed R parameter value (the right plot) for central Au+Au collisions at $\sqrt{s_{NN}}$ = 200 GeV [this thesis].

value changed by 10% ($R > 3.3$ cm). The main difference is visible primarily in the first bin of the function, which is confirmed by the fit parameters listed in Table 8.11. Comparing all centralities together shows that for $\sqrt{s_{NN}}$ = 39 GeV (Table 8.6), this effect for the size of the

source in central collisions and the λ parameter in other centrality intervals is significant. In the case of $\sqrt{s_{NN}}$ = 200 GeV (Table 8.8), the change in R affects the λ parameter to a greater extent for central collisions. In other cases, this contribution is minimal.

Table 8.11: Parameters obtained from theoretical fits correlation functions for different R parameter values for central Au+Au collisions at $\sqrt{s_{NN}}$ = 200 GeV.

	R > 3 cm	**R > 3.3 cm**	**uncertainty [%]**
R [fm]	5.73	5.82	1.52
λ	0.833	0.887	6.57

4. Momentum resolution

The effect of momentum resolution and its impact on the correlation function was mentioned earlier in Section 7.2.2. At this point, it will be shown how large the percentage of this effect is for the correlation of the $K^0_S K^0_S$ system. Figure 8.15 shows the measured correlation function

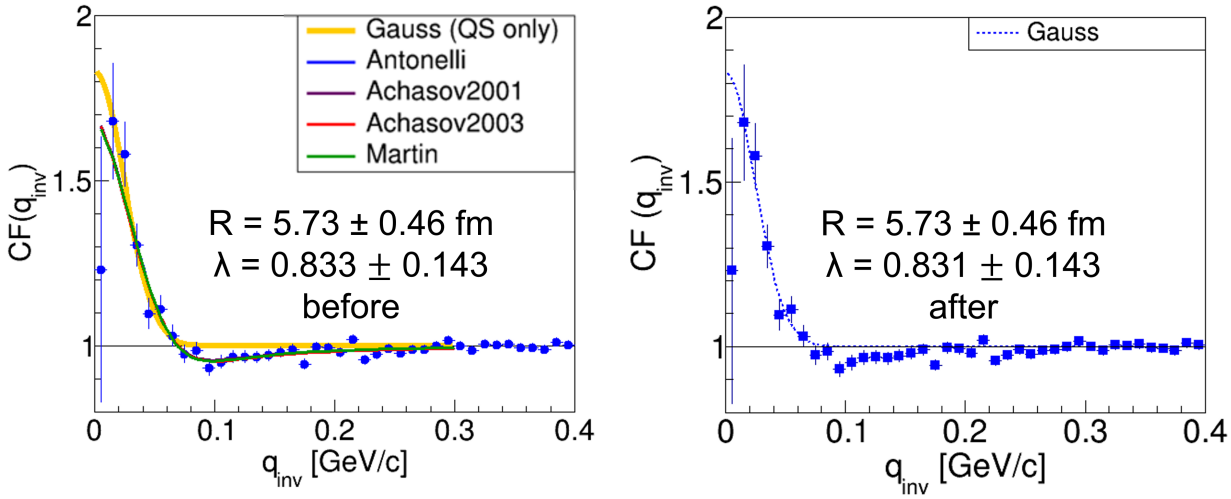

Figure 8.15: Comparison of the measured (the left plot) and smeared (the right plot) correlation function for Au+Au collisions at $\sqrt{s_{NN}}$ = 200 GeV [this thesis].

(the left plot) and the function after momentum smearing (the right plot). As can be seen, this correction does not change the function for two neutral kaons. Therefore, it is treated as one of the contributions to systematic uncertainty. Such uncertainty is expressed as the ratio of the difference between raw and smeared parameters to the measured value. The obtained source sizes, λ parameter values, and calculated uncertainties are summarized in Table 8.12. It can be seen that the fit parameters are close to each other. Hence the systematic uncertainties resulting from this effect are very small.

Table 8.12: Parameters obtained from theoretical fits to measured and smeared correlation functions for Au+Au collisions at $\sqrt{s_{NN}}$ = 200 GeV.

	raw	**smeared**	**uncertainty [%]**
R [fm]	5.73	5.73	0.00
λ	0.833	0.831	0.24

5. Fit range

The theoretical correlation function was fitted to the experimental data over the entire range where the correlation effect is visible, including the first bin. This allows one to determine the parameters of the source. However, there is only sometimes a possibility because there is a smaller number of pairs in the first bin, consequently leading to a large uncertainty of this point. Therefore, it is important to consider this effect when calculating the systematic uncertainties. Figure 8.16 shows examples of correlation functions where the first point of the

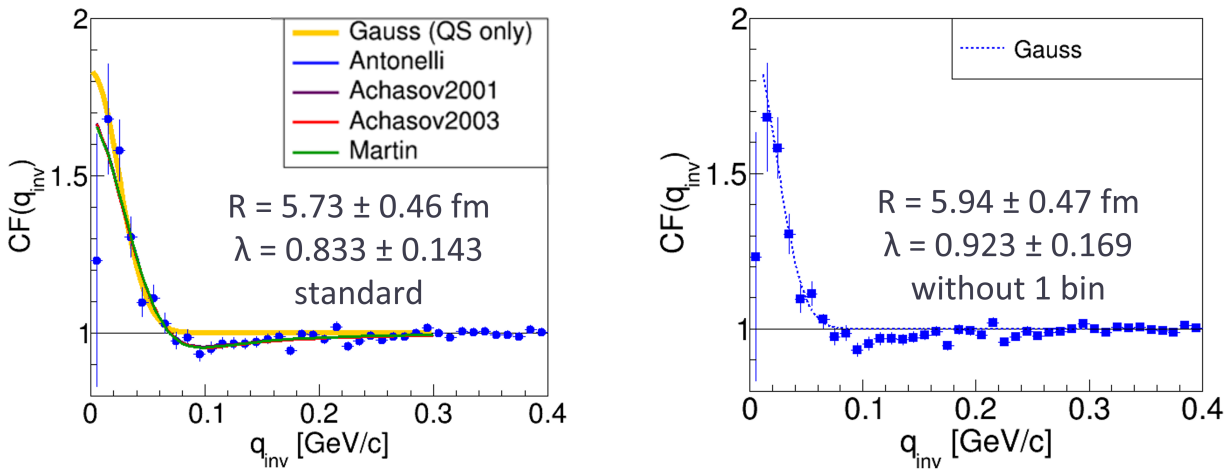

Figure 8.16: Comparison of the correlation function for standard cuts (the left plot) and the changes fit range (the right plot) for Au+Au collisions at $\sqrt{s_{NN}}$ = 200 GeV [this thesis].

function is included in the fit (the left plot) and where it is not (the right plot). As Table 8.13 shows, disabling this point results in a larger source size and λ parameter value. Nevertheless, the impact of this contribution on systematic uncertainties is insignificant, as shown in Tables 8.6 and 8.8. Only at the energy $\sqrt{s_{NN}}$ = 39 GeV, considering the first bin of the correlation function significantly affects the λ parameter.

Table 8.13: Parameters obtained from theoretical fits correlation functions for different fit ranges for central Au+Au collisions at $\sqrt{s_{NN}}$ = 200 GeV.

	with 1st bin	**without 1st bin**	**uncertainty [%]**
R [fm]	5.73	5.94	3.69
λ	0.833	0.923	1.57

6. Difference in Lednicky-Lyuboshitz parametrization

Using four different sets of parameters in the Lednicky-Lyuboshitz parameterization resulted in another factor that should be considered when determining systematic uncertainties. For this purpose, the difference between the largest and smallest value of the source parameters was calculated. Then the obtained result was divided by the calculated values of the radius and the λ parameter. Table 8.14 shows the calculations for central Au+Au collisions at $\sqrt{s_{NN}}$ = 200 GeV. In turn, Tables 8.6 and 8.8 show that this contribution primarily affects the uncertainty of the λ parameter.

Table 8.14: Parameters obtained from theoretical fits correlation functions for difference in Lendicky-Lyuboshitz parametrizations for central Au+Au collisions at $\sqrt{s_{NN}}$ = 200 GeV.

		value	**difference**	**uncertainty [%]**
Antonelli	R [fm]	4.14	0.08	1.93
	λ	0.684	0.101	14.77
Achasov 2001	R [fm]	4.17	0.08	1.92
	λ	0.657	0.101	15.37
Achasov 2003	R [fm]	4.09	0.08	1.96
	λ	0.633	0.101	15.96
Martin	R [fm]	4.13	0.08	1.94
	λ	0.734	0.101	13.76

8.2 $K_s^0 K^{\pm}$ correlation functions

The $K_s^0 K^{\pm}$ correlation functions are obtained for Au+Au collisions at the top RHIC energy $\sqrt{s_{NN}}$ = 200 GeV. All events were collected in 2010. Experimental data are divided into three

centrality classes: central (0-10%), non-central (10-70%), and minimum bias (0-70%) collisions. Due to insufficient statistics, the energy of 39 GeV is not included. Table 8.15 contains information related to the number of events, particles and pairs used to calculate the final correlation functions.

Table 8.15: Information about statistics of data used in this analysis.

	no. of events [M]	**no. of K^0_S [M]**	**no. of K^+/K^- [M]**	**no. of pairs [M]**
200 GeV	∼94	∼35	∼270/∼170	∼16/∼11

8.2.1 Raw data

Experimental correlation functions of the $K^0_S K^\pm$ system were obtained similarly to the two neutral kaons using the method described in Section 5.5. The results obtained for two charge combinations and all centrality intervals are presented in Figures 8.17 - 8.19. A negative correlation is seen in each case due to the strong FSI coming from the $a_0(980)$ resonance. It can be seen that as the centrality changes, the width of the correlation effect also changes.

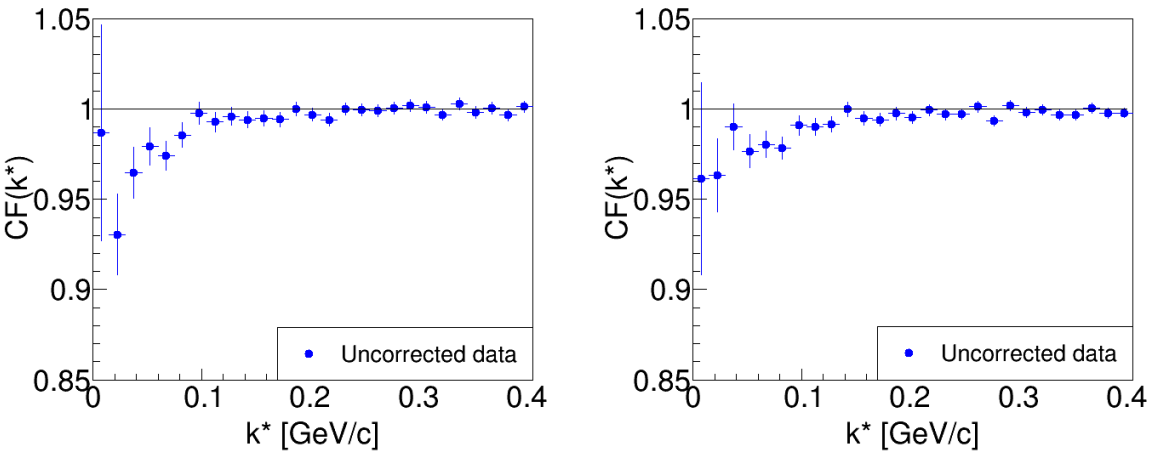

Figure 8.17: The raw $K^0_S K^+$ (the left plot) and $K^0_S K^-$ (the right plot) correlation functions for the most central Au+Au collisions at $\sqrt{s_{NN}}$ = 200 GeV [this thesis].

8.2.2 Pair purity corrections

The first step to obtaining the final correlation functions is to consider the correction for the purity of the pair of particles (the method described in Section 7.2.1). Since information from

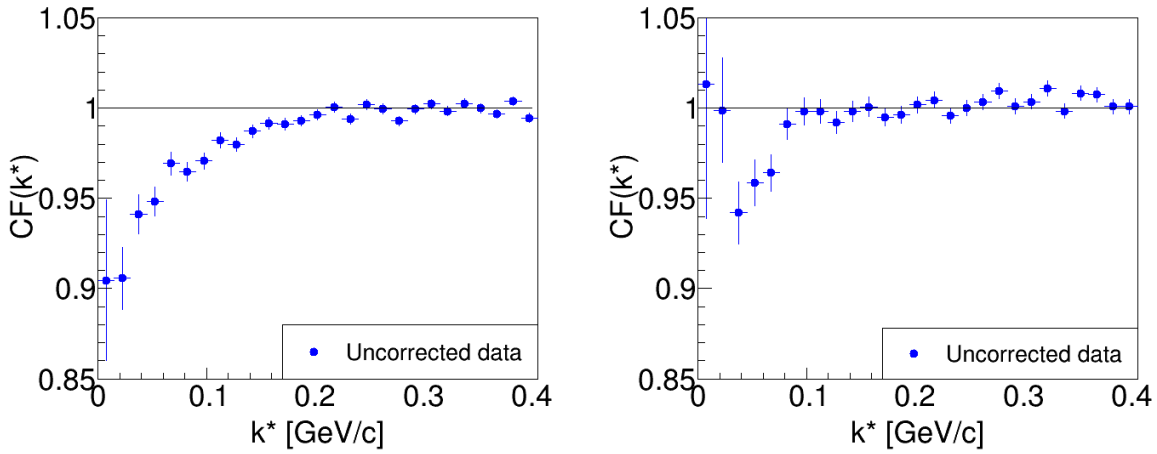

Figure 8.18: The raw $K^0_S K^+$ (the left plot) and $K^0_S K^-$ (the right plot) correlation functions for non-central Au+Au collisions at $\sqrt{s_{NN}}$ = 200 GeV [this thesis].

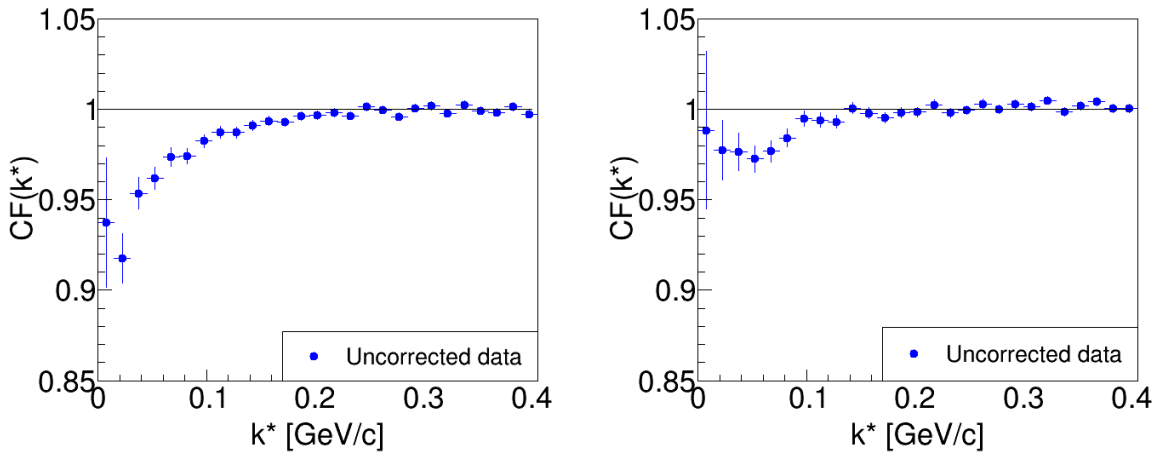

Figure 8.19: The raw $K^0_S K^+$ (the left plot) and $K^0_S K^-$ (the right plot) correlation functions for minimum bias Au+Au collisions at $\sqrt{s_{NN}}$ = 200 GeV [this thesis].

two detectors is required for particle identification, the $K^0_S K^\pm$ purity value should be at least as good as for neutral kaons or even higher. As shown in Table 8.16, these numbers are very high, over 90%. This allows one to assume that the correlation functions before and after taking this correction into account will not change significantly. This is also confirmed by the results presented in Figures 8.20 - 8.22.

Table 8.16: The percentage values of the pair purity.

	0-10%	**10-70%**	**0-70%**
$\mathbf{K^0_S K^\pm}$	93%	97%	96%

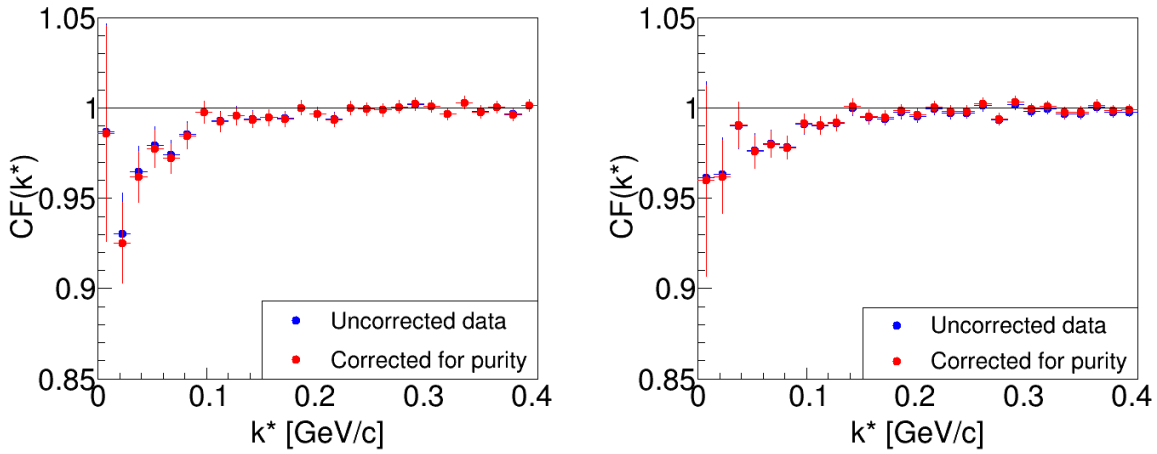

Figure 8.20: The $K^0_S K^+$ (the left plot) and $K^0_S K^-$ (the right plot) correlation functions before and after applying the purity correction for the most central Au+Au collisions at $\sqrt{s_{NN}}$ = 200 GeV [this thesis].

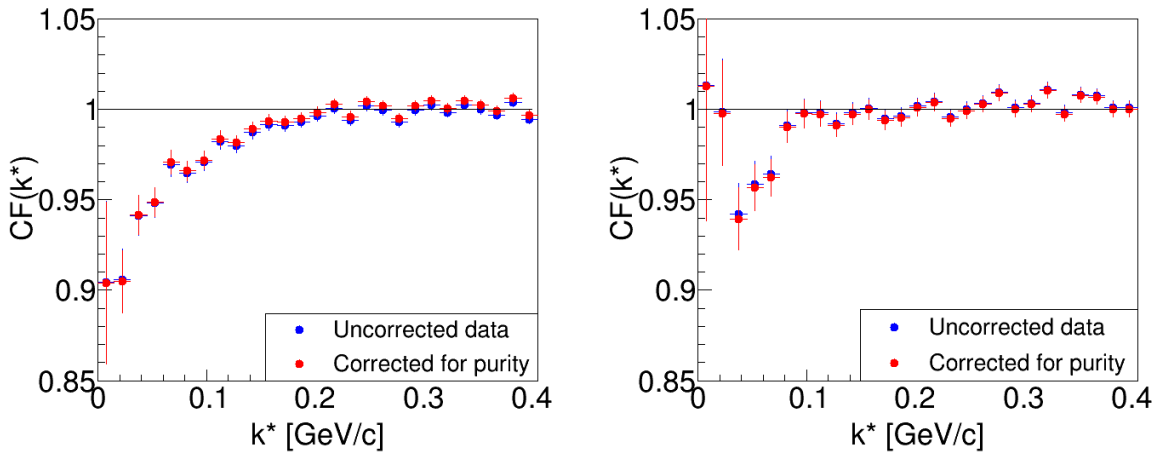

Figure 8.21: The $K^0_S K^+$ (the left plot) and $K^0_S K^-$ (the right plot) correlation functions before and after applying the purity correction for non-central Au+Au collisions at $\sqrt{s_{NN}}$ = 200 GeV [this thesis].

8.2.3 Extraction of femtoscopic parameters

Having the correlation functions corrected for purity, it is possible to fit them with theoretical formulas to determine the parameters characteristic of homogeneity length. For this purpose, the Lednicky-Lyuboshitz parameterization was used in a modified form expressed by the equation 5.37. As mentioned many times, the correlations of the $K^0_S K^\pm$ system depend only on the strong interaction caused by the $a_0(980)$ resonance. Four experiments determined the parame-

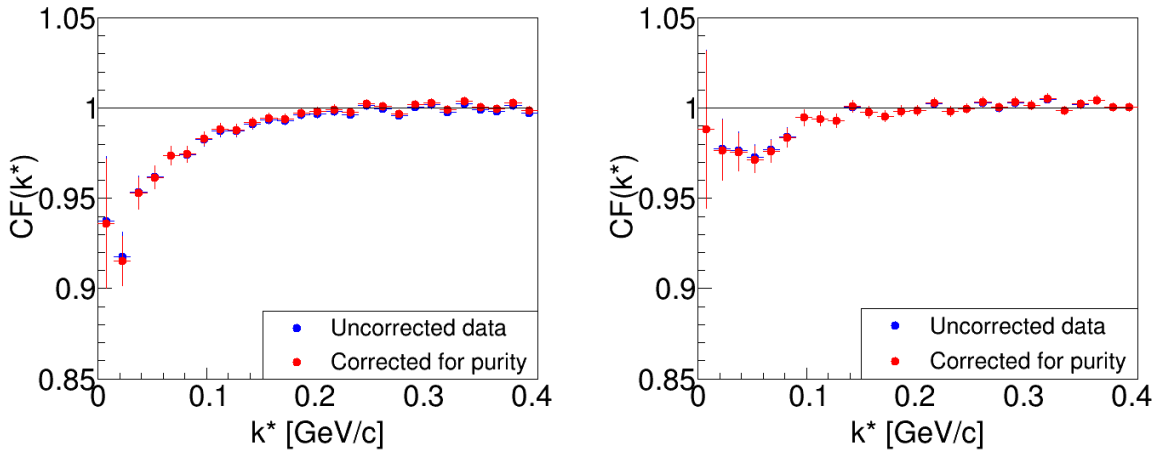

Figure 8.22: The $K^0_S K^+$ (the left plot) and $K^0_S K^-$ (the right plot) correlation functions before and after applying the purity correction for minimum bias Au+Au collisions at $\sqrt{s_{NN}}$ = 200 GeV [this thesis].

ters related to this resonance's mass and decay coupling (Table 5.1). Figures 8.23 - 8.25 show that the choice of such parameterization is appropriate because the signal region of the data is very well represented. One set of parameters - Martin (characterized by the smallest mass a_0) - differs significantly from the other fits.

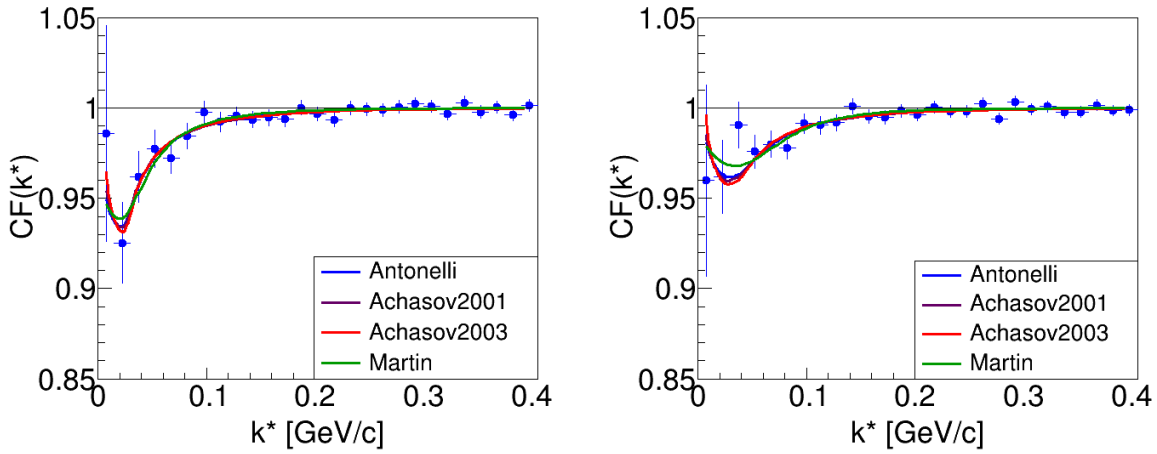

Figure 8.23: The final $K^0_S K^+$ (the left plot) and $K^0_S K^-$ (the right plot) correlation functions with Lednicky-Lyuboshitz fits for the most central Au+Au collisions at $\sqrt{s_{NN}}$ = 200 GeV [this thesis].

Tables 8.17 and 8.18 show the source parameters for the $K^0_S K^+$ and $K^0_S K^-$ systems. As before, the statistical uncertainties were also determined using the χ^2 map curvature, while the systematic ones are affected by several factors (Section 8.2.4). Calculations show that the size of the

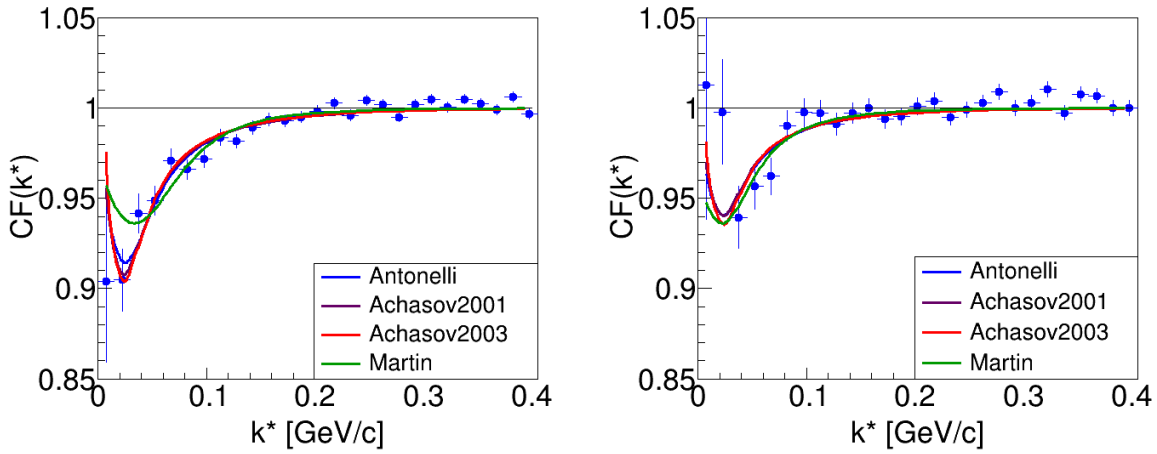

Figure 8.24: The final $K^0_S K^+$ (the left plot) and $K^0_S K^-$ (the right plot) correlation functions with Lednicky-Lyuboshitz fits for non-central Au+Au collisions at $\sqrt{s_{NN}}$ = 200 GeV [this thesis].

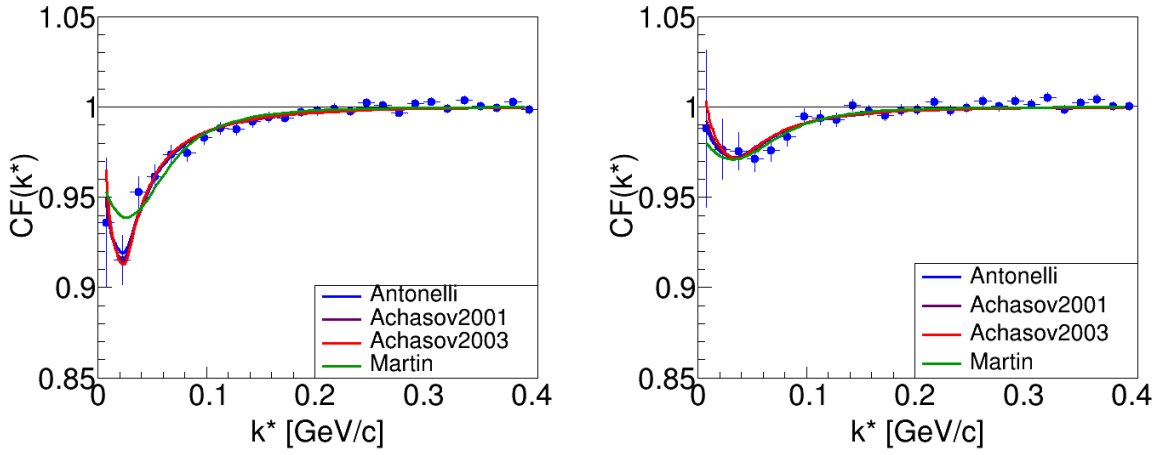

Figure 8.25: The final $K^0_S K^+$ (the left plot) and $K^0_S K^-$ (the right plot) correlation functions with Lednicky-Lyuboshitz fits for minimum bias Au+Au collisions at $\sqrt{s_{NN}}$ = 200 GeV [this thesis].

particle emitting source varies with centrality, and additionally, there is a difference between different sets of parameters. Due to insufficient data statistics, it was impossible to determine the systematic uncertainties for the system $K^0_S K^-$.

8.2.4 Systematic uncertainties calculations

In the case of the $K^0_S K^\pm$ pairs, four contributions to the systematic uncertainty were checked different $N\sigma$ for daughters, different average separation value, finite momentum resolution effect, different normalization range. The base and changed values used to determine the systematic uncertainties are listed in Table 8.19. The total systematic uncertainty was calculated using the

Table 8.17: Extracted source parametres for $K^0_S K^+$ pairs at $\sqrt{s_{NN}}$ = 200 GeV.

		0-10%	**10-70%**	**0-70%**
Antonelli	R	$5.41 \pm 0.66 \pm 0.66$ fm	$3.11 \pm 0.27 \pm 1.41$ fm	$4.10 \pm 0.28 \pm 0.65$ fm
	λ	$1.856 \pm 0.358 \pm 0.382$	$1.404 \pm 0.182 \pm 1.162$	$1.692 \pm 0.185 \pm 0.415$
Achasov	R	$5.92 \pm 0.30 \pm 0.71$ fm	$3.67 \pm 0.13 \pm 1.37$ fm	$4.70 \pm 0.14 \pm 0.63$ fm
2001	λ	$1.945 \pm 0.119 \pm 0.383$	$1.662 \pm 0.068 \pm 1.112$	$1.922 \pm 0.067 \pm 0.363$
Achasov	R	$6.25 \pm 0.32 \pm 0.84$ fm	$4.06 \pm 0.16 \pm 1.26$ fm	$5.04 \pm 0.16 \pm 0.61$ fm
2003	λ	$1.773 \pm 0.107 \pm 0.341$	$1.659 \pm 0.072 \pm 0.900$	$1.806 \pm 0.065 \pm 0.292$
Martin	R	$3.56 \pm 0.50 \pm 1.22$ fm	$1.77 \pm 0.22 \pm 0.89$ fm	$2.22 \pm 0.21 \pm 0.72$ fm
	λ	$0.822 \pm 0.168 \pm 0.437$	$0.588 \pm 0.081 \pm 0.513$	$0.588 \pm 0.074 \pm 0.286$

Table 8.18: Extracted source parametres for $K^0_S K^-$ pairs at $\sqrt{s_{NN}}$ = 200 GeV.

		0-10%	**10-70 %**	**0-70 %**
Antonelli	R	3.17 ± 0.41 fm	2.76 ± 0.52 fm	2.43 ± 0.29 fm
	λ	0.692 ± 0.136	0.827 ± 0.217	0.475 ± 0.081
Achasov	R	3.64 ± 0.19 fm	2.97 ± 0.22 fm	2.66 ± 0.13 fm
2001	λ	0.785 ± 0.049	0.846 ± 0.071	0.495 ± 0.027
Achasov	R	3.99 ± 0.21 fm	3.14 ± 0.23 fm	2.88 ± 0.15 fm
2003	λ	0.782 ± 0.050	0.805 ± 0.064	0.488 ± 0.027
Martin	R	1.97 ± 0.30 fm	2.14 ± 0.48 fm	1.80 ± 0.27 fm
	λ	0.314 ± 0.063	0.522 ± 0.146	0.298 ± 0.054

formula 8.1 based on the values resulting from individual contributions (Table 8.20). As can be seen, for $K^0_S K^+$ pairs these values are enormous for both the source size and the λ parameter. This is due to insufficient data statistics. For the same reason, the systematic uncertainties for

Table 8.19: Limits for different sources for $K^0_S K^\pm$ pairs.

Source	Base value	Changed value
$\lvert N\sigma \rvert$ for daughters	< 3	< 2
Average separation [cm]	> 3	> 3.5
Normalization range [GeV/c]	[0.26 - 0.32]	[0.30 - 0.36]

the $K^0_S K^-$ system have not been calculated. At every attempt to determine these quantities, they turned out to be close to 70%. This did not change with the centrality ranges. Herefore, in the other part of the thesis, the parameters of the source from the $K^0_S K^-$ correlation functions will be shown without systematic ucertainty and will not be taken into account in the conclusions.

Table 8.20: Contributions of systematic uncertainties from different sources for $K^0_S K^+$ pairs at $\sqrt{s_{NN}}$ = 200 GeV.

Source	**0-10%**		**10-70%**		**0-70%**	
	ΔR [%]	$\Delta\lambda$ [%]	ΔR [%]	$\Delta\lambda$ [%]	ΔR [%]	$\Delta\lambda$ [%]
1. Nσ for daughters						
Antonelii	1.48	10.99	21.54	61.61	5.85	16.90
Achasov 2001	1.86	11.41	16.08	50.42	3.40	12.27
Achasov 2003	2.08	12.07	12.56	42.68	2.58	10.85
Martin	28.09	46.96	14.12	70.24	16.67	32.48
2. Different average separation value						
Antonelii	2.96	17.19	34.41	50.36	8.29	11.17
Achasov 2001	1.69	15.94	27.52	38.21	5.11	5.62
Achasov 2003	0.80	14.44	22.66	28.57	3.97	3.77
Martin	5.34	18.25	46.33	51.19	24.77	34.01
3. Momentum resolution						
Antonelii	0.00	0.24	0.00	0.24	0.00	0.24
Achasov 2001	0.00	0.24	0.00	0.24	0.00	0.24
Achasov 2003	0.00	0.24	0.00	0.24	0.00	0.24
Martin	0.00	0.24	0.00	0.24	0.00	0.24
4. Normalization range						
Antonelii	11.65	2.00	19.94	50.36	12.20	13.71
Achasov 2001	11.66	0.67	19.34	21.78	11.91	13.06
Achasov 2003	13.28	3.27	17.24	17.30	11.11	11.18
Martin	19.10	16.79	14.12	7.31	13.06	11.90

1. $N\sigma$ for daughters

As in the case of two neutral kaons, also here, the factor derived from the correct identification of the daughters of the V^0 particle was taken into account. Taking the more restricted cut on $N\sigma$ causes the statistics to decrease. Figure 8.26 on the left shows the correlation function for $N\sigma < 3$ (standard cut), while the one on the right with the changed value of $N\sigma < 2$. There is

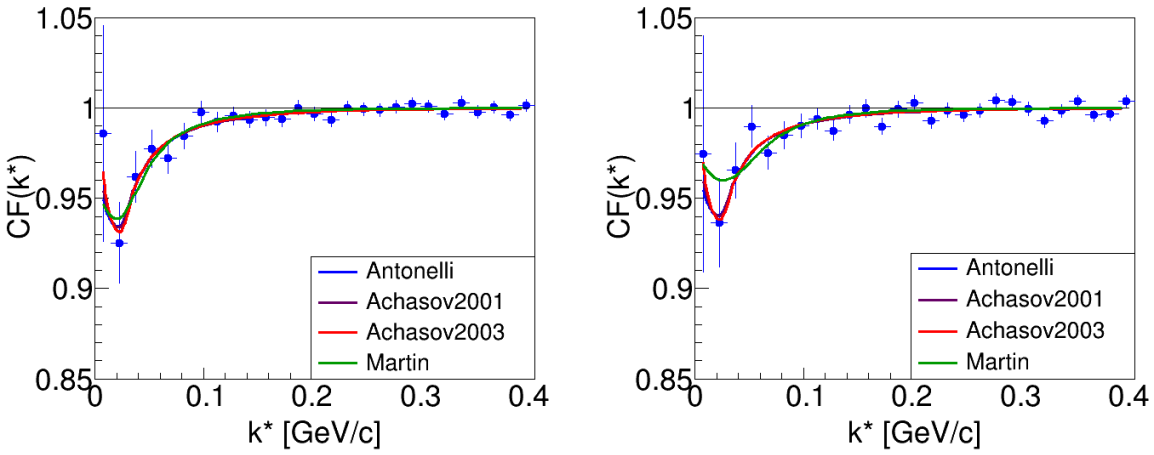

Figure 8.26: Comparison of the correlation function for standard cuts (the left plot) and the changed $|N\sigma|$ value for daughters (the right plot) for central Au+Au collisions at $\sqrt{s_{NN}}$ = 200 GeV [this thesis].

a noticeable difference in the amount of fit, which translates into more significant systematic uncertainty of the λ parameter. Table 8.21 contains the values of the source parameters, which confirm that the relative uncertainty for radius is small, and for λ greater $\sim$10%. The Martin parameterization (differing in parameters from other sets) gives high uncertainty values.

2. Different average separation value

In the case of the $K^0_S K^+$ combination, the average separation cut is used to eliminate the detector effect called merging. Determining this distance between the daughter of the neutral particle and the charged kaon may contribute to systematic uncertainty. The correlation functions for two different average separation ranges are shown in Figure 8.27. In this analysis, the base cut is AveSep > 3 cm (the left plot), while the change consists in narrowing this range by 0.5 cm (the right plot). Numerical calculations (Table 8.22) show that the cut change significantly affects the value of the λ parameter, and the radius changes slightly.

Table 8.21: Parameters obtained from theoretical fits correlation functions for different $N\sigma$ values for daughters for central Au+Au collisions at $\sqrt{s_{NN}}$ = 200 GeV.

		Nσ < 3	**Nσ < 2**	**uncertainty [%]**
Antonelii	R [fm]	5.41	5.33	1.48
	λ	1.856	1.652	10.99
Achasov 2001	R [fm]	5.92	5.81	1.86
	λ	1.945	1.723	11.41
Achasov 2003	R [fm]	6.25	6.12	2.08
	λ	1.773	1.559	12.07
Martin	R [fm]	3.56	2.56	28.09
	λ	0.822	0.436	46.96

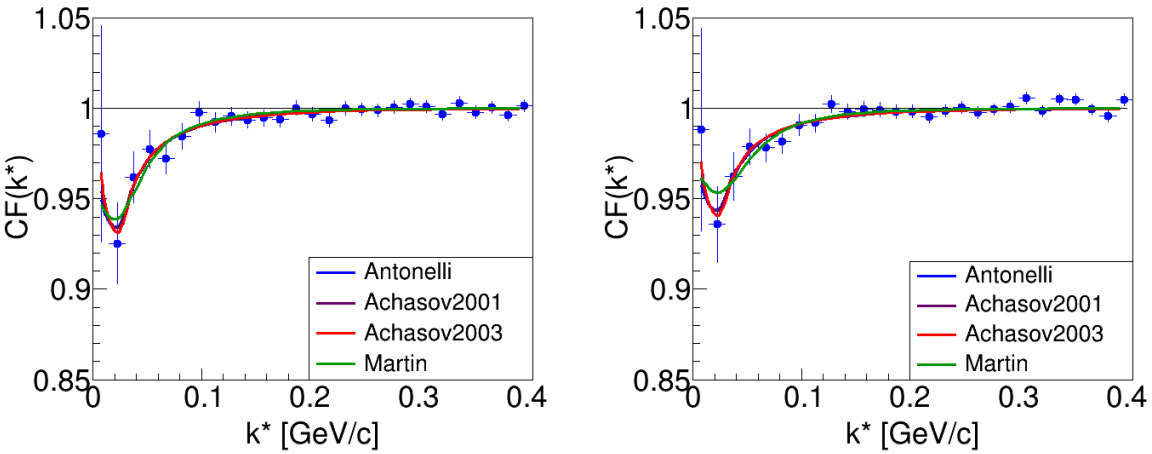

Figure 8.27: Comparison of the correlation function for standard cuts (the left plot) and the changed average separation value (the right plot) for central Au+Au collisions at $\sqrt{s_{NN}}$ = 200 GeV [this thesis].

3. Momentum resolution

The impact of momentum resolution on the parameters of the particle emitting source in the case of $K^0_S K^+$ was assumed to be the same as in the case of two neutral kaons. So it is 0.00% for the radius and 0.24% for the λ parameter, respectively.

Table 8.22: Parameters obtained from theoretical fits correlation functions for different average separation values for central Au+Au collisions at $\sqrt{s_{NN}}$ = 200 GeV.

		AveSep > 3 cm	**AveSep > 3.5 cm**	**uncertainty [%]**
Antonelii	R [fm]	5.41	5.25	2.96
	λ	1.856	1.537	17.19
Achasov 2001	R [fm]	5.92	5.82	1.69
	λ	1.945	1.635	15.94
Achasov 2003	R [fm]	6.25	6.20	0.80
	λ	1.773	1.517	14.44
Martin	R [fm]	3.56	3.37	5.34
	λ	0.822	0.672	18.25

4. Normalization range

The last factor checked was the normalization range of the correlation function. As the results collected in Table 8.23 show, an adequately selected range significantly changes the size of the source (over 10%) and slightly affects the coherence parameter.

Table 8.23: Parameters obtained from theoretical fits correlation functions for different normalization ranges for central Au+Au collisions at $\sqrt{s_{NN}}$ = 200 GeV.

		standard	**changed**	**uncertainty [%]**
Antonelii	R [fm]	5.41	6.04	11.65
	λ	1.856	1.893	1.99
Achasov 2001	R [fm]	5.92	6.61	11.66
	λ	1.945	1.958	0.67
Achasov 2003	R [fm]	6.25	7.08	13.28
	λ	1.773	1.831	3.27
Martin	R [fm]	3.56	4.24	19.10
	λ	0.822	0.960	16.79

Chapter 9

Discussion and summary

9.1 Comparison with model predictions

The obtained correlation functions of the $K^0_S K^0_S$ were compared with the predictions of two UrQMD and Therminator22 theoretical models (described in Chapter 3). Data from Thermina-tor2 generator are only for the most central (0-5%) Au+Au collisions for energy $\sqrt{s_{NN}}$ = 39 GeV and for all centrality intervals in the case of the top RHIC energy. Figures 9.1 - 9.3 show a comparison for central, non-central, and minimum bias collisions. It can be seen that the functions from the UrQMD model reflect the experimental data quite well, in particular for the energy $\sqrt{s_{NN}}$ = 200 GeV. In looks similarly in the case of Terminator2. Only a correlation function for

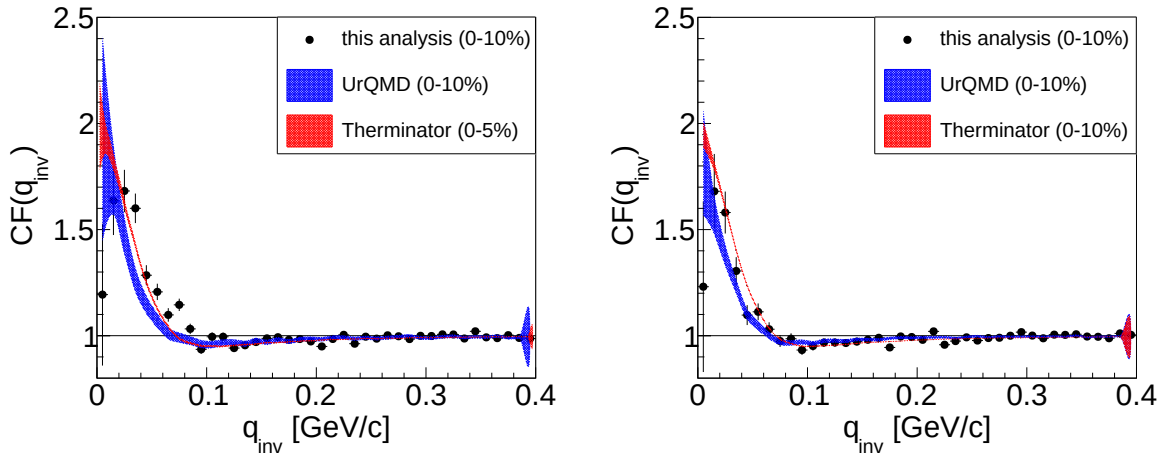

Figure 9.1: $K^0_S K^0_S$ correlation functions for central Au+Au collisions at $\sqrt{s_{NN}}$ = 39 GeV (the left plot) and 200 GeV (the right plot) together with model calculations from UrQMD (the blue band) and Therminator2 (the red band) [this thesis].

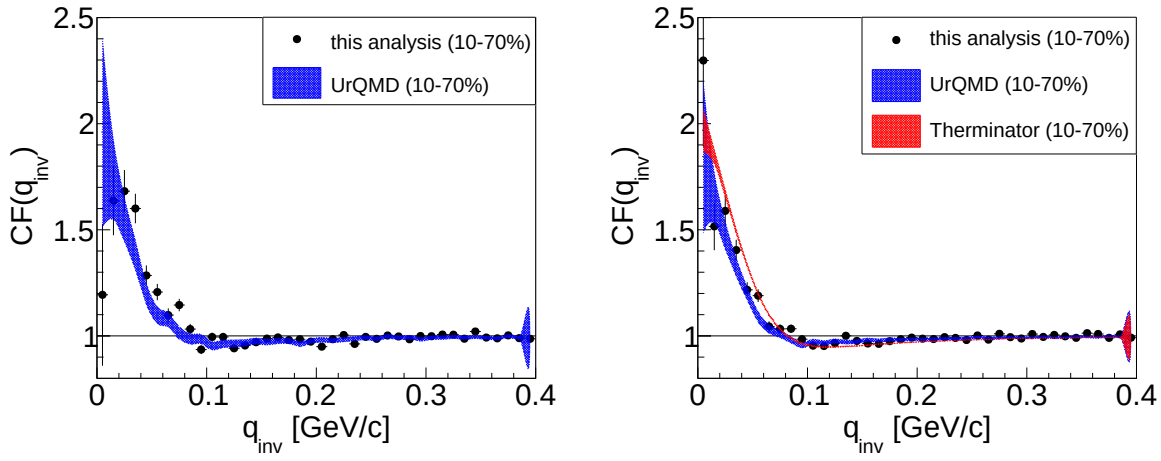

Figure 9.2: $K^0_S K^0_S$ correlation functions for non-central Au+Au collisions at $\sqrt{s_{NN}}$ = 39 GeV (the left plot) and 200 GeV (the right plot) together with model calculations from UrQMD (the blue band) and Therminator2 (the red band) [this thesis].

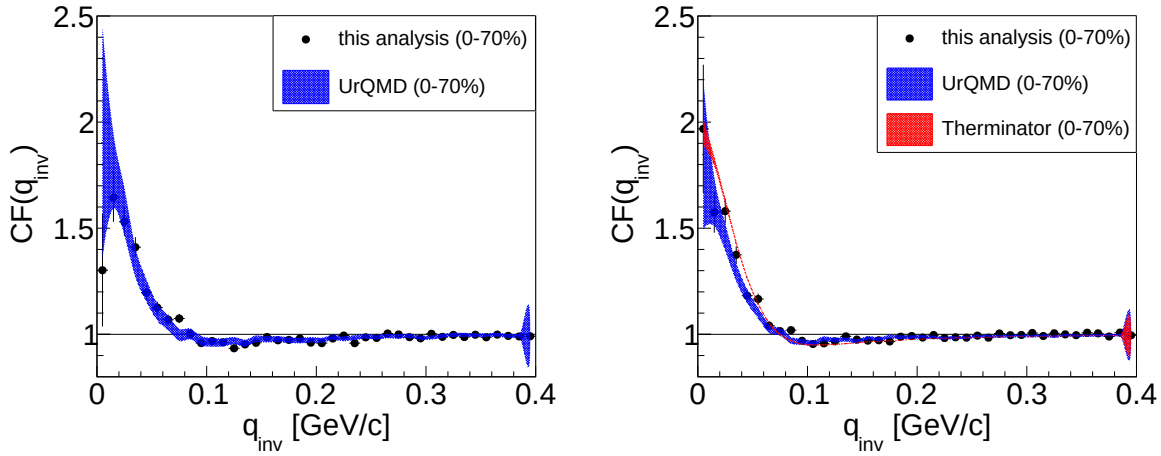

Figure 9.3: $K^0_S K^0_S$ correlation functions for minimum bias Au+Au collisions at $\sqrt{s_{NN}}$ = 39 GeV (the left plot) and 200 GeV (the right plot) together with model calculations from UrQMD (the blue band) and Therminator2 (the red band) [this thesis].

central collisions with energy $\sqrt{s_{NN}}$ = 39 GeV slightly differs from the experimental, caused by a narrower centrality range from the model. In Table 9.1, measured source parameters for data from theoretical predictions were collected. The sizes of homogeneity lengths from models are similar to those obtained from real data analysis. Nevertheless, the transport model, UrQMD, gives larger radii values and smaller λ parameters. The dependence on the centrality of the collision and its energy is visible.

Table 9.1: Parameters of the neutral kaon emitting source obtained from theoretical predictions.

		0-10%	**10-70%**	**0-70%**
			$\sqrt{s_{NN}}$ = 39 GeV	
UrQMD	R [fm]	4.102 ± 0.265	3.394 ± 0.218	3.636 ± 0.232
	λ	0.660 ± 0.087	0.631 ± 0.080	0.679 ± 0.086
Therminator2	R [fm]	3.928 ± 0.026		
	λ	0.882 ± 0.013		
			$\sqrt{s_{NN}}$ = 200 GeV	
UrQMD	R [fm]	4.638 ± 0.209	3.756 ± 0.166	3.772 ± 0.165
	λ	0.636 ± 0.059	0.637 ± 0.057	0.611 ± 0.054
Therminator2	R [fm]	4.065 ± 0.027	3.439 ± 0.027	3.770 ± 0.020
	λ	0.884 ± 0.013	0.869 ± 0.015	0.862 ± 0.010

9.1.1 Studies of Therminator2 at $\sqrt{s_{NN}}$ = 200 GeV

The Therminator2 model was also used to study the effect of the Coulomb correction on the correlation functions of the system of two charged kaons. The data used in this analysis come from Au+Au collisions at $\sqrt{s_{NN}}$ = 200 GeV in eight centrality classes (0-5%, 5-10%, 10-20%, 20-30%, 30-40%, 40-50%, 50-60%, 60-70%) with transverse momentum in the range of 0.15-1.55 GeV/c and pseudorapidity [-1.1]. The one- and three-dimentional correlation functions were determined in six intervals of the transverse mass: 0.53-0.61 GeV/c, 0.61-0.70 GeV/c, 0.70-0.82 GeV/c, 0.82-0.94 GeV/c, 0.94-1.07 GeV/c and 1.07-1.21 GeV/c.

An exemplary function for the K^-K^- system is shown in Figure 9.4. Two parameterizations were taken into account there. The first one considers only QS effects and is described by the equation 5.32. The second also takes into account the Coulomb interaction - the Bowler-Sinyukov formula 5.33. As the plot shows, ignoring the Coulomb interaction leads to a fit that does not describe the region of the correlation effect. Therefore, the use of the Bowler-Sinyukov parameterization is essential. In order to properly perform such a fit, a fixed value of the source's radius should be assumed. This value depends on the energy, centrality, or m_T range. In the analysis presented below, the values of the radius of the Gaussian source depended on the homogeneity lengths obtained by fitting the simple Gaussian distribution. Figure 9.5 show the negatively charged kaons source sizes before applying the Coulomb correction. The results

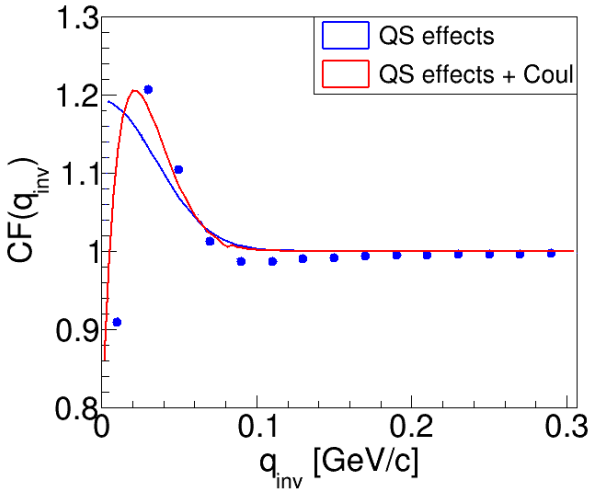

Figure 9.4: An example of K^-K^- correlation function for the most central Au+Au collision at $\sqrt{s_{NN}}$ = 200 GeV. Results are obtained using Therminator2 model [this thesis].

after its calculation are presented in Figure 9.6. It is possible to see that after the correction, the size changes more rapidly as m_T increases. This, in turn, corresponds to the fact that for a larger m_T, after applying the Coulomb correction, the sizes were smaller by about 0.5 fm.

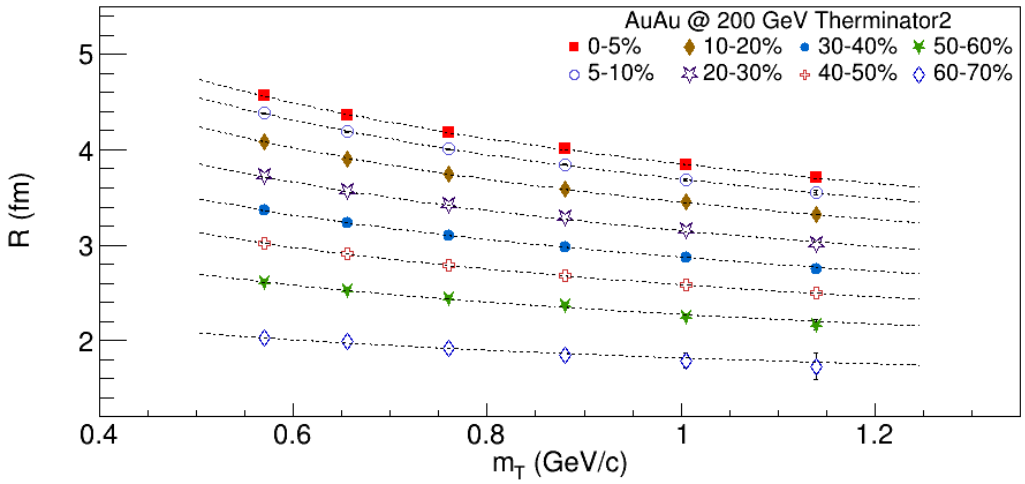

Figure 9.5: Femtoscopic radii obtained from K^-K^- correlation functions before applying the Coulomb correction from Au+Au collisons at $\sqrt{s_{NN}}$ = 200 GeV as a function of pair transverse mass. Results are from Therminator2 model [this thesis].

It shows how important it is to include Coulomb FSI in parametrization in the case of pairs of charged kaons. In addition, the reduction of radii together with centrality and m_T is understood as a consequence of strong collective flows [105]. For the observed size to be small for large m_T, the particles must be emitted relatively close to each other. This situation takes place only when

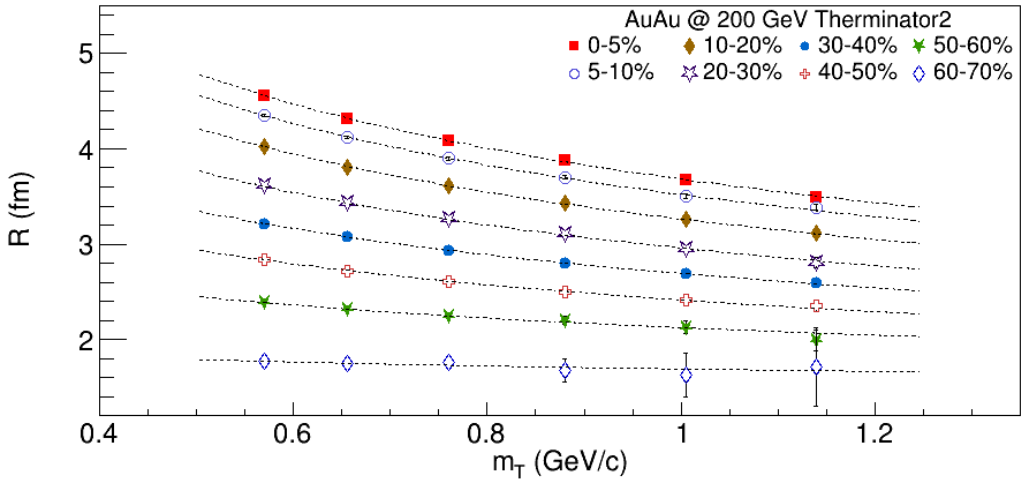

Figure 9.6: Femtoscopic radii obtained from K^-K^- correlation functions after applying the Coulomb correction from Au+Au collisons at $\sqrt{s_{NN}}$ = 200 GeV as a function of pair transverse mass. Results are from Therminator2 model [this thesis].

the two particles have a flow velocity (outward) and a thermal velocity of similar values [106]. Analogous dependencies on m_T are observed for the results with K^+K^+ and three-dimensional correlation functions (Appendix B).

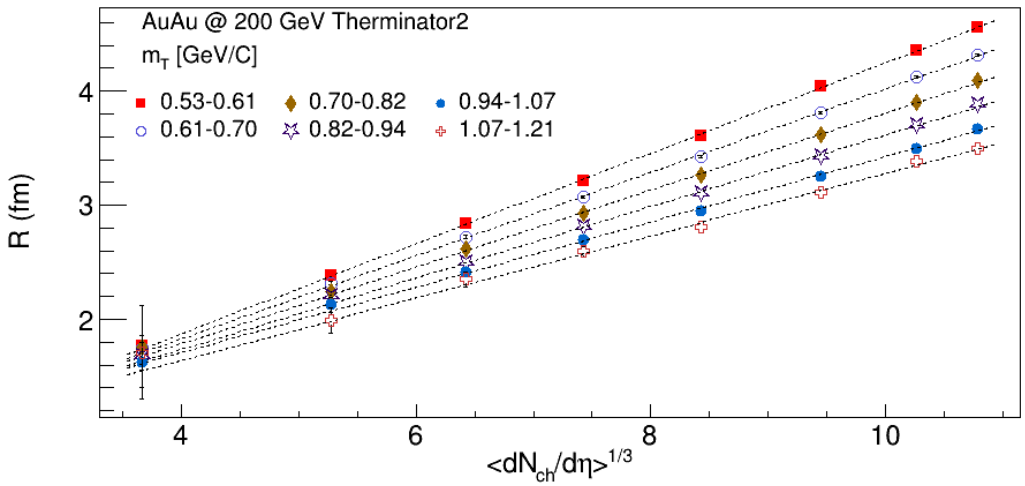

Figure 9.7: Femtoscopic radii obtained from K^-K^- correlations after applying the Coulomb correction from Au+Au collisons at $\sqrt{s_{NN}}$ = 200 GeV as a function of $< dN_{ch}/d\eta >^{1/3}$. Results are from Therminator2 model [this thesis].

According to the predictions of the hydrodynamic models and the results of real measurements, the radius of the source should scale linearly with $< dN_{ch}/d\eta >^{1/3}$ [106]. As Figure 9.7 shows, this is true for the data from the K^-K^- correlation functions from the Therminator2 model. The

results for positively charged kaons and functions in the out, side, and long directions show the same scaling - Appendix B.

9.2 Centrality dependence

The sizes of the particle emitting source, presented earlier in the tabular form, have been plotted on the graph depending on the centrality of the collision. Figure 9.8 shows the results for the $K^0_S K^0_S$ correlation functions for the energy $\sqrt{s_{NN}}$ = 39 GeV. As expected, a larger radius

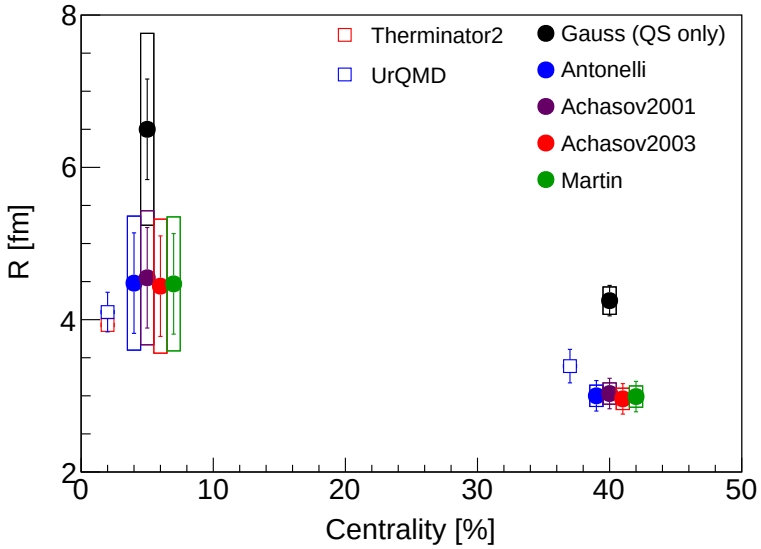

Figure 9.8: Radii of the particle emitting source obtained from neutral kaon femtoscopy versus centrality for Au+Au collisions at $\sqrt{s_{NN}}$ = 39 GeV. Experimental results were placed in the center of the centrality interval, corresponding to 5% for central collisions and 40% for noncentral ones [this thesis].

is observed if the collision is more central. Central collisions have significant statistical and systematic uncertainties. As a result, the agreement between the calculated source sizes from the experiment and theoretical models is better. A similar dependence on centrality is observed in the case of top RHIC energy (Figure 9.9). The obtained radius values for real and simulated data are very consistent. The results for the systems $K^0_S K^+$ and $K^0_S K^-$ are shown in Figure 9.10. As for pairs of neutral kaons, the source size decreases when moving to peripheral collisions. There is a noticeable difference between different sign combinations, especially for central collisions. According to the current state of knowledge, this difference should not be large because they are pairs with similar properties, only the charge of the kaon is different. For

non-central collisions, the consistency between the sizes obtained from the $K^0_S K^+$ and $K^0_S K^-$ correlation functions is high and is within the limit of systematic uncertainty for $K^0_S K^+$.

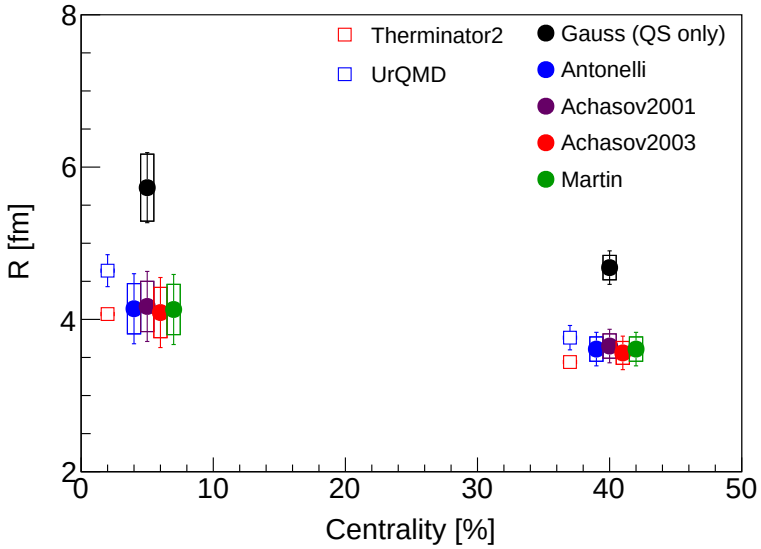

Figure 9.9: Radii of the particle emitting source obtained from neutral kaon femtoscopy versus centrality for Au+Au collisions at $\sqrt{s_{NN}}$ = 200 GeV. Experimental results were placed in the center of the centrality interval, corresponding to 5% for central collisions and 40% for noncentral ones [this thesis].

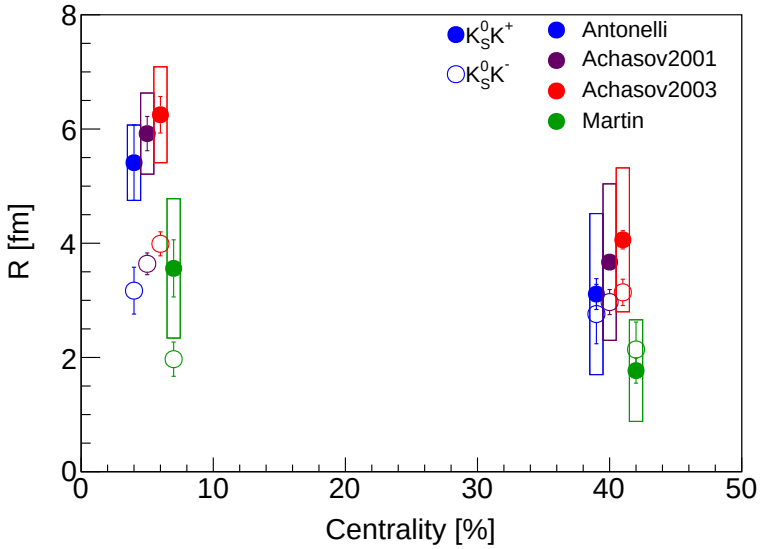

Figure 9.10: Radii of the particle emitting source obtained from $K^0_S K^\pm$ femtoscopy versus centrality for Au+Au collisions at $\sqrt{s_{NN}}$ = 200 GeV. Experimental results were placed in the center of the centrality interval, corresponding to 5% for central collisions and 40% for noncentral ones [this thesis].

9.3 Energy dependence

Another dependence that has been checked is that of collision energy. This was done for the parameters calculated from the correlation functions $K^0_S K^0_S$ with minimum bias collisions and presented in Figure 9.11. An upward trend can be seen, i.e., the higher the collision energy is, the larger the source size is observed. This is true for the Gaussian parameterization (considering only QS effects) and various sets of parameters from the Lednicky-Lyuboshitz model. Comparison with theoretical predictions shows that for $\sqrt{s_{NN}}$ = 200 GeV, the results from UrQMD and Therminator 2 are consistent. In addition, they very well reflect the radius values obtained from the fit, taking into account strong FSI.

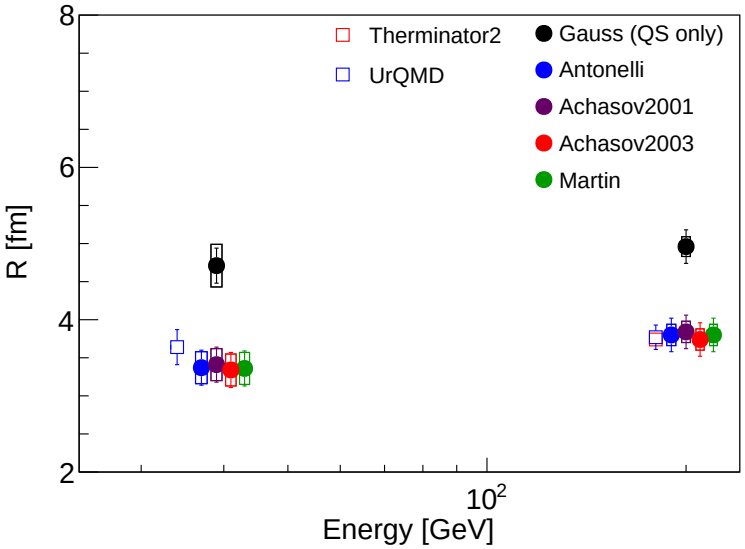

Figure 9.11: Radii of the particle emitting source obtained from neutral kaon femtoscopy versus the energy of minimum bias Au+Au collisions [this thesis].

9.4 Comparison of all data

In the case of the described analysis, it is essential to compare the femtoscopic parameters of the particle emitting source (radius values and correlation strength) for all systems of kaons $K^0_S K^0_S$, $K^0_S K^+$, $K^0_S K^-$ and published $K^\pm K^\pm$ [107]. This will allow studying the structure of the $a_0(980)$ resonance, which is responsible for the strong interaction in the case of $K^0_S K^\pm$ correlation. Over the last fifty years, scientific research shows that a_0 could be a 4-quark state, i.e., tetraquark [89, 90, 91, 92]. Tetraquarks are formed due to a first-order process of directly transferring

existing quarks to the $a_0(980)$ resonance from $K_S^0K^\pm$ collisions. The first step to confirm or reject the assumption about the 4-quark structure of $a_0(980)$ is to check the radius ratio from the $K_S^0K^\pm$ analysis of $K_S^0K_S^0$. The agreement of these values, in the case of elementary collisions (e.g., p+p) and nuclear ones (e.g., Au+Au or Pb+Pb), will be a signature of the tetraquark structure. However, to be sure that this is the structure of the $a_0(980)$ resonance, it is necessary to compare the value of the λ parameter. For p+p collisions, the ratio of λ from the $K_S^0K^\pm$ analysis to that of $K_S^0K_S^0$ should be less than one. Then $a_0(980)$ will be tetraquark. However, for N+N collisions, this ratio must be close to unity (Figure 9.12). Otherwise, the $a_0(980)$ resonance will be a diquark. Figure 9.13 shows a comparison of source sizes for three systems

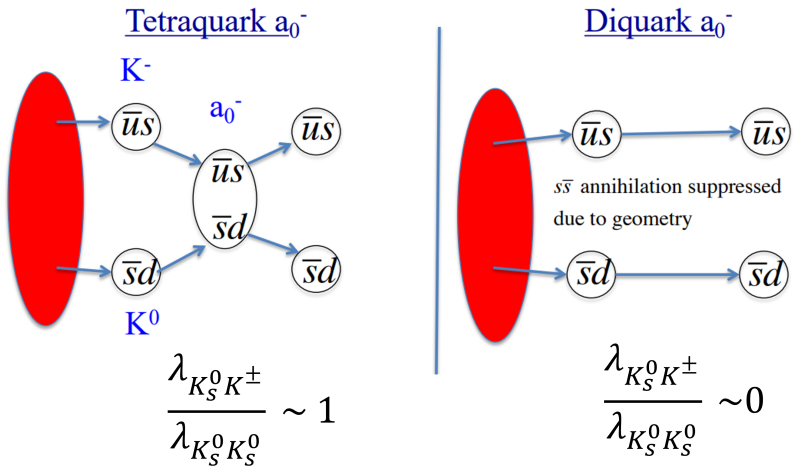

Figure 9.12: Possible states of resonance $a_0(980)$ [108].

for the Antonelli (the top left plot), Achasov2001 (the top right plot), Achasov2003 (the bottom left plot), and Martin (the bottom right plot) parameterizations. As one can see Martin parameter set, characterized by the smaller $a_0(980)$ mass and decay couplings, appear to give source sizes from $K_S^0K^\pm$ smaller than for $K_S^0K_S^0$. The agreement between the results for neutral kaons and $K_S^0K^+$ is observed for central collisions. However, this is due to the significant systematic uncertainty for the $K_S^0K^+$.

The parameters' consistency in non-central collisions is noticeable for the three parameters. On the other hand, there is a visible difference in the obtained sizes of the particle emitting source for central collisions. Antonelli's radius for the $K_S^0K_S^0$ source is between the values calculated for the $K_S^0K^+$ and $K_S^0K^-$ pairs. In turn, Achasov2001 and Achasov2003 parameter sets show the correspondence between the sizes for $K_S^0K_S^0$ and $K_S^0K^-$. The R values for $K_S^0K^+$ deviate from the others and are much more significant. Figure 9.14 shows the results for all systems and parameterizations.

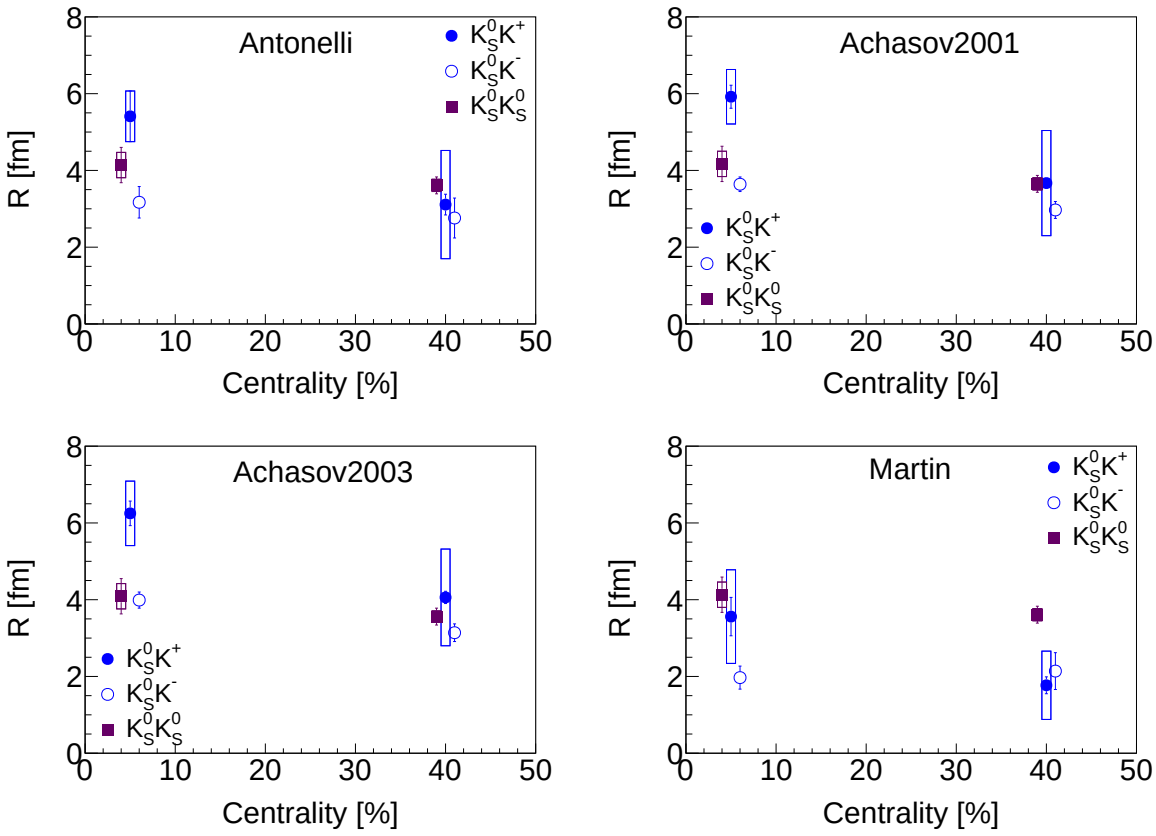

Figure 9.13: Source radius parameters extracted in the analysis from $K^0_SK^0_S$, $K^0_SK^+$ and $K^0_SK^-$ femtoscopy versus centrality for Au+Au collisions at $\sqrt{s_{NN}}$ = 200 GeV. Experimental results were placed in the center of the centrality interval, corresponding to 5% for central collisions and 40% for noncentral ones [this thesis].

In fact, the source sizes for the three kaon systems should be similar. The only reason for the differences could be that the K^0_S and $K^{\pm}$ sources are offset. However, this scenario should not be expected because strong interactions dominate the collision dynamics. These forces are constrained by isospin symmetry. Therefore, it is impossible to unequivocally state that the $a_0(980)$ resonance is a tetraquark. One can only say that Antonelli's parameterization favors such an assumption.

The correlation strength versus centrality results for each parameterization is presented separately in Figure 9.15. The best agreement is noticeable for Martin's parameterization. In the case of $K^0_SK^+$ for the other sets of parameters, the obtained values of λ are much larger (in the order of two times). These results have very large systematic uncertainties. Therefore, drawing unambiguous conclusions is difficult, and more data statistics are needed to be able to say

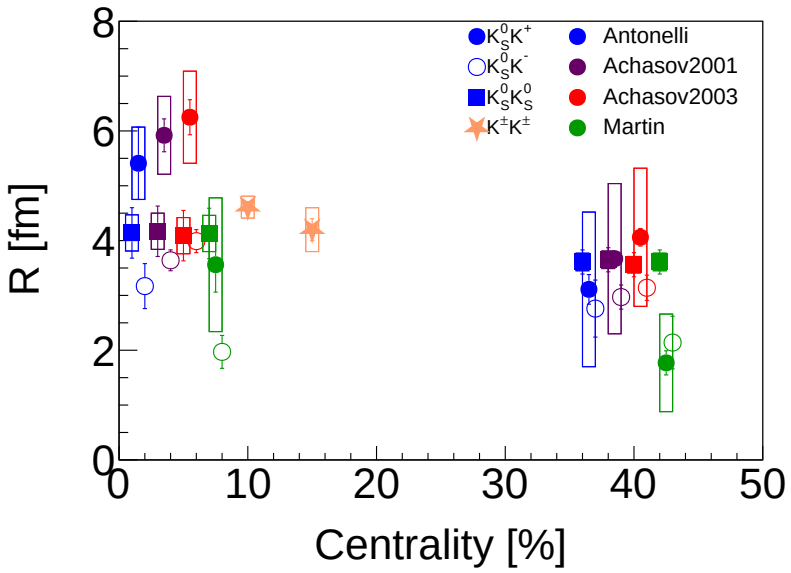

Figure 9.14: Radii of the particle emitting source obtained from the femtoscopy of all kaon combinations versus centrality for Au+Au collisions at $\sqrt{s_{NN}}$ = 200 GeV. Experimental results were placed in the center of the centrality interval, corresponding to 5% for central collisions and 40% for noncentral ones [this thesis]. The results for $K^\pm K^\pm$ come from [107].

something more. All source λ parameter values have been collected in Figure 9.16. There is an explicit agreement between $K^0_S K^-$ and $K^0_S K^0_S$ regarding the uncertainty of $K^0_S K^0_S$.

9.5 Conclusions

This thesis presents the results of neutral kaon femtoscopy from Au+Au collisions at center-of-mass energies $\sqrt{s_{NN}}$ = 39 and 200 GeV. This analysis is the first presentation of $K^0_S K^0_S$ as a function of different centrality and collision energy. In addition, the previously unanalyzed correlation functions of the $K^0_S K^+$ and $K^0_S K^-$ systems obtained from Au+Au collisions at $\sqrt{s_{NN}}$ = 200 GeV appeared in the thesis. Identical and non-identical kaon femtoscopy allows one to extract information about the space-time geometry of the homogeneity length. For each case, the pair-wise interactions between the kaons are different:

- $K^0_S K^0_S$: QS effects, and strong FSI due to the near-threshold $f_0(980)$ and $a_0(980)$ resonances;

- $K^0_S K^\pm$: strong FSI through the $a_0(980)$ resonance.

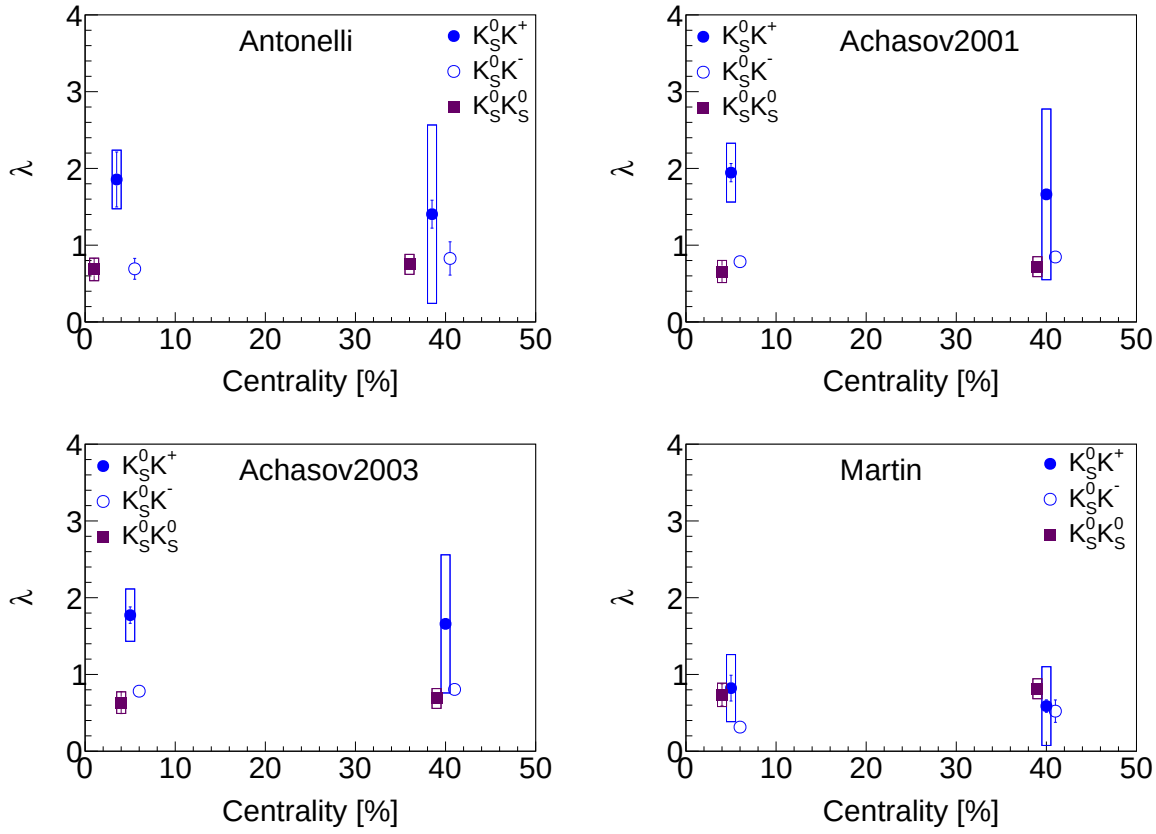

Figure 9.15: Source λ parameters extracted in the analysis from $K^0_SK^0_S$, $K^0_SK^+$ and $K^0_SK^-$ femtoscopy versus centrality for Au+Au collisions at $\sqrt{s_{NN}}$ = 200 GeV. Experimental results were placed in the center of the centrality interval, corresponding to 5% for central collisions and 40% for noncentral ones [this thesis].

The strong interaction plays an essential role in the nature of the interference correlations in detecting the neutral kaon pairs. When parameterizing $K^0_SK^0_S$ correlation functions, it is crucial to include strong FSI. The Gaussian fit assuming the source's spherical shape and considering only QS effects does not describe the dip structure around q_{inv} = 0.1 GeV/c. To perfectly reproduce the shape of the correlation function, the Lednicky-Lyuboshitz analytical model should be used, in which the strong interaction is described by masses and decay couplings of two resonances $f_0(980)$ and $a_0(980)$. The femtoscopic radii obtained from the one-dimentional analysis show dependence on centrality. Source size decrease for non-central events, which reflects a change in the size of the collision region. The parameter determining the correlation strength is in line with the expectations considering the decay of the resonance and the parity of the experimental pairs, i.e., it is in the range of 0.50 - 0.75 [81]. It was also checked how the homogeneity length

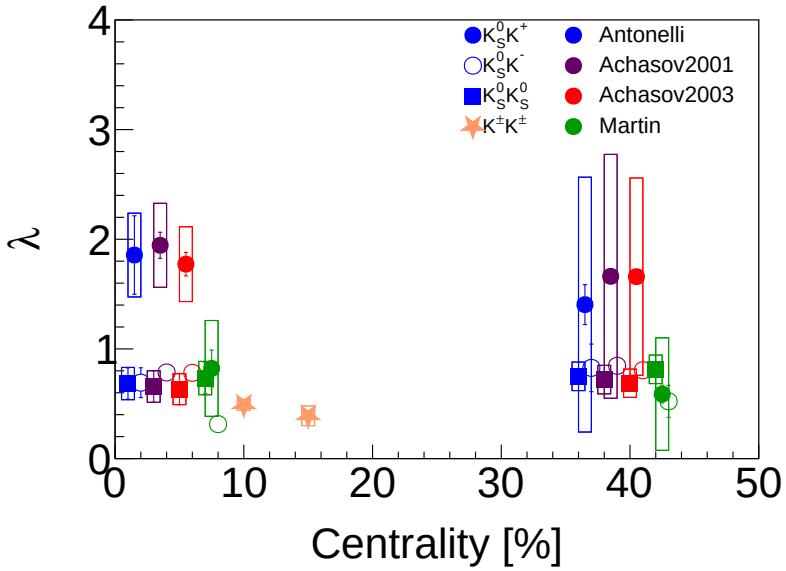

Figure 9.16: λ parameters obtained from the femtoscopy of all kaon combinations versus centrality for Au+Au collisions at $\sqrt{s_{NN}}$ = 200 GeV. Experimental results were placed in the center of the centrality interval, corresponding to 5% for central collisions and 40% for noncentral ones [this thesis]. The results for $K^\pm K^\pm$ come from [107].

changes with the collision energy. As was the case for identical pions [94], also for neutral kaons, the size of the source decreases with decreasing energy. The same trend and radii were obtained from the theoretical predictions of two models: UrQMD and Therminator2. All sizes of the particle emitting source obtained from the $K^0_SK^0_S$ correlation functions show that including the strong interaction in the fit is very important. The Gaussian parameterization gives much larger quantities than expected.

The $K^0_SK^\pm$ pairs interact only with strong FSI through the $a_0(980)$ resonance. There are no QS effects because it is a pair of non-identical particles. There is also no Coulomb FSI because one of the kaons is uncharged. In addition, strong FSI is not caused by the $f_0(980)$ resonance, because the $K^0_SK^\pm$ pair is isospin-1, just like $a_0(980)$. Thus, if there were an effect of $f_0(980)$ with isospin-0, then the isospin of the whole pair would not be conserved. Another important feature of the $K^0_SK^\pm$ pairs interacting via FSI from the $a_0(980)$ resonance is that to conserve the strangeness, only $\bar{K^0}K^+$ pair from $K^0_SK^+$ and K^0K^- pair from $K^0_SK^-$ could form a_0. This makes it possible to examine the $\bar{K^0}$ and K^0 sources separately. The obtained sizes show the expected dependence on the centrality of the collision. However, the difference in the $K^0_SK^+$ and $K^0_SK^-$ radius values for central collisions is surprising. According to the current state of knowledge, these sizes should be close to each other because the difference is only in charge of the kaon.

The reason for this is too small statistics of data collected by the STAR experiment in 2010. Comparison of the femtoscopic source parameters for the $K^0_S K^0_S$ and $K^0_S K^{\pm}$ systems makes it possible to study the properties and structure of the $a_0(980)$ resonance. This is very interesting because many existing publications consider the possibility that $a_0(980)$ is a tetraquark. The evidence for such a resonance structure is the consistency of the size of the homogeneity region and the correlation strength for all combinations of kaons. The results presented in this thesis show that certain sets of parameters in the Lednicky-Lyuboshitz model (in particular Antonelli) favor the $a_0(980)$ resonance as a tetraquark candidate. To ensure the structure of $a_0(980)$, a detailed analysis of more data and a wide energy range should be performed. Such an opportunity will be provided by new data collected from the collisions of gold ions with a stationary target (the Fix Target program in STAR) and from the collisions of two opposite beams (BES-II). This will allow for more detailed measurements, giving lower statistical and systematical uncertainties. This is very important to confirm the hypothesis.

It may also be interesting to perform a three-dimensional analysis of neutral kaons and obtain LCMS out-side-long radii. Thanks to this, it will be possible to extract an average emission proper time for K^0_S based on m_T dependence of R^2_{long}. The results of the ALICE experiment for central Pb+Pb collisions at $\sqrt{s_{NN}}$ = 2.76 TeV indicate that this value is $\sim$ 10 fm/c [81].

In recent years, the study of strong interactions has gained a lot of interest. The presented results are the first step to parameterizing strong FSI for $K^0_S K^{\pm}$ systems and determining the scattering length and the effective radius parameters.

9.6 Future plans

As mentioned earlier, data from Au+Au collisions at $\sqrt{s_{NN}}$ = 200 GeV collected by the STAR experiment in 2010 do not allow one to determine the nature of the $a_0(980)$ resonance. More data statistics are needed to investigate this, i.e., run-16 (about 30 M minimum bias collisions) and another run-23, and run-25. The first results for the 2016 data look very promising. In this case, the same criteria for selecting particles and pairs were used, but there was a difference in the selection criteria of the event. It reduced the $|V_z|$ range from less than 30 cm to less than 6 cm. This change was made due to the excellent acceptance of the new Heavy Flavor Tracker detector inside the TPC.

Figures 9.17, 9.18 and 9.19 show the correlation function corrected to purity for the systems $K^0_S K^0_S$, $K^0_S K^+$ and $K^0_S K^-$ for Au+Au collisions in two centrality ranges 0-10% and 10-30%.

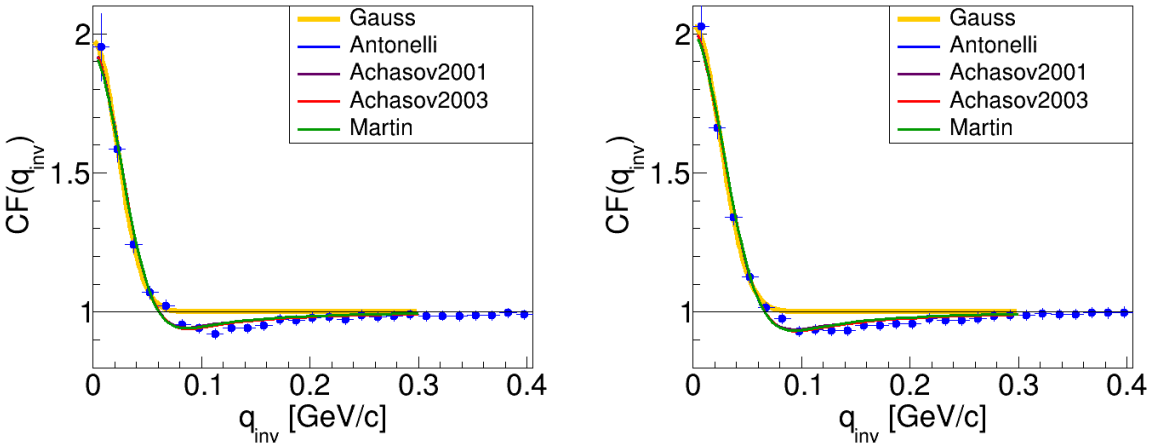

Figure 9.17: The $K^0_S K^0_S$ correlation functions corrected for purity with Gaussian and Lednicky-Lyuboshitz fits for the 0-10% (the left plot) and the 10-30% (the right plot) most central Au+Au collisions at $\sqrt{s_{NN}}$ = 200 GeV from run 2016.

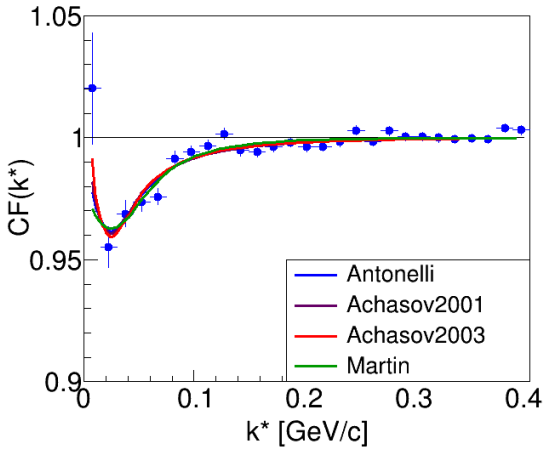

Figure 9.18: The $K^0_S K^+$ correlation functions corrected for purity with Lednicky-Lyuboshitz fits for the 0-10% most central Au+Au collisions at $\sqrt{s_{NN}}$ = 200 GeV from run 2016.

A large amount of data allowed a significant reduce the uncertainties resulting from the statistics, and thus the obtained values of the radius and the λ parameter are more precisely determined. The obtained parameters of the particle emitting source show a clear dependence on centrality - Figures 9.20 and 9.21, which aligns with expectations. The consistency of the results from the $K^0_S K^+$ and $K^0_S K^-$ correlations is also observed. Neutral and negatively charged kaon combinations have a slightly larger radius but are consistent with the second system within uncertainties. The conclusion that can be drawn from the first results for the 2016 data is that the

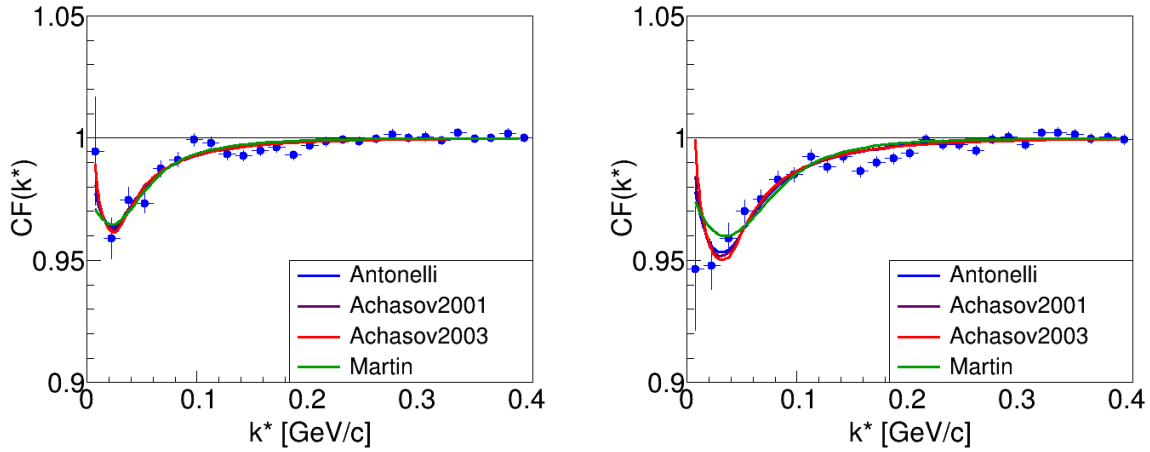

Figure 9.19: The $K^0_S K^-$ correlation functions corrected for purity with Lednicky-Lyuboshitz fits for the 0-10% (the left plot) and the 10-30% (the right plot) most central Au+Au collisions at $\sqrt{s_{NN}}$ = 200 GeV from run 2016.

Achasov parameterizations favor the $a_0(980)$ resonance as a four-quark state, not a combination of two quarks.

From the point of view of modern physics, the study of the structure of resonances is very important. The data of the STAR experiment will allow one to examine this at energies of 200 GeV and lower. The results presented in this chapter will be further analyzed and prepared for publication.

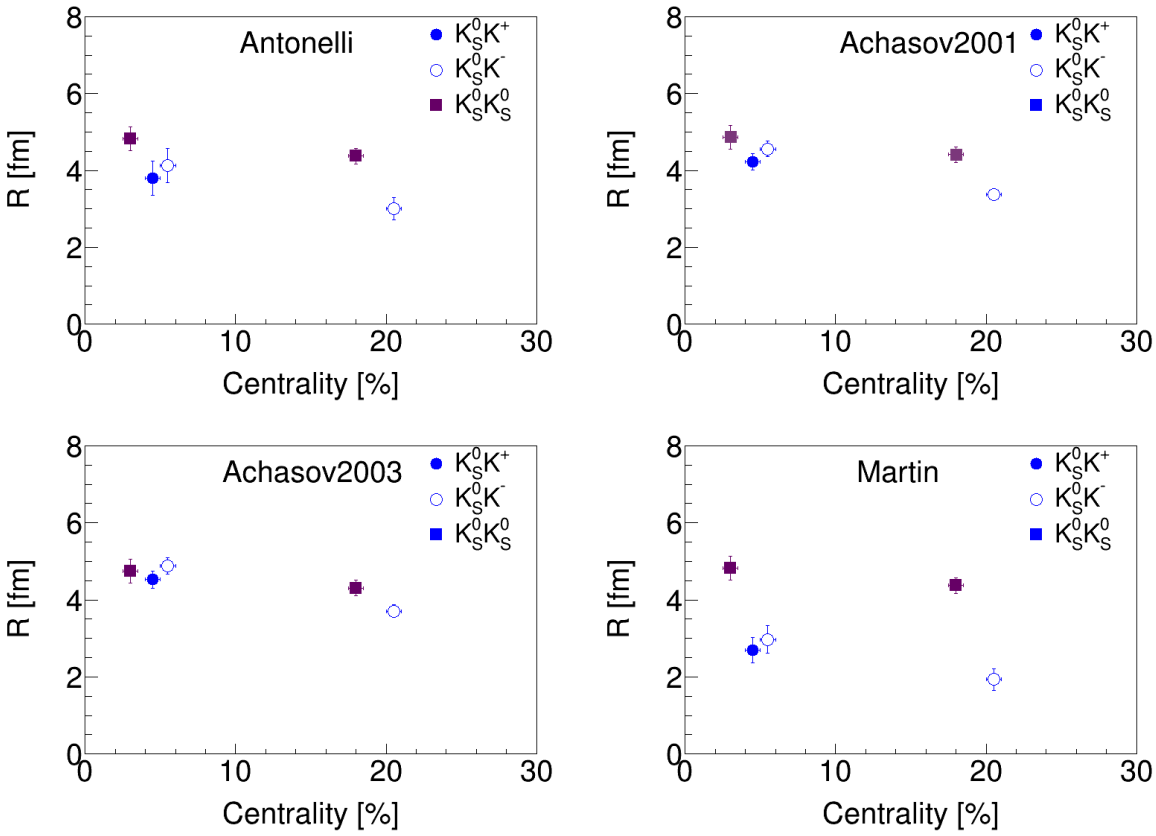

Figure 9.20: Source radius parameters extracted in the analysis from $K^0_SK^0_S$, $K^0_SK^+$ and $K^0_SK^-$ femtoscopy versus centrality for Au+Au collisions at $\sqrt{s_{NN}}$ = 200 GeV. Experimental results were placed in the center of the centrality interval, corresponding to 5% for central collisions and 20% for mid-central ones.

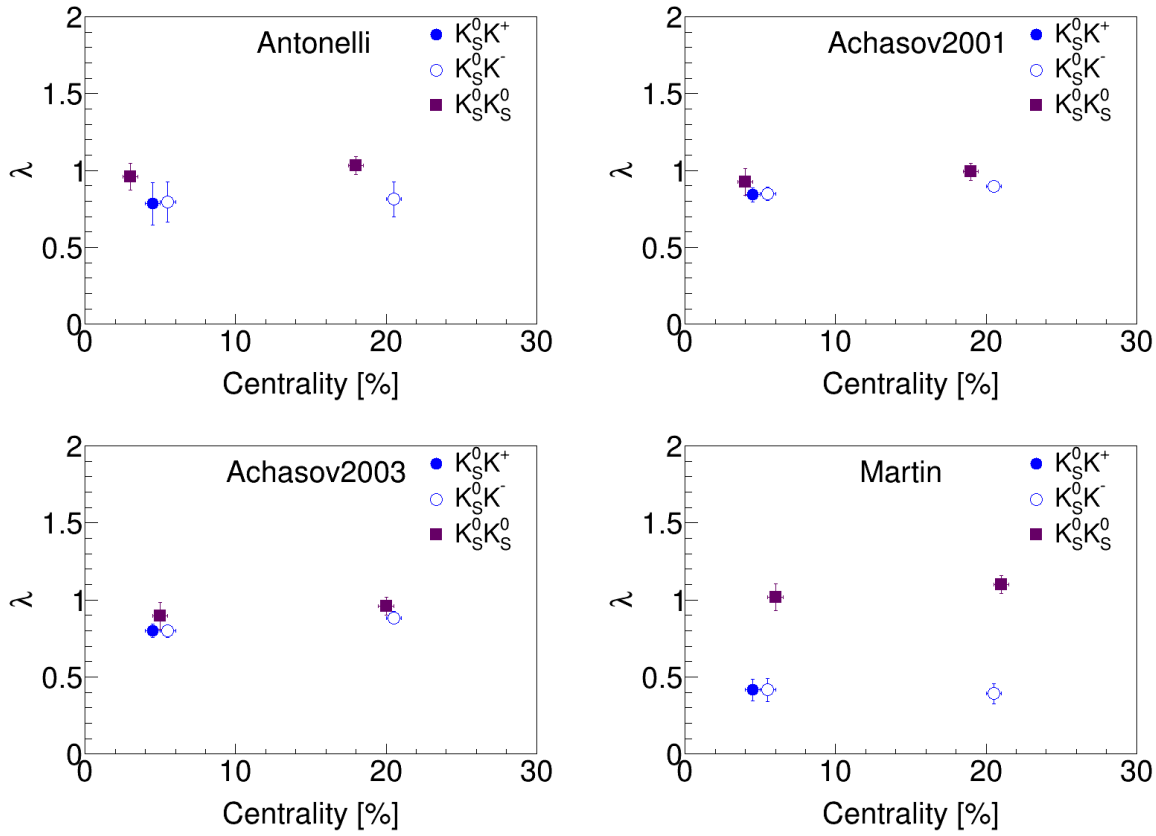

Figure 9.21: λ parameters extracted in the analysis from $K^0_S K^0_S$, $K^0_S K^+$ and $K^0_S K^-$ femtoscopy versus centrality for Au+Au collisions at $\sqrt{s_{NN}}$ = 200 GeV. Experimental results were placed in the center of the centrality interval, corresponding to 5% for central collisions and 20% for mid-central ones.

Glossary

SM - the Standard Model;

QCD - the Quantum Chromodynamics;

QGP - the Quark Gluon Plasma;

BNL - the Brookhaven National Laboratory;

RHIC - the Relativistic Heavy Ion Collider;

AGS - the Alternating Gradient Synchrotron;

STAR - the Solenoidal Tracker At RHIC;

BES - the Beam Energy Scan program;

PHENIX - the Pioneering High Energy Nuclear Interaction eXperiment;

BRAHMS - the Broad RAnge Hadron Magnetic Spectrometers;

TPC - the Time Projector Chamber;

TOF - the Time of Flight;

LHC - the Large Hadron Collider;

CERN - the European Organization for Nuclear Research;

SPS - the Super Proton Synchrotron

ALICE - A Large Ion Collider Experiment;

ATLAS - A Toroidal LHC ApparatuS;

CMS - the Compact Muon Solenoid;

QS - the Quantum Statistics;

FSI - the Final State Interactions;

QED - the Quantum Electrodynamics;

iHKM - the Integrated HydroKinetic Model;

SMASH - the Simulating Many Accelerated Strongly-interacting Hadrons;

UrQMD - the Ultra-relativistic Quantum Molecular Dynamics;

HBT - the Hanbury-Brown-Twiss interferometry;

LCMS - the Longitudinal Co-Moving System;

PRF - the Pair Rest Frame;

DCA - the Distance of Closest Approach;

PV - the Primary Vertex;

DL - the Decay Length;

$\mathbf{V^0}$ - the neutral reconstructed particle.

Appendix A

Signal to background study

In this appendix there are purity distributions of K^0_S as a function of transverse momentum for the most central Au+Au collisions at $\sqrt{s_{NN}}$ = 200 GeV for all analyzed decay lengths. The results show that if the DL is higher, the purity of a single particle is stable in the p_T function, and greater consistency between the individual DCA intervals is observed.

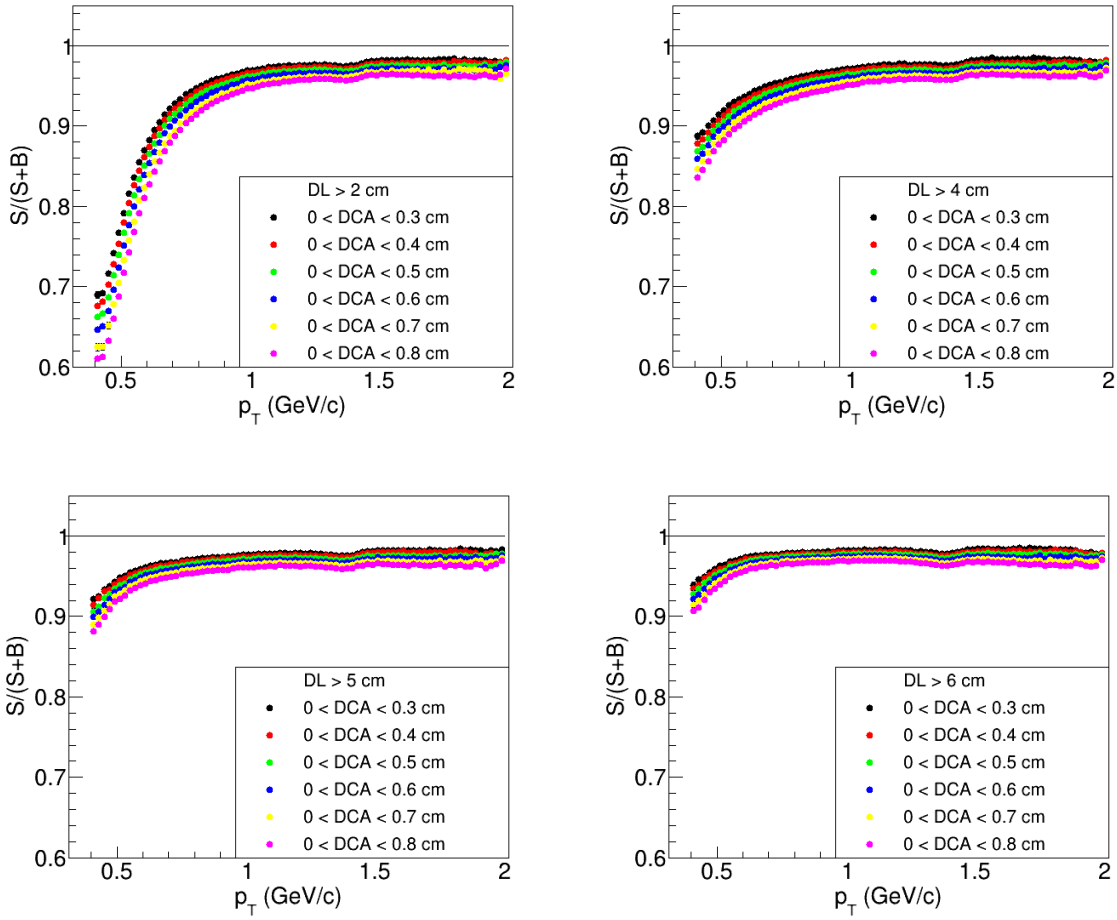

Figure A.1: The purity of K^0_S as a function of transverse momentum for the most central Au+Au collisions at $\sqrt{s_{NN}}$ = 200 GeV for DL > 2, 4, 5 and 6 cm, respectively [this thesis].

Appendix B

Studies of Therminator2

This appendix presents the sizes of the source emitting particles in the *out*, *side*, and *long* directions as a function of m_T and $< dN_{ch}/d\eta >^{1/3}$ for the K^-K^- correlation from Therminator2. Similar relations were obtained for correlation functions K^+K^+. The reduction of the radius, together with the centrality and the m_T range, is a consequence of strong collective flows.

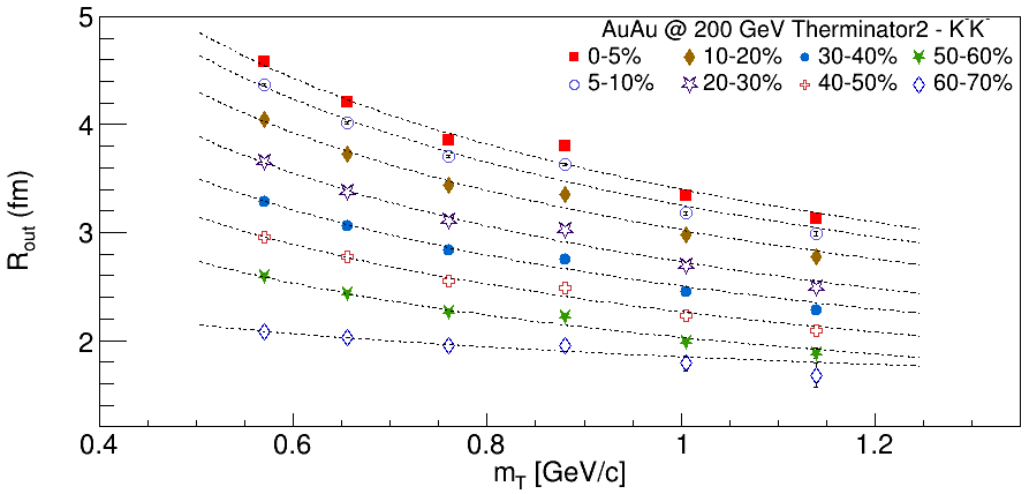

Figure B.1: Femtoscopic radii in *out* direction obtained from K^-K^- correlation functions after applying the Coulomb correction from Au+Au collisons at $\sqrt{s_{NN}}$ = 200 GeV as a function of pair transverse mass. Results are from Therminator2 model [this thesis].

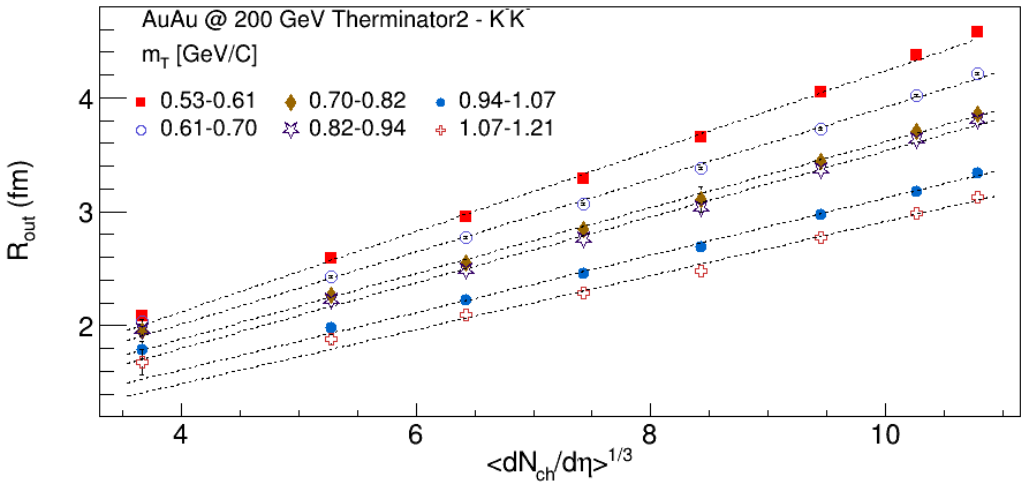

Figure B.2: Femtoscopic radii in *out* direction obtained from K^-K^- correlation functions after applying the Coulomb correction from Au+Au collisons at $\sqrt{s_{NN}}$ = 200 GeV as a function of $< dN_{ch}/d\eta >^{1/3}$. Results are from Therminator2 model [this thesis].

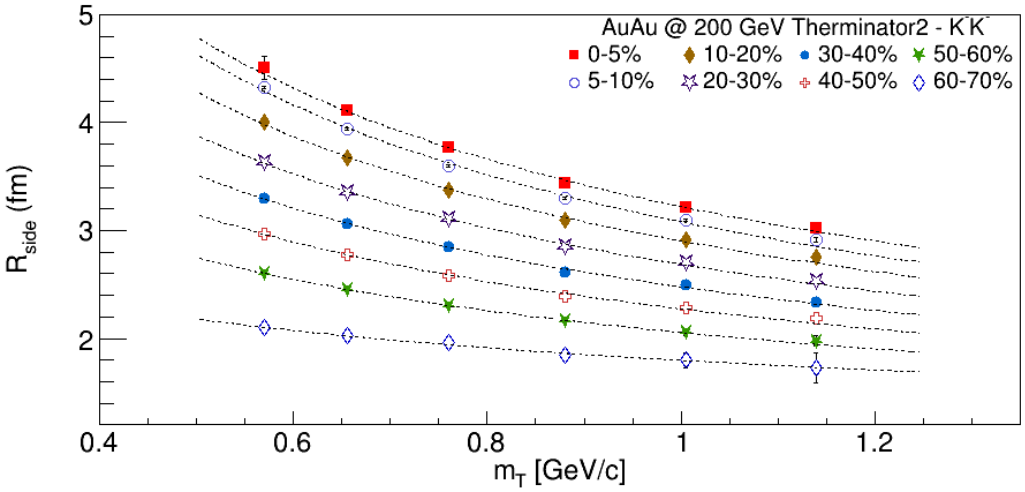

Figure B.3: Femtoscopic radii in *side* direction obtained from K^-K^- correlation functions after applying the Coulomb correction from Au+Au collisons at $\sqrt{s_{NN}}$ = 200 GeV as a function of pair transverse mass. Results are from Therminator2 model [this thesis].

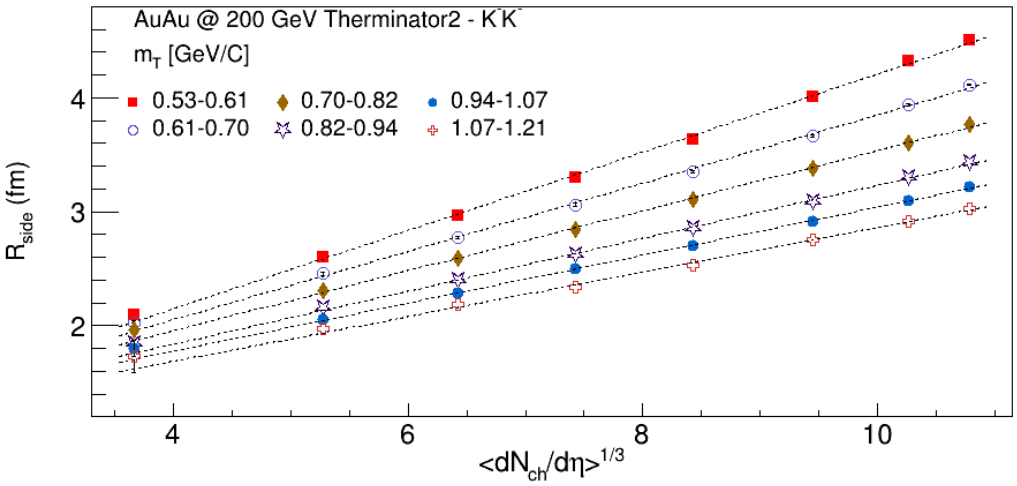

Figure B.4: Femtoscopic radii in *side* direction obtained from K^-K^- correlation functions after applying the Coulomb correction from Au+Au collisons at $\sqrt{s_{NN}}$ = 200 GeV as a function of $< dN_{ch}/d\eta >^{1/3}$. Results are from Therminator2 model [this thesis].

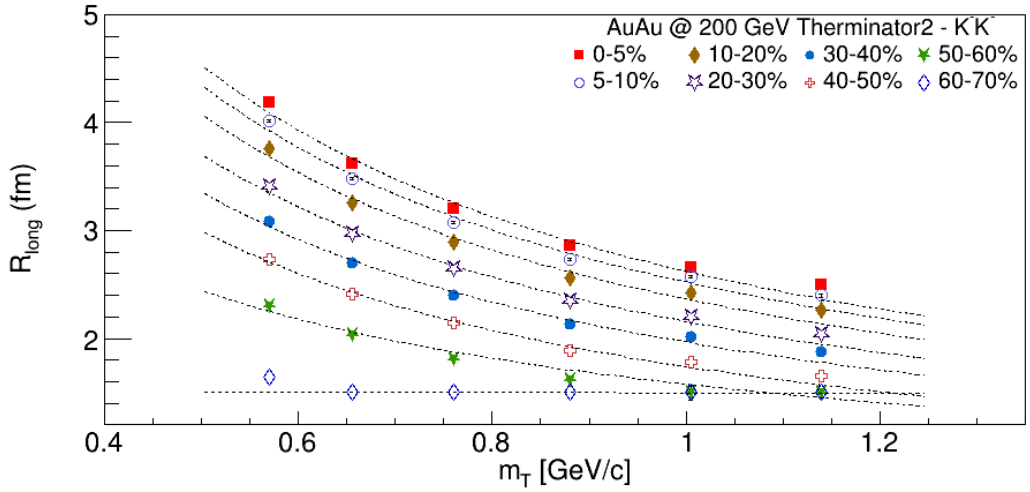

Figure B.5: Femtoscopic radii in *long* direction obtained from K^-K^- correlation functions after applying the Coulomb correction from Au+Au collisons at $\sqrt{s_{NN}}$ = 200 GeV as a function of pair transverse mass. Results are from Therminator2 model [this thesis].

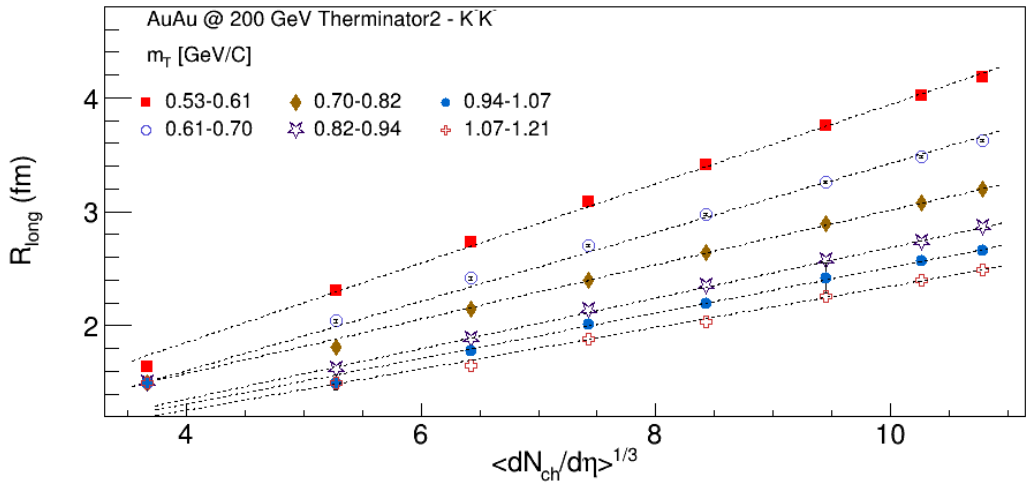

Figure B.6: Femtoscopic radii in *long* direction obtained from K^-K^- correlation functions after applying the Coulomb correction from Au+Au collisons at $\sqrt{s_{NN}}$ = 200 GeV as a function of $< dN_{ch}/d\eta >^{1/3}$. Results are from Therminator2 model [this thesis].

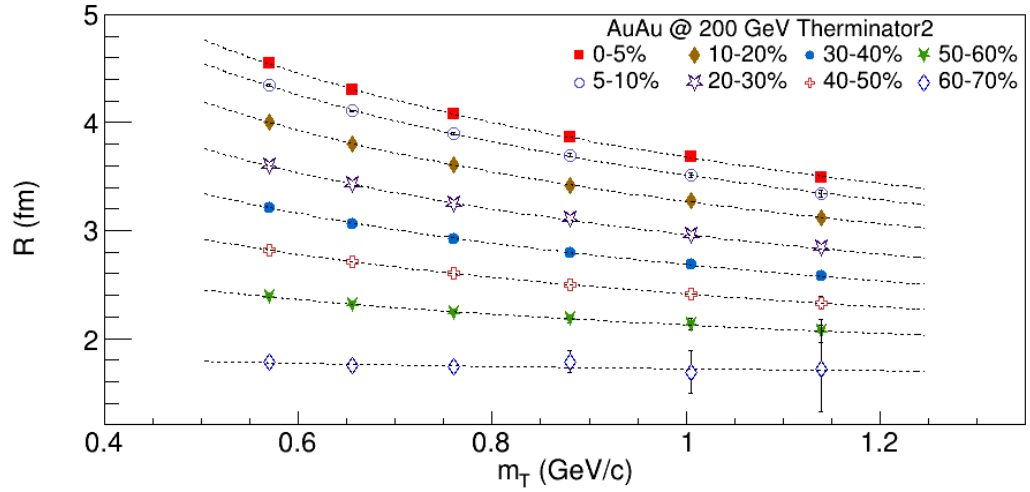

Figure B.7: Femtoscopic radii obtained from K^+K^+ correlation functions after applying the Coulomb correction from Au+Au collisons at $\sqrt{s_{NN}}$ = 200 GeV as a function of pair transverse mass. Results are from Therminator2 model [this thesis].

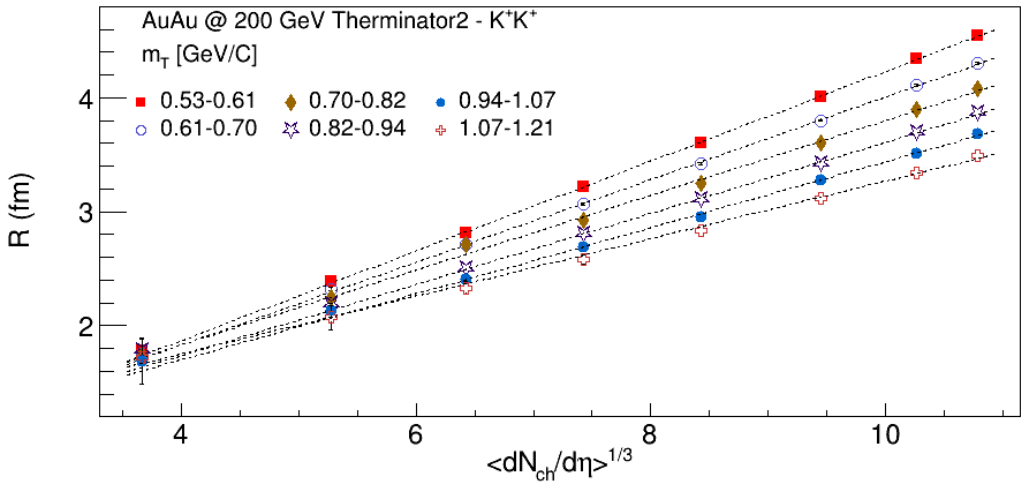

Figure B.8: Femtoscopic radii obtained from K^+K^+ correlation functions after applying the Coulomb correction from Au+Au collisons at $\sqrt{s_{NN}}$ = 200 GeV as a function of $< dN_{ch}/d\eta >^{1/3}$. Results are from Therminator2 model [this thesis].

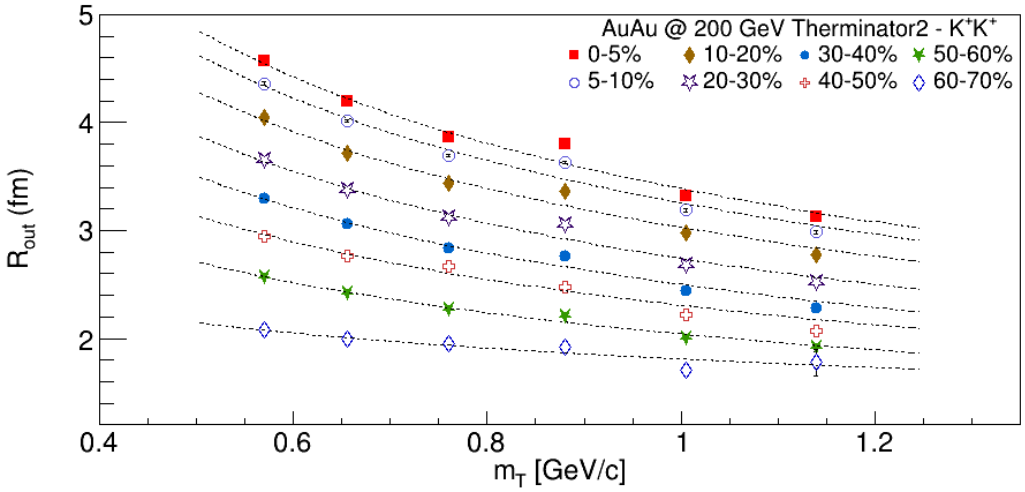

Figure B.9: Femtoscopic radii in *out* direction obtained from K^+K^+ correlation functions after applying the Coulomb correction from Au+Au collisons at $\sqrt{s_{NN}}$ = 200 GeV as a function of pair transverse mass. Results are from Therminator2 model [this thesis].

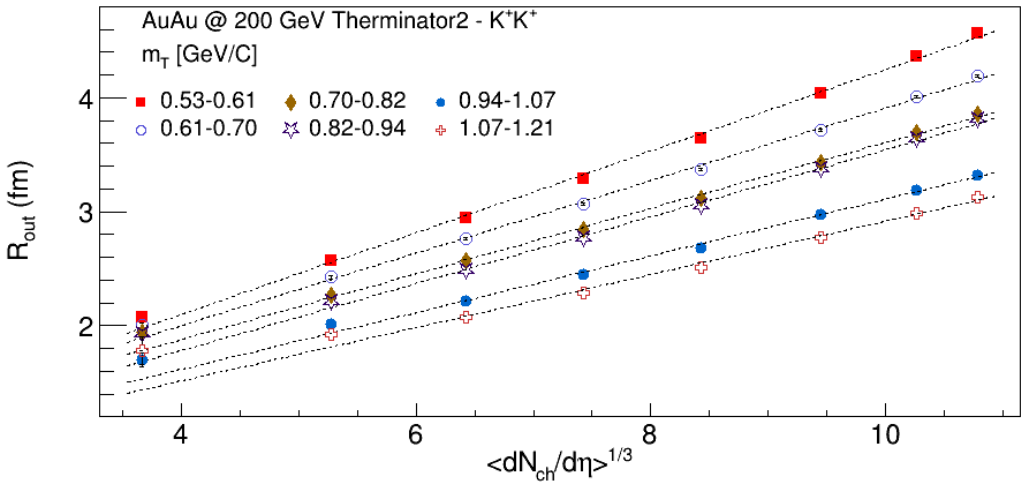

Figure B.10: Femtoscopic radii in *out* direction obtained from K^+K^+ correlation functions after applying the Coulomb correction from Au+Au collisons at $\sqrt{s_{NN}}$ = 200 GeV as a function of $< dN_{ch}/d\eta >^{1/3}$. Results are from Therminator2 model [this thesis].

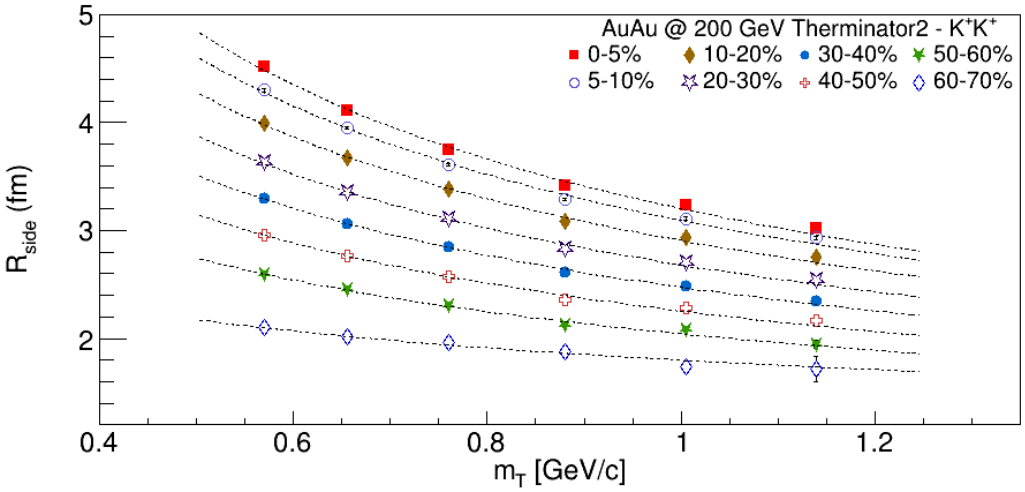

Figure B.11: Femtoscopic radii in *side* direction obtained from K^+K^+ correlation functions after applying the Coulomb correction from Au+Au collisons at $\sqrt{s_{NN}}$ = 200 GeV as a function of pair transverse mass. Results are from Therminator2 model [this thesis].

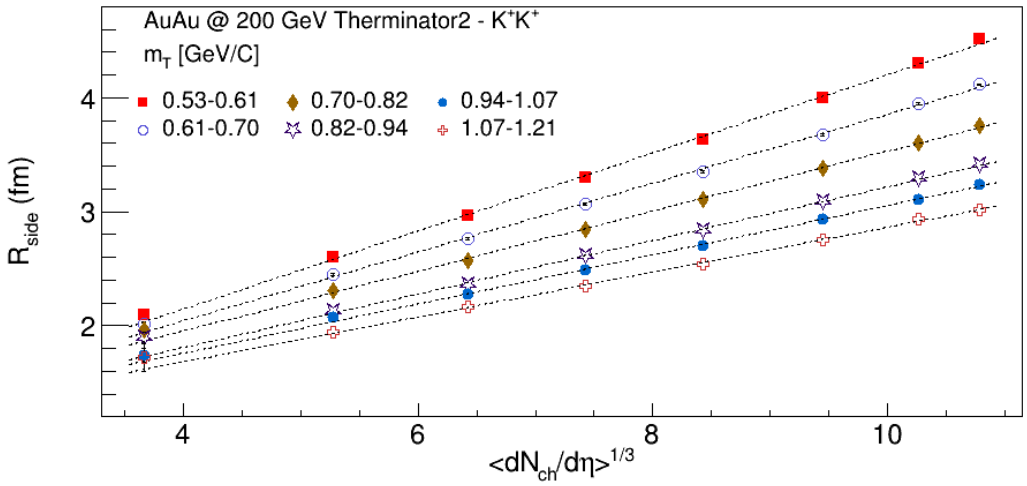

Figure B.12: Femtoscopic radii in *side* direction obtained from K^+K^+ correlation functions after applying the Coulomb correction from Au+Au collisons at $\sqrt{s_{NN}}$ = 200 GeV as a function of $< dN_{ch}/d\eta >^{1/3}$. Results are from Therminator2 model [this thesis].

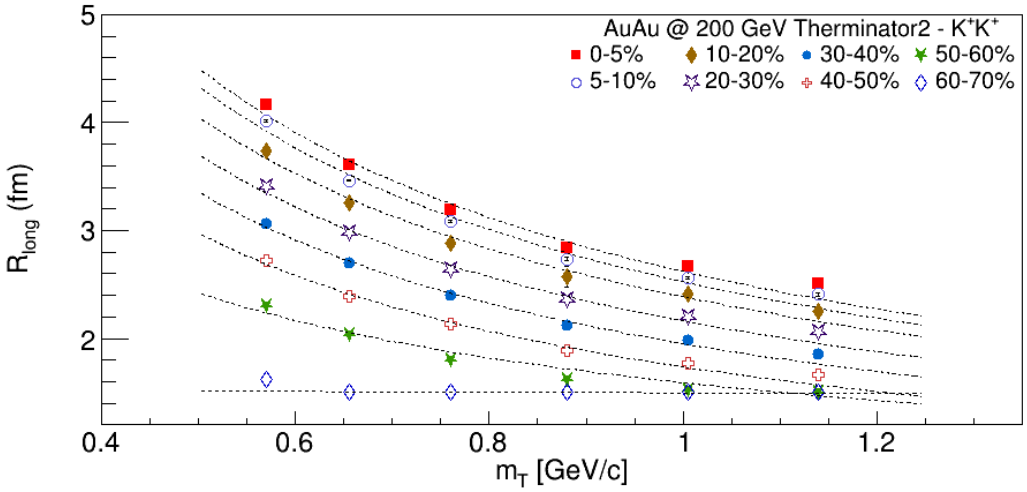

Figure B.13: Femtoscopic radii in *long* direction obtained from K^+K^+ correlation functions after applying the Coulomb correction from Au+Au collisons at $\sqrt{s_{NN}}$ = 200 GeV as a function of pair transverse mass. Results are from Therminator2 model [this thesis].

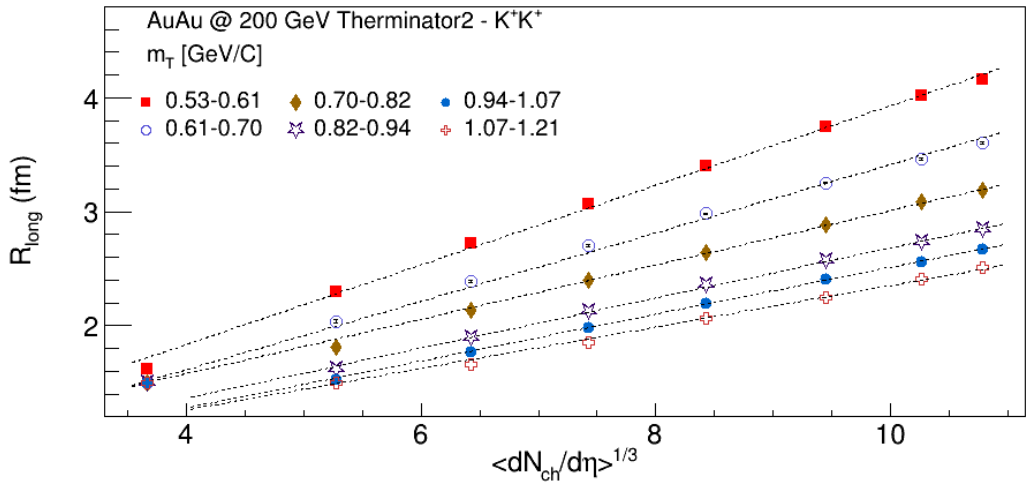

Figure B.14: Femtoscopic radii in *long* direction obtained from K^+K^+ correlation functions after applying the Coulomb correction from Au+Au collisons at $\sqrt{s_{NN}}$ = 200 GeV as a function of $< dN_{ch}/d\eta >^{1/3}$. Results are from Therminator2 model [this thesis].

Bibliography

[1] D. H. Perkins, [*Wstęp do fizyki wysokich energii*], Wydawnictwo Naukowe PWN (2012).

[2] J. Pluta, "Metody i Techniki Jądrowe." access: 17.10.2022.

[3] "Particle Data Group." access: 07.11.2022.

[4] "Teoria neutrin." access: 07.11.2022.

[5] "The Nobel Prize." access: 16.11.2022.

[6] M. Gell-Mann, "A schematic model of baryons and mesons," *Physics Letter* **8**, 214–215 (1964).

[7] J. Bartke, [*Introduction to relativistic heavy-ion physics*], World Scientific (2009).

[8] H. D. Politzer, "Reliable Perturbative Results for Strong Interactions?," *Physical Review Letters* **30**(1346) (1973).

[9] D. J. Gross and F. Wilczek, "Ultraviolet Behavior of Non-Abelian Gauge Theories," *Physical Review Letters* **30**(1343) (1973).

[10] L. Turko, "Looking for the phase transition—recent NA61/SHINE results," *Universe* **4**(3) (2018).

[11] D. Pawłowska, *Badanie zderzeń ciężkich jonów przy pomocy femtoskopowych korelacji układu dwóch protonów*, Master's thesis, Warsaw University of Technnology (2017).

[12] Karpenko, I., Bleicher, M., Huovinen, P., and Petersen, H., "Effects of EoS in viscous hydro+cascade model for the RHIC beam energy scan," *Nuclear Physics A* **956**, 834–837 (2016).

[13] T.Ludlam and S. Aronson, "Hunting the quark gluon plasma," (2005).

[14] H. P. Zbroszczyk, *Studies of baryon–baryon correlations in relativistic. nuclear collisions registered at the star experiment*, PhD thesis, Warsaw University of Technnology (2008).

[15] A. Bialas, M. Bleszynski, and W. Czyz, "Multiplicity distributions in nucleus-nucleus collisions at high-energies," *Nuclear Physics B* **111**(3) (1976).

[16] A. Bialas, M. Bleszynski, and W. Czyz, "Relation between the Glauber model and classical probability calculus," *Acta Physica Polonica* **B8** (1977).

[17] T. Ludlam, A. Pfoh, and A. Shor, "HIJET. A Monte Carlo event generator for p–nucleus and nucleus–nucleus collisions," *BNL-37196* (1986).

[18] A. Shor and R. S. Longacre, "Effects of Secondary Interactions in Proton – Nucleus and Nucleus-nucleus Collisions Using the Hijet Event Generator," *Physics Letters* **B218** (1989).

[19] M. L. Miller and K. Reygers and S. J. Sanders and P. Steinberg, "Glauber Modeling in High-Energy Nuclear Collisions," *Annual Review of Nuclear and Particle Science* **57**(1), 205–243 (2007).

[20] S. Bhatta and V. Bairathi, "An improved method to access initial states in relativistic heavy-ion collisions," *The European Physical Journal C* **82**(855) (2022).

[21] Andersen, E. et al., "Strangeness enhancement at mid-rapidity in Pb Pb collisions at 158-A-GeV/c," *Phys. Lett. B* **449**, 401–406 (1999).

[22] Afanasiev, S. V. et al., "Cascade and anti-Cascade+ production in central Pb + Pb collisions at 158-GeV/c per nucleon," *Phys. Lett. B* **538**, 275–281 (2002).

[23] F. Antinori and others, "Energy dependence of hyperon production in nucleus–nucleus collisions at SPS," *Physics Letters B* **595**(1-4), 68–74 (2004).

[24] B. I. Abelev and others, "Enhanced strange baryon production in au+au collisions compared to p+p at $\sqrt{s_{NN}}$ = 200 gev," *Physical Review C* **77**(4) (2008).

[25] R. Mattiello, H. Sorge, H. Stöcker, and W. Greiner, "K/π ratios in relativistic nuclear collisions: A signature for the quark-gluon plasma?," *Physical Review Letters* **53**(1459) (1989).

[26] B. Muller, "Physics and signatures of the quark-gluon plasma," *Reports on Progress in Physics* **58**(6) (1995).

[27] M. U. Ashraf (on behalf of the STAR collaboration), "Recent Results on Strangeness Production from STAR," *Nuclear Physics A* **1005**, 121815 (2021).

[28] J. Adam and others, "Strange hadron production in Au+Au collisions at $\sqrt{s_{NN}}$ = 7.7, 11.5, 19.6, 27, and 39 GeV," *Physical Review C* **102**(3) (2020).

[29] J. Cleymans and A. Förster and H. Oeschler and K. Redlich and F. Uhlig, "On the chemical equilibration of strangeness-exchange reactions in heavy-ion collisions," *Physics Letters B* **603**(3), 146–151 (2004).

[30] T. Niida and Y. Miake , "Signatures of QGP at RHIC and the LHC," *AAPPS Bulletin* **31**(12) (2021).

[31] T. Sakaguchi (on behalf of the PHENIX collaboration), "Overview of latest results from PHENIX," *Proceedings of Science* **345**(035) (2019).

[32] M. S. Abdallah and others, "Centrality and transverse momentum dependence of higher-order flow harmonics of identified hadrons in Au+Au collisions at $\sqrt{s_{\rm NN}}$ = 200 GeV," *Physical Review C* **105**(6), 064911 (2022).

[33] G. David, "Direct real photons in relativistic heavy ion collisions," *Reports on Progress in Physics* **83**(4) (2020).

[34] M. J. Russcher (on behalf of the STAR collaboration), "Direct photons in d+Au collisionsat $\sqrt{s_{NN}}$ = 200 GeV with STAR," *The Euripean Physical Journal C* **49** (2007).

[35] T. Matsui and H. Satz, "J/ψ Suppression by Quark-Gluon Plasma Formation," *Physics Letters B* **178** (1986).

[36] M. C. Abreu and other, "Observation of a threshold effect in the anomalous J/ψ suppression," *Physics Letters B* **450** (1999).

[37] Z. Hu, N. T. Leonardo, T. Liu and M. Haytmyradov, "Review of bottomonium measurements from CMS," *International Journal of Modern Physics A* **32**(19n20) (2017).

[38] M. Bleicher and E. Bratkovskaya, "Modelling relativistic heavy-ion collisions with dynamical transport approaches," *Progress in Particle and Nuclear Physics* **122**, 103920 (2022).

[39] D. Oliinychenko, "Some models of heavy ion collisions." [online] (december 2015). [access: 29.09.2022].

[40] A. Kisiel, T. Tałuć, W. Broniowski and W. Florkowski, "THERMINATOR: THERMal heavy-IoN generATOR," *Computer Physics Communications* **174** (2006).

[41] M. Chojnacki, A. Kisiel, W. Florkowski and W. Broniowski, "THERMINATOR 2: THERMal heavy-IoN generATOR 2," *Computer Physics Communications* **183** (2012).

[42] V. M. Shapoval and Yu. M. Sinyukov and Iu. A. Karpenko, "Emission source functions in heavy ion collisions," *Physical Review C* **88**(6) (2013).

[43] S. Bass et al, "Microscopic models for ultrarelativistic heavy ion collisions," *Progress in Particle and Nuclear Physics* **41**, 255–369 (1998).

[44] M. Bleicher et al, "Relativistic hadron-hadron collisions in the ultra-relativistic quantum molecular dynamics model," *Journal of Physics G: Nuclear and Particle Physics* **25**(9), 1859–1896 (1999).

[45] H. Petersen and D. Oliinychenko and M. Mayer and J. Staudenmaier and S. Ryu, "SMASH - A new hadronic transport approach," *Nuclear Physics A* **982**, 399–402 (2019).

[46] The UrQMD group, *The UrQMD user guide* (2014).

[47] M. Szymański, *Femtoscopic analysis of baryon correlations in ultra-relativistic heavy-ion collisions registered by ALICE*, PhD thesis, Warsaw University of Technnology (2016).

[48] W. Broniowski and M. Rybczyński and P. Bożek, "GLISSANDO: GLauber Initial-State Simulation AND mOre...," *Computer Physics Communications* **180**(1), 69–83 (2009).

[49] M. Rybczyński and G. Stefanek and W. Broniowski and P. Bożek, "GLISSANDO 2: GLauber Initial-State Simulation AND mOre...,ver. 2," *Computer Physics Communications* **185**(6), 1759–1772 (2014).

[50] P. Bożek and W. Broniowski and M. Rybczyński and G. Stefanek, "GLISSANDO 3: GLauber Initial-State Simulation AND mOre...,ver. 3," *Computer Physics Communications* **245**, 106850 (2019).

[51] H. P. Zbroszczyk, "Adaptation of the THERMINATOR Model for BES Program," *SPIE Proceedings* **11581** (2020).

[52] F. Retière and M. Lisa, "Observable implications of geometrical and dynamical aspects of freeze-out in heavy ion collisions," *Physical Review C* **70**(4) (2004).

[53] W. Broniowski and W. Florkowski, "Strange particle production at RHIC in a single-freeze-out model," *Physical Review C* **65**(6) (2002).

[54] W. Broniowski and W. Florkowski, "Description of the RHIC pT-spectra in a thermal model with expansion," *Physical Review C* **87**(27) (2001).

[55] M.Chojnacki, W. Florkowski, W. Broniowski and A. Kisiel, "Soft heavy-ion physics from hydrodynamics with statistical hadronization - predictions for the Large Hadron Collider," *Physical Review C* **78**(1) (2008).

[56] P. Bożek and I. Wyskiel, "Rapid hydrodynamic expansion in relativistic heavy-ion collisions," *Physical Review C* **79**(4) (2009).

[57] "BNL Nobel Price." access: 10.04.2023.

[58] P. Chaloupka, *Femtoscopy with multi-strange baryons at RHIC*, PhD thesis, Charles University in Prague (2010).

[59] P. Thieberger, "Possible use of synchrotrons as post-acceleration boosters for tandems," *Nuclear Instruments and Methods in Physics Research* **220**(1), 209–210 (1984).

[60] K.H. Ackermann and others, "STAR detector overview," *Nuclear Instruments and Methods in Physics Research Section A: Accelerators, Spectrometers, Detectors and Associated Equipment* **499**(2), 624–632 (2003). The Relativistic Heavy Ion Collider Project: RHIC and its Detectors.

[61] K. Mi, "Femtoscopy of proton, light nuclei, and strange hadrons in Au+Au collisions at STAR," (april 2022). [access: 28.03.2023].

[62] F. Geurts, "STAR BES Overview." [online] (october 2021). [access: 1.12.2022].

[63] G. Odyniec, "The RHIC Beam Energy Scan program in STAR and what 's next ...","
Journal of Physics: Conference Series **455**(012037) (2013).

[64] M. Anderson and others, "The STAR time projection chamber: a unique tool for studying high multiplicity events at RHIC," *Nuclear Instruments and Methods in Physics Research Section A* **499**(2-3), 659–678 (2003).

[65] J. Schambach, "Proposed STAR Time of Flight Readout Electronics and DAQ," *Computing in High Energy and Nuclear Physics, LaJolla, California* **2003**(1) (2003).

[66] W.J Llope and others, "The TOFp/pVPD time-of-flight system for STAR," *Nuclear Instruments and Methods in Physics Research Section A: Accelerators, Spectrometers, Detectors and Associated Equipment* **522**(3), 252–273 (2004).

[67] G. Baym, "The physics of Hanbury Brown–Twiss intensity interferometry: from stars to nuclear collisions," **B29** (1998).

[68] G. I. Kopylov and M. I. Podgoretsky, "Correlations Between the Particles Which Have Small Relative Momenta," (1972).

[69] R. Lednický, "Correlation femtoscopy of multiparticle processes," *Physics of Atomic Nuclei* **67**(1) (2004).

[70] R. Hanbury-Brown and R. Q. Twiss, "A Test of a new type of stellar interferometer on Siriusr," *Nature* **178** (1956).

[71] G. Goldhaber, S. Goldhaber, W. Lee and A. Pais, "Influence of Bose-Einstein Statistics on the Antiproton-Proton Annihilation Process," *Phys. Rev.* **120**, 300–312 (1960).

[72] A.Kisiel, "Non-identical particle femtoscopy at $\sqrt{s_{NN}}$=200 AGeV in hydrodynamics with statistical hadronization," *Physical Review C* **81**(6) (2010).

[73] T. Åkesson and others, "Bose-Einstein correlations between kaons," *Physics Letters B* **155**(1), 128–132 (1985).

[74] A.M. Cooper and others, "A study of KK correlations in pp annihilations at 0.76 GeV/c," *Nuclear Physics B* **139**(1), 45–60 (1978).

[75] W. Florkowski, [*Phenomenology of ultra-relativistic heavy-ion collisions*], World Scientific (2010).

[76] G. Bertsch, M. Gong and M. Tohyama, "Pion interferometry in ultrarelativistic heavy-ion collisions," *Physical Review C* **37** (1988).

[77] H. P. Zbroszczyk, [*Eksperymentalne aspekty badania korelacji femtoskopowych w zderzeniach relatywistycznych ciężkich jonów*], Oficyna Wydawnicza Politechniki Warszawskiej (2018).

[78] A. Kisiel, "Nonidentical-particle femtoscopy at $\sqrt{s_{NN}}$ = 200 GeV in hydrodynamics with statistical hadronization," *Physical Review C* **81**, 064906 (2010).

[79] A. N. Makhlin and Yu. M. Sinyukov, "The hydrodynamics of hadron matter under a pion interferometric microscope," *Zeitschrift für Physik C - Particles and Fields* **39** (1988).

[80] Yu. M. Sinyukov, "Hanbury Brown/Twiss Correlations for Expanding Hadron and Quark - Gluon Matter," *Nuclear Physics A* **498**, 151C–160C (1989).

[81] M. Steinpreis, *Neutral kaon femtoscopy in Pb-Pb collisions at $\sqrt{s_{NN}}$ = 2.76 TeV at the LHC with ALICE*, PhD thesis, Ohio State University (2014).

[82] R. Lednický and V. L. Lyuboshitz , "The influence of final state interaction on two-particle correlations in multiple production of particles and resonances," *Acta Physica Hungarica New Series Heavy Ion Physics* **3**, 93–113 (1996).

[83] L. K. Graczykowski, *Femtoscopic analysis of hadron-hadron correlations in ultrarelativistic collisions of protons and heavy-ions registered by ALICE at the LHC*, PhD thesis, Warsaw University of Technnology (2014).

[84] U. A. Wiedemann and U. Heinz, "Particle interferometry for relativistic heavy-ion collisions," *Physics Reports* **319**(4-5), 145–230 (1999).

[85] K. Aamodt and others, "Femtoscopy of pp collisions at $\sqrt{s}$ = 0.9 and 7 TeV at the LHC with two-pion Bose-Einstein correlations," *Physical Review D* **84**(11) (2011).

[86] M.G. Bowler, "Coulomb corrections to Bose-Einstein corrections have greatly exaggerated," *Physics Letters B* **270**(1), 69–74 (1991).

[87] Yu. M. Sinyukov and R. Lednicky and S. V. Akkelin and J. Pluta and B. Erazmus, "Coulomb corrections for interferometry analysis of expanding hadron systems," *Physics Letters B* **432**(3), 248–257 (1998).

[88] B. I. Abelev and others, "Neutral Kaon Interferometry in Au+Au collisions at $\sqrt{s_{NN}}$ = 200 GeV," *Physical Review C* **74** (2006).

[89] Antonelli, A., "Radiative ϕ decays," *eConf* **C020620** (2002).

[90] N. N. Achasov and V. V. Gubin, "Analysis of the nature of the $\phi \to \gamma\pi\eta$ and $\phi \to \gamma\pi^0\pi^0$ decays," *Physical Review D* **63** (2001).

[91] N. N. Achasov and A. V. Kiselev, "New analysis of the KLOE data on the $\vec{\varphi}\ \eta\pi^0\gamma$ decay," *Physical Review D* **68**, 014006 (2003).

[92] A. D. Martin and E. N. Ozmutlu and E. J. Squires, "The $\pi\pi$ and KK amplitudes, the S^* and the quark structure of 0^{++} resonances," *Nuclear Physics B* **121**(3), 514–530 (1977).

[93] S. Acharya and others, "Measuring $K^0_S K^{\pm}$ interactions using Pb-Pb collisions at $\sqrt{s_{NN}}$ = 2.76 TeV," *Physics Letters B* **774**, 64–77 (2017).

[94] L. Adamczyk and others, "Beam-energy-dependent two-pion interferometry and the freeze-out eccentricity of pions measured in heavy ion collisions at the STAR detector," *Physical Review C* **92**(1) (2015).

[95] J. Adam and others, "One-dimensional pion, kaon, and proton femtoscopy in Pb-Pb collisions at $\sqrt{s_{NN}}$ = 2.76 TeV," *Physical Review C* **92**(5) (2015).

[96] G. Buchalla, "Kaon and Charm Physics: Theory." access: 28.12.2022.

[97] R. Belasevic, [*Neutral kaons*], Springer Berlin (1999).

[98] R. Cahn and G. Goldhaber, [*The experimental foundations of particle physics*], Cambridge University Press (2009).

[99] G. Alexander, "Bose-Einstein and Fermi-Dirac interferometry in particle physics," *Reports on Progress in Physics* **66**(4), 481–522 (2003).

[100] D. Tlusty, *A study of open charm production in p+p collisions at STAR*, PhD thesis, The Czech Akademy of Sciences (2014).

[101] J. Podolanski and R. Armenteros, "III. Analysis of V-events.," *The London, Edinburgh, and Dublin Philosophical Magazine and Journal of Science* **45**(360), 13–30 (1954).

[102] P. Baladrón Rodríguez and others, "Calibration of the momentum scale of a particle physics detector using the Armenteros-Podolanski plot," *Journal of Instrumentation* **16**(06) (2021).

[103] D. Adamova and others, "Elliptic flow of charged pions, protons and strange particles emitted in Pb + Au collisions at top SPS energy," *Nuclear Physics* **894**, 41–73 (2012).

[104] S. Bekele, *Neutral kaon correlation in Au-Au collisions at center of mass energy of 200 GeV per Nucleon Pair*, PhD thesis, The Ohio State University (2004).

[105] S.V. Akkelin and Yu.M. Sinyukov, "The hbt-interferometry of expanding sources," *Physics Letters B* **356**(4), 525–530 (1995).

[106] A. Kisiel, "Measuring the Size and Dynamics of Heavy Ion Collisions with Femtoscopy," *Acta Phys. Polon. B* **45**(12), 2395 (2014).

[107] L. Adamczyk and others, "Freeze-out dynamics via charged kaon femtoscopy in $\sqrt{s_{NN}}$ = 200 GeV central Au+Au collisions," *Physical Review C* **88**(3) (2013).

[108] T. Humanic, "Studying the $a_0(980)$ tetraquark candidate using $K^0_S K^{\pm}$ interactions with ALICE at the LHC." access: 02.03.2023.